Sources of Organic and Inorganic Halogens to the

Polar and Temperate Marine Boundary Layer

Marvin Shaw

Doctor of Philosophy

University of York

Chemistry

August 2011

Abstract

Very short lived halogenated substances (VSLH) are of importance for the transport of reactive halogens to the troposphere and lower stratosphere, whereas molecular halogens are of specific importance to the Marine Boundary Layer (MBL). This thesis describes the field deployment of a ground based gas chromatography mass spectrometry (GC/MS) in the Canadian sub-Arctic for the determination of VSLH in seawater/sea-ice and air with a view to identify dominant sources to the MBL in the region. MBL mixing ratios of VSLH were determined from a surface site (55.28°N, 77.77°W) on the south east of Hudson Bay,(Kuujjuarapik, Canada) during the 19th -27th of February. Elevated mixing ratios of the Volatile Organic Iodine Compounds (VOIC) coincided with airmasses reaching the ground site that had previously transected regions of open water in the Bay (between 10 – 200 km away), suggesting leads/polynyas are the dominant source of VOIC within the region.

This observation is supported by laboratory experiments conducted with artificial sea ice in a cold chamber (School of Earth and Environment, Leeds University) in which physico-chemical properties of the hypersaline brine, sea-ice and the underlying seawater were measured to quantify the vertical transport of a comprehensive range of volatile organic iodinated compounds (VOICs) at air temperatures of -3 and -14 ^{o}C. The results suggest that VOIC gas transfer velocities from diffusion through the sea-ice alone are at least ~60 times lower at -3 ℃ than gas exchange from leads and polynas during the winter (assuming a sea-ice fractional coverage of 0.1). This has significant implications for *in situ* VOIC losses within the brine from chlorination, hydrolysis and photolysis processes and it is unlikely that measurable concentrations of VOICs would survive vertical transport from the underlying seawater to the surface sea ice quasi-liquid layer.

Further laboratory work within this thesis suggests that gaseous I_2 evolution from the oxidation of iodide in the world's oceans by atmospheric ozone is a viable source of iodine to the MBL, but its strongly constrained by the iodide and dissolved organic carbon (DOC) content of the surface ocean.

Contents

List of Figures

List of Tables

Acknowledgements

I would like to thank my supervisor Lucy Carpenter for the opportunity to study such an exciting area of atmospheric chemistry and for being such a good sport over the years. Without the knowledge, guidance and phenomenal patience of such an exceptional academic I truly believe that the completion of my Ph.D studentship would not have been possible. I also wish to thank the Atmospheric Chemistry group of the University of York (past and present); Ruth, Ally, Sarah (despite nearly killing me!), Mustafa, Xiaobing, Jacqui, Katie, Charlotte, Karen, Jimbo, Parthi, Rosie, Martyn and Shalini, for their support and welcome distractions during my study. A big thanks to Kelli, Jaydeene and James for some wild nights out over the years and helping me realise just how much I can drink!

Thanks to all the guys in the "Atmospherics" football team past and present; Rob, James, Jimmy, Gonzalo, Sam, Sean, Steve, Richard, Raph and Lorenz. Football was always a welcome distraction, especially when the labwork wasn't going so smoothly. Best of luck in the chemistry league in the future! Thanks to Adrian and the guys at NCAS for organising such "stimulating" conferences both inside and outside the lecture theatre and re-affirming my belief that learning can be fun.

To the lads in workshops and electronics, thanks for achieving the impossible over the years in turning my over ambitious schemes into working realities. A special thanks to Chris Rhodes in electronics for helping me resolve numerous GC/MS nightmares and taking the time to teach me how to resolve them myself in the future.

Finally to my Mother and Nanna, thanks for supporting me both financially and mentally, particularly during the final 9 months of my Ph.D. I really don't think I would have managed this without your help.

I would also like to thank NERC for the grant that allowed me to do this Ph.D.

Declaration

The candidate confirms that the work submitted in this thesis is his own and that appropriate credit has been given where reference has been made to the work of others. Parts of chapters 3, 4 and 5 have been published in scientific journals with references below.

Chance, R. J. Shaw, M. D. Telgmann, L. Baxter, M. and Carpenter, L. J. A comparison of spectrophotometric and denuder based approaches for the determination of gaseous molecular iodine. *Atmospheric Measurement Technology, 3, 177 – 185,* (2010).

Carpenter, L. J. and Shaw, M. D. Globally important emissions of HOI and I_2 from the sea surface. *manuscript in preparation,* (2011).

Shaw, M. D. Carpenter, L. J. and Parthipan, R. Uptake of ozone and emission of I_2 from iodide solutions in the presence of organic material. *manuscript in preparation,* (2011).

Mahajan, A. S. Shaw, M. D. Oetjen, H. Hornsby, K. Carpenter, L. J. Kaleschke, L. Tian-Kunze, X. Lee, J. D. Moller, S. Edwards, P. Commane, R. Ingram, T. Heard D. and Plane. J. M. C. Evidence of reactive iodine chemistry in the Arctic boundary layer. *Journal of Geophysical Research, 115, 11,* D20303, *doi:10.1029/2009JD013665*, (2010).

Shaw, M. D. Carpenter, L. J. Baeza-Romero, M. T. and Jackson, A. Thermal evolution of diffusive transport of halocarbons through artificial sea ice. *Atmospheric Environment, 45, 35, 6393 – 6402,* (2011).

Chapter 1

Introduction to Atmospheric Halogen Sources and Chemistry

The Earth's atmosphere extends over 100 km from the surface with 90 % of the atmospheric mass residing within the troposphere. Therefore most atmospheric chemistry occurs within this region. The troposphere is the lower most part of the atmosphere typically extending 10 – 17 km from the Earth's surface depending upon latitude and season. At the top of the troposphere there is a transition layer (tropopause), above which air temperature generally increases with altitude into the stratosphere due to enhanced absorption of UV radiation by ozone. This phenomena causes an inversion layer within the tropopause inhibiting vertical transport to the stratosphere, although injections into the lower atmosphere do occur. Clouds, precipitation and atmospheric water vapour are also largely confined to the troposphere, providing important removal mechanisms for atmospheric pollutants.

The lower troposphere from the Earth's surface to 0.5 – 2.0 km in height contains a region of highly turbulent mixing referred to as the boundary layer (BL). This BL is defined as the layer of air directly above the Earth's surface in which the effects of surface (friction, heating and cooling) are felt directly (Garratt, 1992). It is within this region of the atmosphere that most abiotic (chemically produced), biogenic (biologically produced), and anthropogenic (human induced) chemical emissions mainly occur, hence this region is critical is controlling their dispersion, transport and removal mechanisms (Wayne, 2000). This region of the atmosphere, specifically the atmospheric halogen related chemistry therein, is the main focus of this thesis.

1.1 Tropospheric oxidative chemistry

The removal of trace gases within the troposphere is primarily controlled through photolysis and oxidation pathways involving the hydroxyl radical (OH). Removal involving OH essentially controls the "oxidative capacity" of the atmosphere (Prinn, 2003). The global average OH concentration is only $\sim 10^6$ molecules cm^{-3} (Prinn *et al,* 1995), but even at these low concentrations OH is a globally important atmospheric oxidant.

In the troposphere the photodissociation (< 310 nm) of ozone (O_3) in the presence of water vapour is the major source of OH radicals (EQ 1.1 and 1.2). The majority of the excited

atomic oxygen (O(^{1}D)) produced is quenched by N_2 or O_2 back to its ground state (O(^{3}P)) which then recombines with molecular oxygen (O_2) regenerating O_3 (EQ 1.3). The rate of OH production in the atmosphere is dependent upon the quantum yield of O(^{1}D) as a function of wavelength and the relative reaction rates of EQ 1.2 and 1.3.

$$O_3 + h\nu \rightarrow O(^1D) + O_2(^1\Delta_g) \qquad\qquad \text{(EQ 1.1)}$$
$$O(^1D) + H_2O \rightarrow 2OH \qquad\qquad \text{(EQ 1.2)}$$
$$O(^3P) + O_2 + M \rightarrow O_3 + M \qquad\qquad \text{(EQ 1.3)}$$

OH radicals rapidly react with most natural and anthropogenic gases present within the atmosphere, often as the first and rate determining step in their removal. This influences both trace gas lifetimes and the rate of removal of atmospheric pollutants (Levy, 1971). Removal processes within the troposphere are initiated by a combination of oxidation and removal processes. Oxidation via reaction with OH is the dominant removal pathway for many atmospheric pollutants including carbon monoxide (CO), methane (CH_4) and non-methane volatile organic compounds (VOCs). However, the oxidation of atmospheric pollutants by OH can be perturbed by the presence of other trace species such as NO and NO_2 (collectively termed as NO_X) and sulphur compounds (Wayne, 1991).

Under low NO_X conditions, the major fate of OH is reaction with ubiquitous CH_4 (~ 30%) or CO (~ 70%). These reactions produce the reactive species H (EQ 1.4) and CH_3 (EQ 1.5) which subsequently react with O_2 producing the peroxy radicals HO_2 and CH_3O_2 respectively. These peroxy radicals can either cross or self react under low NO_X conditions producing peroxides which are then susceptible to aerosol scavenging or wet deposition processes. As the OH radical involved in this mechanism is generated from O_3 (EQ 1.1 and 1.2), this process represents a significant loss mechanism for O_3.

$CO + OH \rightarrow H + CO_2$

$H + O_2 \rightarrow HO_2$

$HO_2 + HO_2 \rightarrow H_2O_2 + O_2$

$\overline{\text{Net} : CO + OH + HO_2 \rightarrow CO_2 + H_2O_2}$ (EQ 1.4)

$CH_4 + OH \rightarrow CH_3 + H_2O$

$CH_3 + O_2 + M \rightarrow CH_3O_2 + M$

$CH_3O_2 + HO_2 \rightarrow CH_3OOH + O_2$

$\overline{\text{Net} : CH_4 + OH + HO_2 \rightarrow CH_3OOH + H_2O}$ (EQ 1.5)
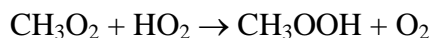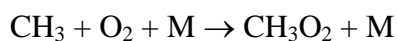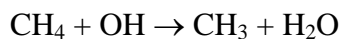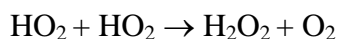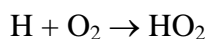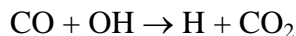
The presence of elevated NO_X concentrations within an airmass perturb this process by altering the fates of the peroxy radicals produced. The peroxy radicals (HO_2 and RO_2) oxidise NO to NO_2, perturbing the predicted photochemical state of NO_X and O_3 in the atmosphere (EQ 1.6 and 1.7) (Crawford *et al.,* 1996). The photolysis of NO_2 is directly responsible for O_3 production during elevated NO_X concentrations. Hence during elevated periods of NO_X concentrations, net O_3 production will occur whilst during periods of low NO_X concentrations O_3 destruction will dominate. This is the only reaction currently known which produces O_3 in the troposphere, highlighting the importance of NO_X chemistry when considering the O_3 budget within this region of the atmosphere.

$HO_2 + NO \rightarrow NO_2 + OH$

$NO_2 + h\nu \rightarrow NO + O(^3P)$

$O(^3P) + O_2 + M \rightarrow O_3 + M$

$\overline{\text{Net} : HO_2 + O_2 \rightarrow O_3 + OH}$ (EQ 1.6)

4

$CH_3O_2 + NO \rightarrow NO_2 + CH_3O$

$NO_2 + hv \rightarrow NO + O(^3P)$

$O(^3P) + O_2 + M \rightarrow O_3 + M$
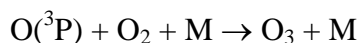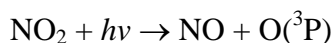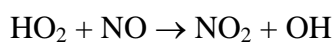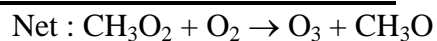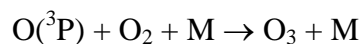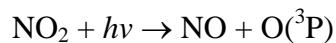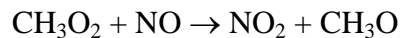
Net : $CH_3O_2 + O_2 \rightarrow O_3 + CH_3O$ (EQ 1.7)

As discussed, O_3 is an important precursor to OH when considering the removal rates of atmospheric pollutants in the lower atmosphere, however in the troposphere it is considered a pollutant in its own right. Elevated concentrations of tropospheric ozone are considered detrimental to agricultural production (Van Dingenen *et al.,* 2009) and air quality, adversely influencing human health (Jerett *et al*., 2009; Sartor, 1995). Tropospheric O_3 is also a significant greenhouse gas contributing to positive radiative forcing of Earth's climate (Houghton *et al.,* 2001).

1.2 Impacts of Tropospheric Halogen Chemistry

Figure 1.1 shows a simplified mechanism for reactive halogen chemistry occuring in the marine boundary layer (MBL), adapted from von Glasow and Crutzen, 2007.
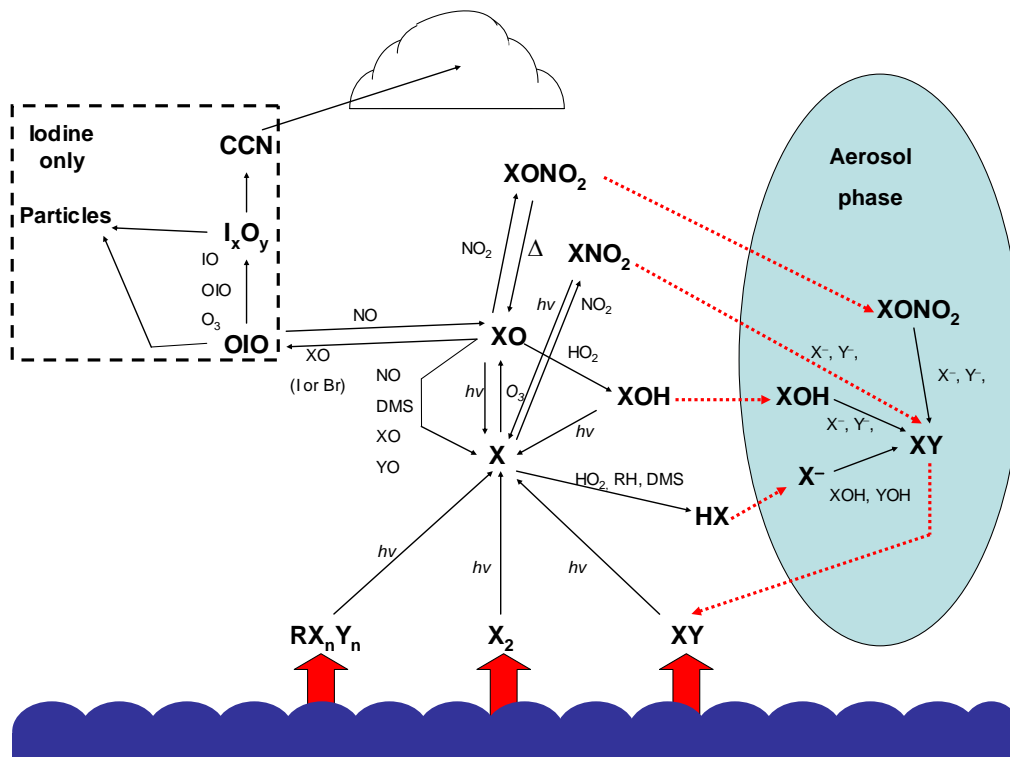
Figure 1.1 Simplified mechanism of reactive halogen cycling in the MBL (adapted from von Glasow and Crutzen, 2007). X and Y = Br or I.

Chemical cycling through the oceans, atmosphere and aerosol, halogens impact atmospheric chemistry in several geographical locations. Halogen-related ozone depletion was first observed in the Arctic boundary layer, with so-called "ozone depletion events" (ODEs) correlated with high bromine monoxide (BrO) concentrations (17 pptv; Barrie *et al.* 1988). Such ODEs are most commonly observed in late winter/early spring in the Arctic (Tarasick and Bottenheim, 2002) and August to October in the Antarctic (Jones *et al.*, 2006), when sunlight returns to high latitudes but temperatures are still low (- 20 ºC). However, ODE are not confined to polar regions. Very high BrO concentrations (up to 176 pptv) were previously observed to coincide with ODE over the Dead Sea in Israel (Matveev *et al.,* 2001). The author suggested that the process responsible for the release of reactive bromine compounds involved the oxidation of salt reservoirs around the Dead Sea.

Halogens also oxidise gas phase mercury causing its deposition to sea ice/snow surfaces, potentially increasing its bioavailability, as discussed in section 4.12 (Schroeder *et al.*, 1998; Slemr *et al.*, 2003). Recent field observations of atmospheric plumes of quiescently degassing volcanoes suggest analogous halogen mediated mercury chemistry caused from the emission of very high concentrations of both gas phase BrO and mercury (Bobrowski *et al.,* 2003; 2007; von Glasow, 2010).

Read *et al.* (2008) suggested that ~ 50% of the daily O_3 depletion observed in the MBL of the tropics may be attributed to the combined contribution of BrO and iodine monoxide (IO), suggesting a widespread influence of halogen chemistry in lower latitudes. Atmospheric halogen chemistry also affects the oxidising capacity of the troposphere through the perturbation of HO_X and NO_X ratios (Bloss *et al*., 2005; von Glasow and Crutzen, 2007), and on regional climate from the formation of ultrafine particles within coastal regions (Mäkelä *et al.,* 2002; McFiggans *et al.,* 2004). The composition of such particles has been shown to be composed of iodine species (Mäkelä *et al.,* 2002), and formation is believed to involve consecutive O_3 and IO self reactions producing higher iodine oxides particles (IOPs) (McFiggans *et al,* 2004). These IOPs can cause enhanced scattering of incoming solar radiation causing a net cooling of the atmosphere through the formation of cloud condensation nuclei (CCN). However, in order to have an influence on global climate significant CCN production would have to occur in the MBL of the open ocean not just coastal regions (Kolb, 2002). Halogens , particularly bromine, also rapidly oxidise dimethyl sulphide (DMS) within the MBL, which is considered to be the most important gaseous precursor for sulphate aerosol CCN over the oceans. The presence of even low concentrations of halogens within the MBL potentially leads to processes that decrease the albedo of stratiform clouds in the MBL (von Glasow and Crutzen, 2004).

The atmospheric lifetimes of halogens directly influence which regions of the atmosphere these species effect chemistry. Iodine species rapidly undergo photolysis, limiting halogen radical production to within the MBL (e.g. I_2 has a photolysis lifetime of ~ 7 s at midday in midlattitude regions). Longer-lived brominated species such as bromomethane (CH_3Br) and

bromochloromethane (CH_2BrCl), with atmospheric lifetimes of $\sim$ 0.9 and 0.4 yr (Wayne *et al.* 1995), respectively, are transported to the stratosphere influencing ozone depletion.

1.2.1 Gas phase halogen chemistry

Halogenated species perturb atmospheric composition and oxidation chemistry through a complicated scheme of gas phase and heterogeneous reactions involving halogen radicals (von Glasow and Crutzen, 2007). Halogen radicals are photochemically produced from precursors such as X_2, XCl, XOH, XONO, $XONO_2$ and RX_n, where X = I, Br or Cl and R = methyl, ethyl or propyl group (Impey *et al.*, 1997; Carpenter, 2003 and references therein; Monks, 2005). The typical fate of these halogen radicals in the troposphere is their rapid catalytic reaction with ozone, forming halogen monoxides (XO) as shown in EQ 1.8. Typical reaction times for EQ 1.8 are $\sim$ 0.1 s for Cl and $\sim$ 1 s for Br and I radicals at background tropospheric O_3 concentrations (Platt and Lehrer, 1996; Platt and Hönninger, 2003). The halogen radicals are then regenerated in a series of reactions including either photolysis or the self reaction of XO (EQ 1.9). If XO photolyzes, both O_3 and X are regenerated and no net reaction occurs (EQ 1.10). The partitioning of X/XO in the atmosphere is largely controlled by the relative rates of XO production (EQ 1.8) and photolysis (EQ 1.10). For instance, gaseous bromine at high O_3 mixing ratios will be prevalently in the form of BrO whereas at low O_3 mixing ratios (<1 ppbv) Br concentrations are more abundant. The catalytic destruction of ozone by halogens provides an alternative route to the production of OH radicals, influencing the oxidative capacity of the atmosphere (EQ 1.11 and 1.12)

$$X^\bullet + O_3 \rightarrow XO + O_2 \qquad\qquad (EQ\ 1.8)$$
$$XO + XO \rightarrow X_2 + O_2 \qquad\qquad (EQ\ 1.9)$$
$$XO + O_2 + hv \rightarrow X^\bullet + O_3 \qquad\qquad (EQ\ 1.10)$$
$$XOH + hv \rightarrow X + OH \qquad\qquad (EQ\ 1.11)$$
$$OH + CO + O_2 \rightarrow HO_2 + CO_2 \qquad\qquad (EQ\ 1.12)$$

For catalytic ozone destruction to occur, XO must efficiently recycle to X radicals without photolysis and the subsequent production of ozone. This occurs via the XO + XO (self

reactions; EQ 1.9), YO + XO (cross reactions; EQ 1.14 – 1.16), the reaction of halogen oxides with hydrogen peroxy radicals (HO_2; EQ 1.27) or in polluted environments, reaction with nitrogen dioxide (NO_2; EQ1.22).

The reactions of halogen oxide compounds are of significant importance for both stratospheric (via ClO and the dimer Cl_2O_2), and tropospheric (IO and BrO) ozone loss (McElroy *et al*., 1999). The lifetime and fates of various XO species are important when considering the relative influence of the various halogen atoms on ozone loss. The atmospheric lifetime of XO species is influenced through photolysis during sunlit periods, with lifetimes varying from several seconds (IO), to two minutes (BrO) and $\sim$ 1 hour (ClO) (Platt and Lehrer, 1996; Platt and Honninger, 2003; Lehrer *et al.* 2004). The high abundance of ubiquitous hydrocarbons in the troposphere (e.g. methane) leads to nearly 50% of the highly reactive chlorine atoms being converted to HCl in the troposphere as shown in EQ 1.13 (Jobson *et al.,* 1994).

$$Cl + RH \rightarrow HCl + R \qquad\qquad\qquad (EQ\ 1.13)$$

Conversely, Br and I atoms react predominantly with O_3, and Br to a more minor extent with aldehydes and olefins. Chlorine atom concentrations are also typically very low in the MBL compared to [Br] and [I]. For a typical tropospheric [Br] to [Cl] ratio of 800 (Boundries and Bottenheim, 2000), chlorine atoms would account for only 2% of ozone depletion. Hence, iodine and bromine radical chemistry are of predominant importance when considering ozone depletion events within the MBL and free troposphere.

Halogen oxide cross reactions (IO + BrO) can increase reaction rates making ozone destruction more efficient if significant concentrations of both halogen oxides exist (Lebras and Platt, 1995). Self or cross reactions of XO are the dominant source of ozone loss in regions of high halogen concentrations. Such reaction cycles have previously been identified as the main cause of polar boundary layer ozone destruction (Barrie et al, 1988). BrO concentrations as high as 18.8 ± 1.0 pptv have been observed in coastal Antarctica during Austral spring (October) (Saiz Lopez *et al.*, 2007). OIO is a product of both the IO

9

self-reaction and the cross reaction of IO with BrO (EQ 1.14 and 1.15). Von Glasow and Crutzen (2007) found the latter to be the dominant source. Formation of OBrO (EQ 1.16) was previously found to be insignificant in reference to its contribution to ozone depletion (Rattigan et al, 1995). The IO self reaction produces OIO (~ 40%) and IOIO (~ 55%) at atmospheric pressure, however the latter is considered thermally labile producing OIO. Hence the net yield of OIO via the IO self reaction is high (Vogt *et al.* 1999; O'Dowd and Hoffman, 2005).

$$BrO + IO \rightarrow BrI + O_2 \qquad\qquad (EQ\ 1.14)$$
$$\rightarrow OIO + Br^{\bullet} \qquad\qquad (EQ\ 1.15)$$
$$\rightarrow OBrO + I^{\bullet} \qquad\qquad (EQ\ 1.16)$$

The photolysis of OIO is critical in determining the ability of iodine species to destroy ozone; only reaction EQ 1.18 will result in the destruction of ozone due to the formation of an iodine radical. Ashworth *et al.* 2002, previously suggested that OIO photolysis to $I + O_2$ is likely to occur within the order of ~ 1 second. If OIO undergoes photolysis to form $O(^3P)$ + IO (EQ 1.17), O_3 is regenerated via reaction EQ 1.19 leading to a null cycle regarding ozone loss. Previous laboratory work by Ingram *et al.* 2000 suggests this is unlikely to occur. If OIO does not undergo photolysis and is converted to a higher iodine oxide, the catalytic species is lost therefore reducing ozone depletion via this reaction pathway.

$$OIO + h\nu \rightarrow IO + O(^3P) \qquad\qquad (EQ\ 1.17)$$
$$\rightarrow I^{\bullet} + O_2 \qquad\qquad (EQ\ 1.18)$$
$$O + O_2 \rightarrow O_3 \qquad\qquad (EQ\ 1.19)$$

The termination of ODEs is likely to occur following the removal of available reactive bromine, through the reactions covered, and from reactions with aldehydes, ketones and alkenes within the MBL (EQ 1.20 and 1.21). Gaseous reactive bromine can also be scavenged onto particles and can also be deposited onto sea-ice/snow pack, seawater and terrestrial surfaces, however as bromine deposited to ice and snow surfaces can be re-released to the atmosphere, only deposition to unfrozen seawater and surface soil

constitutes an actual sink for these species. Another possibility is that the termination of ODEs could be caused by increased vertical mixing between the MBL and the free troposphere. Such phenomena are usually associated with the passage of synoptic systems which disperse the temperature inversion capping the boundary layer leading to the entrainment of ozone to the boundary layer and the transport of reactive bromine to the free troposphere (Lehrer *et al.,* 2004).

$$HCHO + Br \rightarrow HBr + CHO \qquad\qquad\qquad\qquad (EQ\ 1.20)$$

$$BrO + CH_3OO \rightarrow Br + HO_2 + HCHO \qquad\qquad\qquad (EQ\ 1.21)$$

1.2.2 Halogen NO_X chemistry

At sufficiently high NO_x mixing ratios, the production of halogen nitrates ($XONO_2$) can be a significant loss mechanism for XO, EQ 1.22 and 1.23 (Monks, 2005). Once produced, $XONO_2$ can undergo thermal decomposition back to XO and NO_2, photolysis forming $X + NO_3$ or uptake and subsequent photolysis on aqueous surfaces, EQ 1.24, producing hypohalous acids which can re-enter halogen cycles at EQ 1.11.

$$XO + NO_2 \rightarrow XONO_2 + \Delta \rightarrow XO + NO_2 \qquad\qquad (EQ\ 1.22)$$
$$XNO_2 + hv \rightarrow X + NO_3 \qquad\qquad\qquad\qquad (EQ\ 1.23)$$
$$XONO_2 + H_2O \rightarrow HOX + HNO_3 \qquad\qquad\qquad (EQ\ 1.24)$$
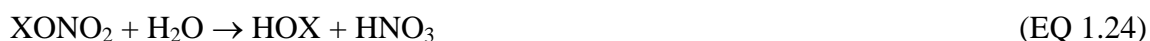
Additionally it has been proposed (Sander *et al.* 1999) that $XONO_2$ can undergo heterogeneous reactions at aerosol surfaces producing reactive halogens without the requirement for acidity, EQ 1.25 and 1.26. However, this reactive halogen pathway is kinetically less favorable ($\sim$ 100 times) than that described in EQ 1.27., hence is expected to play a minor role in the clean MBL. Analogous reactions are expected to exist for iodine and chlorine chemistry.

$$BrONO_2 + Br^-(aq) \rightarrow Br_2\ (aq) + NO_3^-(aq) \rightarrow Br_2(g) \qquad (EQ\ 1.25)$$
$$XONO_2 + Y^-(aq) \rightarrow X_2\ (aq) + NO_3^-(aq) \rightarrow Y_2(g) \qquad (EQ\ 1.26)$$
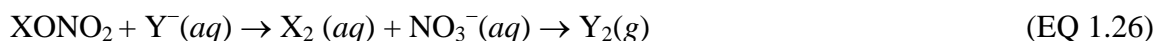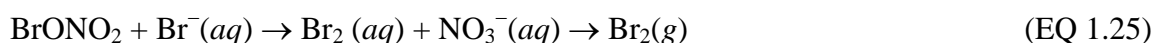
1.3 Sources of halogens to the atmosphere

The primary source of gaseous chlorine and bromine to the MBL (as HCl and Br_2 respectively) is from sea salt aerosol (Duce and Woodcock, 1971, Sander *et al.,* 2003) with minor contributions from organo-bromine and chlorine species such as $CHBr_3$ and $CHCl_3$. (O'Doherty *et al.,* 2001; Carpenter *et al.* 2009). Organo-bromine compounds are the main source of bromine radicals to the free troposphere (von Glasow *et al*., 2004; Yang *et al*., 2005). Approximately $20 - 25\%$ of reactive iodine in the MBL is currently considered to be attributed to short lived iodine precursors such as CH_2I_2, CH_2ICl, C_2H_5I and CH_3I (Carpenter, 2003; Mahajan *et al*., 2010; Jones, *et al*., 2010), with emissions of I_2 dominating in coastal regions (Saiz Lopez *et al.,* 2006; Kupper *et al.,* 2008; Dixneaf *et al.,* 2009).

1.3.1 Sea-ice and sea salt aerosol halogenated source gas emissions

Heterogeneous reactions on various surface types specifically including saline sea-salt aerosol, frost flower structures, saline snow or first year sea ice (FYI) surfaces are the main source of reactive bromine and chlorine radicals to the MBL (McConnell *et al*., 1992; Fan and Jacob, 1992; Foster *et al*. 2001; von Glasow et al., 2004; Kalnajs and Avallone, 2006). These surfaces contain enhanced levels of inactive halides, Br^- and Cl^-. Uptake of hypohalous acids (HOX), formed through reaction EQ 1.27, onto a halide-rich surface initiates an autocatalytic reaction cycle (Vogt *et al.,* 1996) converting Br^- and Cl^- in acidic brine to gaseous BrX. Such reactions require the uptake of strong acids such as H_2SO_4 and HNO_3 (Vogt *et al.,* 1996) prior to activation, or in the case of sea-ice, the precipitation of aqueous buffers such as calcium carbonate-derived carbonate and calcium carbonate (Sander *et al,* 2006). Via this mechanism, two gas phase bromine atoms are potentially released for every bromine atom absorbed, causing an exponential increase in atmospheric bromine which can re-enter the O_3 depletion cycle. This is termed a "bromine explosion", with exponential production of gas phase bromine resulting in a rapid onset of elevated BrO concentrations, ODE and Atmospheric Mercury Depletion Events (AMDE) (Kalnajs and Avallone, 2006). The bromine explosion phenomenon is simplified in figure 1.2.

$BrO + HO_2 \rightarrow HOBr + O_2$

$HOBr\ (g) \rightarrow HOBr\ (aq)$

$HOBr\ (aq) + X^-\ (aq) + H^+\ (aq) \rightarrow BrX\ (g) +\ \ H_2O\ (aq)$ (EQ 1.27)
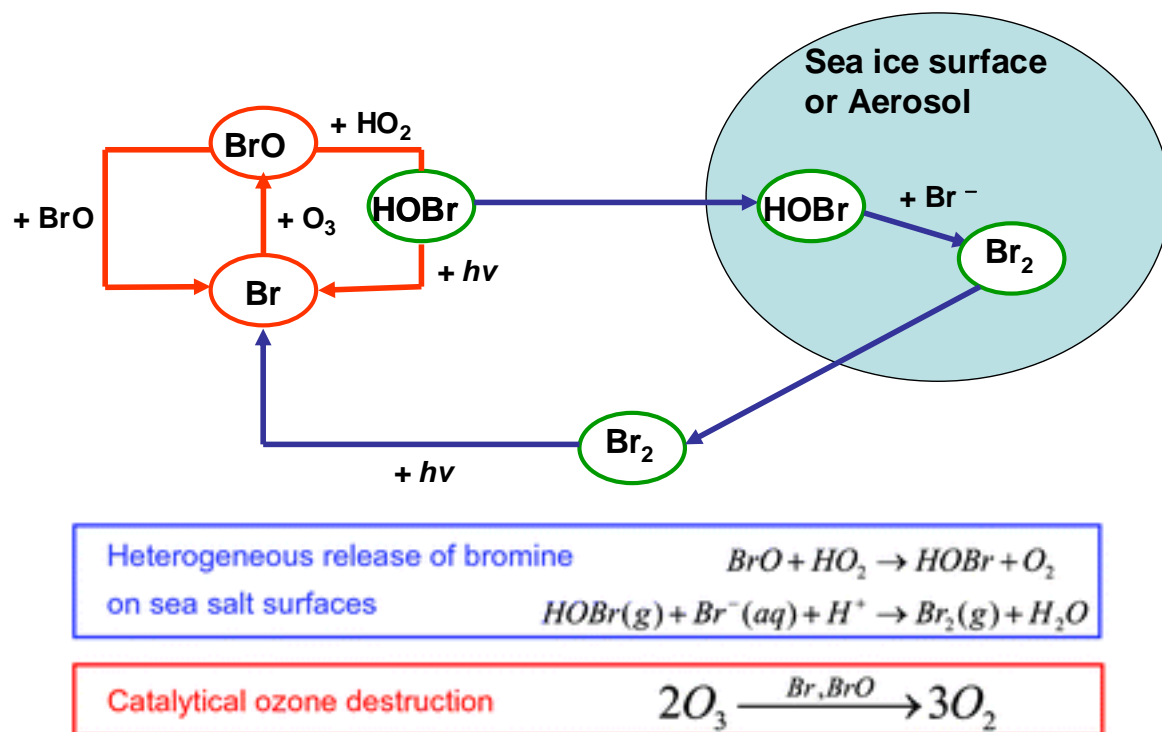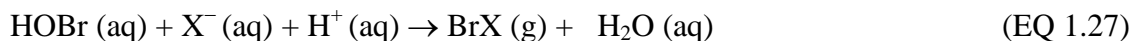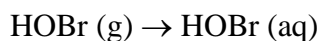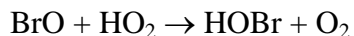
Figure 1.2 A simplified schematic representation of the proposed "bromine explosion" mechanism (Adapted from Frieß *et al.*, 2001).

1.3.2 Organohalogen emissions

Organohalogens are produced by both anthropogenic and natural sources. Anthropogenic emissions generally generate longer lived species which are of particular significance in stratospheric ozone depletion, and were curtailed in the 1980s through legislation (the Montreal Protocol and its subsequent revisions), following the discovery of the Antarctic ozone hole (Molina and Rowland, 1974; Farman *et al.* 1985; Ozone Secretariat United Nations Environment Programme, 2006). Natural sources of halogens (particularly organo iodine species) are generally shorter lived and are of particular importance in tropospheric chemistry, however their sources are not currently fully understood. Table 1.1 shows the

major halocarbon sources to the atmosphere and their atmospheric lifetimes $((\tau_{local})^{-1})$ based upon their lifetimes with respect to OH $((\tau_{OH})^{-1})$ and photolysis $((\tau_{J})^{-1})$.

Source gas	Formula	Local lifetime (days)[a]	Atmospheric source[b]
Trichloromethane	$CHCl_3$	150	AN
Bromochloromethane	CH_2BrCl	150	N
Dibromomethane	CH_2Br_2	120	N
Dibromochloromethane	$CHBr_2Cl$	78	N(A)
Bromodichloromethane	$CHBrCl_2$	69	N(A)
Tribromomethane	$CHBr_3$	26	N(A)
Iodomethane	CH_3I	7	N
Iodoethane	C_2H_5I	4	N
2-Iodopropane	$2\text{-}C_3H_7I$	1.2	N
1-Iodopropane	$1\text{-}C_3H_7I$	0.5	N
Chloroiodomethane	CH_2ICl	0.1	N
Bromoiodomethane	CH_2IBr	0.04	N
Diodomethane	CH_2I_2	0.003	N

Table 1.1 Atmospheric lifetimes of halocarbon source gases (adapted from Wayne *et al.,* 1995).

[a] Local lifetimes are calculated as $(\tau_{local})^{-1} = (\tau_{OH})^{-1} + (\tau_{J})^{-1}$, with [OH] = 1 x 10^6 molecules cm^{-3}, T = 275 K, and a globally and seasonally averaged solar flux for 5 km alltitude.

[b] N = entirely natural atmospheric sources; A = entirely anthropogenic sources; AN = combination of natural and anthropogenic atmospheric sources (minor components shown in parentheses).

1.3.2.1 Biogenic halogenated source gas emissions

The rate of biogenic production of organic and inorganic halogens in the marine environment differs between the open ocean, likely dominated by production by microalgae (phytoplankton) (Wuosmaa and Hager, 1990), and coastal regions, likely dominated by production by macroalgae (kelp beds) (Laturnus, 2000). Coastal regions are inhabited by high densities of macroalgae, however these regions represent only a small fraction of the global ocean. Current global estimates of biogenic iodine flux from macroalgae confined to coastal zones are in of the order of 10^7 -10^8 g I yr^{-1} (Goodwin *et al.,* 1997; Laturnus *et al.,* 2000). Microalgae in the open ocean globally represent a larger biomass than macroalgae and are estimated to contribute in the order of $10^9 – 10^{10}$ g I yr^{-1}.

The biogenic production of mono and poly halogenated organics by marine algae is believed to occur via the enzyme catalysed oxidation of halide ions within the algal tissue. Mono halogenated organics are produced via the the enzyme methyl transferase, present in both micro and macro algae (Wuosama and Hager, 1990). Wuosmaa and Hagner (1990) previously reported a mechanism involving a methyl chloride transferase enzyme, which catalyzes the methylation of halide ions in seawater. Subsequent work yielded CH_3I from incubations of I^- and organic substances in the presence of the methyl transferase enzyme (Itoh *et al.*, 1997).

Similarly, haloperoxidase enzymes present in both macroalgal (Fenical, 1981) and microalgal (Moore *et al.,* 1996) cultures catalyse the production of polyhalogenated organic species. The polyhalogenated organic compounds ($CHBr_3$, CH_2Br_2, CH_2I_2 and CH_2ICl) were previously shown to be produced by the marine diatoms *Nitschia sp., Nitschia arctica* and *Porosira glacialis* grown in laboratory cultures (Moore *et al.*, 1996). The bromoperoxidase enzyme present is capable of oxidizing both I^- and Br^- by H_2O_2, generating an enzyme bound electrophillic halogen (Enz-X^+). A culture of *Navicula sp.* also produced CH_2I_2 and CH_2ICl, but no $CHBr_3$ or CH_2Br_2. This was attributed to the absence of a bromo-peroxidase enzyme and the presence of an iodo-peroxidase enzyme within the algal tissue. The iodoperoxidase enzyme was only capable of oxidizing I^- by H_2O_2. Theiler *et al.,* (1978) suggested that polyhalogenated organics are produced from this enzyme bound proxy from the sequential addition of the Enz-X^+ to the α-carbon of a ketone functionality analogous to the haloform reaction.

Hydrogen peroxide is required for the haloperoxidase-mediated production of poly halogenated organics and is produced when macroalgae are subject oxidative stress. Oxidative stress of macroalgae occurs during low tide periods when algae are exposed to strong oxidants in air (OH and O_3). Low tide periods correlate with previously observed enhanced organic and inorganic halogen emission to the MBL (Laturnus *et al.,* 2000; Palmer *et al.,* 2005). The biogenic production rates of halogenated organics are also considerably higher during enhanced illumination (Moore *et al.*, 1996). This phenomena is

likely to be related to the increased production of H_2O_2 during photosynthesis (Cooper *et al.*, 1981).

The biological function of inorganic iodine species produced by marine algae is currently unknown, however it has been suggested that they may act to deter the grazing of zooplankton. Alternatively, they may simply be a by-product of the intra and inter cellular removal of the toxic oxidant H_2O_2 from algal tissue (Manley and Barbero, 2001).

1.3.2.2 Abiotic halogenated source gas emissions

Previous observations in the North Atlantic ocean suggested that surface saturation anomalies of CH_3I were strongly correlated with light intensity (Happell and Wallace, 1996). Moore and Zafiriou (1994) suggest a photochemical production mechanism for mono-halogenated organics in seawater based upon previous field and laboratory observations following exposure of filtered seawater to sunlight. It was suggested that methyl (CH_3) radicals were formed from the photolysis of dissolved organic matter (DOM) and hydroxyl radicals followed by subsequent recombination with iodine atoms. Martino *et al.* (2009) recently reported observing the production of the VIOCs CH_2I_2, $CHClI_2$ and CHI_3 in seawater when exposed to ambient levels of gaseous ozone. The results within this study suggested that 1% ($\pm$ 0.3%) of the iodide oxidized by ozone reacts with organic matter in natural seawaters to form reactive VIOC. The production of VIOC can be explained by the haloform or a haloform type reaction, in which IOH (or I_2) reacts with dissolved organic compounds (DOC) containing hydrogens α- to keto groups.

1.3.3 Terrestrial halogenated source gas emissions

Over 3500 halogenated species are known to be produced by terrestrial sources such as bacteria, funghi, lichens, marine algae, plant life, insects and mammals (Gribble, 2003). The production of methyl halides by wood rotting fungi through methyl transferase activity has previously been observed (Harper *et al.,* 1985). The oxidation of bromide and chloride by microbial haloperoxidase activity, analogous to that observed in marine algae (section 1.3.2.1), has previously been identified in organic rich soils (Laturnus *et al.* 1995). Subsequent halocarbon production from oxidation during the degradation of organic

material in soil was speculated (Laturnus *et al.*, 1995). Similarly, the emission of the halocarbons CH_3I, CH_3Br and $CHCl_3$ has previously been observed from peatland ecosystems (Dimmer *et al.,* 2000).

Keppler *et al.* (2000) describes a terrestrial abiotic production mechanism of RX in organic rich soils involving the synchronous oxidation of 2-methoxyphenol by ferrihydrite ($5Fe_2O_3·9H_2O$), the most abundant precipitate of iron oxyhydroxides in nature, and the nucleophillic substitution of the methyl group by halide, EQ 1.28. This reaction is specific for mono-iodinated organics, as C_2H_5I and $2/1\text{-}C_3H_7I$ are generated by ethoxyphenol and propoxyphenol respectively. The low RX yields generated during laboratory studies suggest that further oxidation products of methoxyphenol are present, in particular the formation of a methoxyphenol dimer in clay soils (Desjardins *et al.*, 1999). This RX production mechanism could also be of importance within coastal systems subjected to freshwater drainage. Such drainage could possibly contribute to the transport of alkoxylated phenolic structures and minerals from terrestrial soils to coastal seawater.

(where X = Br, Cl, I)   (EQ 1.28)
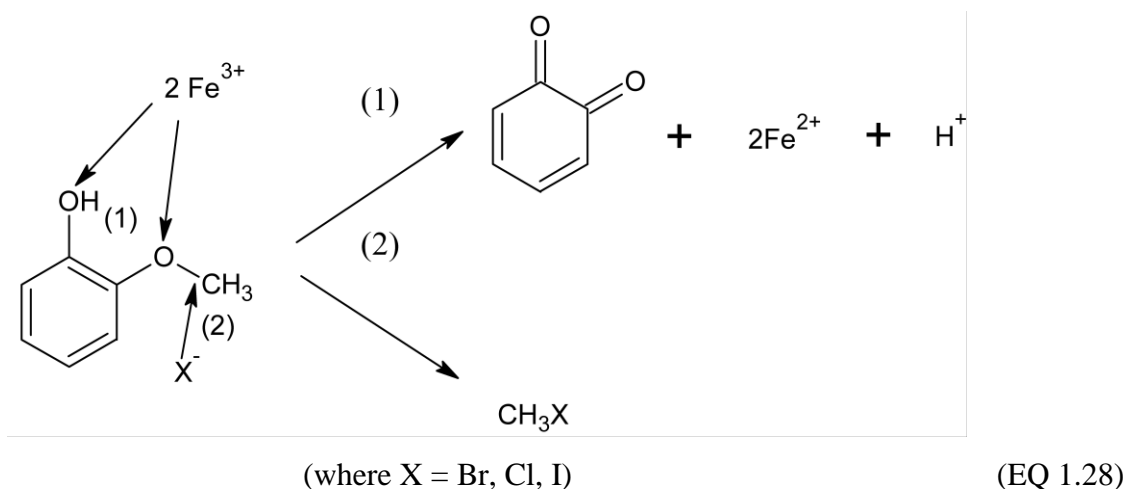
Equation adapted from Keppler *et al.,* 2000.

The emission of mono-halogenated organics have also previously been observed from natural wetlands, rice paddies and biomass burning and it has been suggested that these sources could contribute as much as 30% of the measured levels of CH_3I (Redeker *et al.*, 2000).

Further discussion involving potential iodine sources in temperate ocean regions and factors effecting organohalogen emissions in Polar Regions can be found in section 1 of Chapter 3 and 4 – 5 respectively.

1.4 Thesis outlne

This thesis has two primary objectives. The first objective is to investigate factors influencing the potential abiotic production and emission of I_2 in open ocean regions from the oxidation of aqueous I^- in the presence of gaseous O_3. The second objective is to identify the sources and fates of VSLH trace gases in the MBL of polar regions during periods of sea ice cover.

Chapter 3 describes the development and optimization of a novel spectrophotometric method for the determination of gaseous I_2 and its implementation in laboratory investigations which recover previous work into gaseous I_2 production rates from the $O_3 + I^-$ reaction (Garland *et al*., 1981; Rajendran, 2008). The work represents the first investigation into the effect of dissolved organic matter (DOM) in seawater on gaseous I_2 evolution at the sea surface.

Chapter 4 describes a field campaign conducted in the Canadian sub Arctic to contribute to the existing limited dataset of Arctic VSLH measurements, in the marine boundary layer (MBL). This was conducted to investigate the relative/combined roles of frost flowers, sea-ice/snow pack, sea salt aerosol and biological sources in releasing halogens to the Arctic atmosphere and further develop the understanding of the role of iodine (in concert with bromine) in Arctic gas phase photochemistry, aerosol production and evolution.

Chapter 5 details a laboratory investigation conducted to obtain a better understanding of the mechanisms of sea - air gas exchange in ice-bearing waters and to assess the impact of temperature-dependent sea ice microstructure evolution on the bulk diffusive gas transport of iodocarbons through sea ice. The temperature-dependent iodocarbon diffusion rates through sea ice and the sea-ice-air fluxes determined can be used to better parameterize existing atmospheric chemistry and climate models of Polar Regions**.**

Chapter 2

Experimental Methods

2. Experimental

Sample analysis in this study was carried out using a either a Perkin Elmer (USA) Clarus 600 gas chromatograph/Turbomass Quadrupole Mass Spectrometer (GC/MS) interfaced with a Perkin Elmer Turbomatrix Thermal Desorption Unit (TDU) or a Perkin Elmer dual beam Lambda 25 UV-Vis spectrophotometer. This chapter provides details of the methods of analyte pre-concentration, chromatographic separation, detection and calibration for all samples collected as part of chapters 3, 4 and 5.

2.1 Analyte pre-concentration and injection

Thermal desorption methods trap the compounds of interest on a solid chemical absorbent which is then heated above their boiling points to effect desorption. The TDU can be operated in two modes, online sampling and tube desorption. The tube desorption facility, not utilized in this study, facilitates a two stage desorption process whereby the sample is initially trapped onto chemical adsorbant(s) within the tube then desorbed and trapped on the TDU trap. The online sampling facility, used solely within this study, uses an empty tube heated to 100°C which delivers the sample gas directly to the TDU trap, figure 2.1. Online samples can be trapped for up to 1 hour at flow rates ranging between 10 – 100 ml min^{-1}. The valve (4 port, 2 way Valco) was in position A which connects the sample flow path to the cold trap and inlet split. The inlet split was not used during any part of this study.

Very short lived halogenated substances (VSLHs) are pre-concentrated on the chemical adsorbent trap ("Air monitoring trap" with activated charcoal-based adsorbent, Perkin Elmer) which is held at -30ºC using Peltier plates. Any remaining unretained components and carrier gas are exhausted through the desorb flow vent. Sample injection was achieved by flash heating of the trap to 300ºC whilst sweeping the adsorbent bed with carrier gas, transferring any volatile compounds onto the GC column in a narrow band, figure 2.2. To minimise analyte loss and subsequent carryover within the system, both the valve and the transfer line between the TDU and GC/MS are maintained at elevated temperatures for all analyses, 200ºC and 250ºC, respectively.
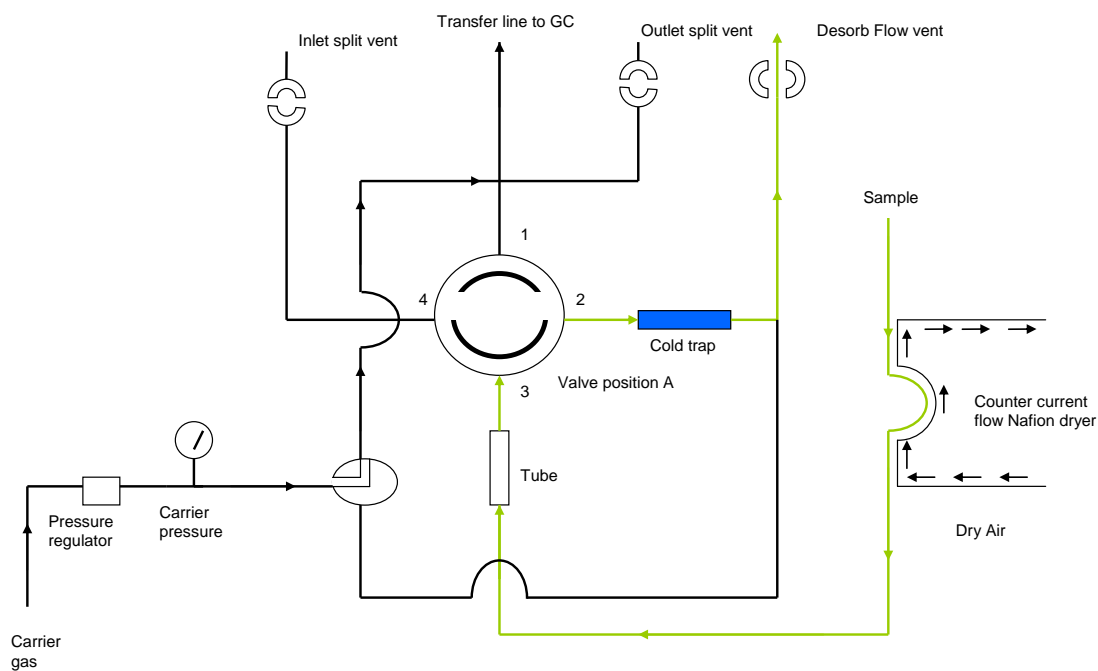
Figure 2.1 Diagram showing valve position and flow channel during online sampling, in this position carrier gas is supplied directly to the GC column via the transfer line.
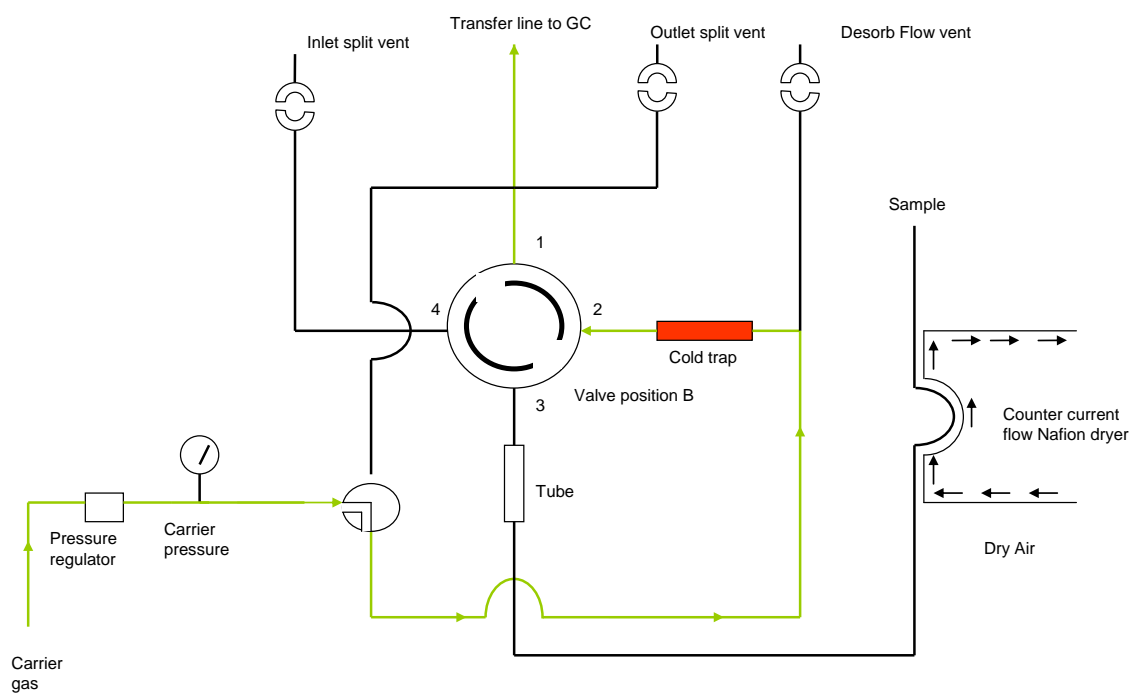
Figure 2.2 Diagram showing valve position and flow channel during sample desorption and injection.

Prior to reaching the cold trap, any residual moisture within the sample stream was removed using a Perma Pure MD Nafion[TM] dryer (Omnifit). The dryer consists of a semi-permeable Nafion tube which is encased in a stainless steel tube housing a counter-flow of dry gas. The sample stream is introduced to the Nafion tube and any water vapour present permeates through the membrane into the counter-flow air. This produces effective gas drying without removal of any VSLHs.

2.2 Purge and trap

Purge-and-trap was used before the TDU stage in order to degas VSLHs from seawater (at typically pM concentrations). A fixed volume of the seawater sample (40 ml) was introduced to a heated gas tight vessel (~70 °C) where nitrogen was used to sparge volatiles from the liquid into the gas phase. The purge tube was covered in insulating lagging and aluminium foil to maintain temperature and to minimise photolytic degradation of the halogenated organics during "sparging". The purge flow rate (50 ml min^{-1}) and trap time (50 min) were determined by purge and trap efficiency tests to ensure efficient quantitative trapping of the volatile compounds (Jones, 2006). The volatile gases are then retained on an activated charcoal adsorbent prior to injection onto the GC, as described in section 2.1. This process facilitates both the extraction of the volatile components from the aqueous media and their pre-concentration prior to detection. A problem with this process is the injection of the pre-concentrated VSLHs onto the column as well as a trapped water volume, which would reduce GC performance. This limitation is overcome successfully by introducing a series of gas driers in-line between the glass purge tube and the TDU, as shown in figure 2.3.
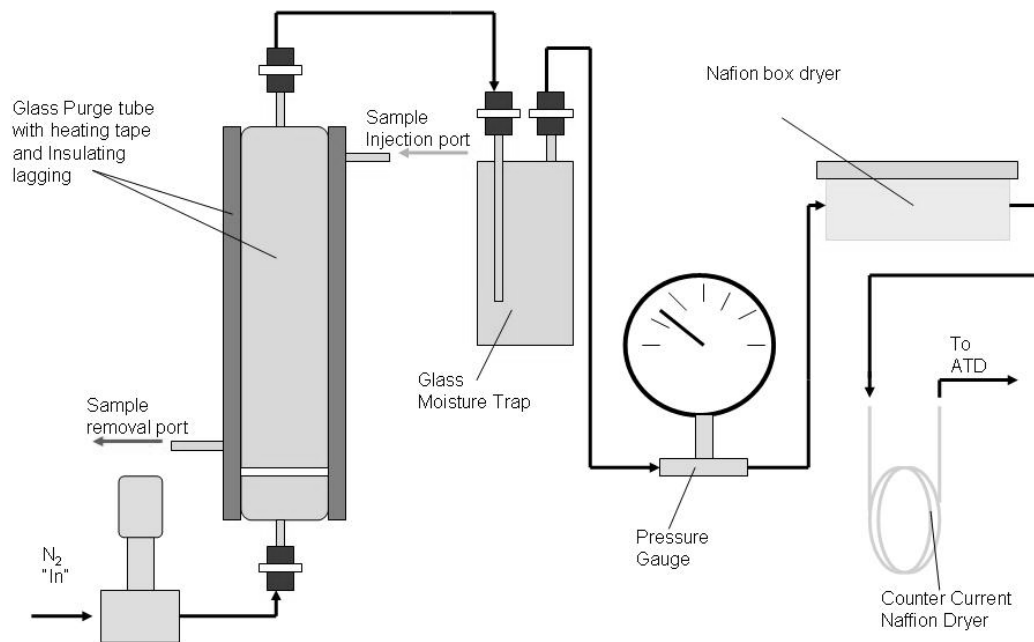
Figure 2.3 Schematic of purge and trap set-up used to extract volatile halogenated organic compounds aqueous samples.

2.3 Gas Chromatography

Gas chromatography (GC) is a chemical analysis used for the separation of complex multi-component mixtures. In GC, the gaseous analytes are transported through a column by a gaseous mobile phase, referred to as the carrier gas (Hinshaw and Ettre, 1994). The GC column contains a stationary phase which the gaseous mobile phase must flow through or over (dependent upon the type of GC column). The concept of GC is that different gaseous species have specific affinities toward the stationary phase which determines their respective retention times (t_R). As a result of these differences in mobilities, sample components will become separated from each other as they travel through the stationary phase. The actual t_R are controlled *via* the temperature of the GC oven, flow rate of the carrier gas, and the column length and dimensions used for the application.

In the schematic shown in figure 2.4, a gaseous sample or volatile liquid is injected into a heated port at the head of the GC column. Here it rapidly evaporates and is swept through the column *via* an inert carrier gas such as H_2, He or N_2 and separated chromatographically before the resolved components reach the detector. The column must be hot enough to provide sufficient vapour pressure for analytes to be eluted in a reasonable time. The

detector must be maintained at a higher temperature than the column so all analytes remain in the gas phase.
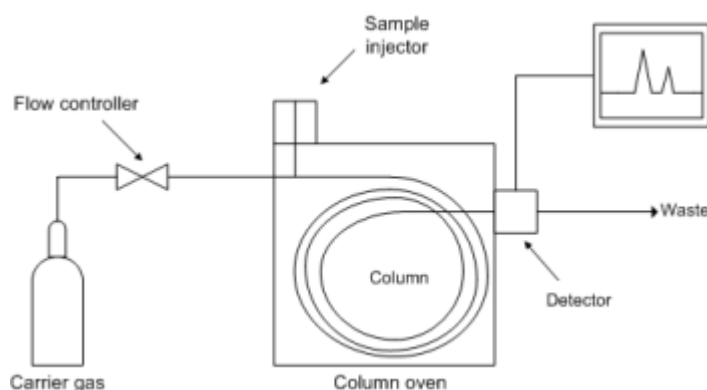
Figure 2.4 Schematic diagram of a GC

2.31 Fundamentals of Chromatographic Separation

In chromatography, the analyte (A) is distributed between the stationary and mobile phases according to EQ 2.1.

$$A_{mobile} \rightleftharpoons A_{stationary} \hspace{4cm} \text{(EQ 2.1)}$$

Species which migrate through the column and do not interact with the stationary phase will elute from the column in a finite time referred to as the dead, or void time (t_0). Species which interact with the stationary phase during migration through the column will elute with a delayed t_R. This is normally corrected for to take into account t_0 to give the corrected retention time (t_R') as shown in EQ 2.2.

$$t_R' = t_R - t_0 \hspace{4cm} \text{(EQ 2.2)}$$

Each analyte has a capacity factor, or retention factor, (k') which is used to describe the migration rates of solutes though columns. In order to achieve chromatographic separation of two components they must have different k' values. Ideally separations are performed under conditions in which the k' for the mixtures are within the range 1 to 5 in order to

accomplish adequate separation whilst minimising elution times. The *k'* can be expressed in terms of the retention properties of an analyte *via* EQ 2.3.

$$k' = \frac{(t_R - t_0)}{t_0} = \frac{t_R'}{t_0} \qquad \text{(EQ 2.3)}$$

The selectivity (α) for two analytes in a column provides a measure of how well the column will separate the two and therefore will depend upon their retention times and thus their *k'* values, as shown in EQ 2.4 where t_R' and *k'* values for solutes B and A respectively.

$$\alpha = \frac{(t_R')_B}{(t_R')_A} = \frac{k'_B}{k'_A} \qquad \text{(EQ 2.4)}$$

2.32   The Plate Theory of Chromatography

The partitioning of analytes between stationary and mobile phase can be considered as a series of adsorption and desorption events. Each interaction of analyte with the stationary phase can be considered as a theoretical plate for separation. Chromatographic column efficiency is measured as the number of theoretical plates (*N*) for that particular column, based on the theoretical plate model. The theoretical plate model does not however take into account any analyte band broadening, which may occur due to dispersive forces during separation, hence the number of theoretical plates must not be used independently when considering column performance. The model assumes that the length of the column is divided into a number of equidistant, discrete sections, or plates. Each plate represents a point of the analyte partitioning between the mobile and stationary phases, hence the number of theoretical plates represent the degree of separation attainable by a particular column. The greater the number of theoretical plates, the greater the separation efficiency of the column. The number of theoretical plates may be determined experimentally using EQ 2.5 where $\frac{1}{2}w_b$ is the peak width at half peak height respectively.

$$N = 5.54 \left(\frac{t_R{}'}{\frac{1}{2} w_b} \right)^2 \qquad \text{(EQ 2.5)}$$

The smaller the plate height, also referred to as the height equivalent of a theoretical plate (*HETP*), the higher the number of theoretical plates per length of column (*L*) and thus higher the degree of separation and column efficiency. These terms are related via EQ 2.6.

$$HETP = \frac{L}{N} \qquad \text{(EQ 2.6)}$$

2.33   The Rate Theory of Chromatography

A more realistic description of the processes at work inside a chromatographic column involves rate theory. This takes into account the time taken for analyte equilibration between the stationary and mobile phase, which isn't accounted for in plate theory which assumes this is instantaneous. A major source of the loss of chromatographic performance is band broadening. During a chromatographic separation a number of physical factors influence the width of analyte bands undergoing separation. They are described mathematically via the Van Deemter equation for plate height, shown in EQ 2.7, where *HETP* is in centimetres and *u* is the linear velocity of the mobile phase per second.

$$HETP = A + \frac{B}{u} + Cu \qquad \text{(EQ 2.7)}$$

A description of each of the diffusion terms are listed below.

Term *A* - Eddy Diffusion term

This term describes the effect of non-uniform flow of the mobile phase through the column packing, and as such only applies to packed columns. For separations using capillary columns, *A* is equal to zero. The relationship between the packing material and *A* is expressed in EQ 2.8, where d_p is the diameter of the column packing and λ is a constant relating to the quality of column packing material.

$$A = 2\lambda d_p \qquad\qquad\qquad\qquad\qquad\text{(EQ 2.8)}$$

Term B – Longitudinal Diffusion term

This term describes the migration of a solute from the concentrated centre of a band to the adjacent more dilute regions toward and opposed to the direction of flow. B is dependent on the solute's molecular diffusion coefficient in the mobile phase (D_m), and the tortuosity (γ) and is inversely proportional to linear velocity. This relationship is expressed in EQ 2.9.

$$B = 2D_m\gamma \qquad\qquad\qquad\qquad\qquad\text{(EQ 2.9)}$$

Longitudinal diffusion is a common source of band broadening in gas chromatography but is of less significance in liquid chromatography because the rate at which molecules diffuse within a gas medium is significantly higher.

Term C - Mass Transfer Coefficients

The term Cu in EQ 2.7 arises from the finite time required for the solute to equilibrate between the mobile and stationary phases. The plate height from equilibration time, or mass transfer term, ($HETP_{mass\ transfer}$) is expressed in EQ 2.10 where, C_s and C_m are the rates of mass transfer through the stationary phase and mobile phase, respectively.

$$HETP_{masstransfer} = Cu = \left(C_s + C_m\right)u \qquad\qquad\qquad\text{(EQ 2.10)}$$

For GC in an open tubular column the mass transfer terms for the mobile and stationary phases are expressed in EQ 2.11 and 2.12, where r is the column radius, d is the thickness of the stationary phase and D_s is the diffusion coefficient of the solute in the stationary phase.

$$C_s = \frac{2k'}{3(k'+1)^2} \frac{d^2}{D_s}$$ (EQ 2.11)

$$C_m = \frac{1 + 6k' + k'^2}{24(k'+1)^2} \frac{r^2}{D_m}$$ (EQ 2.12)

Decreasing stationary-phase thickness, and column temperature, reduces *HETP* by increasing *N* as the solute partitions more effectively between the mobile and stationary phases. Reducing *r* also reduces *HETP* by reducing the distance through which solute must diffuse to reach the stationary phase.

The optimum column flow-rate for capillary GC is therefore a balance between longitudinal diffusion and the mass transfer terms to provide the minimum plate height, EQ 2.7. The optimum flow-rate also varies depending upon the choice of carrier gas. This is illustrated by a series of Van Deemter plots for the same column and solute using nitrogen, helium and hydrogen respectively, figure 2.5. Optimum carrier gas velocity is higher for lighter gases, also the range close to the optimum flow rate is much broader. The minimum *HETP* therefore occurs at higher gas velocities and is less critical than for nitrogen over a much broader range. However, helium is commonly the carrier gas of choice as it provides a compromise between *HETP* and analysis times without the risk of explosion, as with the flammable gas hydrogen (Moody, 1982).
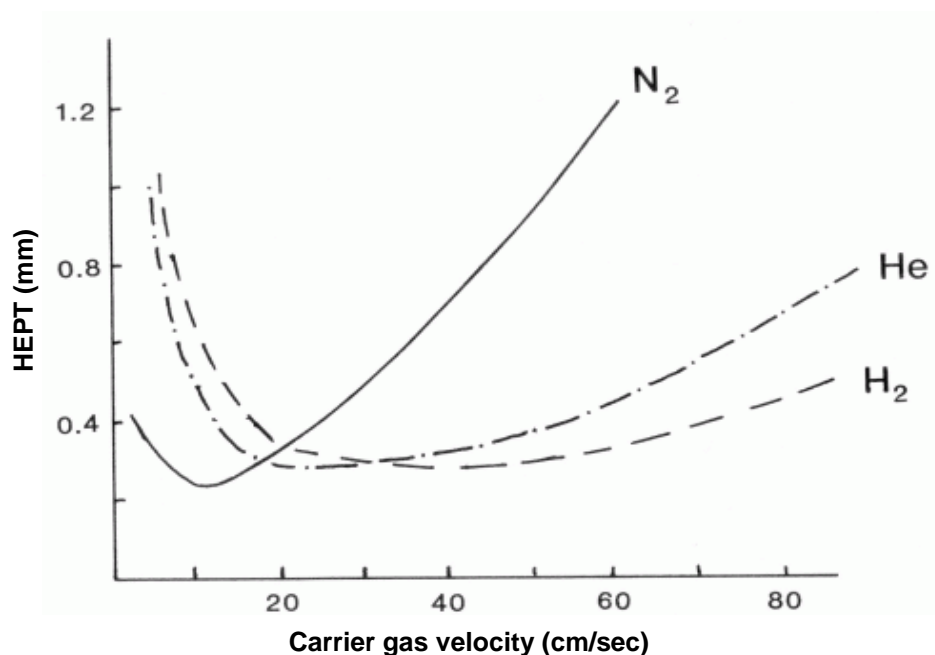
Figure. 2.5 Van Deemter plots for *HETP* versus carrier gas velocity for nitrogen, helium and nitrogen (Christie, 1989).

The resolution of a column (R_s) provides a quantitative indication of its ability to separate two analytes and is determined via EQ 2.13.

$$R_s = \frac{2(t_{R2} - t_{R1})}{w_{b1} + w_{b2}}$$
(EQ 2.13)

The significance of this term is illustrated in figure 2.6, which shows chromatograms of two closely eluting species, peak X and peak Y, on two columns of with different resolving powers. Resolution should be maximised for optimum separation, values of 1.5 or higher are desirable as they describe baseline resolved peaks. R_s values of less than 1.5 lead to overlap or even co-elution of peaks, reducing the accuracy and precision of peak integration. The resolution of a given stationary phase may be increased by lengthening the column thus increasing N. Adverse effects of increasing column length, however, are increased run time and band broadening.
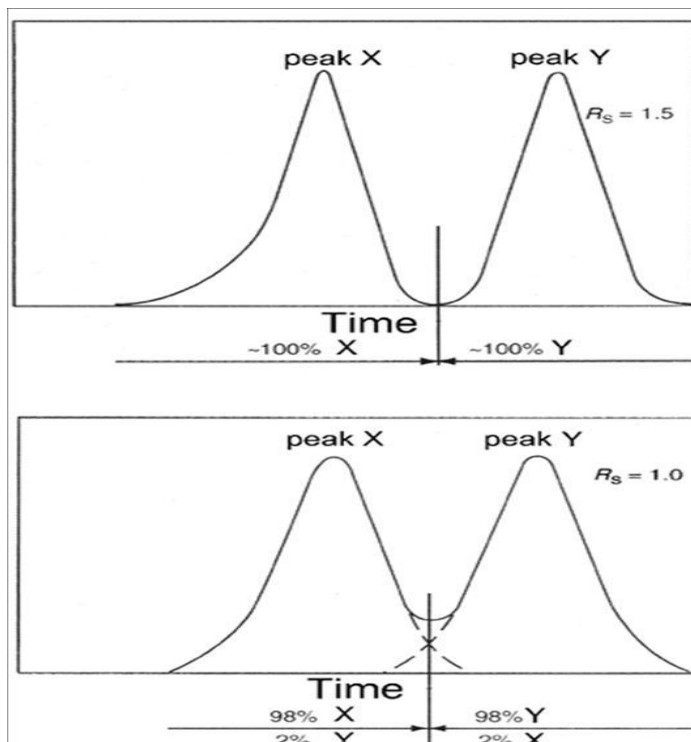
Figure. 2.6 Chromatographic resolution of adjacent peaks. Upper image: $R_s \geq 1.5$, Lower image: $R_s \sim 1.0$ (Mallik *et al.,* 2008).

2.4 Mass Spectrometry

The mass spectrometer (MS) is an instrument that will separate and measure ionised molecules, as gaseous ions, according to their mass-to-charge ratios (*m/z)*, and finally determine the abundance of each ion at the detector. The sequence of internal components that an MS possesses is illustrated in figure 2.7.
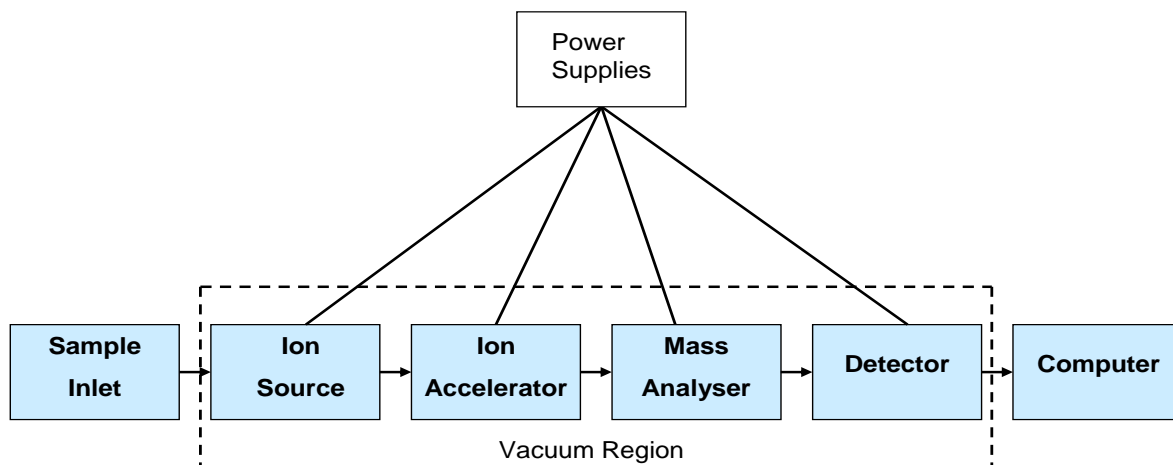
Figure 2.7 Schematic of basic components within a mass spectrometer (adapted from Ewing, 1997).

2.4.1   The Ion Source

When a GC is coupled to a mass spectrometer, the gaseous analyte eluent is introduced to the ion source of the spectrometer via the GC capillary column. Species exiting the column pass into the ionisation chamber which is pumped to maintain a pressure of 10^{-6} Torr, using a high speed turbomolecular pump. There are many different types of ionisation used in mass spectrometry. The focus of this discussion, and the most commonly used technique, is electron ionisation (EI) which is illustrated in figure 2.8. Electrons are emitted from a heated filament and further energized by accelerating them through a potential of ~70 V. The electron acceleration potential directly determines the amount of ionisation that can occur as these electrons must possess a quantity of energy greater than the first ionization enthalpy of the species. The energized electrons are directed across the sample stream toward an anode/trap electrode whilst being constrained into a beam by a magnetic field. Approximately 0.01% of the sample molecules (M) absorb as much as 12-15 electron volts (eV), enough to induce electron ionisation, as shown in EQ 2.14. The remainder of M remain neutral species and are pumped away. A small positive potential is applied to the repeller plate of the ion source which extracts cations from the ion source toward the MS. A small potential is also applied to the ion guide optics en-route which focuses the ions into a beam which is introduced to the mass analyser.

$$M + e^- \rightarrow M^{+\bullet} + 2e^-$$
(EQ 2.14)

31
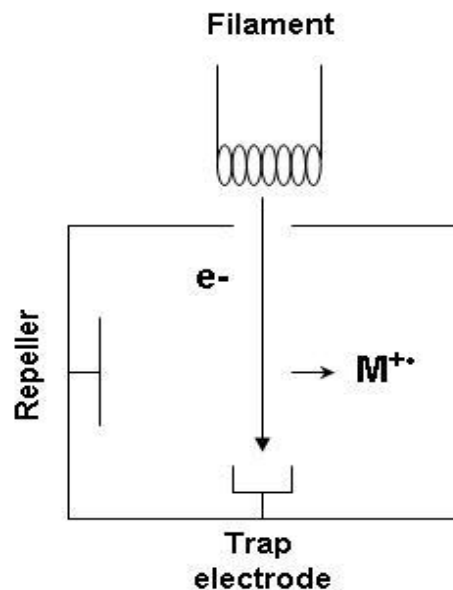
Figure 2.8 EI source showing electron beam orientation within source housing**.**

The majority of the ions generated will have a charge of +1 resulting from the displacement of 1 electron, although it is possible for both negatively charged and multiply charged positive ions to form within the ion source. Any negative ions formed will discharge upon the repeller or trap electrode and will not enter the mass analyser. Following ionisation, the molecular ion ($M^{+\bullet}$) usually has enough internal energy (~1eV) to extensively fragment into "fragment ions". Such fragmentation can provide a great deal of structural information about the analyte, although this can be so extensive that the $M^{+\bullet}$ is not observed in the resulting mass spectra.

2.4.2 The Mass Analyser

The analyte ions produced during EI in the source region of the mass spectrometer pass into the mass analyser where they are separated according to their *m/z* ratio. There are currently several different types of commercially available mass analyser, however the following discussion is limited to the principles of operation for the mass analyser used in this work, the quadrupole mass spectrometer (QMS).

The QMS is an example of a scanning mass analyser and is capable of recording 2 - 8 spectra per second, covering a mass range as high as 1,000 m/z (in EI mode). The QMS operates at constant resolution, which means that the mass resolution is independent of the mass analysed, unlike magnetic sector and time of flight instruments which lose mass resolution as *m/z* increases (Harris, 2010). Instrument operation is independent of the kinetic energy and velocity that ions initially possess on entering the analyser. This allows GC to be interfaced to QMS without any appreciable loss in mass resolution. A significant disadvantage of the QMS, however, is that increasing the mass range to be scanned reduces sensitivity as the time spent monitoring each *m/z* ratio is reduced. Single ion monitoring (SIM), where only ions of a specific *m/z* ratio are monitored over a fixed time period in the absence of all other ions, is commonly used to significantly enhance detector sensitivity.

The QMS consists of a set of four electrodes, ideally of hyperbolic cross section, that are accurately positioned in a radial array. For economical as well as practical reasons, most mass filters consist of electrodes of circular cross section, as shown in the top of figure 2.9.

The mass filtering action of the quadrupole mass analyzer is obtained by the application of a combination of time independent, fixed dc potential (*U*), 500-2000 V, and a time-dependent ac radio frequency (RF) field, 0-6000 V. The positive dc potential is applied to the opposing rods in the X-Z plane and the negative dc potential is applied to the rods in the Y-Z plane. The ac potential is applied to both opposing pairs of rods but the potential applied to one pair is the opposite sign of the other, i.e. 180° out of phase. The applied potential (Φ), to the opposed rods in the X-Z and Y-Z planes are expressed by EQs 2.15 and 2.16, respectively. The RF field is expressed in terms of amplitude (*V*) and frequency (*w*), thus as *cos wt* cycles with time (*t*) the applied voltages on opposed pairs of rods in the X-Z and Y-Z planes alternate as shown in figure 2.10.

$$\Phi = U - V \cos wt \qquad\qquad\qquad\qquad \text{(EQ 2.15)}$$

$$\Phi = -(U - V \cos wt) \qquad\qquad\qquad\qquad \text{(EQ 2.16)}$$
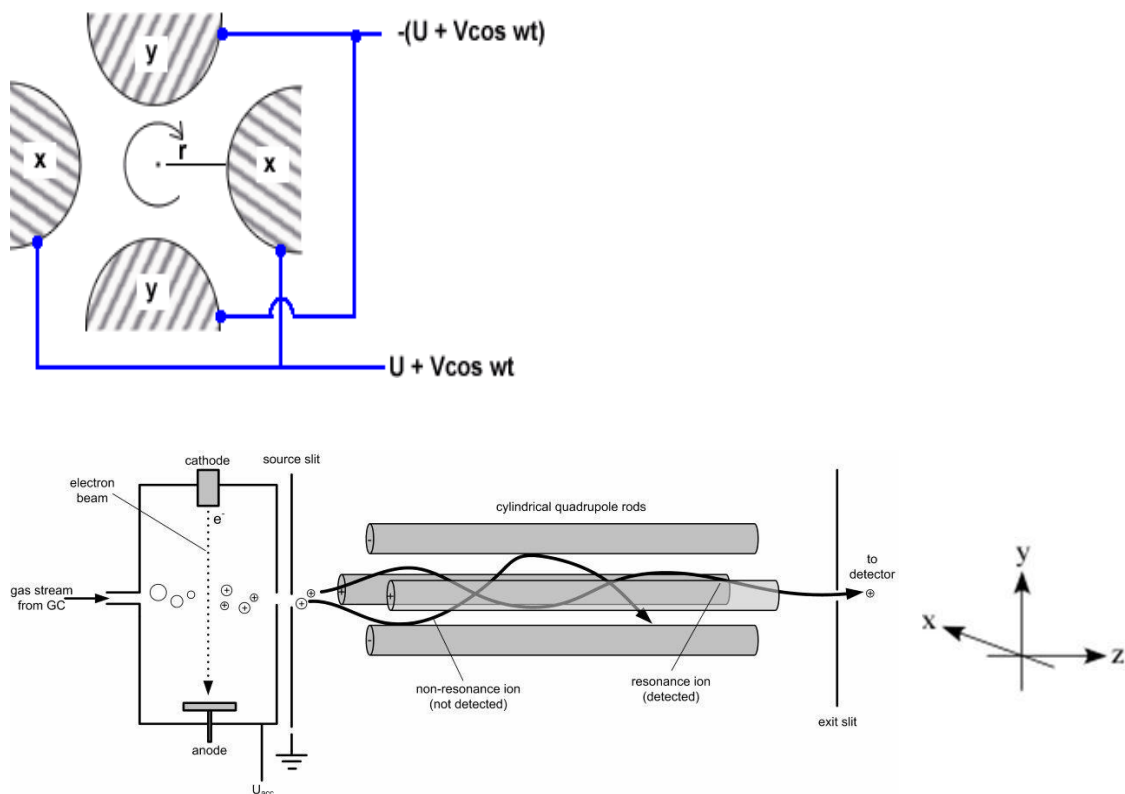
Figure 2.9 Schematics showing a cross section of quadrupole region and an EI source interfaced with a QMS (Witmann, 2007).
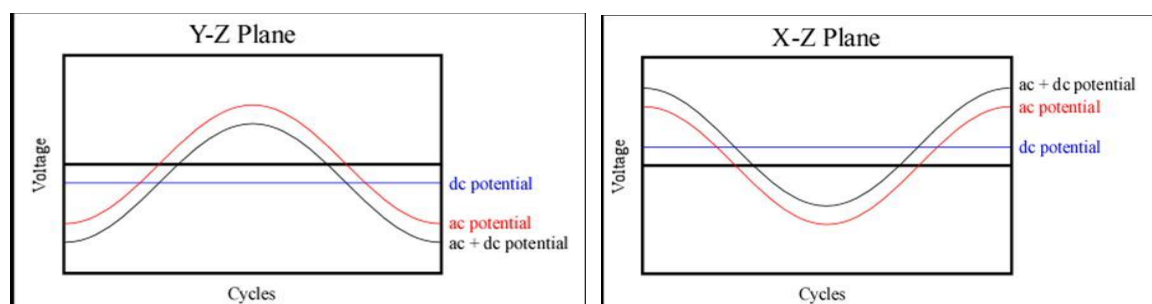
Figure 2.10 Applied ac and dc potential in the QMS (Dunnivant and Ginsbach, 2010).

Although the potentials applied to the rods within the QMS result in the acceleration and repulsion of positively charged ions in the X-Y plane, as long as the ions travel less than the radial distance of the quadrupole (*r*) the ions will not discharge on the rods. These ions are referred to as resonance ions and have a stable trajectory through the quadrupole to the detector, figure 2.9. Ion resonance within the X-Y plane is responsible for mass selection

34

within the QMS. Factors that influence whether or not an ion is in resonance in the QMS are the amplitude and frequency of the ac potential, the mass of the particular ion, the charge of the ion and its position within the quadrupole. Ion mobility along the z-axis is controlled by maintaining a potential difference between the source and exit slits of the QMS, figure 2.9.

Quadrupoles operate by keeping the ratio of ac and dc constant whilst altering their amplitude which changes the *m/z* ratio of the ions that have a stable trajectory through the mass analyzer. The result of this is the mass scan line intersecting the stability diagram in figure 2.11. Values of dc/ac within the stable ion trajectory region provide a stable trajectory through the QMS for the respective masses.
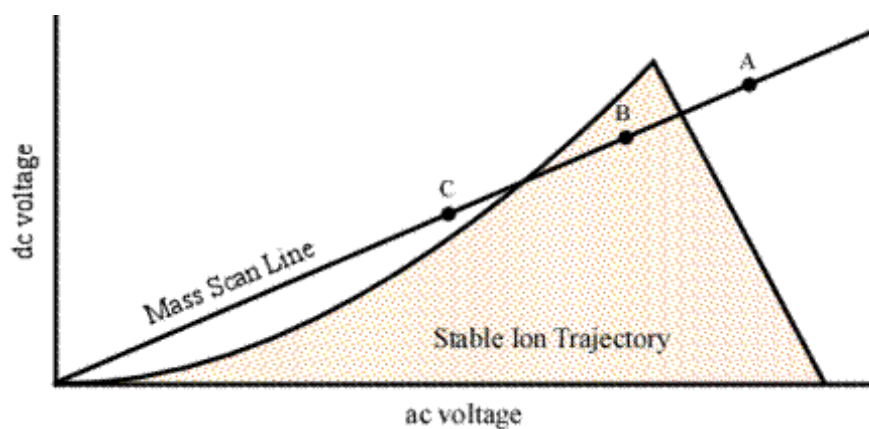
Figure 2.11 Stability diagram for ions of different masses (Dunnivant and Ginsbach, 2010).

At point A in the diagram the ion is too light to pass through the X-Z plane because of the high magnitude of the ac and dc potentials. The ions oscillation through the quadrupole region is therefore unstable, and it eventually discharges on the rod and pumped away. Conversely, at point C, the ac potential is too low to allow the ion to pass through the detector, its overwhelmed by the negative dc potential in the Y-Z plane, and it discharges on the rod. At point B the amplitude of voltages has been altered so the trajectories of the ion in both the X-Z and Y-Z plane are stable and the ion successfully reaches the detector.

Changing the ac/dc ratio, the slope of the mass scan line in figure 2.11, affects mass resolution. Optimum resolution can be obtained when the mass scan line intercepts the peak apex of the stable ion trajectory region. This is however impractical due to fluctuations in the ac and dc potentials applied to the quadrupole. Therefore the mass scan line commonly intersects below the peak apex to account for any deviation in applied potentials, producing nominal mass resolution.

2.4.3 Detectors

The role of a detector in mass spectrometry is to convert incident cations to a quantifiable signal. The QMS used within this work utilizes a conversion dynode and phosphorescent screen coupled to a photomultiplier tube (PMT) for signal amplification, figure 2.12. Incident cations leaving the QMS are accelerated toward the conversion dynode, which is held at a negative potential, and the resulting collisions results in the emission of electrons. These electrons are repelled from the negative potential of the conversion dynode onto a phosphorescent screen. Electron contact on this screen produces photons which are emitted through the transparent window of the PMT. The PMT is essentially a vacuum tube which contains a photo-emissive cathode and a number of secondary electron emitting stages called dynodes. The potential applied to the dynodes is such that the electrons from each are delivered to the next dynode in series, 100-300 volts depending on the number of dynodes (Lancaster, 1980). Incident electrons emitted from the photo-emissive cathode are accelerated toward the first dynode, where their impact induces the emission of secondary electrons. These electrons are accelerated toward each of the dynodes in series generating more secondary electrons, D1 to D5, before finally being collected at the anode. On contact with the anode, a large current pulse is generated and the resulting analogue signal is recorded as peak intensity. Values of amplification of the PMT vary between 100,000 to 1,000,000, thus 100,000 electrons or more are collected by the anode for each photon reaching the PMT.
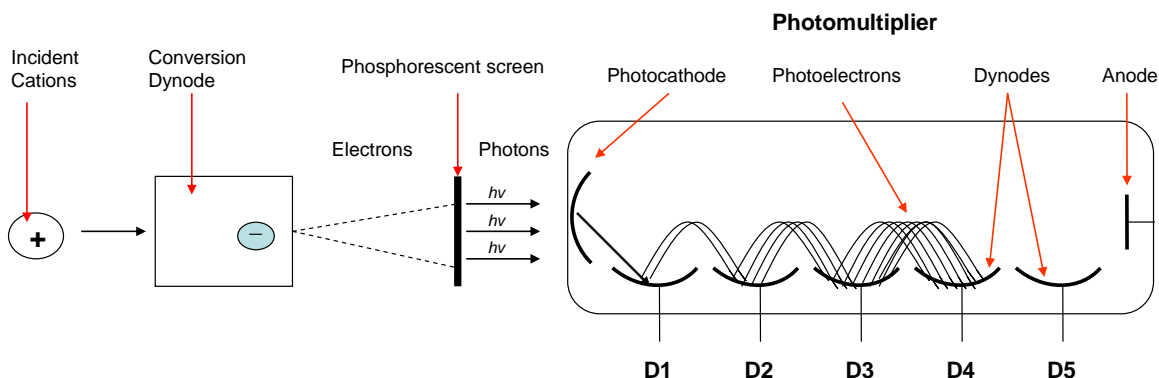
Figure 2.12 Schematic of photomultiplier detector (adapted from Lancaster, 1980).

2.5 GC/MS Experimental Set-up

Analyses were carried out using one of two GC columns.

5%Phenyl-methylpolysiloxane (DB-5) capillary column

The Perkin Elmer GC coupled to the quadrupole mass spectrometer, incorporated a 60 m x 0.53 mm internal diameter wall coated open tubular (WCOT) non polar DB-5 (Supelco) capillary column and used CP grade helium (BOC gases) as a carrier gas (3.0 mL min^{-1}). Following injection, the GC oven temperature was held at 35 °C for 3 minutes before ramping up to 180 °C at a rate of 10°C min^{-1}. The oven was then held for 1 minute before finally ramping to 200 °C at a rate 25 °C min^{-1}. The oven was then held at 200 °C min^{-1} for adequate conditioning between sample runs.

CP-Porabond Q (PQ) capillary column

GC-MS separation was also performed on a 25 m WCOT Styrene-divinylbenzene column, 0.32 mm (id), (CP Porabond Q, Chrompack) using a helium flow rate of 1.5 ml min^{-1}. Following analyte injection onto the GC the oven temperature was held at 40 °C for 2 minutes to refocus the analytes at the front of the column then heated to 240 °C at a ramp rate of 10 °C min^{-1} which was held for 10 minutes to ensure adequate conditioning of the column between sample runs.

The MS was operated in selective ion recording mode (SIR) mode using EI with a dwell time of 0.15 seconds for each ion monitored for identification and quantitation, tables 2.1 and 2.3. For each analyte, the ion signal was the sum of the constituent ions. A 5 minute solvent delay was used so that there was a delay after sample injection before the mass spectrometer started scanning. This was to avoid monitoring the pressure pulse which occurred during injection of the analytes onto the GC column.

Peak number	Halocarbon species	Mean Retention time CP-Porabond Q (mins)	Ion(s) Monitored Porabond Q	Mean Retention time DB-5 (mins)	Ions monitored DB-5	Boiling Point (°C)
1*	CD_3I	10.33	145	-	-	42
1	CH_3I	10.39	127,142	6.24	127,142	42
2	$CHCl_3$	13.66	83,85	10.36	83,85	61
3*	C_2D_5I	13.89	161	-	-	71
3	C_2H_5I	13.96	127,156	10.14	127,156	71
4	CH_2Br_2	15.16	172,174	12.78	172,174	97
5	CCl_4	15.33	117,119	11.44	117,119	76.5
6	CH_2ICl	16.10	176,178	13.39	176,178	108.5
7*	$2\text{-}C_3D_7I$	16.25	177	-	-	89
7	$2\text{-}C_3H7I$	16.36	170	11.86	127,170	89
8	$1\text{-}C_3H7I$	17.07	170	13.07	127,170	101.5
9	CH_2IBr	18.25	220, 222	13.35	220,222	139.5
10	$CHBr_3$	20.29	171,173	16.82	171,173	148
11	CH_2I_2	21.19	254,268	17.57	254,268	180

Table 2.1 Mean retention times and ions monitored for compounds on both columns during SIR.

A chromatogram of the resolved target analytes using the DB-5 column described, used previously, is shown in figure 2.13. As the capillary column utilizes a non polar divinyl-benzene stationary film, compound adsorption out of the gas phase was non selective and elution was dependent upon their respective boiling points, table 2.1. Although the

majority of the compounds were baseline resolved, inherent problems with the separation were evident. Firstly both C_2H_5I and $CHCl_3$ co-eluted, requiring analytical de-convolution using their characteristic ions thus causing a considerable decrease in their sensitivity. Secondly, CH_3I suffered from a significant reduction in the signal/noise ratio due to its elution upon the tail of the initial injection pressure pulse.
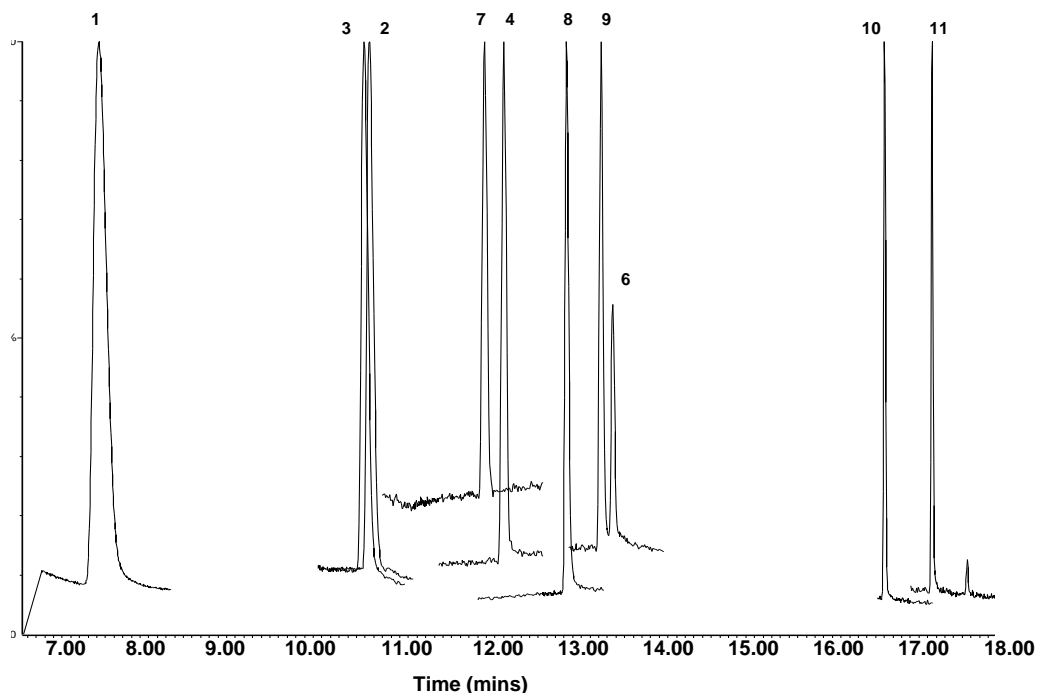
Figure 2.13 Chromatogram of SIR of gaseous halocarbon permeation standards (3 x 10μl loops) using DB-5 column, analytes can be identified using table 2.1

A similar more polar GC capillary column was selected in an attempt to fully resolve all the analytes (CP-Poraband Q), figure 2.14. This column significantly increased the signal to noise ratio for all analytes, including CH_3I which was completely resolved from the tailing of the pressure pulse.

The resolution between all the analyte peaks in both figures 2.14 and 2.15 are shown in table 2.2, calculated using equation 2.13. All analytes are baseline resolved (resolution >1.5) on the PQ column whereas both $CHCl_3$, C_2H_5I and $1-C_3H7I$, CH_2ICl aren't typically resolved within the DB5 chromatogram. The PQ column was the column of choice for all analyses due to its superior chromatographic performance. The DB-5 column was only

39

used during aqueous VOIC analysis during the COBRA campaign (chapter 4) when a second PQ column was not available.
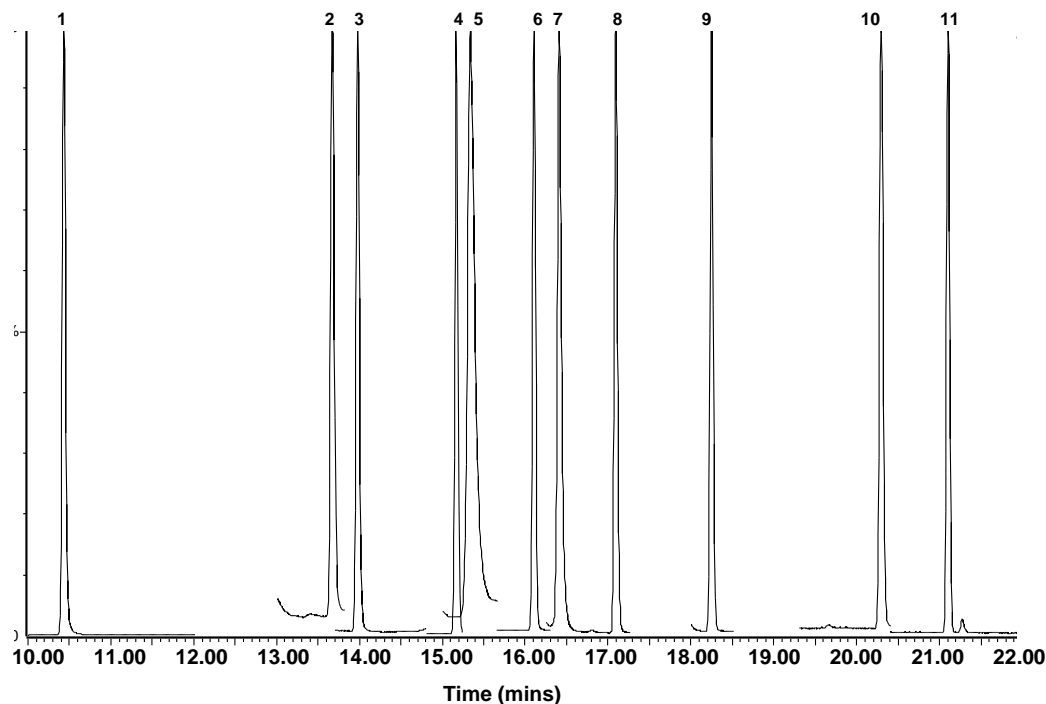
Figure 2.14 Chromatogram of SIR of gaseous halocarbon permeation standards (3 x 10µl loops) using CP Porabond Q column, analytes can be identified using table 2.1

Figure 2.15 shows a typical chromatogram of an aqueous internally standardized purge and trap analysis. CH_3I, C_2H_5I and 2-C_3H_7I were not fully resolved from their deuterated equivalents and had to be separated using their characteristic masses, significantly increasing their detection limit. An elevated baseline is observed during SIR 11 (*m/z* 254 and 268) toward the end of the GC run. This baseline elevation was present during all aqueous analyses during the cold chamber experiment (chapter 5), and caused un-reproducible peak integrations of CH_2I_2. Therefore, for this experiment the dataset for CH_2I_2 was disregarded. Further investigation suggested that this elevated baseline was caused by artifact(s) within the experimental ice tank as neither aliquots of "blank" water (HPLC grade, Fisher), deionised water or the external gas standard yielded an elevated baseline within this retention window. This method was only used during laboratory experiments where the concentrations of these compounds were significantly higher than

40

the limit of quantification of the detector and was not applied to atmospheric field measurements.
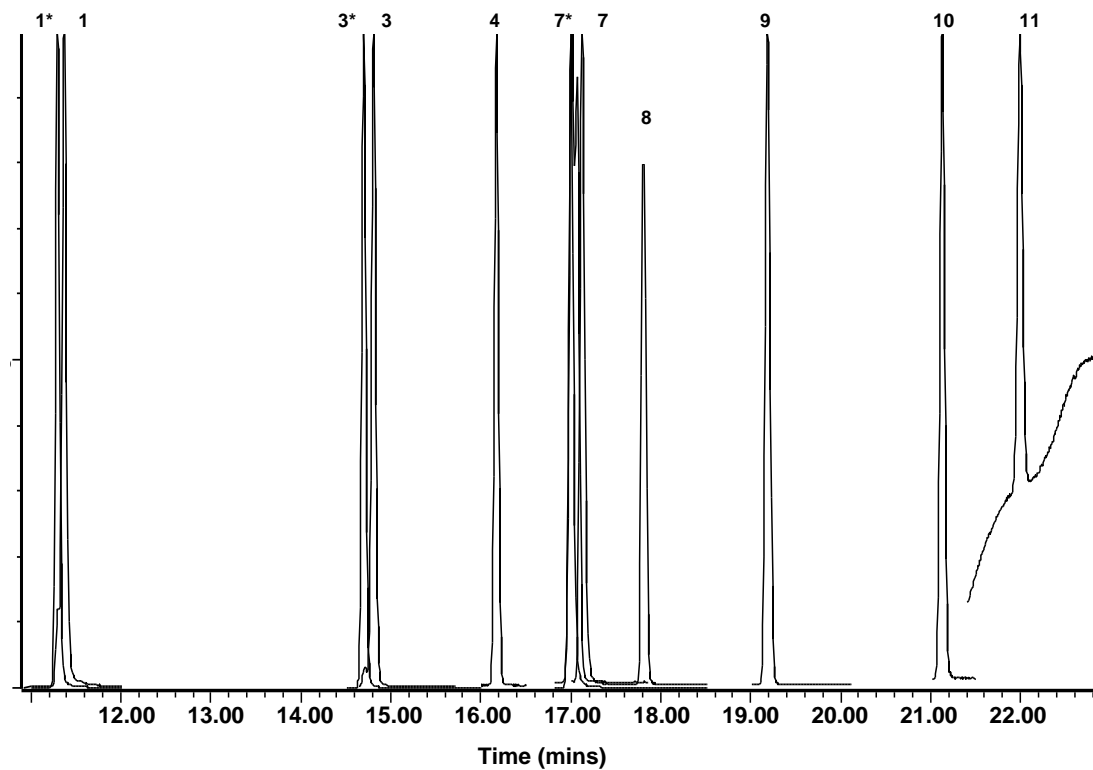
Figure 2.15 Chromatogram of SIR of aqueous halocarbon standards and gaseous deuterated internal standards using CP Porabond Q column, analytes can be identified using table 2.1

Halocarbon species	Peak width (secs) Porabond Q	Peak width (secs) DB5	Resolution Porabond Q	Resolution DB5
CH_3I	6.6	22.8	28.17	10.55
$CHCl_3$	7.2	10.2	2.69	8.8
C_2H_5I	6.6	12	10.82	0.38
CH_2Br_2	6.6	6.6	1.75	6.64
CCl_4	7.8	-	6.30	-
CH_2ICl	6	4.8	2.53	19.1
$2\text{-}C_3H7I$	8.4	7.8	5.05	1.83
$1\text{-}C_3H7I$	7.8	6.6	9.28	3.6
CH_2IBr	7.2	6.6	18.55	1.2
$CHBr_3$	6	3.6	8.20	8.6
CH_2I_2	6	4.2	7.21	7.14

Table 2.2 Resolution between halocarbon peaks for PQ and DB-5 columns. The mean resolutions were 9.14 and 6.78, respectively.

Halocarbon Species	Ion(s) Monitored	Ion Fragments
CD_3I	145	CD_3I^+
CH_3I	127,142	I^+, CH_3I^+
$CHCl_3$	83,85	$CH^{35}Cl_2^+$, $CH^{35}Cl^{37}Cl_3^+$
C_2D_5I	161	$C_2D_5I^+$
C_2H_5I	127,156	I^+, $C_2H_5I^+$
CH_2Br_2	172,174	$CH_2^{79}Br^{79}Br^+$, $CH_2^{79}Br^{81}Br^+$
CCl_4	117,119	$C^{35}Cl_3^+$, $C^{35}Cl_2^{37}Cl^+$
CH_2ICl	176,178	$CH_2I^{35}Cl^+$, $CH_2I^{37}Cl^+$
$2\text{-}C_3D_7I$	177	$2\text{-}C_3D_7I^+$
$2\text{-}C_3H7I$	127,170	I^+, $2\text{-}C_3H_7I^+$
$1\text{-}C_3H7I$	127,170	I^+, $1\text{-}C_3H_7I^+$
CH_2IBr	220, 222	$CH_2I^{79}Br^+$, $CH_2I^{81}Br^+$
$CHBr_3$	171,173	$CH^{79}Br_2^+$ $CH^{79}Br^{81}Br^+$
CH_2I_2	254,268	I_2^+, $CH_2I_2^+$

Table 2.3 All quantifying masses used during SIR and their corresponding ion fragments

2.6 Normalization and Calibration of Instruments

The TD-GC/MS instruments were calibrated in the field against a halocarbon gas standard. The concentrations of gases in this standard were determined pre and post campaign by an "in house" built permeation oven (Wevill and Carpenter, 2004), as described in section 2.64. Halocarbon mixing ratios within the gas standard and MS response reproducibility % RSD (determined from triplicate analysis of external standard measurements in the field) are shown in table 2.4.

Halocarbon	Mean mixing ratio, pptv	RSD %
CH_3I	1894.62	7.93
C_2H_5I	275.81	6.42
CH_2Br_2	67.37	9.92
CH_2IBr	127.47	12.84
$2-C_3H7I$	305.22	7.32
CH_2ICl	56.64	8.95
$1-C_3H7I$	5.28	8.13
$CHBr_3$	7.18	32.47
CH_2I_2	4.23	13.73

Table 2.4 Halocarbon mixing ratios within external calibration gas standard

2.6.1 Preparation of halocarbon gas standard

The halogenated compounds within the gas standard are photolytically labile, volatile and relatively insoluble in water. Therefore the halocarbon stock standard solutions (>99% purity, Sigma Aldrich) were initially prepared in 50 mL methanol (Fisher HPLC grade), within a 100 ml airtight round bottom flask whilst minimizing headspace. The vessel was covered with aluminium foil to prevent loss to the gas phase and photolytic degradation. The preparation of the standard involved the addition of microlitre volumes of each halocarbon stock standard to 50 ml of methanol, which was then mixed for 30 min with a glass coated magnetic stirring bar. This solution was diluted to 1 L with sparged H_2O within a sealed 1 L round bottom flask. The resulting solution was stirred for 18 hours with a glass coated magnetic stirrer to ensure complete halocarbon homogeneity throughout. A 40 ml aliquot of the solution was applied to a pressurized, heated gas tight purge tube and

sparged into a passivated 10 L electropolished aluminium lined cylinder (Aculife) with zero grade nitrogen gas, purge method as outlined in 2.2. The flow rate of nitrogen gas through the purge tube was maintained at a 100 ml min^{-1} for 100 mins (10 L) using a mass flow controller (MKS, 1L min^{-1} capacity).

2.6.2 National Physics Laboratory standard

A primary gas standard from the National Physics laboratory (NPL) containing $\sim$ 100 ppbv concentrations of 14 chlorinated hydrocarbons was diluted 5 times, using zero grade N_2 into a 10 L electropolished aluminium lined cylinder (Aculife), and used as an external standard for monitoring detector sensitivity on the GC-MS. The standard was introduced to the TD-GC-MS at a flow rate of 20 ml min^{-1} for 5 min (100 ml). Of the 14 chlorinated hydrocarbons in the multi-component mixture, only $CHCl_3$ and CCl_4 were monitored .

2.6.3 Deuterated halocarbon gas standard

A gas standard containing $\sim$ 10 ppbv certified concentrations (Clarks) of deuterated iodo-methane (CD_3I), iodo-ethane (C_2D_5I) and iodo-isopropane ($2-C_3H_7I$) in zero grade N_2 (99% purity) within a 10 L aluminium electropolished cylinder (Aculife) was used as an internal standard for monitoring detector sensitivity during purge and trap analyses.

2.6.4 Permeation oven calibration

The "in house" constructed permeation oven essentially consisted of a 6-port valve, 2 way switching valve (Restek, UK) with a 10 μl loop (Restek, UK), and two glass permeation tube housings linked to a nitrogen supply (zero grade, BOC) maintained at 100 ml min^{-1} with a MFC (MKS) refer to figure 2.16. Valve switching times used were either 10 or 60 s, refer to section 2.6.5. Permeation tubes were housed in the two glass housings within two temperature controlled aluminium heating blocks, maintained at either 40 °C or 70 °C, dependent upon halocarbon volatility. The 70 ºC perm holder contained: CH_2I_2, $CHBr_3$, 1-C_3H_7I, $2-C_3H_7I$ and CH_2IBr. The 40 ºC perm holder contained: CH_2Br_2, CH_3I, $CHBr_2Cl$, CH_2ICl and C_2H_5I. Both were covered in aluminum foil to reduce photolytic degradation of the permeation standards.

The valve had two positions - 'load permeation gas' and 'inject permeation gas', refer to figures 2.17 and 2.18 respectively. In the load position, permeation gas was delivered to the loop and directly out to waste through a hydrocarbon trap. When the valve was switched to the inject position, nitrogen gas flowed through the loop "sweeping" the 10 μl plug of gas to the TDU for pre-concentration. Successive switching of the valve position allowed a small calibrated volume (10 μl) of permeation gas to be injected into the nitrogen gas stream, allowing halocarbon concentrations in moles per loop to be calculated.

The permeation tubes used (Ecoscientific) consisted of a polymer permeable membrane window (Teflon) within a stainless steel casing filled with pure halocarbon standard (> 99%). A two-phase equilibrium exists between the halocarbon's liquid and gas phase within the permeation tube. When held at constant temperature, these tubes emit the compounds through the permeation window at a constant rate. The permeation rate of each of the halocarbon permeation tubes is determined by gravimetric weight loss over a known period of time at a constant flow rate and temperature. The halocarbon permeation tubes were removed from their housings on a monthly basis and their gravimetric weight loss assessed over time using a 5 figure top pan balance (KERN 770), figure 2.19. The mass loss can then be converted to the number of moles per loop using equation 2.17.

$$M_{loop} = \frac{P_r(L_v/RMM)}{F} \qquad\qquad\qquad (EQ\ 2.17)$$

where M_{loop} is moles injected per loop, Pr is the permeation rate in g min^{-1}, L_v is the loop volume in mL, RMM is the relative molecular mass and F is the flow rate in mL min^{-1}.
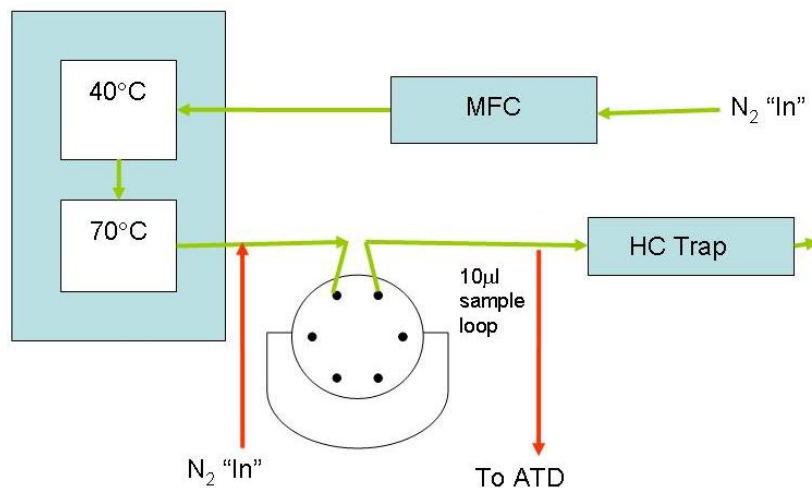
Figure 2.16. Schematic of permeation oven. Green path depicts flow of N_2/permeation gas during "load permeation gas". Red path depicts flow of N_2/permeation gas during "inject permeation gas"
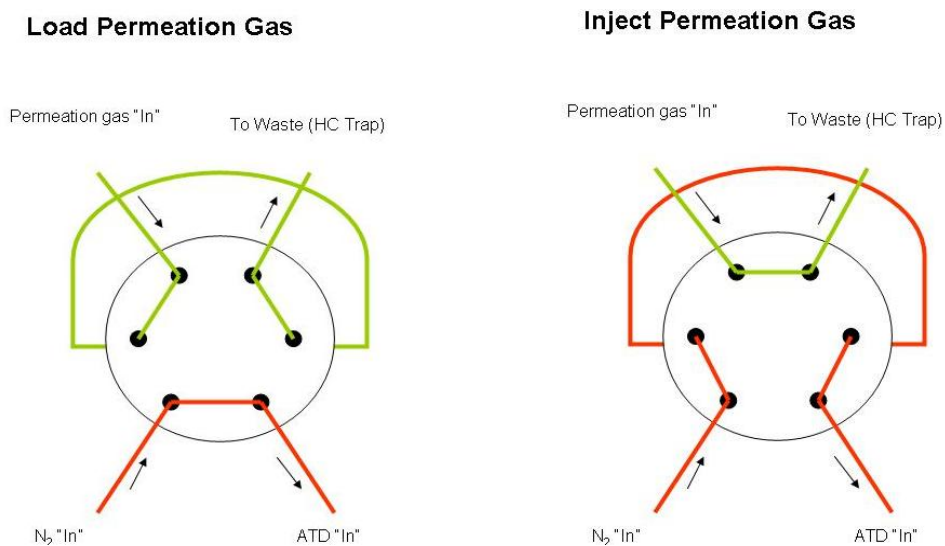
Figures 2.17 and 2.18. 6-port 2 way switching valve with a small calibrated $10\mu l$ loop used for injection in load and inject positions respectively.

A calibration curve was constructed of moles of halocarbon versus instrument response, the slope from which was used to convert instrument peak response to concentration (figure 2.20).
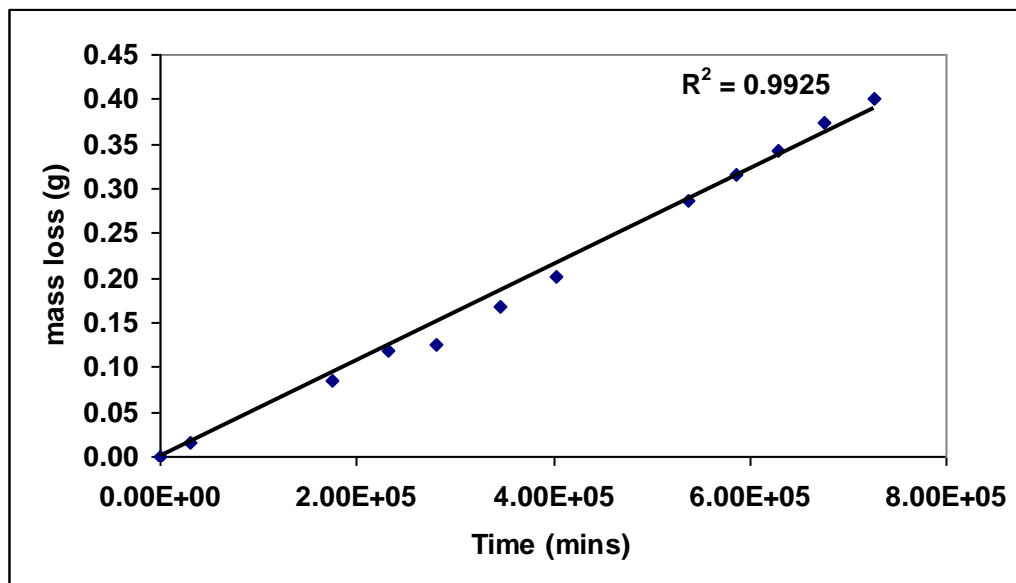
Figure 2.19 Plot of CH_3I permeation tube mass change over time, used to calculate permeation rates.
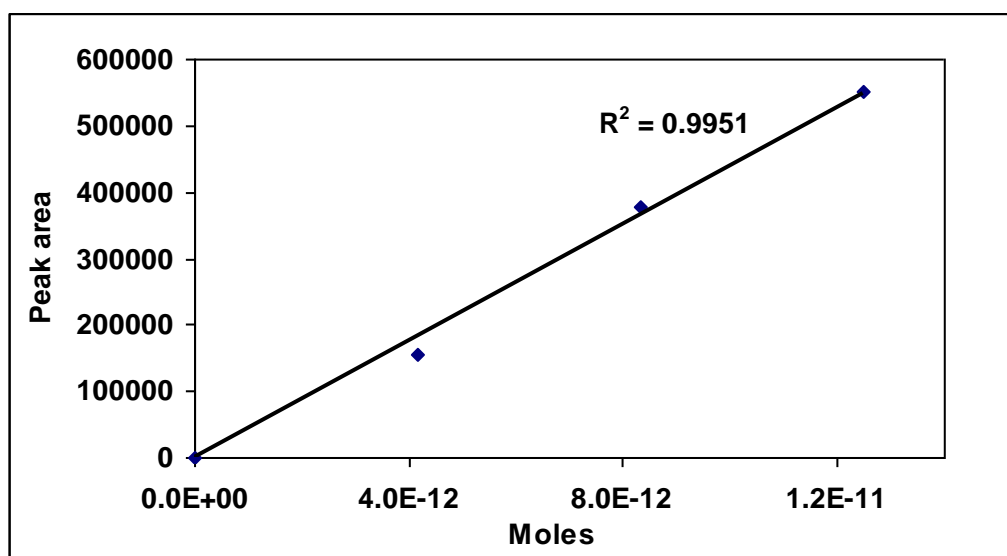
Figure 2.20 Plot of instrument peak area versus moles for CH_3I.

2.6.5 Perm oven valve optimization

Calibration using the "in house" permeation oven was carried out using a 6 port, 2 way switching valve with a 10 µl sample loop (1.6 mm OD and 0.05 mm ID $\pm$ 0.001mm), as described in section 2.6.4. An investigation into sample loop switching times suggested that there was a significant linear increase in permeation oven internal pressure with

increasing valve switching times, figure 2.21. These measurements were made by introducing a barometer (Bell and Howell) in-line between the high temperature permeation holder and the valve, figure 2.16. Data acquisition (1 Hz) was carried out using Labview 8.6 (National Instruments) data logging software. On further investigation, all halocarbon concentrations increased linearly with permeation oven positive pressure (Δ pressure) for each valve switching time (10, 30, 60 s), figure 2.22. The resulting peak area linear regression lines were extrapolated to zero Δ pressure (ambient pressure) and the values used to calculate correction factors for each Δ pressure. Table 2.5 lists the relevant correction factors applied to the data.

This internal pressure increase was attributed to a flow restriction introduced to the flow stream when the permeation gas passed through the 0.05 mm ID sample loop in the "load permeation gas" position, figure 2.17. Halocarbon % concentration increases were significantly higher for all permeation tubes housed in the 40 ℃ holder than the 70 ℃ holder; mean increases over a load time of 1 minute were 60.6% (54.13 – 66.09%) and 42.5 % (38.02 – 48.81%), respectively, as depicted in table 2.5. This discrepancy in averaged % halocarbon increases could be attributed to enhanced losses of the higher molecular weight compounds onto internal surfaces at higher pressures. In an attempt to prevent any valve internal pressure fluctuations during future permeation calibrations, a larger ID (0.40mm) 25µl sample loop was introduced to the valve as well as reducing the sample load time to 10 s. No pressure increase was observed within the system with this optimized set-up.

Calibrations carried out for the COBRA campaign (chapter 4) used a valve switching time of 60 s with the 10µl loop, therefore the discussed corrections were applied. All other work was calibrated against the permeation oven using a valve switching time of 10 s with the 25 µl loop.
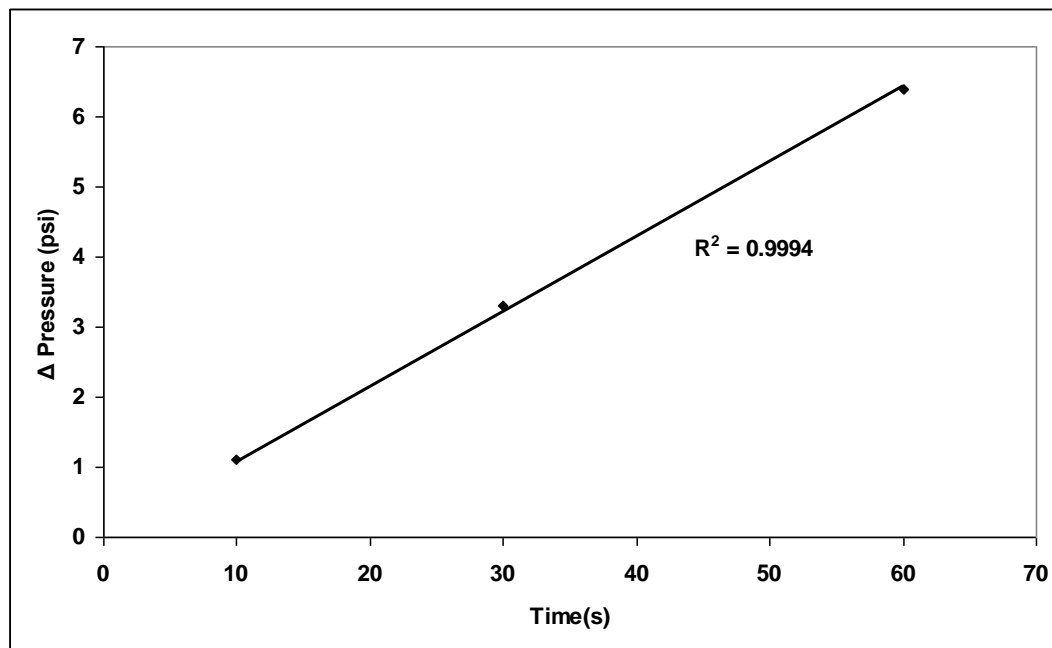
Figure 2.21 Plot depicting pressure change within permeation system against valve switching times.
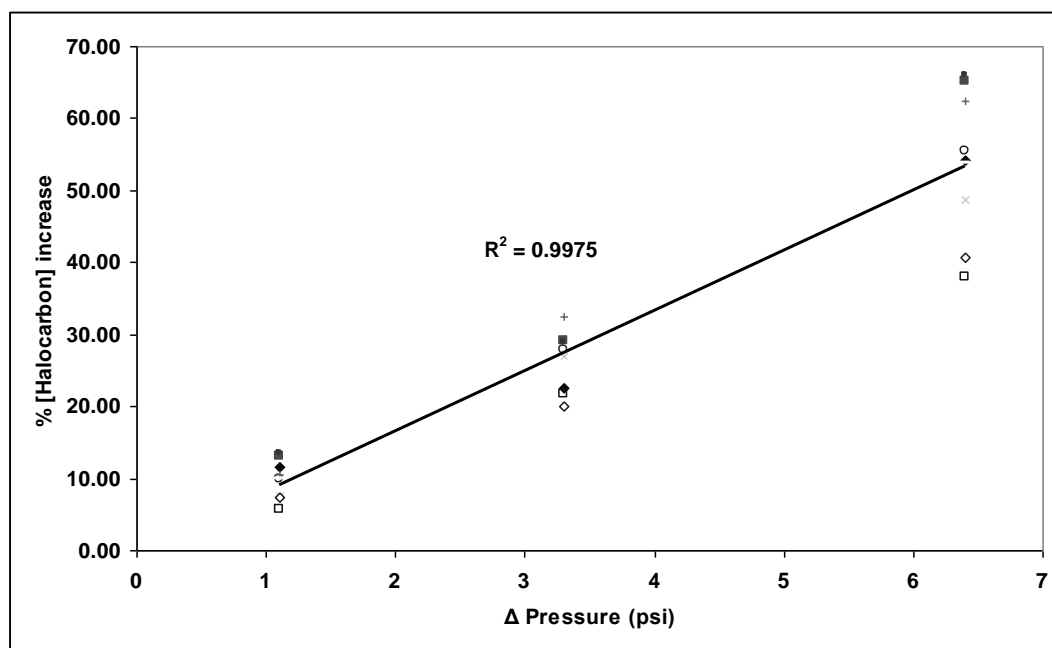
Figure 2.22 Plot depicting % halocarbon concentration increase with increasing pressure (Filled diamonds CH_3I, filled squares $CHCl_3$, filled circle C_2H_5I, cross 2-C_3H_7I, empty circle CH_2Br_2, empty diamond 1-C_3H_7I, cross CH_2ICl, empty square CH_2IBr).

Halocarbon	10 s switching time (%)	30 s switching time (%)	60 s switching time (%)	Correlation coefficient (R^2)
CH_3I	11.58	22.53	54.13	0.97
C_2H_5I	13.53	28.95	66.09	0.99
$CHCl_3$	13.05	29.18	65.11	0.98
CH_2Br_2	9.83	27.80	55.36	0.99
CH_2IBr	5.64	21.71	38.02	0.99
$2-C_3H7I$	7.62	26.98	48.81	0.99
CH_2ICl	10.55	32.53	62.34	0.99
$1-C_3H7I$	7.38	20.00	40.62	0.99

Table 2.5 Table of % halocarbon concentration increase for each valve switching time and correlation coefficients for their relationship against Δ pressure.

2.6.6 Permeation tube degradation study

The composition of permeation gas from each tube was determined periodically over its lifetime to assess degradation of the liquid standards over time. Each permeation tube in turn was cleaned with isopropanol and placed in isolation within the oven and allowed to equilibrate for ~ 15 hours to obtain optimum permeation output. Both a full scan (5-10 sample loops) and a 3 point calibration (10, 20 and 30μl) in SIR mode, table 2.1, were carried out on each tube. Using this method, the % contributions of each perm tube can be calculated for their respective analyte, table 2.6. The tube was then removed from the permeation oven and allowed to equilibrate for ~ 1 hour before 3 loops of the nitrogen carrier gas was analyzed for carryover within the system between tube analyses. No significant carry over of any compound was observed.

The CH_2IBr permeation tube emitted significant amounts of both CH_2Br_2 and CH_2I_2 after only 150 days within the oven, contributing ~18% and ~25% of their total amounts within the permeation gas respectively, table 2.6. This increased to ~35% CH_2Br_2 and ~49% CH_2I_2 after 750 days suggesting significant degradation of the CH_2IBr standard. To correct for this the total permeation output of the CH_2IBr tube was quantitatively determined against a second permeation oven containing both CH_2I_2 and CH_2Br_2 permeation tubes. The CH_2IBr, CH_2I_2 and CH_2Br_2 molar ratios from the permeation gas were 0.88, 0.05 and 0.07, respectively after 750 days, which were the correction factors applied to data calibrated

against the perm oven during this period. There was no measurable indication of any other permeation standard degrading over this time.

Halocarbon	150 Days (3/9/2007)	750 Days (3/5/2009)	New perm tubes (7/7/2009)
CH_3I	100.00	100.00	100.00
$CHCl_3$	100.00	100.00	100.00
C_2H_5I	100.00	100.00	100.00
CH_2Br_2	82.24	65.45	100.00
CH_2ICl	100.00	100.00	100.00
$2\text{-}C_3H_7I$	100.00	100.00	100.00
$1\text{-}C_3H_7I$	100.00	100.00	100.00
$CHBr_2Cl$	100.00	100.00	100.00
CH_2IBr	100.00	100.00	100.00
$CHBr_3$	100.00	100.00	100.00
CH_2I_2	75.65	51.83	100.00

Table 2.6 Table of % contribution for each analyte from their respective permeation tubes for 3 time periods in the permeation oven.

Following 672 days within the oven, approximately monthly molecular iodine (I_2) determinations were also carried out on the permeation gas from all 11 tubes simultaneously using an optimized I_2 solvent trap (100 mL/min^{-1}), section 3.2, positioned on the permeation oven exhaust. Measurable concentrations of I_2 were observed within the permeation gas, which increased over time, figure 2.23. However, assuming that this I_2 all originates from the most photolytically unstable permeation standard CH_2I_2 (section 1.3, table 1.1), the I_2 concentrations measured after 872 days only represent a negligible over estimation of CH_2I_2 concentrations in the permeation gas (3.74%).

The most likely cause of permeation standard degradation is primarily from photolysis, especially during weighing of the tubes during which the tubes are exposed to sunlight, and long-term thermal degradation within the oven. The observations discussed prompted the replacement of the tubes (7/7/2009) with new certified permeation tubes (Ecoscientific)

which, following analysis, showed no signs of compound degradation, table 2.6.
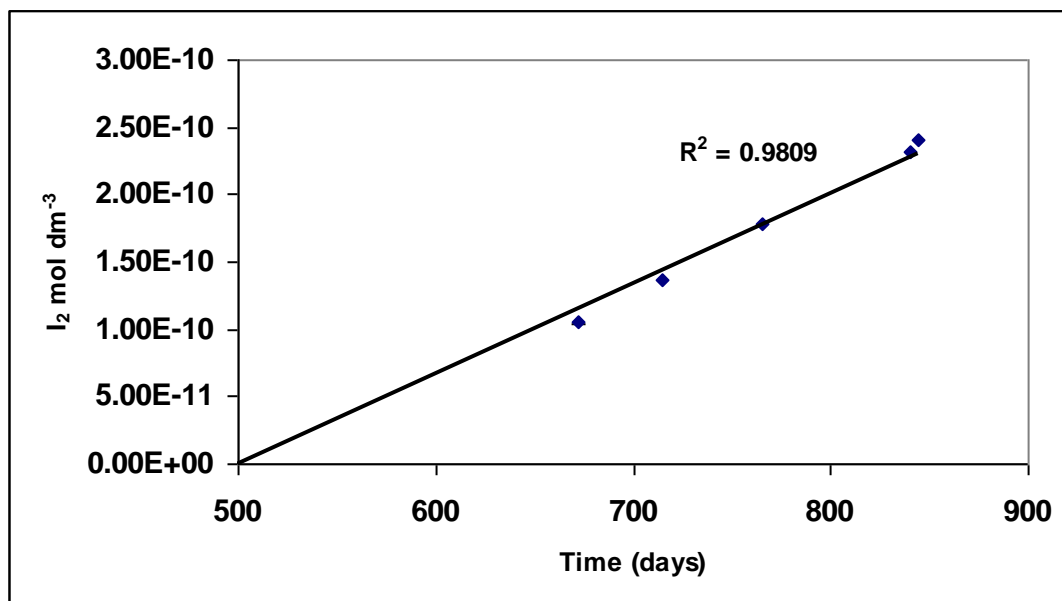
Figure 2.23 I_2 concentration from halocarbon permeation oven against time permeation tubes housed in oven.

2.6.7 Propagation of errors for calibration

Each component of EQ 2.17 has an error associated with it which affects the repeatability of each measurement. The propagation of these errors places a total uncertainty upon the measurements, usually expressed as percentage relative standard deviation (% RSD). The % RSD of the permeation rates (figure 2.19) and calibration curves are calculated from the deviation of data points from the linear regression line, divided by the mean. The standard deviation of linear regression (S_m) is calculated from the sum of the squares of the deviation for x (S_{xx}) assuming no errors in y, the sum of the squares of the residuals (SS_{resid}) and the number of degrees of freedom ($N–2$) using EQ 2.18 (Skoog *et al.*, 1991). S_{xx} was calculated using EQ 2.19 where x_i and $\bar{x}$ are the measurement and mean value of component x respectively. The SS_{resid} was calculated using least squares regression as shown in EQ. 2.20, where y_i, m and b are the y component measurements, the linear regression slope and the intercept respectively. From S_m, measurement uncertainty can be calculated and expressed as % RSD. The % RSDs for permeation rates and calibration curves for each compound are given in table 2.7.

$$S_m = \sqrt{\frac{SS_{resid}}{S_{xx}(N-2)}}$$ (EQ 2.18)

$$S_{xx} = \Sigma(x_i - \bar{x})^2$$ (EQ 2.19)

$$SS_{resid} = \sum_{i=1}^{N}[y_i - (b + mx_i)]^2$$ (EQ 2.20)

Compound	%RSD Calibration curve Chamber experiments	%RSD Calibration curve COBRA Campaign	%RSD Permeation rate
CH_3I	6.93	13.45	0.46
$CHCl_3$	-	6.06	0.64
C_2H_5I	8.32	11.46	6.72
CH_2Br_2	-	11.62	0.98
CH_2ICl	-	13.35	2.25
$2\text{-}C_3H_7I$	1.19	10.96	6.92
$1\text{-}C_3H_7I$	2.53	12.07	2.07
CH_2IBr	-	13.63	6.75
$CHBr_3$	-	12.53	2.75
CH_2I_2	-	13.43	5.12

Table 2.7 % RSD values for permeation tube weighings and calibration curves for each species.

The most significant sources of error with the TD-GC/MS instrumentation are from the calibration. However, a full assessment of errors of all hardware associated with the permeation oven calibration is shown in table 2.8.

Component	%RSD Uncertainty Chamber experiments	% RSD Uncertainty COBRA Campaign	Notes
Sample loop	0.25	2.00	Loops have a tolerance of ± 0.001mm.
			COBRA campaign - 10µl loop (ID 0.05mm).
			Chamber experiments -25 10µl loop (ID 0.40mm).
Mass balance (5 fig)	1.00	1.00	As stated by manufacturer.
Perm oven flowrate	1.50	1.50	Variation in perm flow rate during period.
Permeation rates	0.46 – 6.75	0.46 – 6.75	Compound specific permeation rate uncertainties.
Calibration curve	1.19 – 8.32	6.06 – 13.63	Compound specific calibration curve uncertainties.
Total	2.22 - 10.86	6.66 -15.45	

Table 2.8 Total uncertainty associated with calibration for the COBRA campaign and laboratory chamber experiments.

2.6.8 COBRA campaign data normalization

The halocarbon online air measurements obtained were normalized using both an *in situ* internal standard, carbon tetrachloride (CCl_4), and a gaseous external halocarbon standard mixture, 2.6.1. Carbon tetrachloride is a stable gaseous compound (atmospheric lifetime of ~ 34 ± 5 years; Allen *et al.,* 2009) observed at relatively high concentrations in the atmosphere. Due to the lack of rapid tropospheric removal mechanisms, CCl_4 is typically present in the troposphere at mixing ratios of ~ 100 pptv (Allen *et al,* 2009). Due to this compounds long term stability and uniform distribution within the MBL it can be directly used as a measure of instrument sensitivity over time, making it an ideal *in-situ* internal standard for air analyses. Halocarbon mixing ratios normalized *via* this method were

corrected for variations in detector sensitivity, trapping volume and trapping efficiency incurred during the analysis period.

During the analysis period (18th of February to 28th of February) the external gas standard mixture (200 mL) was analyzed, approximately every 2 days, and an instantaneous CCl_4/halocarbon ratio for each compound with respect to time calculated. A linear regression line was fitted to these values and from its regression equation, instantaneous CCl_4/halocarbon ratios were extrapolated for each online air analysis time. These values were then multiplied by the CCl_4 response for each corresponding analysis to generate equivalent peak areas (*epa*) for each halocarbon for each their respective analysis times, figure 2.24. The *epa* values are effectively a compound-specific measure of instrument sensitivity during the analysis period.
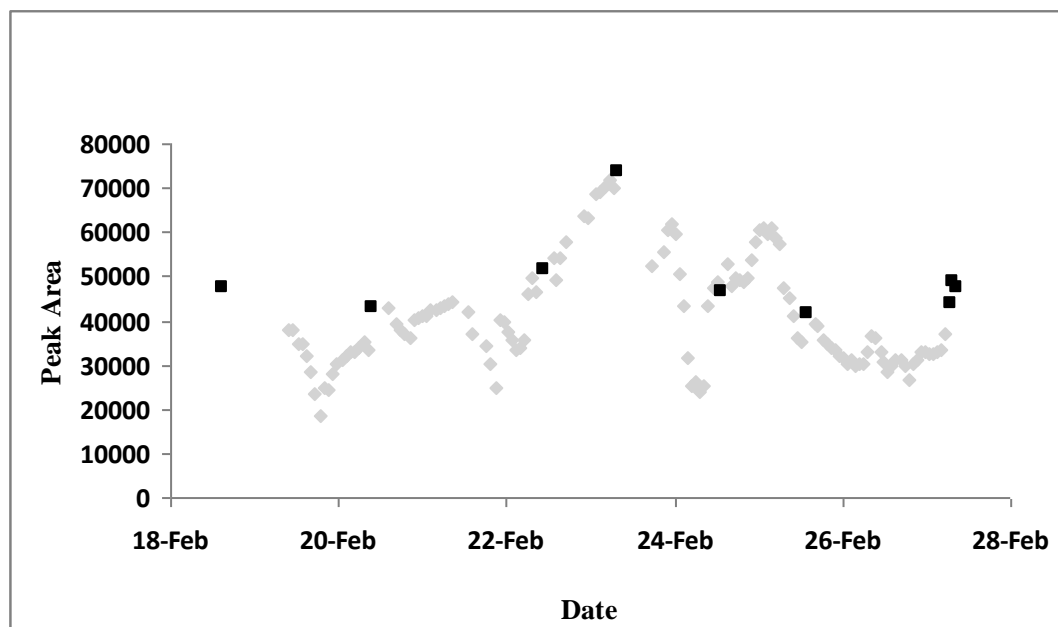
Figure 2.24 2-C_3H_7I external standard peak area with *epa* values during the COBRA campaign (Black squares are peak areas from external standards, Grey triangles are epa values assigned for each analysis time).

The *epa* values are used to normalize the raw data, the concentrations from which can be calculated from the external gas standard mixture via EQ 2.21.

Concentration (mol dm^{-3}) = $\dfrac{\left([HC_{standard}]xPA_{sample}\right)}{epa}$ (EQ 2.21)

where [$HC_{standard}$] is the halocarbon concentration in the external gas standard mixture (mol dm^{-3}), and PA_{sample} is the halocarbon peak area within the sample.

The aqueous halocarbon purge and trap analyses were normalised against CCl$_4$ within the NPL external standard during a 2.5 day analysis period, refer to section 2.6.2. Each aqueous sample was bracketed with a known volume of NPL standard (100 mL), prior to and immediately after purge and trap analysis. A linear regression line was then fitted to the CCl$_4$ responses and used as a measure of MS sensitivity over time. The regression equation from the linear regression line was then used to generate CCl$_4$ *epa* values with respect to time, figure 2.25. The generated *epa* values were then used to normalize the aqueous halocarbon data using EQ 2.21.
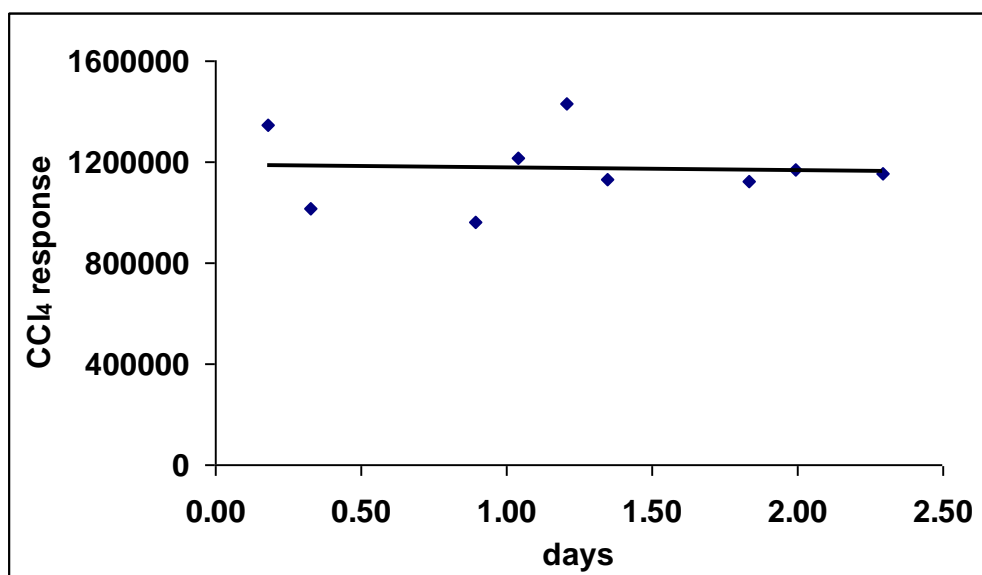
Figure 2.25 Polynomial fitting of CCl$_4$ MS response during aqueous analysis period.

2.6.9 Laboratory cold chamber data normalization

All laboratory chamber data (chapter 5) was normalized against a mixed deuterated standard, section 2.6.3, in a continuous restricted flow set-up. The deuterated standard flow rate into the sample gas stream was controlled by using a non polar fused silica transfer line

(2.75 m, 0.32mm ID) and by regulating the output pressures of both the deuterated standard and the nitrogen sparge gas cylinders, 0.8 and 1.0 bar gauge pressure, respectively, figure 2.26. Fine adjustments to the flow rate were carried out using a variable flow needle vale upstream of the purge and trap set-up. Sample gas and deuterated standard gas flow-rates into the TDU adsorbent trap were maintained at 50 mL min^{-1} and 20 mL min^{-1} for the duration of the analysis. The purge trap set up and methodology was outlined in section 2.2.

Regulator output pressure = 0.8 Bar

2.75 metres
(ID 0.32mm)

20mL/min^{-1}

Deuterated
Standard

**ATD
GC/MS**

Regulator output pressure = 1.0 Bar

50mL/min^{-1}

**Purge
set-up**

Stop flow valve

Variable flow
needle valve

Nitrogen
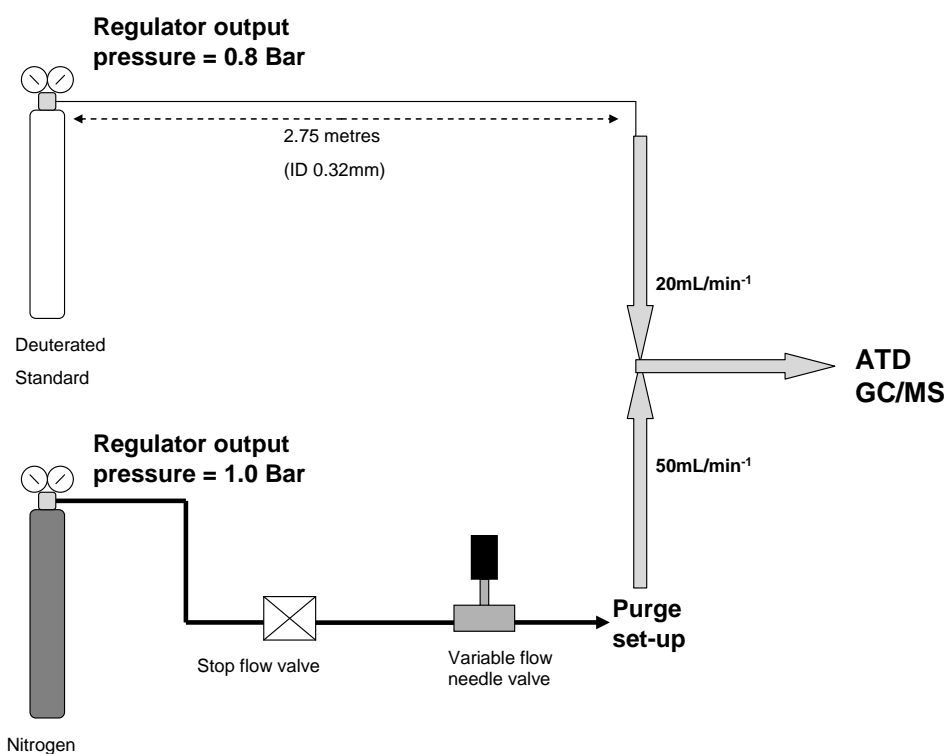
Figure 2.26 Restricted flow internal standard set-up.

During operation the photo-multiplier was set at 550 a.u. (arbitary units) to produce optimum analyte sensitivity, at pptv concentrations. The voltages applied to the repeller and ion focusing lenses are set during a tuning process, against the tune gas perfluorotributylamine (Sigma Aldrich), to optimize detector sensitivity. The potentials set are dependent upon the level of ion burn upon the ion focusing lenses and repeller, which can vary MS sensitivity over time. Validation of the internal standardization technique was carried out to evaluate if the changes in detector sensitivity experienced during operation were the same for the compounds in the deuterated standard as for the compounds under

investigation. This was accomplished by replacing the nitrogen sparge gas, figure 2.26, with a mixed halocarbon gas standard, section 2.6.1, and running the set-up under the same conditions used during sampling. The voltages to the multiplier, repeller and ion focusing lenses were varied over a 3 day period to simulate a typical drop off in detector sensitivity over time; the altered tune parameters are shown in table 2.9. Replicate analyses were obtained ($n = 4 - 7$).

	Day 1	Day 2	Day 3
Repeller potential (V)	1.5	1.3	1.1
Ion focusing lens 1 potential (V)	6	8	8
Ion focusing lens 2 potential (V)	52	62	62
PMT (a.u.)	550	530	500

Table 2.9 Mass spectrometer tune parameters altered during internal standard validation.

Despite these alterations, the correlations plots of the deuterated against the non deuterated compounds show that all of the halocarbons are satisfactorily tracked by one or more of the deuterated compounds with the exception of CH_2I_2, table 2.10. The R^2 values suggest that the most suitable deuterated standard to be used for internal standardization is specific for each compound, with the best correlations found between deuterated standards of a similar molecular weight to the target compound. Possible reasons for this include that nearer eluting compounds exhibit a closer match in column resolution as well as mass dependency during ion transmission/focusing onto the QMS from the ionization source. This leads to inaccuracy when internally standardizing against a compound of a significantly different molecular weight. To take this into account the compounds under investigation were each internally standardized against the deuterated compound with the highest R^2 value, table 2.10. Figure 2.27 shows the most suited deuterated standard versus non-deuterated standard correlation plots for each of the compounds, R^2 values range between $0.996 - 0.976$. Due to the fact that no suitable internal standard for CH_2I_2 could be found, as well as the

chromatography issues describes in section 2.5, all CH_2I_2 cold chamber data (chapter 5) was disregarded.
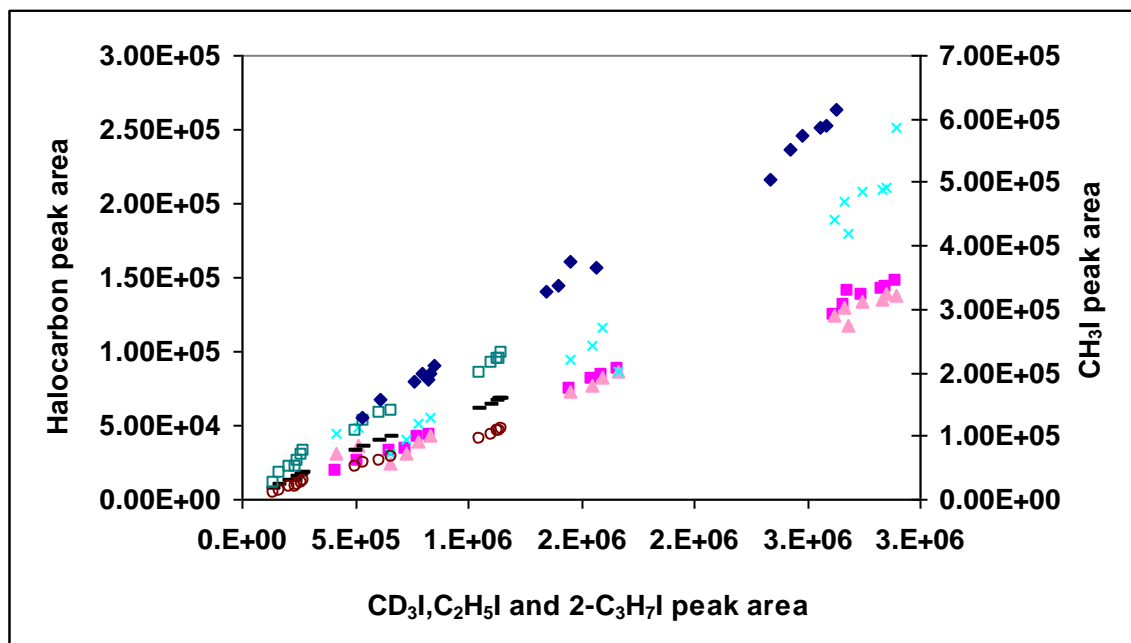
Figure 2.27 Correlation plots of the deuterated standard peak areas against halocarbon peak areas. Dark blue diamonds, CH_3I; filled pink squares C_2H_5I, filled pink triangles, CH_2Br_2, crosses CH_2ICl, dashes 2-C_3H_7I, empty circles 1-C_3H_7I empty squares CH_2IBr.

Halocarbon	CD_3I	C_2D_5I	2-C_3D_7I
CH_3I	0.991	0.936	0.923
C_2H_5I	0.955	0.996	0.962
CH_2Br_2	0.982	0.982	0.975
CH_2ICl	0.955	0.967	0.950
2-C_3H_7I	0.994	0.994	0.994
1-C_3H_7I	0.960	0.980	0.993
CH_2IBr	0.975	0.970	0.976
CH_2I_2	0.923	0.931	0.939

Table 2.10 Linear regression coefficients (R^2 values) for each halocarbon compound when plotted against the deuterated species, to 3 sig fig.

2.7   UV-Visible spectrophotometry

2.7.1 Principles of UV-Vis spectrophotometry

Many molecules absorb light in the ultraviolet (UV) or visible (Vis) range providing a non-specific technique for the detection of most analytes. The absorption of UV-Vis wavelengths of radiation corresponds to the promotion of outer electrons from a low energy to high energy orbital. There are 3 types of electron types to be considered: σ electrons, π electrons and non bonding (n) electrons (transitions involving charge-transfer electrons and d and f electrons are also possible but beyond the scope of this discussion). Possible electronic transitions include:

$\sigma \rightarrow \sigma^*$ transitions

Occurs when an electron from the bonding σ orbital is promoted to the corresponding anti-bonding orbital, figure 2.28. This requires large amounts of energy to undergo transition which may result in a breakdown of chemical bonds (< 190 nm). Compounds such as saturated hydrocarbons typically absorb in this region (C - H bonds).

$\pi \rightarrow \pi^*$ transitions

This is regarded as the most analytically useful type of electronic transition as the energy required to induce the transition is moderate and can be obtained from sources operating in the UV/VIS range (Christian, 1994).

$n \rightarrow \sigma^*$ and $n \rightarrow \pi^*$ transitions

Compounds containing lone pairs of electrons which do not participate in chemical bonds are capable of $n \rightarrow \pi^*$ (if the molecule has π bonds) or $n \rightarrow \sigma^*$ transitions. $n \rightarrow \sigma^*$ transitions usually require much more energy and can be initiated by radiation in the wavelength region of 150 - 250 nm. For chemical analysis the most useful of the electronic transitions are $\pi \rightarrow \pi^*$ and $n \rightarrow \pi^*$. This is because the absorption peaks for these transitions are within an experimentally useful region of the spectrum (200 -700 nm).

It is these electronic transitions which are responsible for I_2 in hexane observed during work conducted in this study, as described in section 3.

60
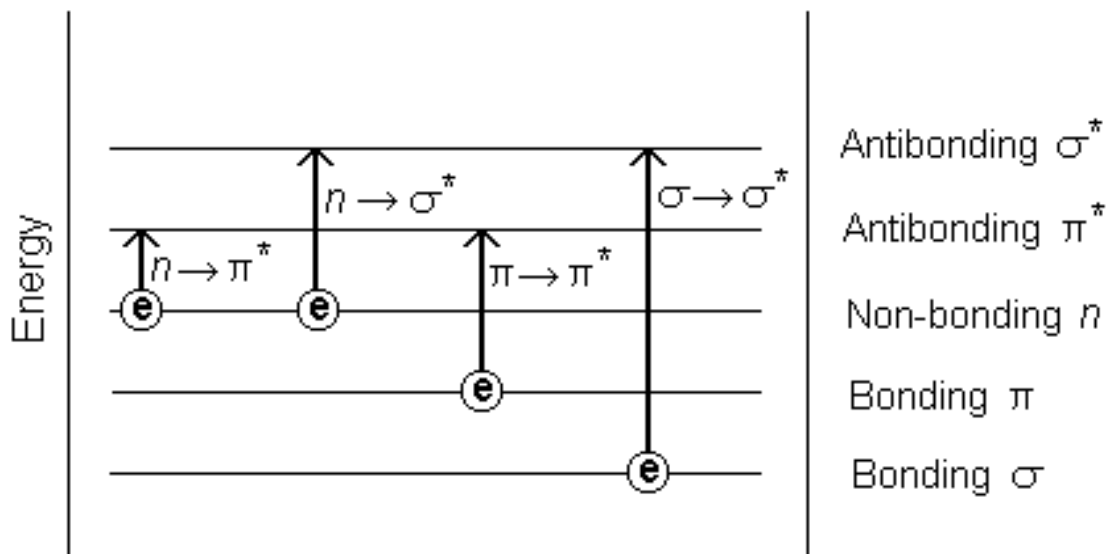
Figure 2.28 UV-Vis absorption electronic transition types

A typical commercially available spectrophotometer uses two light sources to generate a continuous spectrum within the wavelength range 200 - 700 nm, figure 2.29. The source of UV radiation involves the electrical excitation of hydrogen or deuterium at low pressure within lamps. Both deuterium and hydrogen lamps emit radiation in the wavelength range 160-375nm. Quartz windows and sample cuvettes must be used as silicate absorbs radiation < 350 nm. A tungsten filament lamp is commonly employed as a visible light source as it covers both the far UV and near IR range (350-2500 nm). This composite of wavelengths is then passed through a wavelength selector known as a monochromator (a prism, reflection grating) and a filter to select a wavelength range. The preset wavelength range, I_0, is then split by a suitable beam splitter and passed through the quartz sample and reference cell (containing the dissolved analyte in solvent and pure solvent respectively) to parallel detectors. The intensity of the beam transmitted from the cells, *I,* is dependent upon the amount of absorbance by the sample. This is expressed as the Beer Lambert law where *A* is absorbance (in absorbance units), ε is molar absorptivity ($dm^3 \ mol^{-1} \ cm^{-1}$), and *l* is the optical path length (cm), EQ 2.22.

$$A = \varepsilon \, c \, l \qquad\qquad\qquad \text{(EQ 2.22)}$$

The amount of absorbance is therefore directly proportional to the concentration of the light absorbing species within the sample. This relationship between absorbance and concentration is linear at low analyte concentrations. At high concentrations, deviation from the Beer Lambert law occurs resulting in a loss of linearity.

Incident light transmittance through the sample and reference cells are determined using photodiode detectors and the ratio of their electronic output plotted. This dual beam approach has two advantages over its single beam predecessors. Firstly, it is via this process that the UV-Vis cross section of the solvent can be subtracted from that of the sample. Secondly, both deuterium and tungsten lamp outputs can fluctuate over time resulting in inaccuracies. To compensate for any fluctuations in output from the lamp, the intensity of the beam transmitting through the sample is compared with the intensity of the beam transmitted through an identical cell containing solvent.
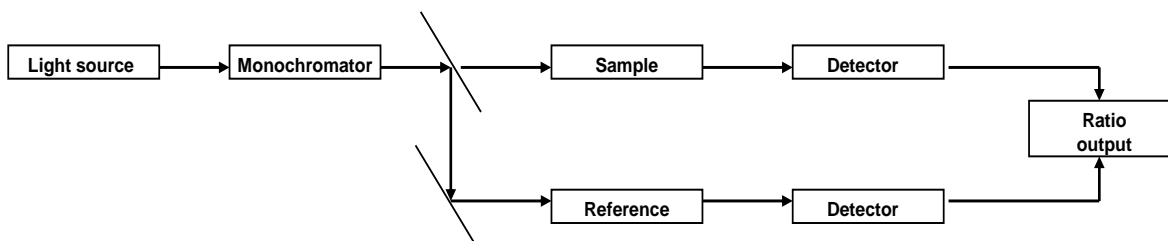
Figure 2.29 Schematic of a dual-beam spectrophotometer, adapted from Harris 2010.

A dual beam Lambda 25 UV-Vis spectrophotometer (Perkin Elmer) was used for the experiments (section 3.2) with quartz cells of both a 1 cm and 10 cm light path. A calibration curve was plotted to quantitatively determine iodine (I_2) trapped in hexane during both the optimization of the solvent trap and during experiments involving the exposure of ozone to iodide solutions (figure 2.30). This calibration curve was produced daily, using a 10 mm quartz cell (figure 2.30) or a 100 mm (figure 2.31) quartz cell, to correct for any variation in response resulting in absorbance offsets over time. I_2 had a maximum absorption at 522.48 nm in the visible region.
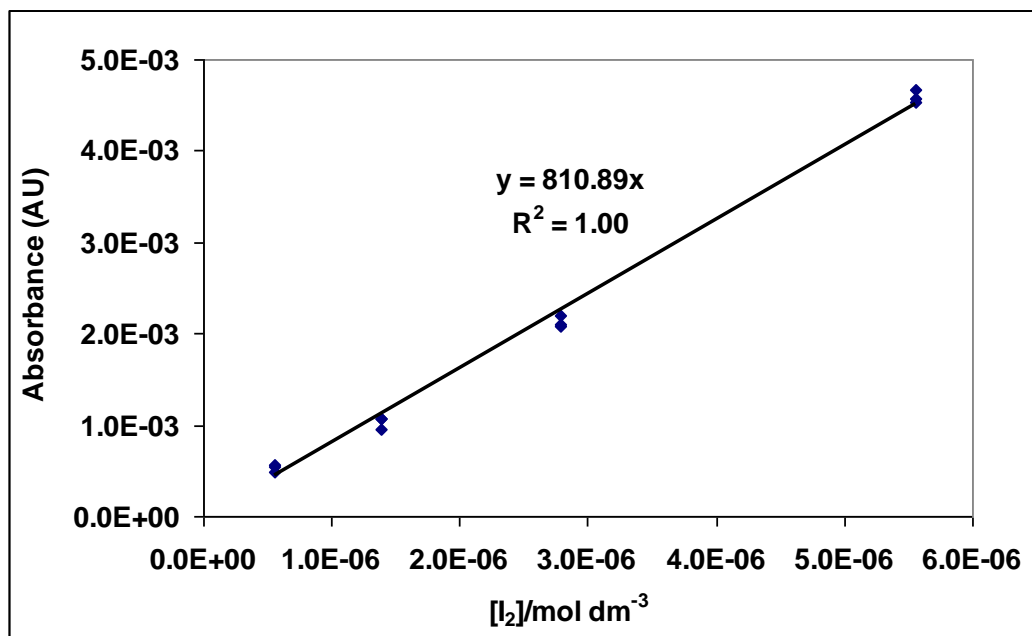
Figure 2.30 Calibration curve for the I_2 in hexane solution used to quantify $[I_2]$ during experiments in section 3.2.2, using a cuvette with a 10 mm pathlength
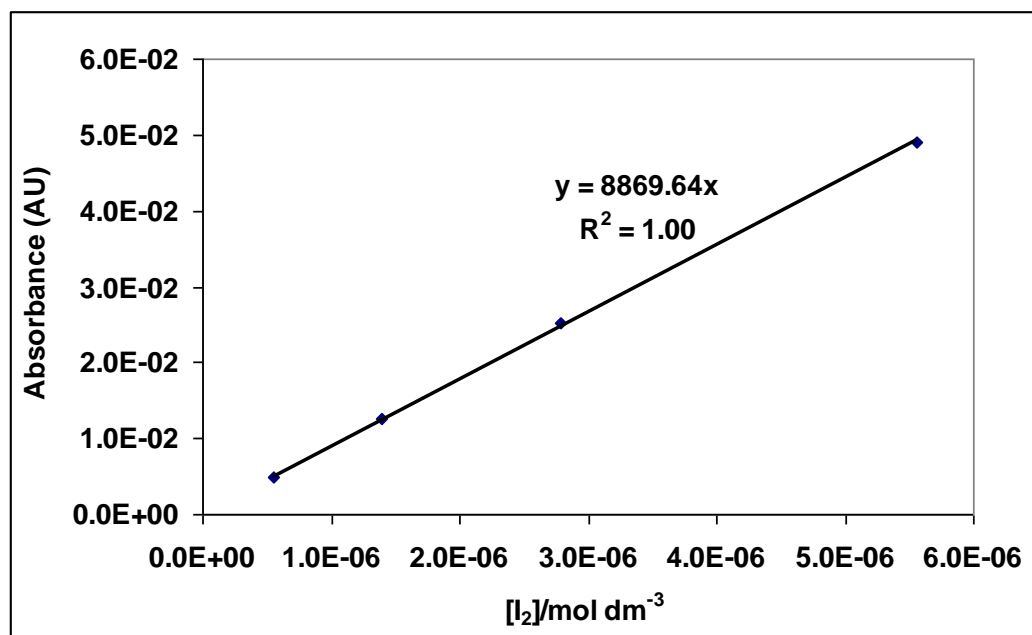
Figure 2.31 Calibration curve for the I_2 in hexane solution used to quantify $[I_2]$ during experiments in sections 3.2.2, 3.24 and 3.5, using a cuvette with a 100 mm pathlength.

Figure 2.32 shows a calibration curve which was plotted daily to quantitatively determine iodide (I^-) in phosphate buffer solution (PBS), pH 8, during the experiments involving the

exposure of ozone to iodide solutions (section 3.5). I^- had a maximum absorption range between 223 -227 nm in the ultra-violet region.
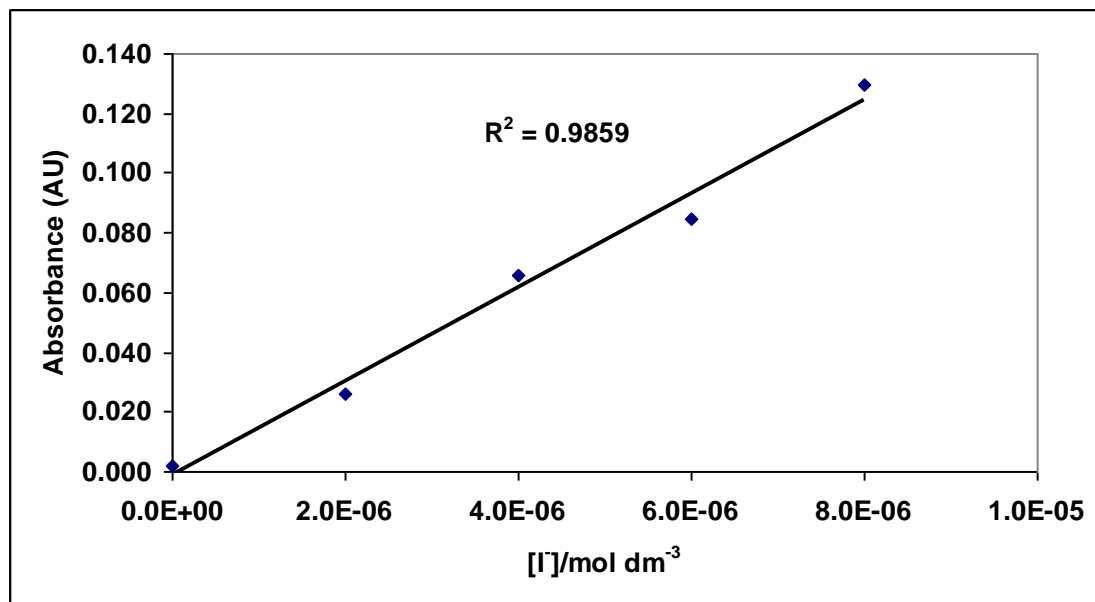
Figure 2.32 Calibration curve for I^- in PBS (pH8) used to quantify $[I^-]$ during experiments in section 3.5.

2.7.2 Solution preparation

All aqueous solutions used in chapter 3 were prepared in degassed HPLC water (Fisher Scientific) which had been prepared using zero grade N_2 (BOC gases) whilst held at a temperature of 70 ºC for ~1 hour. Volumetric glassware (grade A), and Finnpipettes™, 20-200µl (Thermo scientific) and 100-1000 µl (Fisherbrand), were used accordingly during solution preparation. Precision five figure balances (KERN 770) were utilized for all standard weighings. All vessels containing photo-labile substances were covered in aluminium foil and stored at ambient temperature to reduce degradation. Primary stock standards were re-prepared on a monthly basis where as secondary standards (used to plot the calibration curve) were re-prepared every 2 weeks.

2.7.3 Preparation of 0.01 M phosphate buffer solution

Basic buffer (pH 9), used in chapter 3, was prepared by dissolving the target amount of sodium dihydrogen phosphate (NaH_2PO_4, Fischer. 99%) in degassed HPLC water (800 mL). The final pH of the solution was adjusted by titrating freshly prepared aqueous sodium hydroxide (NaOH, Fischer, 99%) solution while stirring using a pH meter, prior to making the final volume up to 1 L. The pH of the solutions were checked and found to be within a suitable tolerance (±2%) prior to use on a weekly basis.

2.7.4   Preparation of iodine solutions

The experiments involved preparation of both aqueous I^- solutions and concentrations of I_2 in hexane. Solutions of I_2 in hexane were prepared by over night stirring of I_2 flakes (Riedel-de Haen), with a glass stirring bar, in hexane (HPLC grade, Fischer) in volumetric glassware covered in aluminium foil. Subsequent dilutions were made in hexane using Finnpipettes™. Solutions of I^- were prepared by overnight stirring of KI (analytical grade, Fischer) in PBS, as described in 2.7.4, and covered in aluminium foil.

2.7.5 Preparation of dissolved organic carbon extract

A dissolved organic carbon (DOC) extract was prepared from coastal seawater (10 L, Bridlington coast) which was collected in airtight glass bottles (4 x 2.5 L) wrapped in aluminum foil before transportation to the lab. The bottles were refrigerated and stored at 2 - 8º for ~12 hours prior to preparation. The seawater was first degassed using zero grade N_2 whilst being heated to 70 ºC for 1 hour to remove any volatile organics. The matrix was then filtered through a 0.45 µm cellulose nitrate membrane filter (Whatman) under vacuum. The filtering capacity of each filter was reached after a few litres of seawater, therefore the filters were replaced as and when necessary.

Pre-concentration of the organic constituents onto a hydrophobic Solid Phase Extraction (SPE) device (Strata-X, 500mg) was then carried out. The SPE device was pre-conditioned using methanol (5 mL), and the matrix loaded under vacuum at a flow-rate not exceeding 5 mL min^{-1}. Once loaded, the sorbent was washed using 5% methanol (5 mL) in HPLC water and dried under vacuum ~ (1 min). The organic constituents were eluted with

methanol (10 mL) and concentrated to dryness (Biotage V10 solvent concentrator) and re-suspended in 10 mL HPLC water. All preparation and pre-concentration steps discussed were completed within 24 hours of sample collection.

2.7.6 Quantitative determination of the dissolved organic extract

Quantitative determination of the DOC extract was carried out using a flash 2000 CHNS elemental analyzer (Thermo Scientific). This instrument consists of a heated furnace, to which the liquid sample is injected, interfaced to a non polar fused silica capillary column and thermal conductivity detector (TCD). The heated furnace contains a mixture of quartz wool and copper oxide, the latter oxidizing carbon, nitrogen and sulphur to their dioxide forms (XO_2) in the presence of oxygen which is continuously administered to the vessel. This is based on the principle of the "Dumas method" which involves the complete and instantaneous oxidation of the sample by "flash combustion". CO_2 is then resolved from these other XO_2 compounds on a non-polar fused silica column with an isothermal temperature program (100 ℃) and detected via the TCD.

The sample (500 µl) was introduced to the instrument and analysed in duplicate. Quantitative determination was carried out by injecting standards (500 µl) of successive carbon concentrations to generate a 5 point calibration curve, figure 2.33. The standard L-alanine (99% purity, BDH supplies) was used to determine DOC concentration, 40.44% carbon by mass.
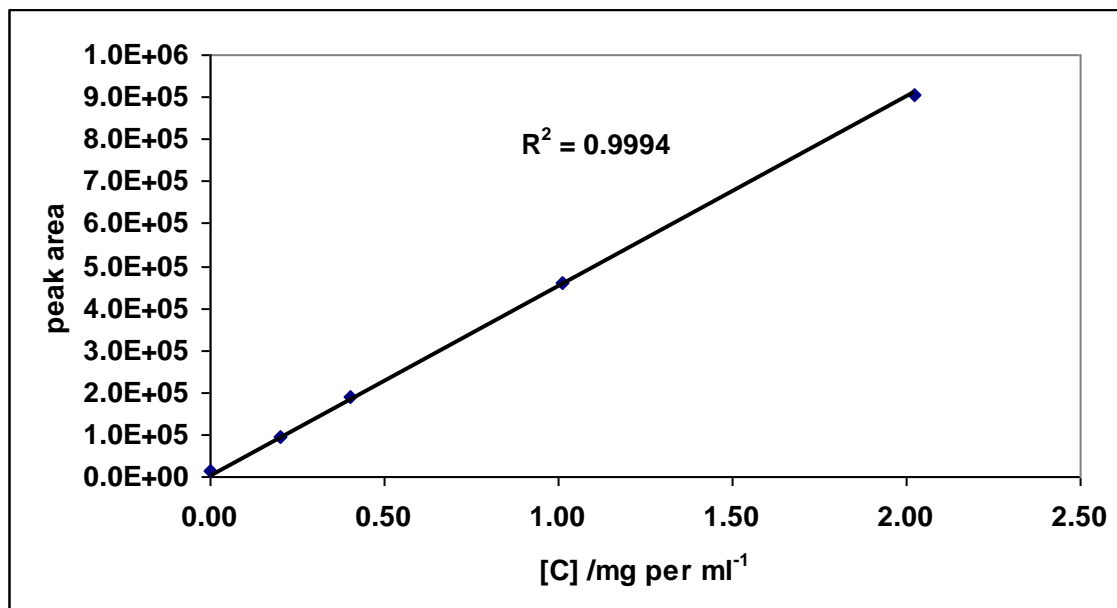
Figure 2.33 Calibration curve for [C] used to determine DOC during experiments in chapter 3.

2.7.7 Quantitative determination of Chlorophyll a

Chlorophyll a concentrations were measured from ice core meltwater and under ice water samples by H. Atkinson (British Antarctic Survey) using a Turner AU-10 fluorometer following extraction overnight (in darkness at 4 ^{o}C) in 10 ml of 90% acetone buffered with MgCO$_3$ (sections 4 and 5). Concentrations were corrected for interference from *phaeophytin a* by measuring fluorescence before and after acidification with 8% HCl and calibrated using a pure *chlorophyll a* standard (*chlorophyll a* from *Anacystis nidulans* − 1 mg diluted in 90% buffered acetone, Sigma-Aldrich), the concentration of which was determined spectrophotometrically.

Chapter 3

Evidence for the abiotic production and direct emission of iodine from surface seawater in the presence of gaseous ozone

A comparison of spectrophotometric and denuder based approaches for the determination of gaseous molecular iodine.

Chance, R. J. Shaw, M. D. Telgmann, L. Baxter , M. and Carpenter, L. J

Atmospheric Measurement Techniques, 3, 177 – 185, (2010).

Globally important emissions of HOI and I$_2$ from the sea surface

Carpenter, L. J. and Shaw, M. D. *manuscript. in preparation.* (2011).

Uptake of ozone and emission of I$_2$ from iodide solutions in the presence of organic material

Carpenter, L. J. and Shaw, M. D. and Parthipan, R. *manuscript in preparation.* (2011).

3.1 Introduction

3.1.1 Abiotic molecular iodine evolution from seawater

The ocean is a major global reservoir of the halogens chlorine, bromine and iodine. All three of these elements exist as halide ions within seawater, the major species of iodine being the oxidized form, iodate (IO$_3^-$). It has been shown that in addition to the flux of particulate halides in sea salt, both volatile organic and inorganic halogens are of importance for the transfer of these elements from the ocean to the atmosphere (Vogt *et al.,* 1999*;* Chuck *et al.,* 2005; Saiz Lopez *et al.,* 2007*;* Wada *et al.,* 2007). It is generally believed that the primary sources of reactive iodine compounds in the marine boundary layer (MBL) are volatile organic iodinated compounds (VOIC) (Carpenter, 2003) and, in coastal regions, biogenic molecular iodine (I$_2$) (Saiz Lopez *et al.,* 2006; Kupper *et al.,* 2008; Dixneaf *et al.,* 2009). Iodine compounds are rapidly photolyzed into I atoms, which are oxidized to iodine monoxide (IO) (Saiz Lopez *et al.,* 2006). VOIC are rapidly photolyzed and/or react with OH, Cl or NO$_3$ forming IO, potentially perturbing the HO + HO$_2$ (HO$_X$) and NO + NO$_2$ (NO$_X$ cycles) (Cotter *et al.,* 2001; Enami *et al.,* 2007). Generated halogen radicals also catalytically destroy tropospheric ozone (Read et al., 2008), and nucleate new particles (O'Dowd et al., 2002) and thus potentially impact climate through the generation of cloud condensation nuclei (CCN).

Recent observations of IO at an open ocean site, Cape Verde Atmospheric Observatory (CVAO) indicate iodine chemistry plays an important role in the oxidizing capacity of the open ocean MBL (Read *et al.*, 2008; Mahajan *et al.*, 2010). The observed VOIC fluxes could not sustain the observed IO concentrations, and unlike many coastal sites Cape Verde is not influenced by kelp bed emissions, suggesting there may be additional iodine production mechanisms taking place in the surface ocean (Mahajan *et al.*, 2010; Jones *et al.*, 2010). Such field measurements suggest that current atmospheric box models parameterised using biogenic organo-iodine emission rates alone cannot account for previously observed gas phase mixing ratios of iodine species within the MBL (Read *et al.,* 2008). The recent detection of both IO(*g*) and OIO (*g*) during nighttime also suggests the

significance of a dark iodine source (Saiz Lopez *et al.,* 2004; Cainey *et al.,* 2007). These field and model observations suggest an additional unknown ubiquitous I$_2$(*g*)/IO(*g*) source.

Miyake and Tsunogai (1963) previously demonstrated the production and subsequent volatilization of I$_2$ from the surface of sea water in the presence of UV light. The laboratory experiment was conducted by passing ambient air over seawater samples at low flow rates under various light conditions predominantly in the UV range. Evolved gaseous I$_2$ was trapped from the output air via the use of a reflux condenser and alkaline/acidic solutions. Quantitative determinations of the I$_2$ solutions were then carried out using spectrophotometry and a radiometric method using ^{131}I as the tracer.

In this instance, the reaction mechanism postulated to explain the gaseous I$_2$ evolution from the surface seawater involved the photochemical oxidation of iodide by dissolved molecular oxygen (O$_2$), as shown in EQ 3.1 to 3.3 (Miyaki and Tsunogai, 1963).

$$4I^-(aq) + O_2(aq) + 2H_2O(aq) + hv \rightarrow 2I_2(aq \text{ or } g) + 4OH^-(aq) \qquad \text{(EQ 3.1)}$$

$$I_2(aq) + H_2O(aq) \rightarrow HOI + H^+ + I^- \qquad \text{(EQ 3.2)}$$

$$I_2(aq) \rightarrow I_2(g) \qquad \text{(EQ 3.3)}$$
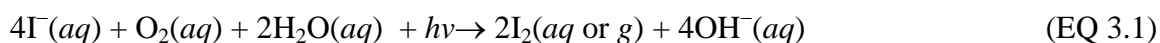
Truesdale (2007) recently demonstrated that the half life of iodide (I$^-$), with respect to EQ 3.1, in seawater under atmospheric conditions was ~29 months. Therefore this mechanism is too slow to contribute to the evolution of significant amounts of gaseous I$_2$ to the marine boundary layer MBL under atmospheric conditions. Truesdale (2007) suggested that the evolution of I$_2$ from surface seawater is only of significance at high irradiances within the UV region of the electromagnetic spectrum, which explains the observations of Miyake and Tsunogai in which UV discharge lamps were used to simulate solar radiation.

Garland and Curtis (1981) were the first to demonstrate the emission of I$_2$ from the surface of seawater following the oxidation of I$^-$ by ozone (O$_3$). Ozone is a much stronger

atmospheric oxidant than O_2 and on deposition to the sea surface readily oxidizes I^-, destroying ozone (EQ 3.4 and 3.5). The work of Garland and Curtis (1981) inferred an I_2 release rate of 22 - 38 ng m^{-2} h^{-1} which is equivalent to an annual flux from global oceans to the atmosphere of 6 - 12 x 10^{10}g. Based on experiments conducted by Garland *et al.* (1980), the enhanced uptake of ozone by iodide is responsible for 20% of the reactivity of ozone toward seawater. This was calculated from the experimentally determined second order rate constant of the iodide ozonation reaction at pH 8 (2 x 10^9 dm^3 mol^{-1} s^{-1}; Garland *et al.*, 1981) and the assumption that I_2 was produced within the laminar layer of the sea surface. Truesdale (2007) suggested that a fraction of this I_2 would undergo a rapid reaction with available I^- in the laminar layer producing tri-iodide (I_3^-), EQ 3.6. This I_3^- would then undergo mixing into the bulk liquid limiting gaseous I_2 evolution. Field measurements conducted by Moller *et al.* (1995) showed nanomolar I_2 concentrations in some samples of surface coastal seawater, but as yet there are insufficient measurements of I_2 in seawater to confirm whether proposed mechanisms for I_2 production operate efficiently in the marine environment.

Experiments conducted by Cheng *et al.* (2008) suggested that another ozonation reaction pathway could be taking place at the air-liquid interface which competes with I_2 production. This involves the stepwise ozonation of I^- to form IO_3^- in the laminar layer, as shown in EQ 3.7 to EQ 3.9. Measured IO_3^- concentrations were typically 10 - 60 times higher than I_3^- concentrations and increased linearly with increasing gaseous O_3 concentrations (ppmv).
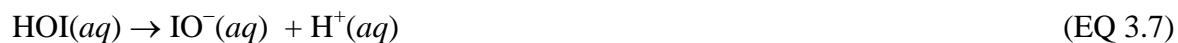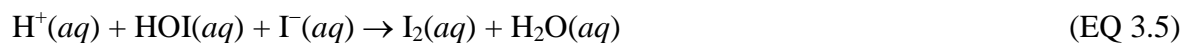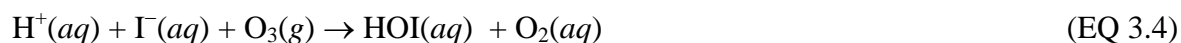
$$H^+(aq) + I^-(aq) + O_3(g) \rightarrow HOI(aq) + O_2(aq) \qquad \text{(EQ 3.4)}$$

$$H^+(aq) + HOI(aq) + I^-(aq) \rightarrow I_2(aq) + H_2O(aq) \qquad \text{(EQ 3.5)}$$

$$I_2(aq) + I^-(aq) \rightarrow I_3^-(aq) \qquad \text{(EQ 3.6)}$$

$$HOI(aq) \rightarrow IO^-(aq) + H^+(aq) \qquad \text{(EQ 3.7)}$$

$IO^- (aq) + O_3(g) \rightarrow O_2(aq) + IO_2^-(aq)$ (EQ 3.8)

$IO_2^-(aq) + O_3(g) \rightarrow IO_3^-(aq)$ (EQ 3.9)

In a recent laboratory study, Sakamoto *et al*. (2009) reported the direct emission of both I_2 and IO during the heterogeneous reaction of gaseous ozone with aqueous potassium iodide ($[I_2](g)] > 100[IO(g)]$). Sakamoto *et al.* (2009) proposed that the formation of IO occurred at the air/water interface from the ozonation of I^- via an unstable trioxide intermediate ($IOOO^-$). The mechanism of IO production at the air/water interface could be explained by several uni-molecular and/or bimolecular reactions involving the $IOOO^-$ intermediate, as described by EQ 3.10 to 3.14.

$I^-(aq) + O_3(g \text{ or } interface) \rightarrow IOOO^- (interface)$ (EQ 3.10)

$IOOO^- (interface) \rightarrow IO (interface) + O_2^- (interface)$ (EQ 3.11)

$IOOO^- (interface) + IOOO^- (interface) \rightarrow IO (interface) + \text{products}$ (EQ 3.12)

$IOOO^-(interface) + HOI (interface) \rightarrow IO (interface) + \text{products}$ (EQ 3.13)

$IO (interface) \rightarrow IO (g)$ (EQ 3.14)
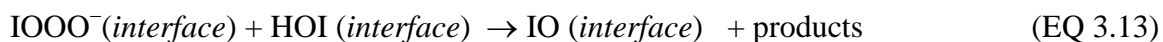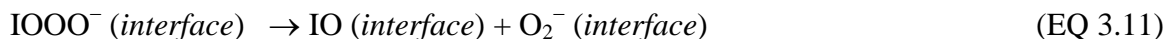
Recent field observations of VOIC and IO in the tropical open ocean MBL at the CVAO lend some support to oceanic inorganic iodine release mechanisms (Mahajan *et al.*, 2010; Jones *et al*., 2010). The data obtained suggests that the measured fluxes of VOIC in the region are insufficient to account for the observed levels of IO, and that an additional I atom source is required, possibly from the oxidation of iodide in the surface ocean by ozone (EQ 3.4 and 3.5). Considering an ozone deposition velocity of 0.05 cm s^{-1} (Chang *et al.*, 2004) and a mixing ratio of 35 pptv, the deposition of ozone to the surface ocean could have been responsible for the emission of 3 I atoms to the gas phase for every 100

molecules of O$_3$ deposited. The oxidation of iodide by gaseous ozone has the potential to make an appreciable contribution to both global atmospheric ozone and iodine budgets within the MBL. Additionally, such abiotic I$_2$ production in the surface oceans may also provide a viable reaction pathway for the evolution of VOIC (Martino *et al*., 2009). Table 3.1 shows estimated global oceanic iodine source estimates.

Compound	Iodine Flux (Tg yr^{-1})
CH$_3$I[a,b]	0.21 – 0.30
C$_2$H$_5$I[b]	0.02
1-C$_3$H$_7$I[b]	< 0.01
CH$_2$ICl[b]	0.17
CH$_2$IBr[b]	0.05
CH$_2$I$_2$[b]	0.11
I$_2$[c]	0.06 – 0.12
Total	**0.63 – 0.78**

Table 3.1 Global oceanic iodine source estimates

[a] Bell *et al*. (2002)

[b]Jones *et al*. (2010)

[c]Garland and Curtis (1981).

3.1.2 Measurement techniques previously used for gaseous I$_2$ determination

A significant limitation for gaseous I$_2$ determinations both in the laboratory and in the field is the lack of a simple and robust method for measuring concentrations approaching those in the atmosphere (0.2 to 93 pptv, Saiz-Lopez *et al*., 2006; Finley and Saltzmann, 2008). The most common method for determining gaseous atmospheric concentrations of I$_2$ is using long path differential optical absorption spectroscopy (LP-DOAS, Saiz-Lopez *et al*., 2006). The major limitations of this technique however are that the instrument spatially averages concentrations over several kilometers and that it cannot be used for open ocean or onboard ship measurements. The recent development of broad band cavity enhanced absorption spectroscopy (BBCEAS) techniques for the measurement of gaseous I$_2$ at

atmospheric concentrations has allowed *in situ* point determinations (Dixneuf *et al*., 2009). However, this technique is not available to most researchers as it is both technically demanding and expensive to operate. Huang and Hoffman (2009) recently reported the use of denuder tubes with an alpha-cyclodextrin coating for trapping gaseous I$_2$ in coastal locations. Subsequent analysis is carried out using inductively coupled plasma mass spectrometry (ICP-MS).

Palmer *et al.* (2005) previously described a solvent trap and subsequent spectrophotometric detection for determining gaseous I$_2$ at ppbv – ppmv concentrations. Such a method has the advantage of being relatively cheap, simple, and able to produce time-averaged rather than spatially-averaged measurements. Also, depending upon the stability of I$_2$ in the chosen solvent, such a method would allow the sample to be collected and analysis to be carried out at a later date.

This chapter describes the development and optimization of a novel spectrophotometric method for the determination of gaseous I$_2$, and its implementation in laboratory investigations of gaseous I$_2$ production rates from the O$_3$ + I$^-$ reaction (Garland *et al.*, 1981; Pathipan, 2008). The work herein represents the first investigation into the effect of dissolved organic matter (DOM), present in seawater, on gaseous I$_2$ evolution and O$_3$ deposition velocities at the sea surface.

3.2 Development and optimization of a hexane solvent trap and spectrophotometric methods for the determination of gaseous I$_2$

The purpose of this investigation was the development of a simple, reproducible method for molecular iodine (I$_2$) enrichment which could either be used for *in-situ* measurements in the field or for laboratory experiments. This involved using a solvent with a high affinity for I$_2$ cooled to subzero temperatures (-9 to -50°C) to facilitate efficient I$_2$ removal from the gas phase whilst minimizing evaporative solvent losses.

3.2.1 Generation of a molecular iodine test source

The solvent trap was optimized using a permeation oven (Kin-Tek™, USA) fitted with a commercial I_2 permeation tube (Kin-Tek™, USA) which provided a constant source of gaseous I_2. The I_2 source concentration was controlled by altering the oven temperature and a zero grade nitrogen (BOC) makeup flow downstream of the oven. The permeation chamber temperature in this investigation was set at either 30 °C to 60 °C with a permeation chamber flow rate of 0.05 L min^{-1}. The outlet flow was further diluted with nitrogen, the flow rate of which was varied to achieve the final concentration of molecular iodine (up to 2.95 L min^{-1}), as shown in figure 3.3. A needle valve and T-piece was used to maintain gas flow rates through the solvent trap apparatus. The concentrations attainable *via* this method were between 190 - 285 ppbv. The I_2 emission rates at these operating temperatures were determined directly from repeated weighings of the permeation tube (n=5) every two weeks. The weighings over the experimental period are shown in Appendix 3.1 and 3.2 for oven temperatures of 30 °C and 60 °C, respectively. Gaseous I_2 wall losses within the system were minimized by ensuring all the tubing and fittings were of Teflon or glass and by heating (to ~60°C) the outlet line from the permeation oven using heating tape. The *in-situ* photo degradation of I_2 was minimized by covering the permeation chamber in aluminum foil and any external tubing in black tape.

3.2.2 Optimization of a spectrophotometric method for I_2 detection

Absorption spectra within the range 190-650 nm were measured using a dual beamed Perkin Elmer Lambda 25 UV/VIS spectrophotometer which was initially fitted with 10 mm quartz sample and reference cells (section 2.7). The instrument was auto-zeroed against *n*-hexane daily. Instrument drift was corrected for by bracketing each sample/calibrant with blank runs and taking into account this response at the given wavelength. The concentrations of I_2 in hexane were determined at 522 nm, as shown in figure 3.2 b. The I_2 calibration curves were constructed using standard solutions prepared from ground molecular iodine (puriss, p.a., Riedel-de Haen) dissolved in hexane (HPLC grade, Fischer UK) within the concentration range 500 – 5000 nmol dm^{-3} (figures 2.30 and 2.31). To prevent cross contamination between samples, the sample cuvette was thoroughly rinsed with hexane between each scan. The spectrophotometric limit of detection (LoD) was

calculated using EQ 3.15 (Harris, 2002) where σ_{STD} is the standard deviation of the mid range standard (n = 3) and the sensitivity is defined as the slope of the calibration curve.

$$LoD = 3 \times (\sigma_{STD}/\text{sensitivity}) \qquad \text{(EQ 3.15)}$$

$$LoQ = \sigma_{STD} \text{of blank} \times 10 \qquad \text{(EQ 3.16)}$$

The determined LoD of I$_2$ in *n*-hexane using a sample cuvette with a path length of 10 mm was 213.3 nmol dm^{-3}, figure 2.30. In order to reduce this LoD as far as possible, sample and reference cuvettes of 100 mm pathlength were used in dual beam mode which reduced this calculated LoD to 20.3 nmol dm^{-3}, figure 2.31. Hence the minimum limit of quantitation (LoQ), calculated using EQ 3.16 (Harris, 2002), for I$_2$ determinations in hexane using a 100 mm cell was 67.7 nmol dm^{-3}.

3.2.3 Molecular iodine derivatisation using leucocrystal violet.

The use of the colorimetric reagent leucocrystal violet (*N, N*-dimethylaniline) was investigated as a method to further reduce the LoD of I$_2$ in hexane. Leuco crystal violet (HCV) has been previously used in aqueous iodine assays (Hatch, 1984; Lambert, 1975) as it reacts with both I$_2$ and IOH producing a violet product which can be measured spectrophotometrically (~592 nm). The reactivity of HCV in aqueous solution is shown in EQ 3.17 and EQ 3.18 where CV$^+$ is the coloured crystal violet species (Hatch, 1984).

$$I_2 + HCV \rightarrow 2I^- + CV^+ + H^+ \qquad \text{(EQ 3.17)}$$

$$HOI + HCV \rightarrow I^- + CV^+ + H_2O \qquad \text{(EQ 3.18)}$$

As seen in EQ 3.17 and EQ 3.18 for equivalent amounts of iodine, HOI produces twice the amount of CV$^+$, hence colour intensity, of I$_2$. In aqueous solutions, HOI is in equilibrium with I$_2$, from in-situ hydrolysis (Hatch, 1984), EQ 3.2. However, within hexane the reaction of I$_2$ with H$_2$O would not occur due to the low concentrations of water present, hence the CV$^+$ concentration would be directly proportional to I$_2$ in the stoichiometric ratio 1:1, EQ 3.17. The direct trapping of gaseous/aerosol HOI by the hexane trap was not investigated

within this chapter, high mixing ratios of which could potentially cause an overestimation of I_2 via this colorimetric method.

The colorimetric determination of I_2 in hexane involved the addition of 0.2 mL of HCV indicator (1.5 g L^{-1} in hexane, Sigma Aldrich) to 20 mL of I_2 in hexane sample in an amberised bottle. The leuco crystal violet indicator was made up in hexane on a daily basis. Upon addition of indicator, the sample was mixed for exactly 1 minute prior to immediate determination of the I_2 absorbance at 568 nm using the 100 mm path length cell, figure 3.2 c. The sensitivity of the colorimetric method in hexane was investigated against the direct spectrophotometric determination of I_2 within the concentration range of 0.56 to 5.60 µmol dm^{-3}. Figure 3.1 shows the mean I_2 responses of triplicate measurements for this method comparison. The *y* errors represent the total precision error calculated from the propagation of the standard deviation of the I_2 permeation rates and the standard deviation of replicate analyses. The initial comparison (t_0) suggested that the response of the colorimetric method (at 568 nm) was a factor of 17 higher than by spectrometry alone (at 522 nm). However, when the procedure was replicated 7 days later (t_7), I_2 sensitivity was observed to have dropped by ~ 66 % over the same concentration range. This reduction in sensitivity between t_0 and t_7 was attributed to the hydroscopic nature of HCV and its exposure to lab air affecting its solubility in hexane. Despite the observed increase in sensitivity between the two methods, the calculated LoD (EQ 3.15) achieved with leuco-crystal violet derivatisation (120 ± 34 nmol dm^{-3}) was ~6 times higher than with hexane alone. This was due to the σ_{std} values of the triplicate measurements observed at each concentration for the colorimetric method being at least a factor of 10 higher (3.6 – 9.8 %) than for the spectrophotometric method (0.2 -0.5 %). This increase in σ_{std} is attributed to the relatively short lifetime of CV^+ in hexane, the concentration of which is observed to decrease exponentially over time accounting for a 27 % loss over an hour after initial mixing, (Appendix 3.3). Due to the instability of CV^+ in hexane, this method was not used further in this study. However, with further work, it may be possible to develop a derivatisation method that yields reproducible results in organic solvent and a lower LoD.
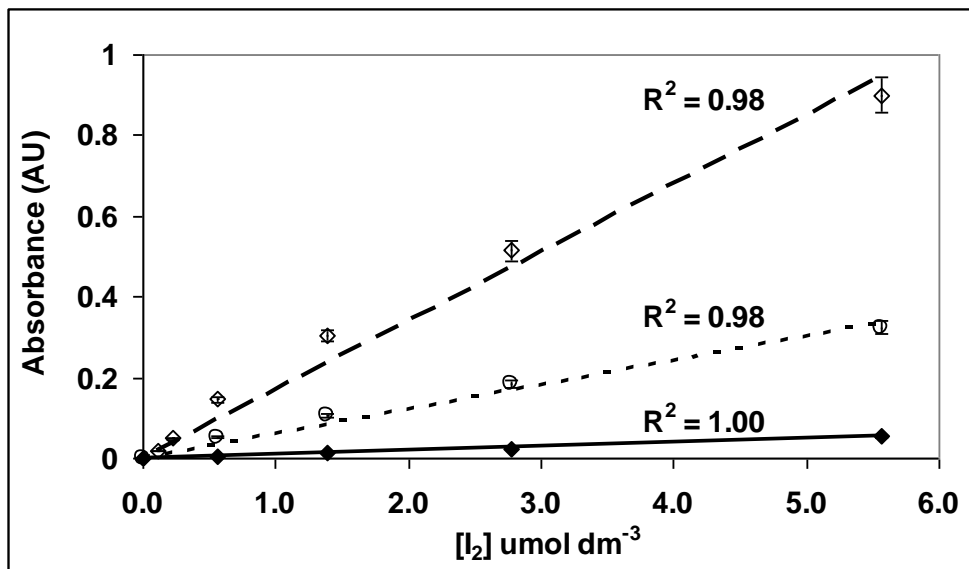
Figure 3.1. Comparison of I_2 responses for the HCV method. Dashed line, HCV method response at t_0; dotted line, HCV method response at t_7; solid line, response using spectrophotometric method.

3.2.4 Optimisation of solvent trap for gaseous I_2 enrichment

Previously gaseous I_2 enrichment has been carried out by bubbling gaseous sample though ethanol (Palmer, 2005). In basic solution such as ethanol, I_2 disproportionates (EQ 3.19) rapidly producing a number of iodine species including I^-, IOH and I_3^- which makes the spectrophotometric quantitative determination of I_2 problematic, as shown in figure 3.2a. I_2 determination in ethanol is usually carried out by comparing the I^- absorbance (at ~225 nm) in the solvent to those of calibration standards. Recent work by Chance *et al.* (2010) suggests that the action of passing the sample gas through ethanol purges the solvent of dissolved gases, and consequently disrupts the complex pH dependent equillibria that govern the disproportionation of the dissolved I_2. Subsequent comparisons of I_2 calibration curves prepared in pre-purged and un-purged ethanol suggested that the I^- signal in purged ethanol was 1.2 to 1.8 fold higher than in un-purged ethanol, resulting in an overestimation in the I_2 concentration. Further limitations in using ethanol as the trapping solvent are that it severely reduces the spectrophotometric LoD as not all the iodine in solution is present as I^-.

Molecular iodine is also very soluble in the non polar solvent *n*-hexane, which preliminary studies (Parthipan, 2008) have suggested is effective in I_2 enrichment from the gas phase. In *n*-hexane I_2 shows no indication of disproportionation and absorbs strongly at 522 nm, as shown in figure 3.2b. Therefore *n*-hexane is a suitable solvent for gaseous I_2 enrichment and subsequent optimization of trapping conditions were carried out using this solvent. The I_2 trapping efficiency of *n*-hexane was investigated by placing two solvent traps in series, as shown in figure 3.3. The traps were deployed for periods of up to five hours and their I_2 content determined spectrophotometrically (section 3.2.2). Recovery and trapping efficiency (T.E) were calculated using EQ 3.20 and EQ 3.21.

$$3I_2 + 6OH^- \rightarrow 5I^- + IO_3^- + 3H_2O \qquad\qquad \text{(EQ 3.19)}$$

$$\text{Recovery (\%)} = 100 \text{ x } [I_2]_{measured}/[I_2]_{expected} \qquad\qquad \text{(EQ 3.20)}$$

$$\text{T.E (\%)} = 100 \text{ x } [I_2]_{\text{solvent trap 1}}/([I_2]_{\text{solvent trap 1}} + [I_2]_{\text{solvent trap 2}}) \qquad \text{(EQ 3.21)}$$
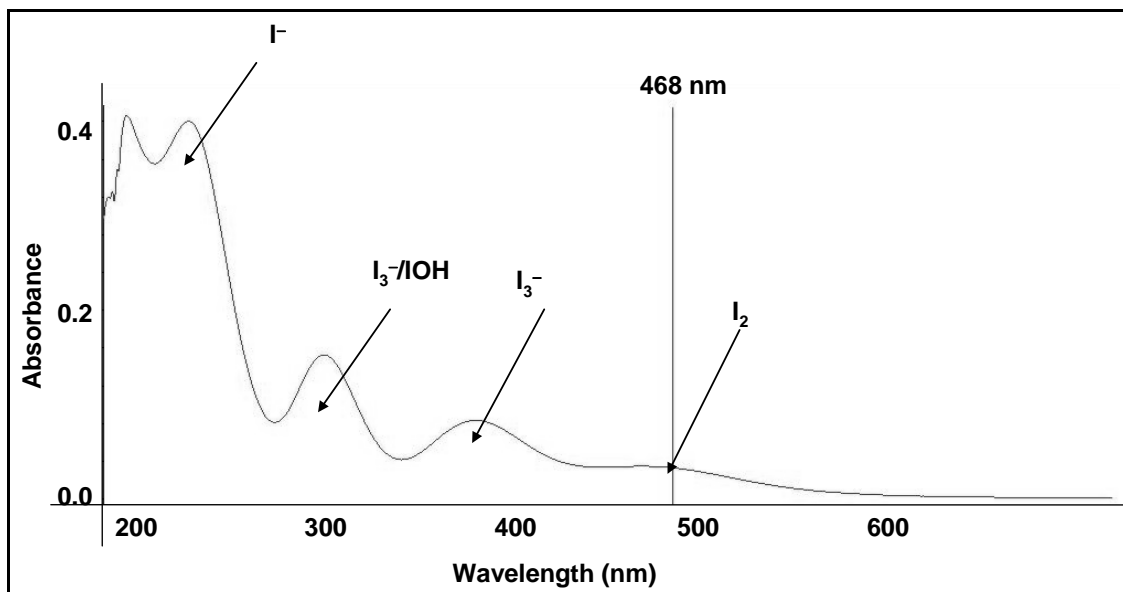
Fig 3.2a UV cross section of 1.0×10^{-4} mol dm^{-3} I_2 in ethanol using a 10mm cell path length.
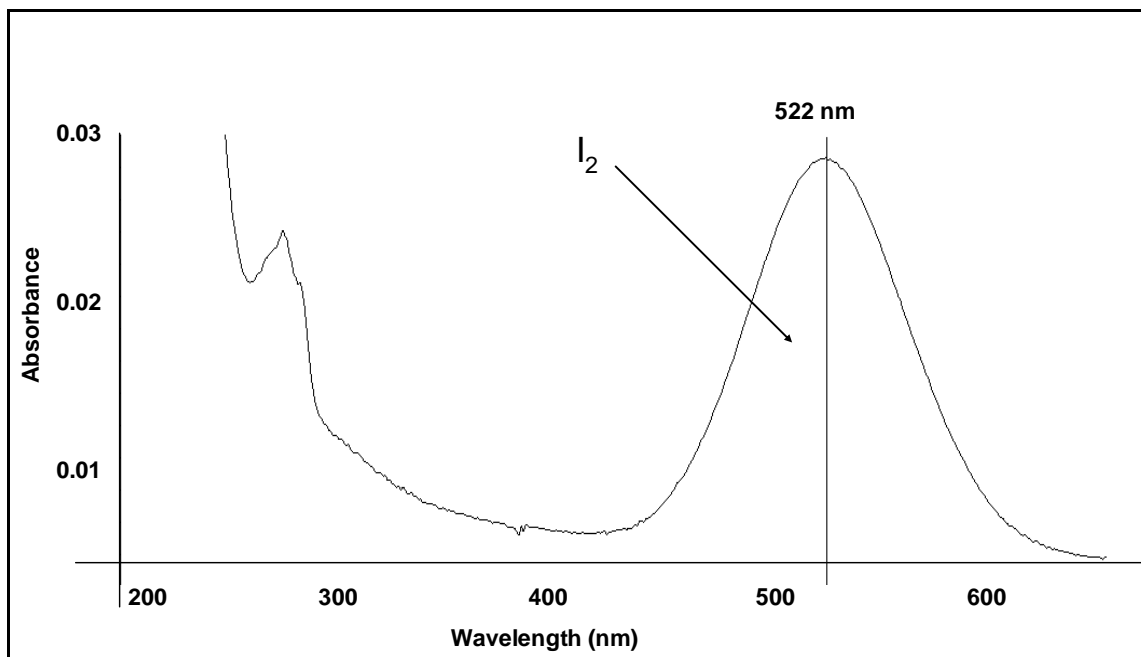
Figure 3.2b UV cross section of 2.8 x 10^{-6} mol dm^{-3} I_2 in hexane using a 100 mm cell path length.
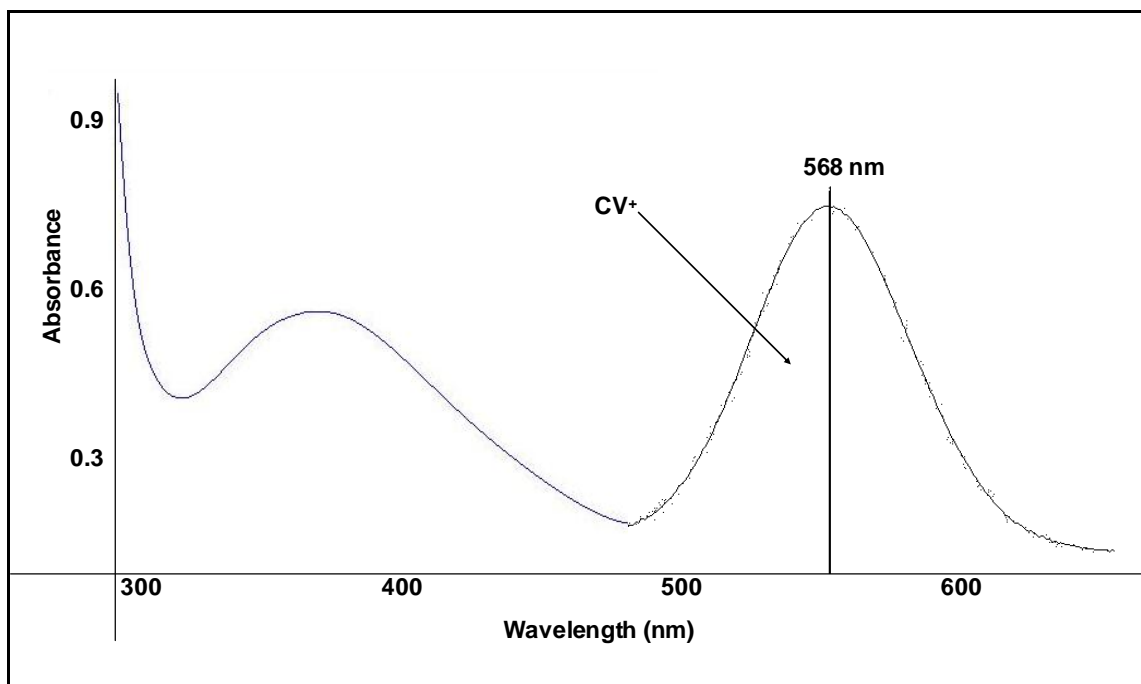
Figure 3.2c UV cross section of CV^+ colorimetric agent generated in 2.8 x 10^{-6} mol dm^{-3} I_2 in hexane using a 100 mm cell path length.
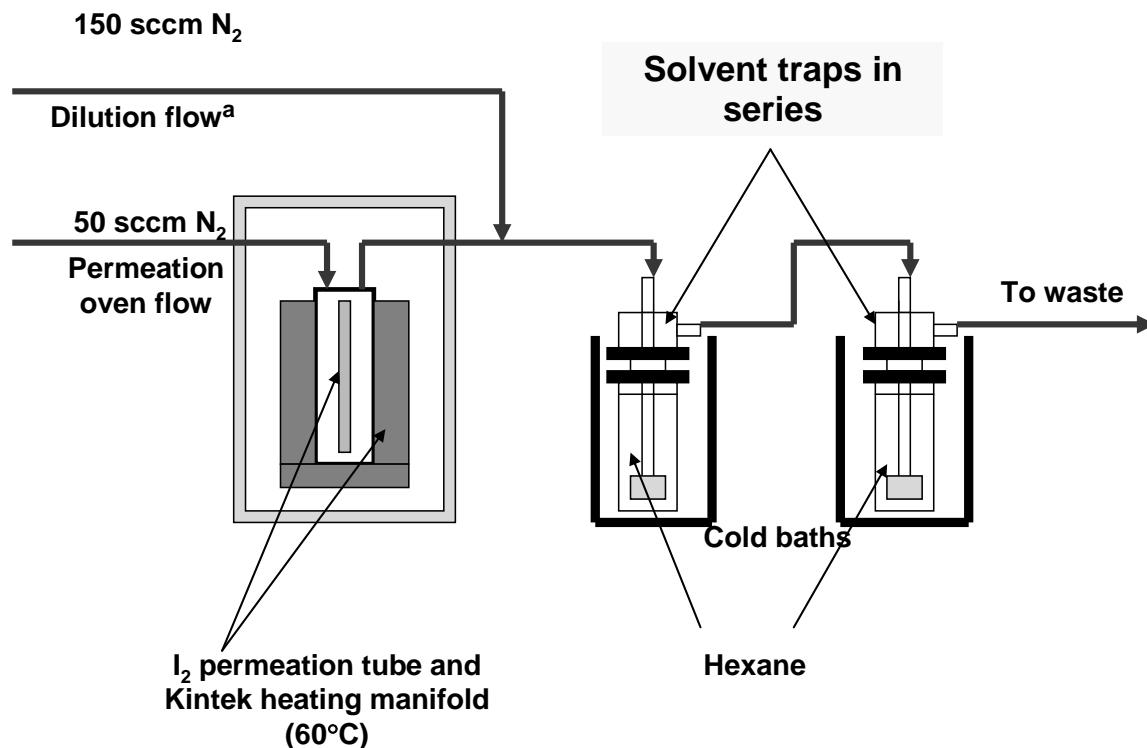
Figure 3.3 Solvent trap optimization set up.
[a]Dilution flow only used in optimization of Trap C (≤-50°C).

Initial work was carried out using a prototype solvent trap (Trap A, -9°C), as described by Parthipan (2008), which consisted of a 100 mL round bottom flask containing 50 mL of hexane. The flask was fitted with ground glass fittings with an inlet tube reaching below the solvent surface and an outlet tube above the solvent surface. The I_2 source gas (243 ppbv) was bubbled through the solvent at a flow rate of 0.05 L min^{-1}. The trap was wrapped in aluminum foil to prevent the photolysis of I_2 and immersed in a cold bath consisting of sodium chloride and ice (-9°C) to both aid trapping efficiency and minimize hexane evaporation. The hexane volumes within the traps were measured gravimetrically using a 5 figure mass balance (KERN 770) before and after the trapping periods to calculate the volumetric loss to evaporation. The I_2 concentrations for each trapping period represent the mean of triplicate experiments.

The prototype solvent trap A (-9 °C) gave a mean recovery of 86 ± 13%, figure 3.4, over the trapping periods investigated and a minimum T.E. of 67 % after 5 hours (table 3.2). Measured I_2 concentrations were close to the expected concentrations calculated from the

permeation oven, but fell below the 1:1 line after 2 hours of trapping (overall $R^2 = 0.96$, figure 3.4). The hexane evaporation rate under the trapping conditions was 1.3 mL r hr^{-1}, figure 3.8. The T.E. of the solvent trap was observed to drop from 105 % to 67 % between the trapping periods of 1 to 5 hours. This was most likely due to the loss of hexane during the trapping periods. Given the dimensions of the solvent trap, the loss of hexane over a 5 hour period (~13 %) significantly reduced the depth of the trapping solvent within the vessel hence its potential contact time with gaseous I$_2$, reducing trapping efficiency. The I$_2$ losses observed within this experiment were due to a combination of direct volatilization and decreased trapping efficiency, both of which increase for longer trapping periods.
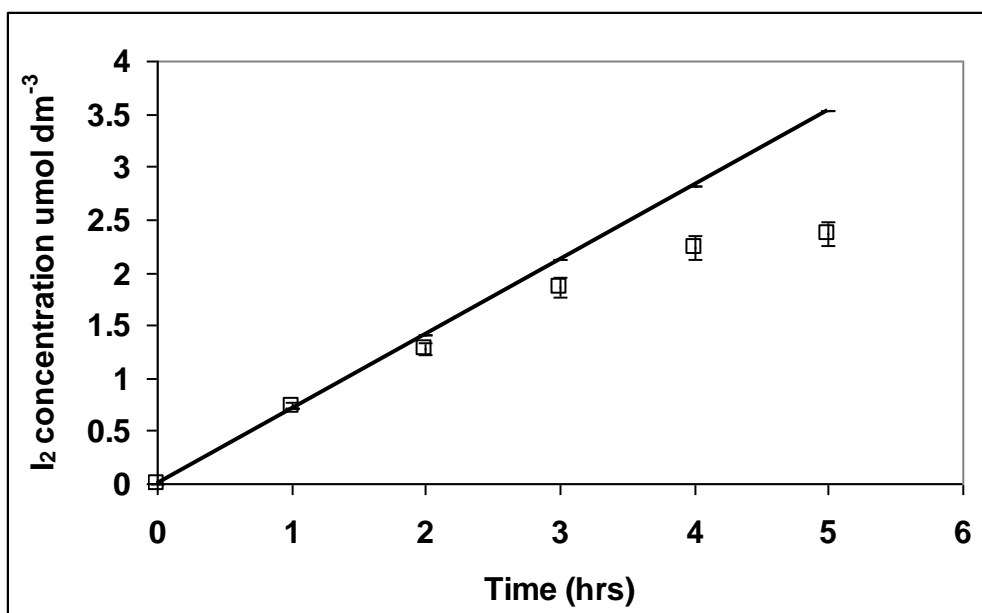
Figure 3.4 Observed and expected I$_2$ concentrations in hexane solvent trap A (-9°C). Error bars represent $\pm$ 1 standard deviation. Black line, expected concentrations; empty squares, measured concentrations.

The second prototype solvent trap, solvent trap B (-20 °C) was developed to minimize hexane evaporation during trapping and maximize T.E. In order to enhance the contact time between the gaseous I$_2$ analyte and the trapping solvent, the vessel used for trap A was replaced with a 50 mL round bottom flask and a glass frit (porosity 0, Cole Palmer) was added to the gas inlet tube. Solvent evaporation was minimized by using an ice/acetone cold bath (-20 °C) instead of the ice/sodium chloride mixture used for trap A. All other conditions were the same as those described for trap A.

The prototype solvent trap B (-20°C) gave a mean recovery of 84 ± 4%, figure 3.5, over the trapping periods investigated and a minimum T.E. of 86 % (table 3.2). A plot of measured I_2 concentrations against those expected produced an R^2 value of 0.99 (1:1 line, see Figure 3.5). The hexane evaporation rate under the trapping conditions was 1.0 mL hr^{-1}, figure 3.8. Solvent trap B has a much larger T.E than that measured for trap A and the reduction in cold bath temperature has also reduced the hexane evaporation rate by 0.2 mL hr^{-1}. However, complete T.E and analyte recovery could not be obtained using this trap.
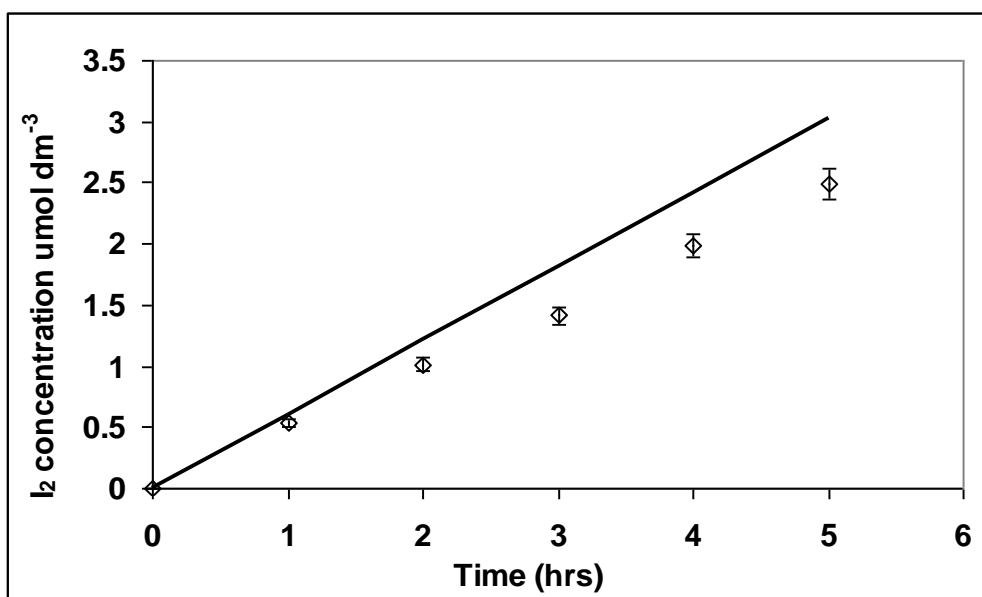
Figure 3.5 Observed and expected I_2 concentrations in hexane solvent trap B (-20°C). Error bars represent ± 1 standard deviation. Black line, expected concentrations; empty diamonds, measured concentrations.

The final prototype solvent trap, solvent trap C (≤ -50°C) was developed to further minimize solvent evaporation during trapping whilst maximizing T.E. The contact time between the gaseous I_2 analyte and the trapping solvent was further enhanced by replacing the round bottomed flask with a 25 mL capacity midget bubbler (Supelco) with a glass frit on the gas outlet tube. In order to reduce hexane evaporation to the absolute minimum during trapping, the temperature of the cold bath had to be reduced further using a CO_2/acetone (≤ -50 °C) mixture. The volume of hexane used as the trapping solvent was

decreased to 20 mL while the test gas flow rate was increased to increase the sensitivity of subsequent analysis.

Volumetric losses of hexane by evaporation within this new experimental set-up were investigated as a function of nitrogen flow rate for a trap time of 60 minutes, as shown in figure 3.6. At flow rates of up to 0.2 L min^{-1} hexane showed no appreciable loss other than that caused by uptake to the scintered glass frit (0.5 mL). Above this flow rate, evaporative losses of 0.17 mL per 0.1 L min^{-1} increase in flow rate were observed. Therefore an optimum sample gas flow rate of 0.2 L min^{-1} was selected when using trap C. On further investigation, evaporative losses at this flow rate were linear with respect to time with a hexane loss rate of 0.19 mL hr^{-1}, as shown in figure 3.8. This hexane loss rate was 5 - 6 times lower than previously observed for traps A and B which allowed for a longer duration of trapping when using trap C.

An I_2 permeation gas concentration of 24.3 ppbv was generated from the oven using a 0.15 L min^{-1} dilution flow and by reducing the temperature of the oven to 30°C. Using the optimized trapping conditions of trap C, the recovery of I_2 from the permeation oven source was 105 ± 6%, with no detectable I_2 concentration within the second trap (T.E. =100%). A plot of measured I_2 concentrations against those expected (1:1 line) produced an R^2 value of 0.99, figure 3.7. This data demonstrates that the trapping performance of solvent trap C is considerably higher than that of prototypes A and B. A comparison of the properties of the solvent traps developed in this investigation is shown in table 3.2

Figure 3.6. Volume of hexane lost over 60 min at a trapping temperature of -50°C, as a function of nitrogen flow rate. Error bars represent ± 1 standard deviation.
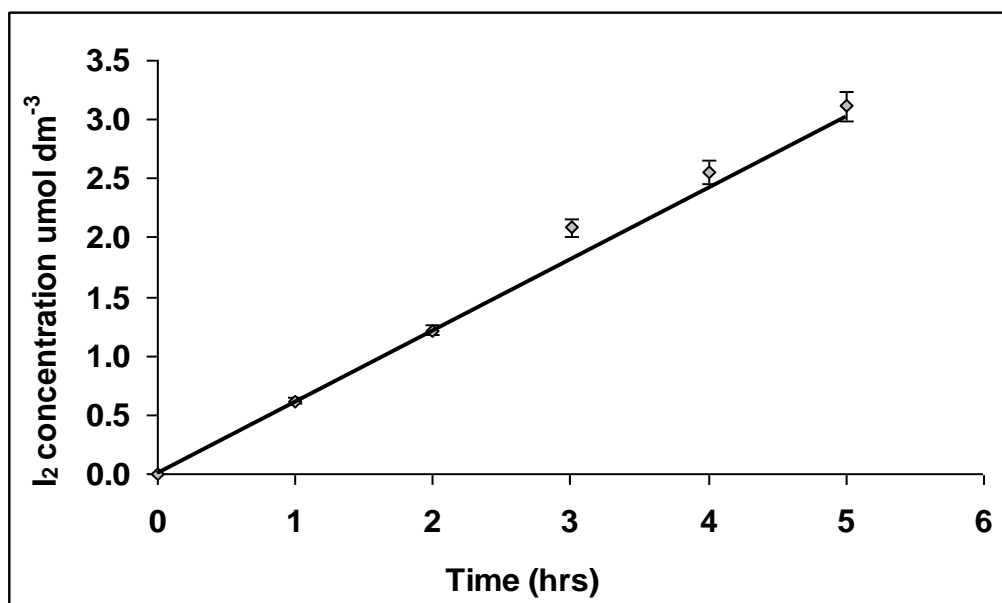
Figure 3.7 Observed and expected I_2 concentrations in hexane solvent trap C (≤-50°C). Error bars represent ± 1 standard deviation. Black line, expected concentrations; empty diamonds, measured concentrations.
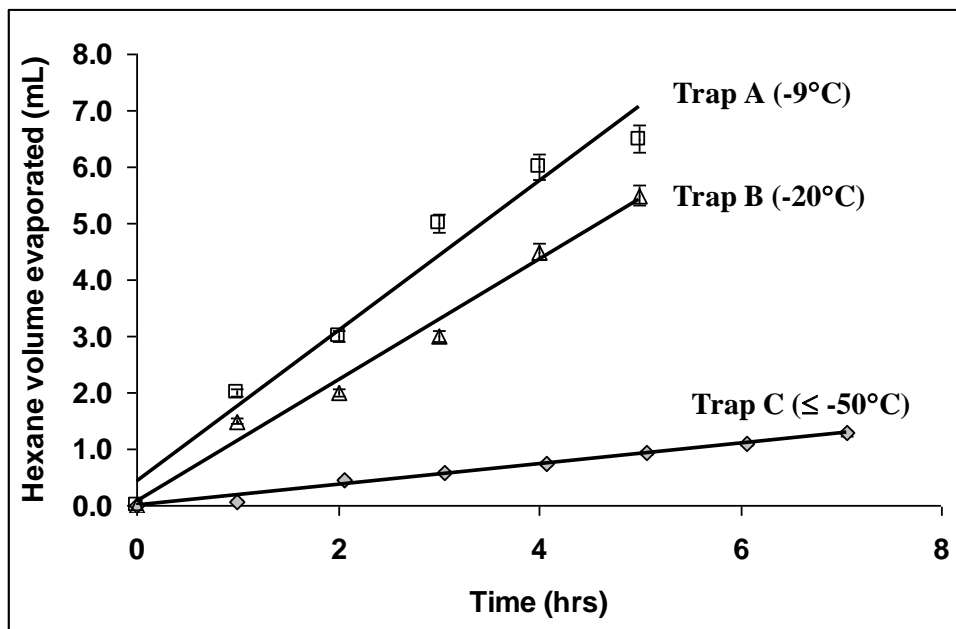
Figure 3.8 Hexane evaporation rates under the different trapping conditions.
Error bars represent ± 1 standard deviation.

Combining the improved spectrophotometric LoD with the enhanced trapping efficiency of trap C (≤ -50°C), meant that longer trapping times and higher sample gas flow rates were attainable yielding a considerably improved atmospheric limit of detection for I_2. The utility of a solvent trap depends on the rate of solvent evaporation- the lower the evaporation rate, the longer the trap may sample for and thus the lower the LoD attainable. Chance *et al*. (2010) demonstrated that the ratio of I_2 loss to solvent loss was dependent upon trapping conditions but was in the order of 0.47 ± 0.03 (n=3). Therefore, 10% hexane loss equates to approximately 5% I_2 loss, a level considered sufficiently low as not to be corrected in this work. For a hexane volume of 20 mL, under the optimized conditions of trap C (≤-50°C) it would take 10 hrs and 45 mins for 10% of the trapping solvent to be lost. The LoD for these conditions is equivalent to an atmospheric mixing ratio of 69 pptv and the LoQ is 230 pptv.

The LoD is comparable to peak concentrations of I_2 in coastal air observed at low tide (93 pptv; Saiz Lopez *et al.*, 2006), suggesting the traps may be suitable for use in laboratory investigations (for e.g., seaweed chamber studies) at concentrations close to those observed in the atmosphere. The trap is believed to be selective for I_2 over VOIC, HOI and I_3^-, which

all have absorption maxima at shorter wavelengths (Wall *et al*., 2003; Palmer and Lietzke, 1982; Paquette, 1985). There may be some overlap in absorption spectra between I$_2$ and the dihalogens IBr and ICl, which absorb 492 and 465 nm respectively in carbon tetrachloride (CCl$_4$; Augdahl and Klaeboe, 1965). However, the absorption cross sections of ICl and IBr are red shifted and weaker than that of I$_2$, so that their concentrations would have to be similar to or in excess of I$_2$ to comprise a significant interference. Care would need to be exercised in experiments where relatively high concentrations of these interhalogens are expected to be present.

Trap[a]	Temperature (°C)	T.E[b] (%)	Recovery[c] (%)	Evaporation rate (mL hr^{-1})	10% evaporation time (hr)	LoD for gaseous I$_2$ (pptv)
A	-9	67	86	1.3	3.9	2033.7
B	-20	86	84	1.0	4.7	1595.8
C	≤ -50	100	105	0.2	10.8	69.1

Table 3.2 Comparison of trap properties

[a]10cm cell
[b] Calculated taking LoD (spec) as minimum concentration
[c] Average from 1 to 5 hours

3.2.5 Iodine losses due to interactions with ozone in hexane

Razumovski and Zaikov (1971) previously investigated the temperature dependent solubility of gaseous ozone in non aqueous media including hexane. Their experiments were conducted by passing a stream of gaseous ozone (60 − 0.3 parts per thousand) at a flow rate of 0.22 L min^{-1} through hexane (30 − 150 mL) in a thermostatically controlled bubbler solvent trap. Ozone concentrations in hexane were then determined spectrophotometrically at 254 -310 nm. Although the recovery or T.E. of ozone in hexane was not established during this study, the authors suggested appreciable amounts of gaseous ozone were trapped by the solvent. This observation is supported by experiments within this chapter in which gaseous ozone concentrations of 140 ppbv were reduced to 20 ppbv for 30 minutes once bubbled through hexane (20 mL) at a flow rate of 0.2 L min^{-1} (Appendix 3.4). The presence of ozone within hexane has important implications for the *in-situ* lifetime of I$_2$.

Vikis and MacFarlane (1985) previously described experiments in which gaseous I_2 was shown to react with gaseous ozone forming a solid iodine oxide (I_4O_9) in the absence of light. The reaction was suggested to proceed via a cyclic transition state producing the iodine species I, IO, IO_2 through two reaction channels, EQ 3.22. The final product (I_4O_9) could then be produced from the successive oxidation of these primary products, EQ 3.23. Previously Vikis and MacFarlane (1985) established that the rate law of this reaction was first order with respect to $[I_2]$, as shown in EQ 3.24 where k is the temperature dependent reaction rate constant.

(EQ 3.22)

$I + O_3 \rightarrow IO + O_2$ (EQ 3.23)

$IO + O_3 \rightarrow IO_2 + O_2$
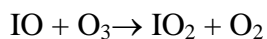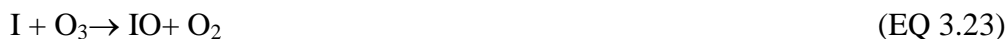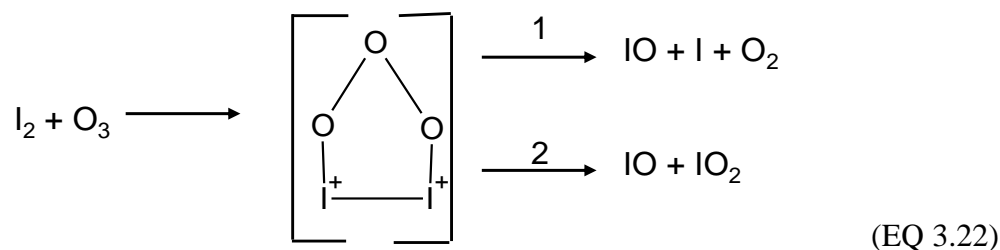
$-d[I_2]/dt = k[I_2][O_3]$ (EQ 3.24)

A series of experiments were conducted to investigate I_2 losses in hexane from its reaction with ozone under dark conditions, EQ 3.22. Ozonised gas and gaseous I_2 were directly introduced into the experimental set up (figure 3.12) at a combined flow rate of 0.2 L min^{-1} under dark conditions and subsequently trapped using solvent trap C ($\leq$ -50 °C). Experiments were repeated with and without gaseous ozone. Molecular iodine losses with respect to ozone concentration, I_2 concentrations and trapping time were investigated.

Figure 3.9 shows the amount of I_2 trapped from an I_2 gas concentration of 40 ppbv during a 90 minute trap time at several ozone concentrations. The *y* error bars represent the combined standard deviation of triplicate measurements and the calculated error of the I_2

permeation rate (3.86 %). The x error bars represent the manufacturer quoted error of the mass flow controllers (2.5%, MKS). The amount of I_2 in hexane decreased exponentially with increasing ozone concentrations within the range 0 to 400 ppbv. The amount of I_2 trapped from the gas stream in an ozone concentration of 400 ppbv was ~33% of that in the absence of ozone, clearly indicating its importance on the lifetime of I_2 within the system.

Figure 3.10 shows the trapped amounts of I_2, from a gas concentration of 40 ppbv, in the absence and presence (70 ppbv) of ozone during different trapping periods. The y error bars represent the standard deviation of triplicate measurements and the established error of the I_2 permeation rate (3.86%). The observed losses of I_2 due to the presence of ozone proceeded at a rate constant of 0.06 nmol min^{-1} with losses ranging from 7 – 29% between 30 – 150 minutes.

Figure 3.11 shows the amounts of I_2 trapped from various I_2 concentrations during a 90 minute trap time at 70 ppbv of ozone. The y error bars represent the standard deviation of triplicate measurements and the established error of the I_2 permeation rate (3.86 %). The x error bars represent the quoted error of the mass flow controllers (2.5%, MKS). The loss rate of I_2 during these conditions was 0.22 nmol ppbv^{-1} of I_2, resulting in an I_2 loss of 32 % at 40 ppbv of I_2 and 70 ppbv O_3.

Using previous literature values of the rate constant for the dark I_2/O_3 reaction at 25 °C ($2.25 \pm 0.19 \times 10^3$ mol^{-1} dm^{-3} s^{-1}; Vikis and MacFarlane, 1985), I_2 loss rates can be determined using EQ 3.24. Taking into account a 10 minute gas residence time in the system under the conditions investigated, an I_2 loss rate of 1.45 pmol min^{-1} is calculated at ozone and I_2 mixing ratios of 70 ppbv and 40 ppbv, respectively. This loss rate for I_2 is 2.4% of the observed value obtained under the same conditions from figure 3.10 (60 pmol min^{-1}). Therefore, it is likely that the majority of the I_2 loss occurs from the I_2/O_3 interaction within hexane during their subsequent enhancements in concentrations. The corrections used for I_2 losses incurred during trapping as a function of O_3 concentration, time and gaseous I_2 concentration are the inverse of the regression equation in figure 3.9 (and those shown in the Appendix 3.5 and 3.6 respectively).
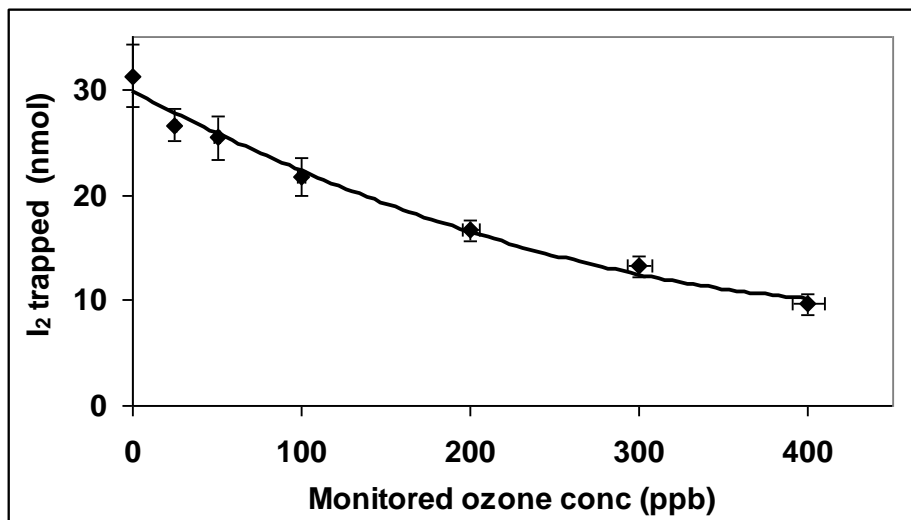
Figure 3.9. Iodine lost within hexane at increasing ozone concentrations.
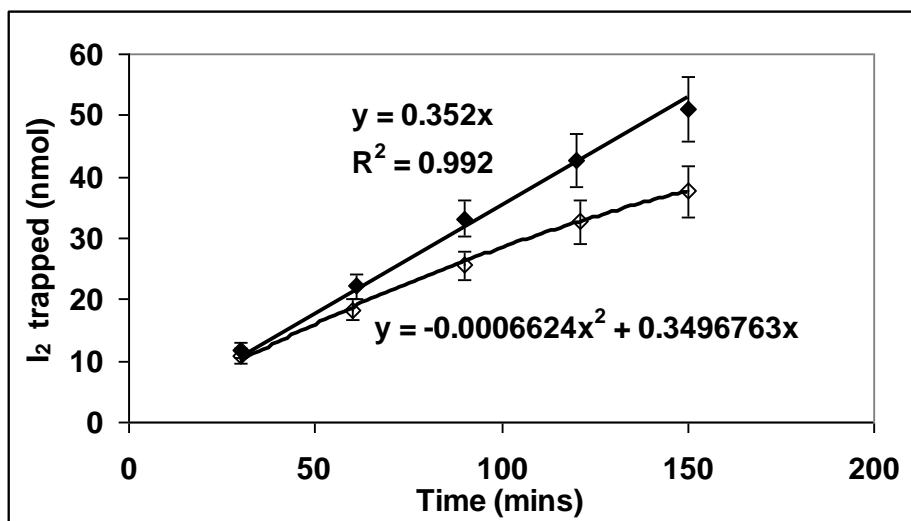
Figure 3.10 Iodine lost within hexane over time from reaction with ozone. Filled diamonds, observed amount in the absence of ozone; empty diamonds, observed amount at 70 ppbv ozone.
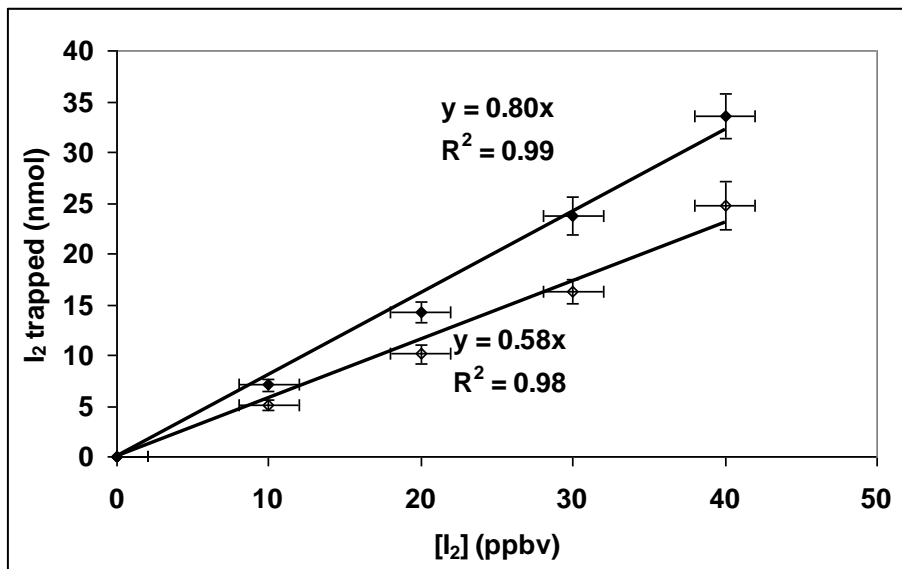
Figure 3.11. Iodine lost within hexane at increasing permeation oven flow rates. Filled diamonds, observed amount in the absence of ozone; empty diamonds, observed amount at 70 ppbv of ozone.

3.3 Experiments of iodide oxidation using ozone

3.3.1 Experimental set-up
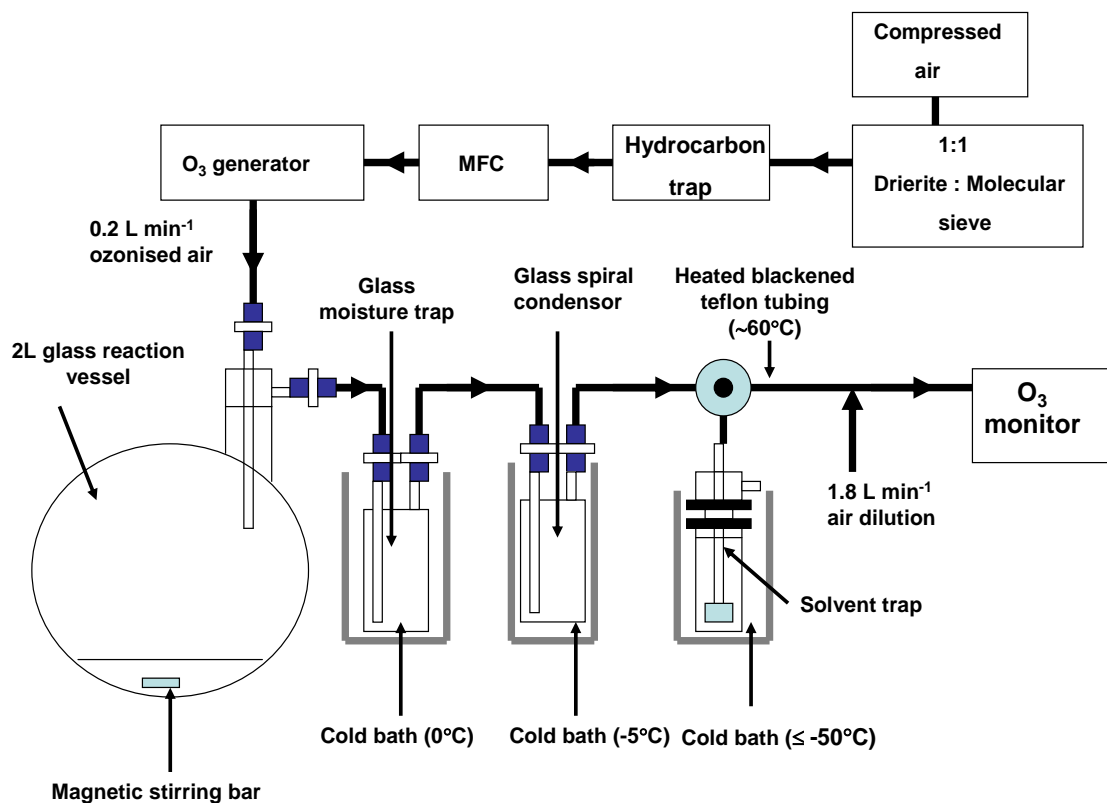
Figure 3.12. Experimental set up used to investigate ozone uptake by iodide solutions/seawater and quantify molecular iodine emission.

3. Evidence for the abiotic production and direct emission of I₂ from surface seawater in the presence of O₃

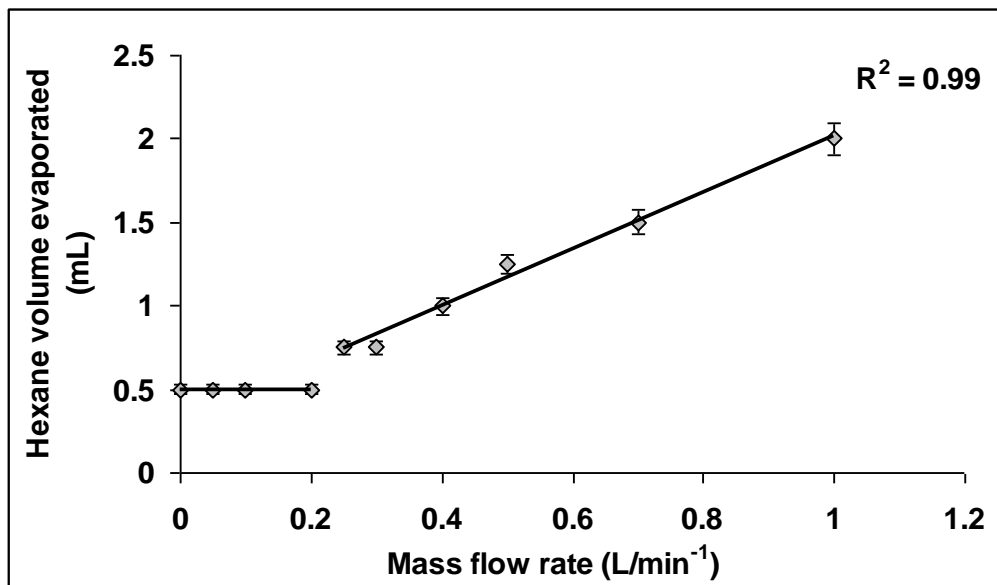

3. Evidence for the abiotic production and direct emission of I_2 from surface seawater in the presence of O_3

Figure 3.12 shows the experimental set up used for the experimental study of molecular iodine production from iodide solutions buffered at pH 8 (prepared within HPLC water), and seawater collected from the coastal waters of Cargese, Corsica (geographical coordinates: 42.136º N 8.596º E). The experimental set up was designed to supply dry ozone to the reaction vessel (2 L round bottom flask, Cole Palmer) over iodide phosphate buffer solution (PBS) solutions and seawater ($\sim 10^{-6}$ - 10^{-5} mol dm^{-3}). Molecular iodine evolved from the reaction of ozone with iodide was trapped using solvent trap C ($\leq$ -50°C), section 3.2.4, and quantified using the optimized spectrophotometric method described herein, section 3.2.2.

While the colder temperature of trap C ($\leq$ - 50 °C) used in this investigation offered improved performance in terms of solvent evaporation and T.E., it also caused any moisture in the sample gas stream to condense and subsequently freeze on the sintered frit of the inlet, blocking the system. Great care had to be taken to ensure the sample stream was completely dry. The use of a Nafion box drier upstream of the solvent traps led to $\sim 60\%$ I_2 loss, whilst chemical drying agents such as K_2CO_3, drierite and molecular sieve gave 50% to 80% I_2 loss. The most suitable means of removing moisture from the gas stream identified was two spiral condensers in series held at 0 and -10°C ($20 - 60 \pm 2.2\%$ total gaseous I_2 loss to condensers and experimental system, section 3.5.1); these were used during this series of experiments, figure 3.12.

The air flow rate and O_3 concentrations through the experimental set up were metered and monitored respectively by a mass flow controller (MKS technologies) and ozone monitor (Model 49i ozone analyzer, Thermo Scientific). Ozone was produced from dry hydrocarbon-free air by its exposure to a commercial ozone generator (185 nm excitation, UVP). Prior to each run, the experimental set up was equilibrated with ozone at a flow rate of 0.2 L min^{-1} until a constant concentration of ~ 70 ppb $\pm 2.5\%$ was observed. The buffered iodide solution/seawater sample (20 mL) was then administered into the reaction vessel using a gas tight syringe (Samco) *via* a Luer lock tap. Initial iodide concentrations of the order of 10^{-6} - 10^{-5} mol dm^{-3}(i.e., a factor of 10 - 100 higher than in surface seawater) were used so that the minimum LoD of the optimized spectrophotometer was met. The seawater

matrix (20 mL) was spiked with an aqueous iodide solution (0.2 mL, 1 x 10^{-3} mol dm^{-3}) and thoroughly mixed prior to its addition to the reaction vessel.

Following each experimental run of 1 to 5 hours, both the reaction chamber and the solvent trap were removed and analysed for I^-, I_3^- and I_2 using a UV/Vis spectrophotometer (section 3.2.2). Triodide in aqueous solution was not present at detectable concentrations for any of the experiments. Calibrations used for the quantification of iodine and iodide are given in sections 2.31 and 2.32.

3.3.2 Ozone deposition control experiments

Figure 3.13 shows results of control tests conducted on the experimental system at an ozone concentration of 100 ppbv. The control experiments were conducted to establish whether ozone was deposited to the experimental system in the absence of solution, to HPLC water (20 mL) or to the phosphate buffer solution (pH 8, 20 mL) in the absence of iodide. The peaks in ozone concentration at ~ 300 seconds are caused by an increase in internal pressure within the system as solutions were injected into the reaction chamber.

The uptake of ozone to the system in the absence of any solution was small and very similar to that observed in the presence of HPLC water, 5.1 x 10^{-3} ppbv s^{-1} and 5.5 x 10^{-3} ppbv s^{-1} respectively (~7% over 30 minutes). These losses can be attributed to ozone deposition to the walls of the experimental system. This was despite every effort being made to minimize ozone deposition within the system, including heating all gas lines (~60 °C) downstream of the reaction chamber using heating tape, figure 3.12. The final ozone deposition control test was conducted on phosphate buffer (0.1 mol dm^{-3}) solutions used for the iodide suspensions used within the experiments. Observed ozone loss to the PBS buffer was minimal (~8.5 %) during the 30 minute experiment time and followed a first order loss rate. This error was taken into account when calculating the margins of error of ozone uptake by iodide solutions at pH 8 within this study.
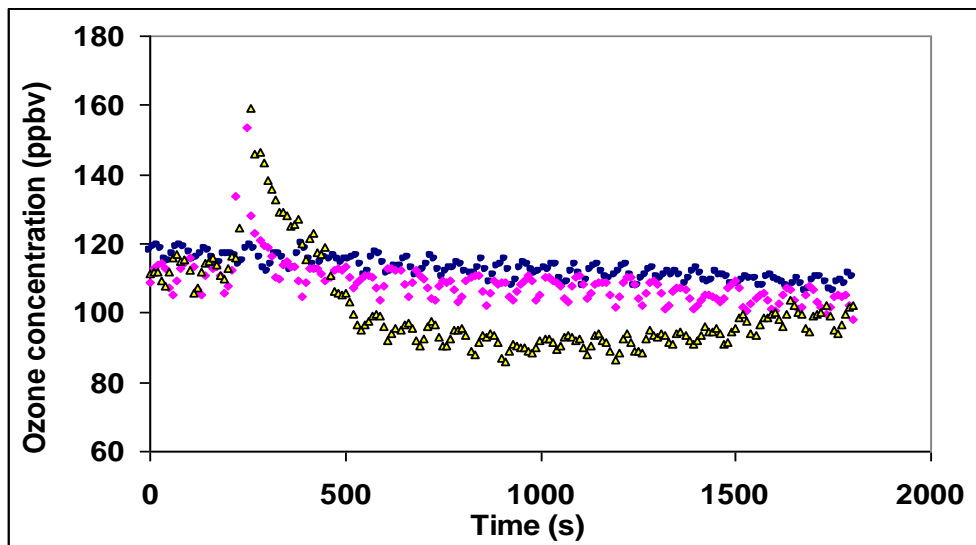
Figure 3.13 Control experiments of ozone loss during exposure to the experimental System (blue squares), HPLC water (pink diamonds) and pH 8 phosphate buffer (yellow triangles).

3.3.3 Iodine emission control experiments

Iodine blank tests using HPLC water and phosphate buffer (pH 8) from the experimental system in the presence of ozone (0.2L min^{-1}, 100 ppbv) were established prior to the iodide/seawater experiments. Iodine blanks were also conducted between each of the iodide/seawater experiments to establish any carry over between experiments. Iodine was not observed above the spectrophotometric LoD (20.3 nmol dm^{-3}), under the experimental conditions highlighted in section 3.2.1, for any of these control experiments. This would suggest that the iodine carry-over between experiments was negligible and that any subsequent I_2 emissions from the system are a direct result of the interaction of ozone with iodide.

3.4 Enhanced ozone uptake by seawater and iodide solutions

Enhanced ozone uptake was observed on the introduction of both buffered iodide solutions in phosphate buffer solution (PBS) and seawater during each experiment. Exponential curves fit the observed data with R^2 values of 0.99 and ~0.95 for experiments involving the buffered iodide solutions (pH 8) and seawater respectively, figures 3.14 and 3.15. The *y* error bars in figures 3.14 and 3.15 represent the observed error of the ozone monitor ($\pm$ 2.5 ppbv) used during the investigation. In the iodide solutions (pH 8), the O_3 concentrations

dropped to 30 and 25 ppbv, from an initial concentration of 70 ppbv, over 10 minutes for iodide concentrations of 5 x 10^{-6} and 1 x 10^{-5} mol dm^{-3} respectively, figure 3.14a. Similarly, O_3 concentrations were observed to drop to 60 and 25 ppbv over 10 minutes for natural seawater and 1 x 10^{-5} mol dm^{-3} spiked iodide in seawater respectively, figure 3.15a and 3.15b. These observations demonstrate the rapid rate of reaction between O_3 and iodide in the laminar layer of the liquids (reactions 3.4 to 3.6). The O_3 uptake is pseudo first order with respect to ozone concentrations at the experimental conditions. The reaction kinetics of ozone uptake by iodide is postulated as second order under natural conditions (Garland *et al.*, 1980). As the iodide concentrations used during these laboratory experiments were a factor of ~1.7 - 3.4 x 10^3 times larger than the ozone concentrations, pseudo first order kinetics were employed as given in EQ 3.25, where k_{obs} is the observed ozone uptake rate constant and t is time.

$$-ln\ [O_3] = k_{obs}\ t - \ln[O_3]_0 \qquad\qquad\qquad\qquad (EQ\ 3.25)$$

The average measured pseudo first order rate constants for ozone loss over buffered solutions (pH 8) were 1.7 x 10^{-3} s^{-1} and 2.2 x 10^{-3} s^{-1} for iodide concentrations of 5 x 10^{-6} and 1 x 10^{-5} mol dm^{-3} respectively. Similarly the average measured pseudo first order rate constants of seawater were 5.9 x 10^{-4} s^{-1} and 2.0 x 10^{-3} s^{-1} for natural seawater and seawater spiked at an iodide concentration of 1 x 10^{-5} mol dm^{-3}, respectively.

a)
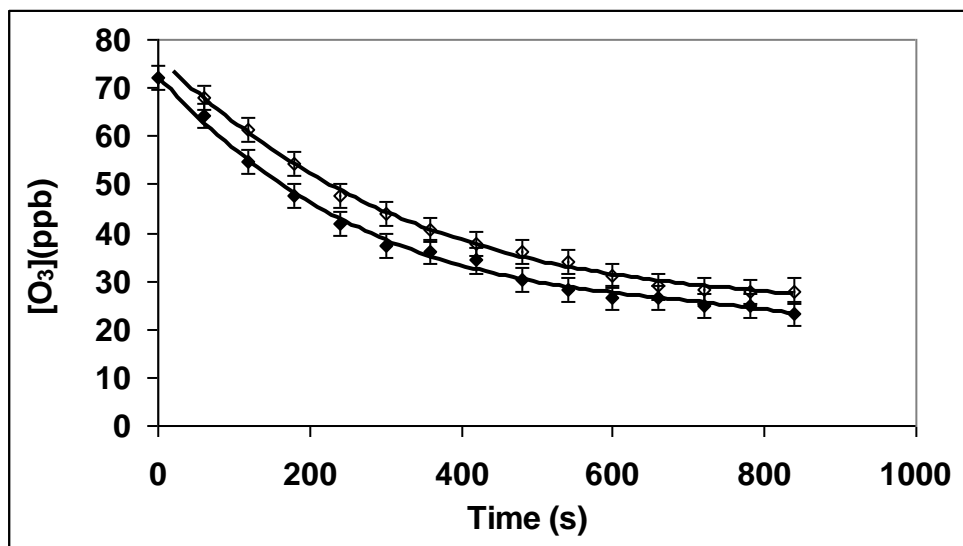
b)
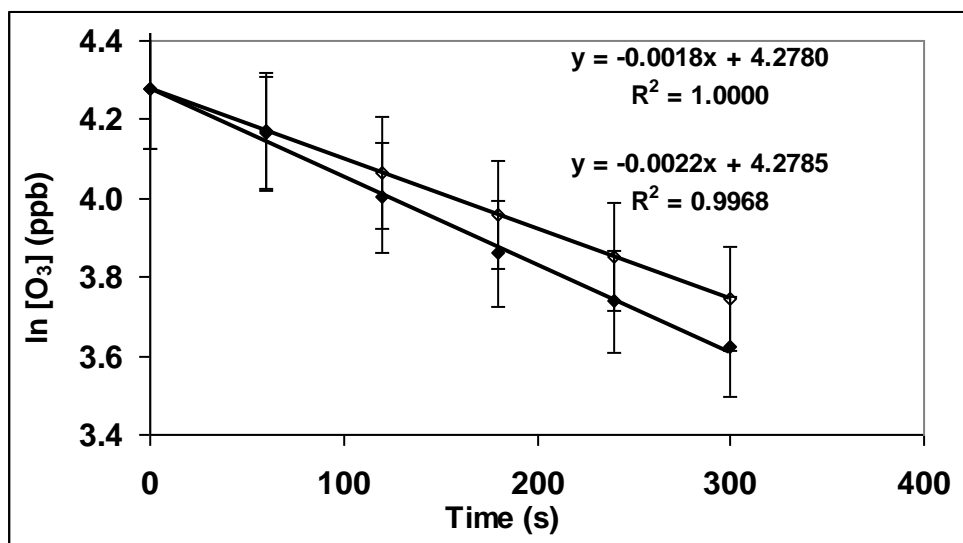
Figure 3.14. a) Exponential uptake of ozone by iodide solutions (pH 8). **b)** Pseudo first order ozone uptake corresponding to 3.14a. Empty diamonds, 5 x 10^{-6} mol dm^{-3}; filled diamonds, 1 x 10^{-5} mol dm^{-3}.

a)

b)

Figure 3.15. a) Exponential uptake of ozone by seawater. **b)** Pseudo first order ozone uptake corresponding to 3.15a. Empty diamonds, natural seawater; filled diamonds, 1×10^{-5} mol dm^{-3} spiked seawater.

Several investigations over recent decades have shown that dry ozone deposition to surface seawater is its principal removal pathway operating within the MBL (Muller, 1992; Kramm, *et al*., 1995). The observed deposition velocities reported in the literature vary significantly with values ranging from 0.01 to 0.12 cm s^{-1} (Gallagher *et al.*, 2001; Lenschow *et al.*, 1982; Galbally and Roy, 1980; Oh *et al*., 2008). This wide range of deposition velocities is controlled by the uptake efficiency of seawater which is limited by both dynamic physical and chemical processes (Lenschow*et al.*, 1982; Nightingale *et al.*, 2000).

The ozone uptake potential of seawater can be considered as a mechanism involving two layers, an overlying air and surface water layer. The overlying air layer offers an aerodynamic resistance (r_a) to ozone deposition from the air to seawater and the surface water layer provides an aqueous phase resistance (r_s). The total resistance (r_t) is the sum of the resistance in these layers, as shown in EQ 3.26, which is related to the deposition velocity (v_d) by EQ 3.27 (Chang *et al.*, 2004; Gallagher *et al*., 2001).

$$r_t = r_a + r_s \qquad \qquad \text{(EQ 3.26)}$$

$$v_d = (r_a + r_s)^{-1} \qquad \qquad \text{(EQ 3.27)}$$

The dependence of physical processes such as wind speed and sea surface roughness (Galbally and Roy, 1980; Gallagher *et al*., 2001) on deposition velocities has previously been investigated. Being relatively insoluble, atmospheric ozone deposition is determined (~95%) by r_s which itself is controlled by physical factors such as wind speed and sea surface roughness as well as chemical reactions in the laminar layer (Lenschow, 1982). Equation 3.28 represents the relationship between these resistances and the flux (F) of ozone from air to sea, where C_w, H and C_g are the aqueous phase concentration of ozone, the Henry's law constant and the gas phase concentration of ozone respectively. Within all the work described in the chapter $C_g \gg H C_w$, therefore EQ 3.28 can be simplified to EQ 3.29. Finally v_d can be incorporated into EQ 3.29 by substituting for the inverse of total

resistance, as shown in EQ 3.30, so that the flux of ozone can be estimated. The v_d values of iodide in PBS and seawater are shown in table 3.3.

$$F = (C_g - (H \ C_w)) / (r_a + r_s)^{-1} \tag{EQ 3.28}$$

$$F = C_g / (r_a + r_s)^{-1} \tag{EQ 3.29}$$

$$F = C_g \bullet v_d \tag{EQ 3.30}$$

The term r_a is determined by mixing in the atmosphere and will be similar in value to the corresponding resistance to the transfer of heat and other trace gases (Garland *et al.*, 1980). The r_a within this work does not represent that within the atmosphere, and as such the results obtained cannot be directly translated to environmental conditions. However, r_a in this study can be determined from the v_d using experimental conditions at which the r_s is zero. Galbally and Roy (1980) previously determined r_a using very high iodide concentrations (0.02 mol dm^{-3}) at which r_s would have been negligible.

The r_a for the reaction vessel used within this study, figure 3.12, was determined from the measured v_d for a 0.02 mol dm^{-3} aqueous solution of iodide. This was established under the same experimental conditions used in the study (an ozone concentration of 70 ppbv at a flow rate of 0.2 L min^{-1}). Equations 3.31 (Galbally and Roy, 1980) and 3.32 were used to estimate r_a. The 5/6th is an empirically determined factor in equation 3.31 where $t_{1/2(surface)}$ is the half life of ozone within the reaction vessel, $t_{1/2(measured)}$ is the measured half life of ozone during the exposure to the 0.02 mol dm^{-3} solution, and $t_{1/2(control)}$ is the observed half life in an empty vessel. The mean $t_{1/2 \ (surface)}^{-1}$ for the reaction chamber studied under conditions of zero r_s was found as 1.4×10^{-1} s^{-1} (the result of triplicate measurements of $t_{1/2(measured)}$ and $t_{1/2(control)}$).

$$t_{1/2 \ (surface)}^{-1} = t_{1/2(measured)}^{-1} - 5/6 \ t_{1/2(control)}^{-1} \tag{EQ 3.31}$$

$$v_d = (V/A) \times t_{1/2 \ (surface)}^{-1} \tag{EQ 3.32}$$

3. Evidence for the abiotic production and direct emission of I_2 from surface seawater in the presence of O_3

The v_d of ozone at an iodide concentration of 0.02 mol dm^{-3} was calculated using EQ 3.32, where V is the headspace volume of the reaction chamber (2.0×10^{-3} m^3) and A is the surface area of the liquid surface (4.9×10^{-3} m^2). The calculated v_d was 5.7×10^{-2} m s^{-1}, hence using EQ 3.27 (assuming r_s is zero for the experiment) the r_a value inferred from this value was 17.7 m^{-1}s. This r_a value is considerably lower than previously calculated for experimental systems used by Parthipan (2008), 2675 m^{-1} s, and Garland *et al.* (1980), 108 m^{-1} s. These values reflect the differences in gaseous ozone flow rates and reaction vessels employed during these studies. The calculated r_a is specific to the experimental set up used in this chapter and can be used to calculate the r_s of the solutions investigated using EQ 3.27, as shown in table 3.3 and 3.4.

Theoretical r_s values can be determined for different concentrations of iodide solutions using EQ 3.33 (Garland et al, 1980) by considering the molecular ozone diffusion transfer into a liquid film, where H is the Henry's law constant ($\sim$3.0 at 20 °C), D is the molecular diffusivity of ozone in water (1.2×10^{-9} m^2 s^{-1} at 20 °C), and λ is the integrated chemical loss rate, given by EQ 3.34. In EQ 3.34, C_i is the concentration of iodide and k_i represents the second order kinetic rate constant for the aqueous $O_3 + I^-$ reaction at pH 8 (2×10^9 dm^3 mol^{-1} s^{-1}, Garland *et al.*, 1980; 1.2×10^9 mol^{-1} s^{-1}, Liu *et al.*, 2001). Calculated theoretical r_s values using the k_i values from Garland *et al.* (1980) and Lui *et al.* (2001) for different iodide concentrations are tabulated against previously observed values and the values derived in this study, table 3.3. Figure 3.16 compares the calculated theoretical r_s values in table 3.3 against the observed r_s values of seawater and iodide solutions in this study.

$$r_s = H / (\lambda \times D)^{1/2} \qquad \text{(EQ 3.33)}$$

$$\lambda = k_i C_i \qquad \text{(EQ 3.34)}$$

The r_s values of the iodide PBS solutions (5 and 10 µmol dm^{-3} iodide in PBS) observed in this study are between 90 − 118% of the calculated theoretical values (figure 3.16). Enhanced values could be the product of iodide depletion in the thin aqueous layer, associated with these experiments. A previous laboratory study (Parthipan, 2008) of

gaseous ozone interaction with iodide in PBS solutions, produced r_s values which were ~1.5 times larger than the calculated theoretical values. The difference between the observed and theoretical r_s values in this chapter is appreciably smaller as the aqueous iodide solutions were continuously stirred allowing faster iodide replenishment in the surface laminar layer.

The observed r_s value of the 5 µmol dm^{-3} iodide in seawater in this study was 102 -133% of the theoretical values, similar to that observed for the iodide in PBS solutions. However, the observed r_s values for seawater in the absence of spiked iodide was considerably lower than expected, between 56 – 72% of the calculated theoretical value (figure 3.16). This is in good agreement with previous r_s observations (Aldaz, 1969; Lenschow *et al.,*1982; Regener, 1974), figure 3.16 and is likely to be due to O$_3$ reactions with dissolved organic carbon (DOC) in seawater (as discussed in section 3.6).

Solution	O$_3$ deposition velocity, v_d (cm s^{-1})	O$_3$ flux (nmol m^{-2} s^{-1})	Liquid phase resistance to O$_3$, r_s(m^{-1} s)
Seawater	0.032	0.92	3065
	0.031	0.91	3179
	0.031	0.91	3179
average	**0.031 ± 2.1%**	**0.91 ± 2.1%**	**3141 ± 2.1%**
15 µmol dm^{-3} I$^-$ in seawater	0.148	4.28	656
	0.109	3.12	898
	0.111	3.17	879
average	**0.123 ± 19.0%**	**3.52± 19.0%**	**811 ± 19.0%**
5 µmol dm^{-3} I$^-$ in PBS	0.103	2.96	955
	0.110	3.16	889
	0.097	2.78	1124
average	**0.103 ± 6.2%**	**2.97± 19.0%**	**994 ± 6.2%**
10 µmol dm^{-3} I$^-$ in PBS	0.115	3.30	855
	0.129	3.70	753
	0.151	4.33	645
average	**0.132 ± 13.8%**	**3.78 ± 13.8%**	**747 ± 13.8%**

Table 3.3 Measured v_d and r_s values of ozone to buffered iodide solutions and seawater.

Iodide solution (mol dm^{-3})	Observed r_s (m s^{-1})	Theoretical r_s (m s^{-1})
1.7×10^{-1}	6[a]	5 - 6
3.4×10^{-2}	6[a]	11 - 14
1.0×10^{-3}	-	61 -79
3.3×10^{-4}	164[b]	107 - 138
1.0×10^{-4}	-	194 - 250
1.0×10^{-5}	747[c]	612 - 791
Seawater 1.0×10^{-5}	811[c]	612 - 791
6.7×10^{-6}	730[a]	748 - 966
5.0×10^{-6}	994[c]	866 - 1118
6.7×10^{-7}	2400[a]	2800 - 3055
2.0×10^{-7}	1100 - 4400[d]	4330 - 5590
Seawater ~ 2.0×10^{-7}	3141[c]	4330 - 5590
	2400 – 3400[e]	
	1690 - 1890[f]	
	650 – 1250[g]	
	1000[h]	
Freshwater	9000[i]	-

Table 3.4 Comparison of r_s values amongst buffered iodide solutions and seawater.
[a] Garland *et al*. (1980).
[b] Rajendran (2008).
[c] Work in this chapter.
[d] Galbally and Roy (1980).
[e] Aldaz (1969)
[f] Lenschow *et al*. (1982)
[g] Regener (1974)
[h] Gallagher *et al.* (2001)
[i] Wesley *et al*. (1981)
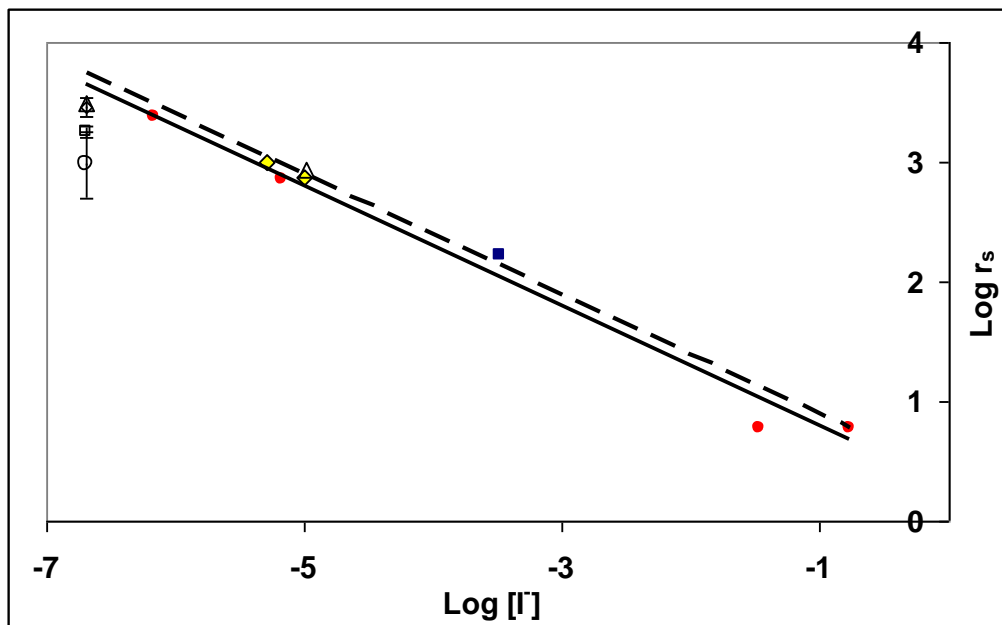
Figure 3.16 Comparison of observed and predicted r_s values tabulated in table 3.2. Black line, predicted r_s values using $k_{i=}$ 2.0 x 10^9 mol^{-1} dm^{-3} s^{-1} (Garland *et al.,* 1980; EQ 3.33, 3.34); dashed line, predicted r_s values using $k_{i=}$ 1.2 x 10^9 mol^{-1} dm^{-3} s^{-1} (Liu *et al.,* 2001; EQ 3.33, 3.34); yellow diamonds, observed iodide PBS solution r_s values in this work; filled red circles, Garland *et al*. (1980) iodide solution r_s values; filled blue square, Parthipan (2008) iodide solution r_s value; empty diamond, Aldaz (1969) seawater r_s value; empty square, Lenschow *et al*. (1982) seawater r_s value; empty circle, Regener (1974) seawater r_s value; empty triangles, observed seawater r_s values in this work.

3.5 Comparison of observed ozone uptake coefficients to theoretical estimates

The effective ozone uptake coefficient (γ_{eff}) for O₃(g) of the 5.0 x10^{-6} and 1.0 x10^{-5} M KI(*aq*) PBS solutions used in this study was obtained from the rate of decrease of [O₃(g)] during the calculated contact time (t = 600 s). These values were compared to calculated γ_{eff} values from a previous study conducted by Garland and Curtis (1980). As the first order rate constant (k_{O3}, s^{-1}) for the heterogeneous O₃ + I⁻ reaction is related to the number of collisions on the KI(*aq*) surface and the fraction of the collisions that undergo uptake, $\gamma_{eff,}$ the concentration of O₃ (g) removed at the KI(*aq*) surface is given by EQ 3.35 (Sakamoto *et al.*, 2009), where *A* is the KI(*aq*) surface area (49 cm²), u_{av} is the mean thermal velocity of O₃(g), $((8RT/\pi m)^{0.5} \sim 3.6$ x 10^4 cm s^{-1}) and *V* is the volume over the KI(*aq*) solution (1980 cm³). The loss rate of O₃(g) is first order with respect to [O₃(g)],therefore γ_{eff} is given by EQ 3.36 (Sakamoto *et al.*, 2009).

104

$$k_{O3}[O_3(g)] = \frac{A(u_{av}/4)}{V}[O_3(g)]\gamma eff$$

(EQ 3.35)

$$\gamma_{eff} = \frac{k_{O3}t}{A/V(u_{av}/4)t}$$

(EQ 3.36)

Under conditions where liquid phase reaction drives uptake from the gas phase, the O_3 uptake coefficient is expected to take the form of EQ 3.37 (Davidovits, *et al.*, 2006), where H_{O3} is the Henry's law constant for ozone (1.13 M atm⁻¹), R is the gas constant (K⁻¹ atm⁻¹ M⁻¹), T is the ambient temperature (293 K), and D is the aqueous diffusion coefficient of ozone (1.18 x 10⁻⁵ cm² s⁻¹). The γ_{eff} values calculated within this study (at 70 ppbv $O_3(g)$), and those of Garland and Curtis (1980), (at 40 ppbv O_3 (g)), were fitted to this relationship (Figures 3.17 and 3.18).

$$\gamma_{eff} = \frac{4H_{O_3}RT\sqrt{k_s}[I^-bulk]D_{O_3}}{u_{av}}$$

(EQ 3.37)

Iodide has previously been shown to preferentially partition to the air/water interface of bulk aqueous solutions (Ghosal *et al.*, 2005; Cheng *et al.*, 2008). The reaction of I^-(aq) with O_3(aq) is diffusion controlled with rate constants (k_s) in the literature of between 1.2 x 10⁹ mol⁻¹ dm⁻³ s⁻¹ (Liu *et al*., 2001) to 2.0 x 10⁹ mol⁻¹ dm⁻³ s⁻¹(Garland *et al.*, 1980) at 293 K and is believed to proceed predominantly at the air/water interface (Sakamoto *et al*., 2009). Both these k_s values were considered when fitting the γ_{eff} values calculated within this study and those of Garland and Curtis (1980).

Figures 3.17 and 3.18 show a plot of ozone uptake coefficient against the square root of the aqueous iodide bulk concentrations ([I^-(*bulk*)], EQ 3.37. The fitting curves show that the observed ozone uptake coefficients of Garland *et al.* (1980) and those from work in this chapter exhibit a square root dependence on [I^- (*bulk*)] over the concentration range

2 x 10^{-7} to 2.0 x 10^{-5} M. Over higher [I$^-$ (bulk)] ranges, the increase in γ_{eff} plateaus (Figure 3.18), which reflects the mass transfer limitations experienced by ozone deposition into the laminar layer at higher [I$^-$(bulk)] concentrations (Sakamoto *et al.,* 2009). The discrepancies between the observed ozone uptake coefficients and the fitting curves likely reflect the effect of segregation of iodide from the bulk into the laminar layer. This is expected to be of particular importance at low [I$^-$(bulk)] such as those observed in the worlds oceans (Cheng *et al.*, 2008). The observed ozone uptake coefficients of Garland *et al.* (1980) are slightly higher than those from work in this chapter due to the lower gaseous ozone concentrations employed during their experiments. Sakamoto *et al.* (2009) previously established that ozone uptake coefficients of KI (*aq*) solutions decrease at high ozone uptake.
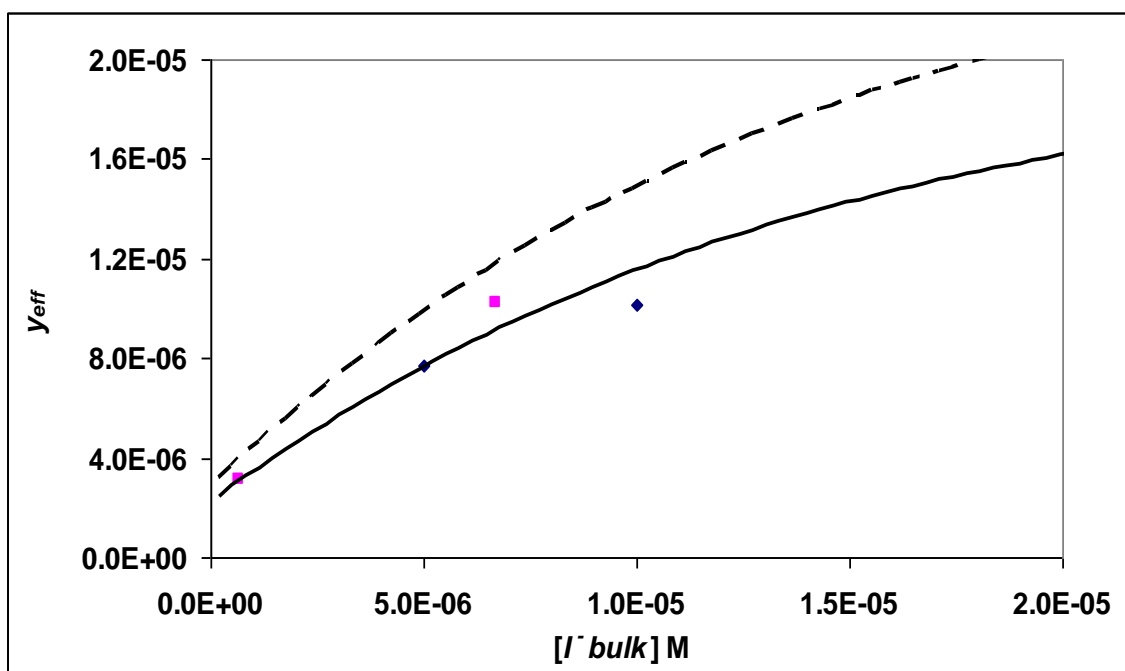
Figure 3.17 Ozone uptake coefficients as a function of the square root of [I$^-$ (*bulk*)] in PBS. Dashed line, fitting curve using EQ 3.37 and $k_s = 1.2$ x 10^9 mol^{-1} dm^{-3} s^{-1}(Liu *et al.*, 2001); filled line, fitting curve using EQ 3.37 and $k_s = 2.0$ x 10^9 mol^{-1} dm^{-3} s^{-1}; pink squares, γ_{eff} values from Garland and Curtis (1980); blue diamonds, γ_{eff} values from this work.
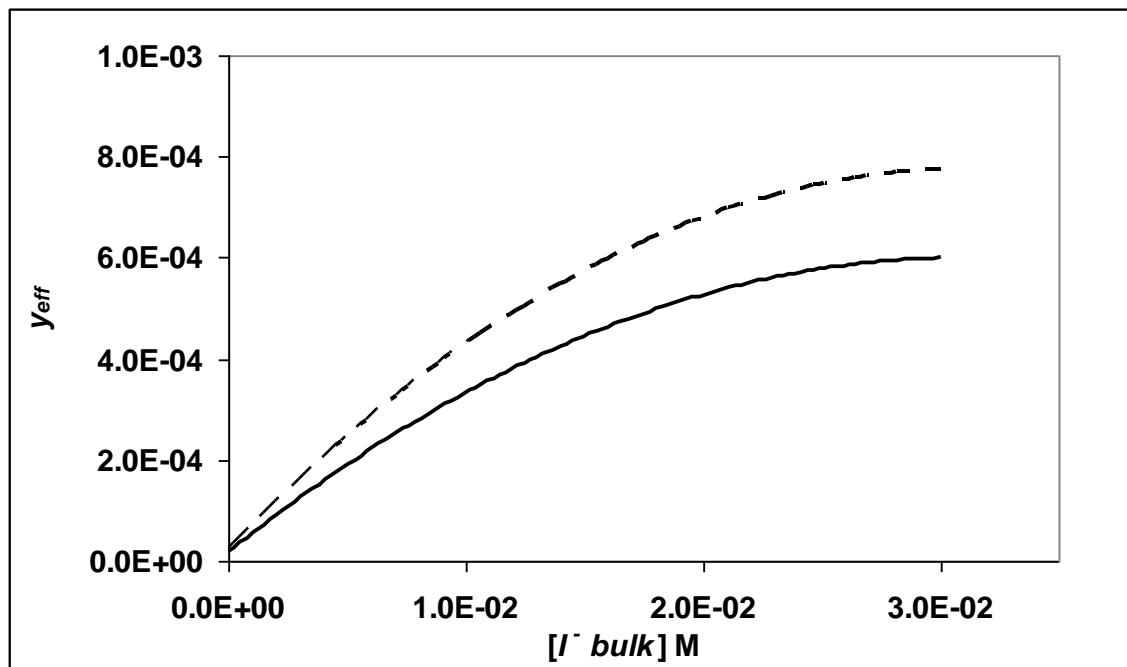
Figure 3.18 Ozone uptake coefficients as a function of the square root of [I^- (*bulk*)] in PBS. Dashed line, fitting curve using EQ 3.37 and k_s 1.2 x 10^9 mol^{-1} dm^{-3} s^{-1}(Liu *et al*., 2001); filled line, fitting curve using EQ 3.37 and k_s 2.0 x 10^9 mol^{-1} dm^{-3} s^{-1}.

3.6 Molecular iodine evolution from salt solutions via the I^- + O_3 interaction

3.6.1 Molecular iodine losses attributed to wall loss

Previous laboratory experiments involving gaseous I_2 (Garland and Curtis, 1980; Parthipan, 2008) have reported appreciable losses of iodine caused from condensing on the walls and tubing of the apparatus (13 − 40 %). Prior to conducting any of the experiments in this chapter, all tubing exposed to gaseous I_2 was continuously heated (~60 °C) to minimize losses (section 3.3.1). A series of control experiments were also conducted to establish I_2 losses attributed to wall losses under the experimental conditions utilized.

As established previously, ozone reacts with I_2 *via* a dark reaction both in the gas phase and in hexane (section 3.2.5), hence these wall loss experiments were conducted in ozone free nitrogen (zero grade, BOC). Experiments consisted of triplicate measurements of gaseous I_2 trapped under optimized conditions directly from the permeation oven (maximum output ~ 40 ppbv) and after being passed through the experimental system. The difference in the gradients of these two curves was attributed to I_2 condensing onto the walls of the apparatus. Molecular iodine wall losses were determined as a function of time and gaseous

I_2 concentration via this method. The fixed error bars on the mean values in figures 3.19 and 3.20 represent the propagation of the relative standard deviation (RSD) of the triplicate measurements, the quoted MFC error (2.5%) and the calibration error.

Figure 3.19 shows total I_2 trapped observed as a function of time during an experiment with a constant I_2 concentration (~ 40 ppbv). Gaseous I_2 was found to condense to the walls of the system at a constant rate of 0.05 nmol min^{-1} under the experimental conditions. Molecular iodine wall losses were observed to range between $\sim 60 - 24$ % for trapping periods between $30 - 120$ minutes.

Figure 3.20 shows total I_2 trapped observed as a function of gaseous I_2 concentration with a constant trap time of 90 minutes. Gaseous I_2 was found to condense to the walls of the system at a constant rate of 0.13 nmol per ppbv of gaseous I_2. Molecular iodine wall losses were observed to range between $\sim 58 - 22$ % for gaseous I_2concentrations between $10 - 40$ ppbv. Appendices 3.7 and 3.8 show the plots for I_2 lost against I_2 observed used for correcting wall losses during experiments conducted in this chapter.
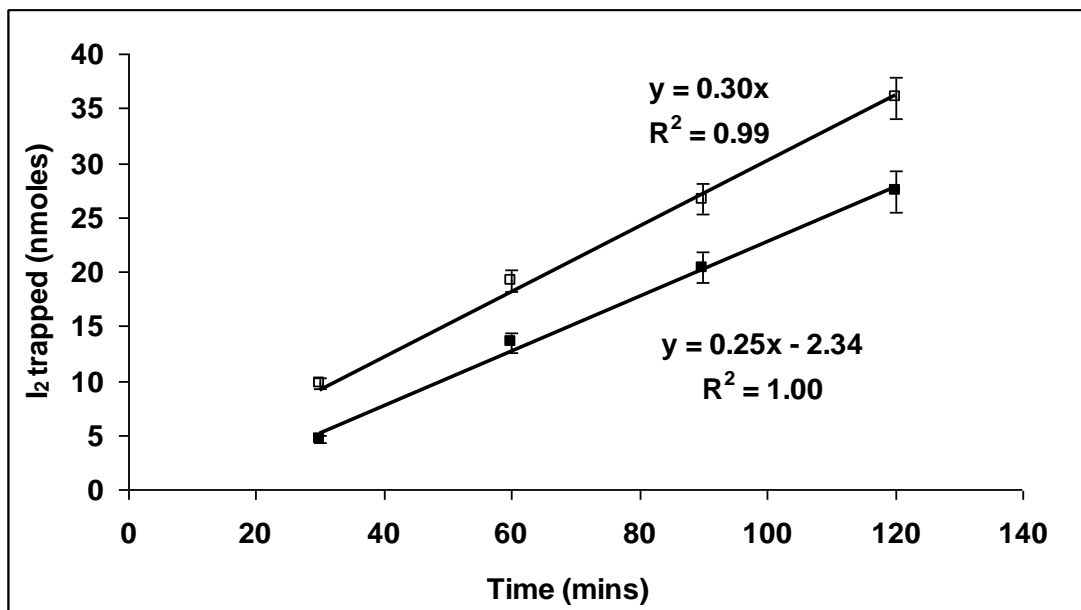
Figure 3.19. Total amount of I_2 trapped with respect to time. Empty squares - I_2 trapped from permeation source; filled squares - I_2 trapped after passed through the experimental system.
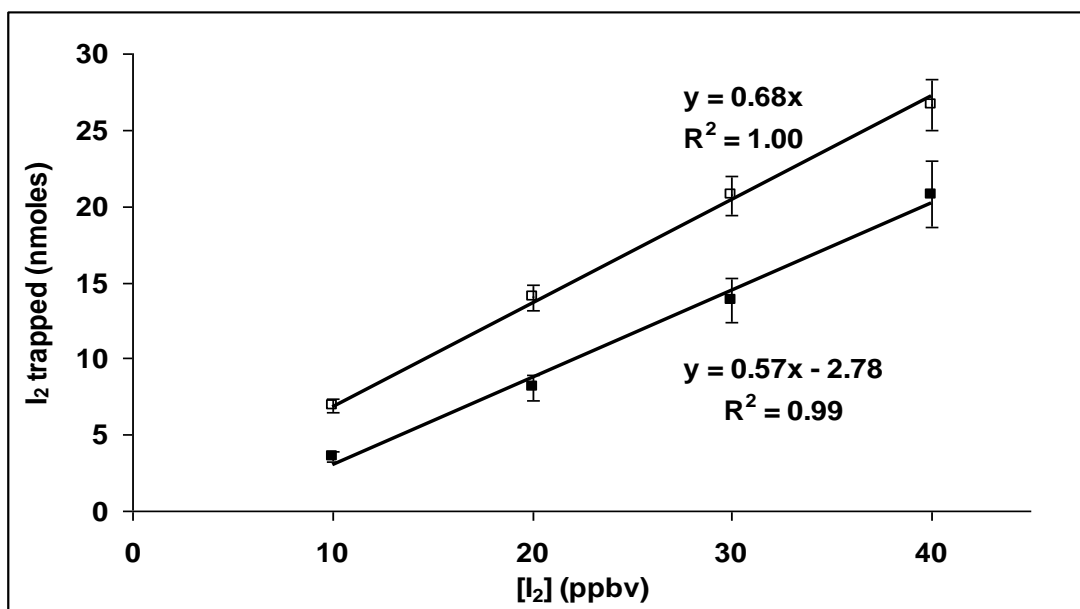
Figure 3.20. Total amount of I_2 trapped (during 90 minutes) with respect to gaseous $[I_2]$. Empty squares, I_2 trapped from permeation source; filled squares, I_2 trapped after passage through experimental system.

3.6.2 Molar balance of iodine species in experimental system

A molar balance of total iodine within the experimental set up was carried out at the end of each experiment. This was done by comparing the total molar amounts of I^-, I_2 and I_3^- in the aqueous solution and the gaseous I_2 trapped in hexane. The number of moles of I^- lost from the reaction vessel on its exposure to ozone in each experiment was converted to equivalent amounts of I_2 and compared with that trapped during the experiments, along with any I_2 remaining in the reaction vessel as I_3^-. A mathematical expression for the molar balance given as the total percentage I_2 detected (% $I_{2\ det}$) is shown in EQ 3.38, where Δ indicates change, n is the number of moles and subscripts *reactor* and *trap* denote the vessels analysed. Using this expression, all of the iodine within the system can only be accounted for when the molar amount of I_2 corresponding to the loss of I^- is detected as gaseous I_2 and aqueous I_3^-, in the trap and reactor respectively. However, I_3^- was not identified in the aqueous solutions of any experiment, probably due to it being below the LoD of the spectrophotometer at the initial low aqueous I^- concentrations employed.

$$\%I_{2det} = ((2\Delta[nI_2]_{trap} + 3\Delta[nI_3^-]_{reactor}) / (\Delta[nI^-]_{reactor})) \times 100 \qquad (EQ\ 3.38)$$

3.6.3 Evolution of I_2 from aqueous iodide in the presence of gaseous ozone

The first series of experiments were conducted to elucidate the production rates of I_2 and the evolution of aqueous I^- from the exposure of ozone (70 ppbv) to PBS at I^- concentrations of 10 μmol dm^{-3}. The mean values of gaseous I_2 evolved and I^- lost from PBS are shown in figure 3.21. These molar amounts are obtained from a two step correction of the initial amounts measured spectrophotometrically. The first correction involved correcting the measured I_2 molar amounts for time dependent losses from the $I_2 + O_3$ dark reaction in air and hexane at 70 ppbv ozone (figure 3.10, Appendix 3.5). These values were then corrected for the time and $[I_2]_{(g)}$ dependent losses to the walls and tubing of the apparatus observed in figures 3.19 and 3.20, (Appendix, figures 3.7 and 3.8). Therefore the final I_2 amounts plotted in figure 3.21 represent the amounts of I_2 directly emitted from the solutions in the presence of ozone. The I_2 *y* errors are estimated through the propagation of the total errors of each correction, the MFC error during the experiment (2.5%), and the mean calibration error. The I^- *y* errors reflect the propagation of the standard error of triplicate measurements, the MFC error (2.5%) and the calibration error. Quantitative I_2 and I^- determinations were carried out against an aqueous potassium iodide calibration curve (~225 nm) run daily (section 2.7.1, figures 2.31 and 2.32).

The rate of I_2 production was determined as 7.2 x 10^{-5} mol m^{-2} d^{-1} during exposure of a PBS surface area of 4.9 $\times$ 10^{-3} m^{-2} to 70 ppbv of ozone at a flow rate of 0.2 L min^{-1}. The observed iodide loss in PBS was linear with respect to time during the experiments and proceeded at a loss rate of 1.1 nmol min^{-1}. Using EQ 3.38, the total percentage of iodine detected as gaseous I_2 in the PBS experiments was ~ 48 %. The total percentage iodine detected can be assumed to be as high as ~ 49 % from the direct emission of IO previously observed during the heterogeneous reaction of gaseous ozone with aqueous potassium iodide ($[I_2](g)] > 100[IO(g)]$, Sakamoto *et al*., 2009). The remaining iodine unaccounted for in the experimental system is likely to have been present as aqueous dissolved organic iodine (DOI), HOI, IO_3^- and as undetectable concentrations of I_3^-.

Sherrill *et al.* (2004) previously reported that the ozonation of artificial seawater alters iodine speciation in aqueous systems such that DOI and I^- concentrations decrease and $[IO_3^-]$ increases systematically with increasing exposure to ozone. At an ozone concentration of 800 mV (oxidative reductive potential) in seawater, both I^- and DOI concentrations decreased to $\leq$ LoD whereas IO_3^- concentrations increased by 155 %. This observation is supported by work conducted by Cheng *et al.* (2008) and could mechanistically proceed via EQ 3.7 to 3.9. A large amount of iodine at the end of the experiments in this chapter could have been present in aqueous solution as IO_3^-, which would explain why only half of the iodine in the experimental system could be accounted for.
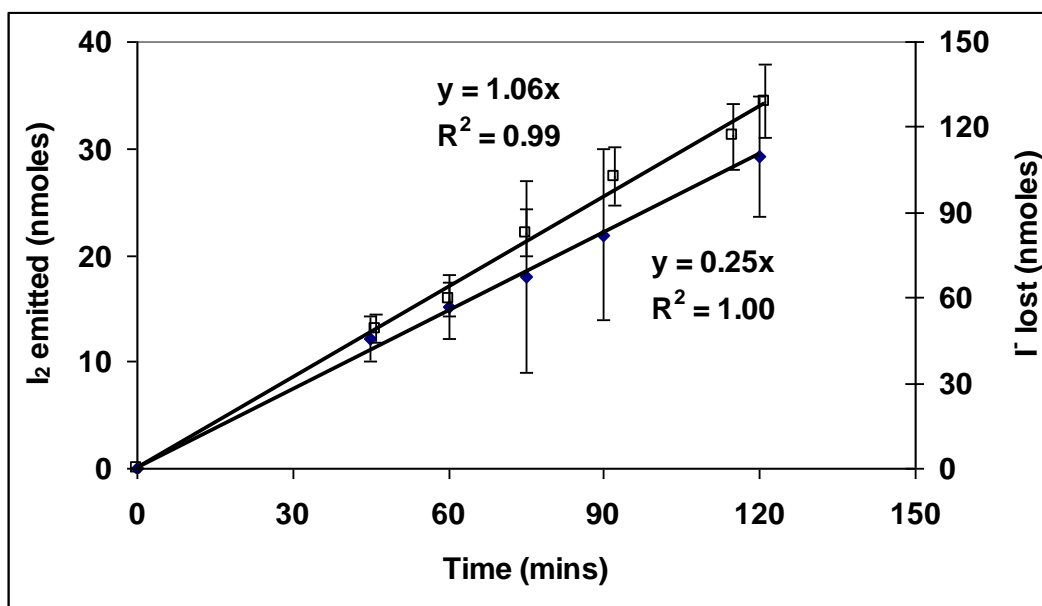
Figure 3.21 Gaseous I_2 emitted and aqueous I^- upon ozonation of 10 µmol dm^{-3} PBS as a function of time. Filled diamonds, $I_2(g)$; empty squares, $I^-(aq)$.

3.6.4 Rate of I_2 evolution as a function of $[O_3]$ and $[I^-]$

A series of experiments were conducted to investigate gaseous I_2 evolution rates as a function of both gaseous ozone and aqueous iodide concentrations. The established *y* error bars on figures 3.22, 3.23 and 3.24 are from the propagation of the quoted MFC error (2.5%), the calibration error and the established errors on the applied corrections (from figures 3.9 and 3.11, 3.20 respectively). Figure 3.22 shows the evolution of $I_2(g)$ from

seawater and PBS as a function of ozone concentration at a fixed iodide concentration (15 μmol dm^{-3}) over a 90 minute trap time. The rate of iodine evolution increased approximately linearly with ozone concentration up to 100 ppbv, but there was clearly strong evidence of the rate of evolution reaching an upper limit at higher ozone concentrations. Garland and Curtis (1981) report a similar observation in that the release of iodine vapour from 12.5 μg dm^{-3} iodide solutions in the presence of ozone (2 L min^{-1}) was reduced at concentrations above 100 ppbv O$_3$. A possible explanation for these observations is a saturation of ozone at the liquid surfaces at increasing gaseous ozone concentrations, limiting the rate of mass transfer reducing the potential for further ozone deposition and subsequent gaseous I$_2$ evolution.

It was observed that the rate of I$_2$ evolution from seawater was $\sim$20 - 50 % that of the PBS. This supports comparisons of a previous laboratory study of iodine evolution rates under similar conditions (Garland and Curtis, 1981) in which I$_2$ evolution from seawater ranged between 45% - 68% of that from buffered solutions at several gaseous ozone concentrations. This reflects both the competition of iodide with other species reactive to ozone (Garland *et al*., 1980), which are not present in the PBS, reducing the efficiency of iodide oxidation in natural seawater and the presence of insoluble surface surfactants reducing gas transfer rates (Frew *et al*., 2004). The [I$^-$(*aq*)]/[DOM(*aq*)] ratios were considerably higher in the seawater used in this study than those typically observed naturally (100 – 150 times, assuming 1- 2 ppm [DOM]). Hence the competing surface reactions of DOM with ozone under natural conditions are likely to be of greater significance (section 3.6.1 and 3.6.2).
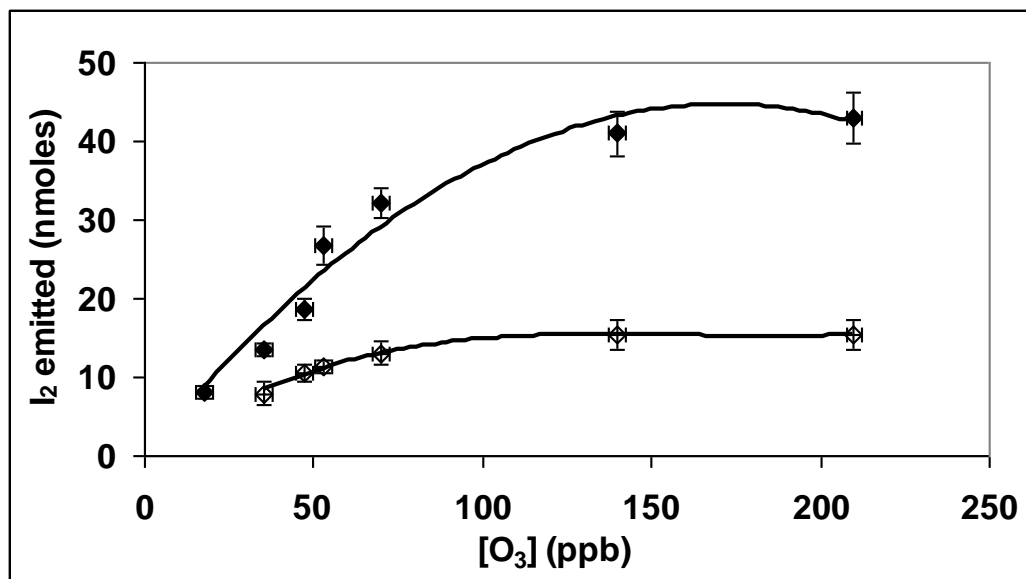
Figure 3.22 I$_2$ emitted from seawater and PBS as a function of ozone concentration. Filled diamonds, PBS experiments; empty diamonds, seawater experiments.

Similarly, Figure 3.23 shows the evolution of I$_2(g)$ from seawater (15 μmol dm^{-3} of I$^-$) as a function of ozone flux to the surface. Ozone flux to the surface was calculated using the measured gaseous ozone concentrations and the experimentally determined v_d (0.12 cm s^{-1}) for 15 μmol dm^{-3} I$^-$ in seawater) using EQ 3.30 (table 3.3). The results suggest air-aqueous interface mediated reaction kinetics, with ozone mass transfer limitations occurring at higher [O$_3$(g)]. Such kinetic behavior for the reaction of ozone with iodide at air-aqueous interfaces (Garland and Curtis, 1981; Sakamoto *et al.,* 2009; Hayase *et al.*, 2010) and several other species (Mmereki and Donaldson, 2003; Clifford *et al.,* 2008) has previously been observed, and is consistent with a Langmuir-Hinshelwood mechanism for the O$_3$ + I$^-$ reaction. The Langmuir-Hinshelwood mechanism (Adamson, 1990) for surface reactions proposes that reactions occur between co-adsorbed species, in which one reactant is more strongly adsorbed and the other is in rapid equilibrium between bulk and surface phases. It has been previously established that ozone absorbs on the aqueous laminar layer (Clifford *et al.,* 2008; Sakamoto *et al.,* 2008). Assuming Langmuir absorption behavior of O$_3$(g) to the aqueous laminar layer from the gas phase, the dependence of the measured I$^-$(aq) loss rate (k_{obs}) can be described using EQ 3.39 where k^{II} represents the two dimensional reaction rate coefficient, N^{surf} is the maximum number of surface sites available to ozone and *B* represents the ratio of desorption to adsorption rate coefficients involving both phases

113

(Donaldson, 1997; Clifford *et al.,* 2008). The solid line in figure 3.23 shows a fit of the data to the Langmuir-Hinshelwood mechanism, taking ($k^{II}N^{surf}$) as a single parameter. The *A* parameter obtained from the fit to the data was 5 x 10^{-6}, approximately 1000 times smaller than previously observed for heterogeneous interfacial ozone reactions with chlorophyll (3.6 x 10^{-2}, Clifford *et al.* 2008). The differences in this *A* parameter likely reflect the differences in aqueous surface area available for ozone deposition. The *B* parameter of ozone can vary depending largely on the aqueous concentrations of halide and organic species. The value determined from the fit to the data was 7.4 x 10^{11} molecules cm^{-3}.

$$k_{obs} = \frac{(k^{II}N^{surf})[O_3(g)]}{B+[O_3(g)]}$$

(EQ 3.39)
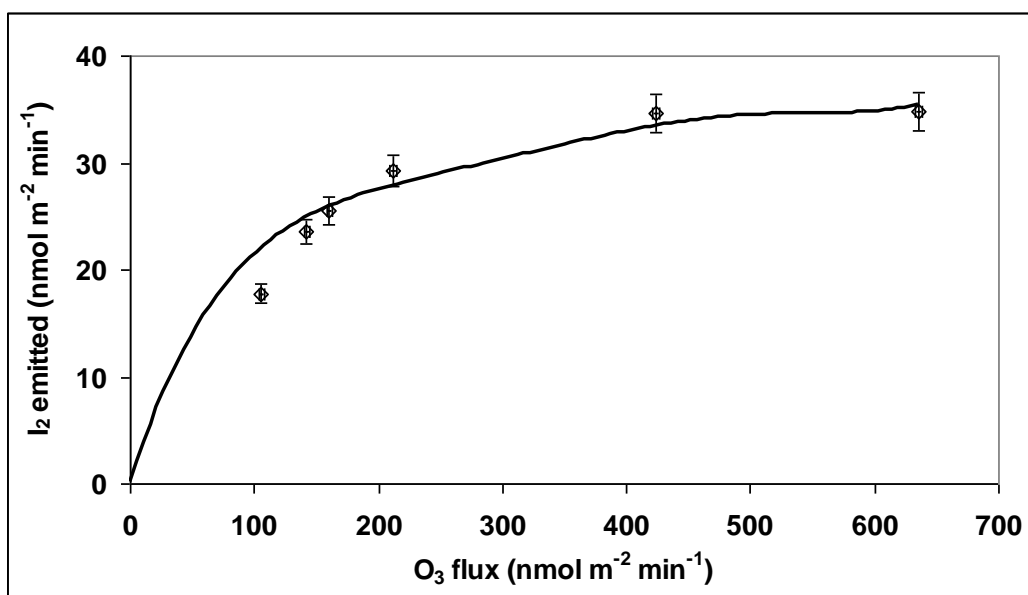
Figure 3.23 I_2 emitted from seawater (15 µmol dm^{-3}) as a function of ozone flux to the surface. Empty diamonds, triplicate measurements; Filled line, fitted Langmuir Hinshelwood mechanism (EQ 3.39).

Figure 3.24 shows I_2 evolution as a function of aqueous iodide concentration in PBS at a fixed gaseous ozone concentration (70 ppbv) and a trap time of 60 minutes. The rate of iodine evolution increased linearly ($R^2 \sim 1.0$) between the aqueous iodide concentrations investigated (10 – 40 µmol dm^{-3}). During each experiment iodine, measured as gaseous I_2, accounted for ~ 40% of the initial iodide concentrations in PBS. The rate of I_2 evolution

was observed to be directly proportional to the aqueous iodide (10 – 40 μg dm^{-3}) and gaseous ozone concentrations (18 – 70 ppbv). Note that the observed ozone uptake coefficients of both Garland *et al.* (1980) and those from work in this chapter exhibit a square root dependence on [I$^-$ (*bulk*)] (figures 3.17 and 3.18), whereas I$_2$ production *via* the O$_3$ + I$^-$ reaction directly increases with [I$^-$ (*bulk*)] (Garland *et al.,* 1980; Garland and Curtis, 1981; Lui *et al.*, 2001).

Because of the multiple non-linear effects of chemical and physical conditions on I$_2$ flux rates (not least the laminar layer thickness which will influence the rate of mass transfer of I$_2$ and available time for O$_3$ to react with I$^-$), extrapolating I$_2$ flux rates from these laboratory studies to environmental conditions is outside the scope of this study. However, these experiments have confirmed the potential for I$_2$ emission, at much lower O$_3$ and I$^-$ concentrations than have been used in several other studies (Sakamoto *et al.,* 2009; Hayase *et al.*, 2010). In the next sections, the effects of dissolved organic material on iodine emissions are discussed.
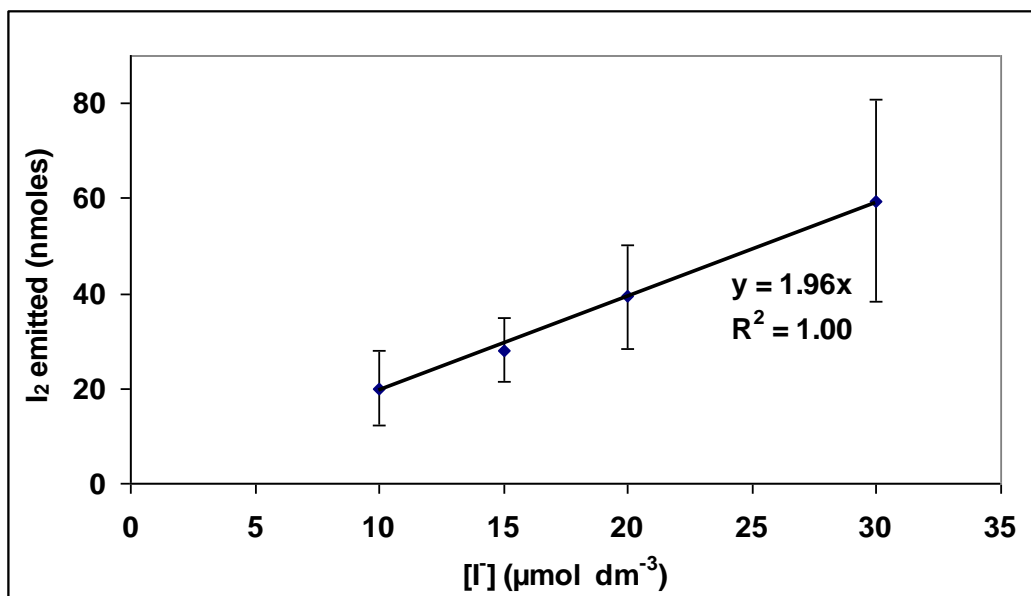
Figure 3.24. The quantity of I$_2$ emitted per hour as a function of aqueous iodide concentration in PBS at 70 ppbv [O$_3$(g)].

3.7 Study of the effect of DOC concentrations on O_3 deposition and I_2 evolution

Dissolved organic material in seawater is a complex organic mixture consisting of various functionalities; due to its complexity the components within it have not previously been identified. Dissolved organic carbon concentrations in seawater vary significantly between locations depending on geochemistry and season but have been reported to be in the range 0.3 - 2.0 ppm (Akkanen, 2002). The constituents of DOM in surface seawaters are considered to be predominantly humic substances (HS) with a global average HS contribution of the order of 50% (Thurman, 1985). The remainder of DOM is considered as non-humic material and constitutes the labile fraction of the material consisting of mainly carbohydrates, organic acids and fatty acids. A large portion of HS in natural waters (54-68%, Ma *et al.*, 2001) consist of fulvic acids (FA) which are known to be enriched in the laminar layer of surface seawaters and stable in solution for long durations (Calace, 2004).

The effect of organic surfactants in reducing gas transfer velocities in the surface ocean has long been recognized. The presence of insoluble surfactant films (slicks) act as a barrier to gas exchange, either by forming an insoluble layer on the sea surface (Springer and Pigford, 1970) or by providing a secondary liquid phase that provides a resistance to mass transfer (Liss, 1983).

Goldman *et al.* (1988) previously reported that gas transfer velocities could be influenced by biological activity in the surface ocean due to the exudation of soluble surface active material by phytoplankton. Supporting evidence (Frew *et al.*, 1990; Nightingale *et al.*, 2000) from laboratory experiments conducted on seawater and tracer experiments in the North Sea have shown that gas transfer velocities correlate inversely with increasing bulk water chlolophyll, DOC, and coloured dissolved organic matter (CDOM) concentrations. Frew *et al.* (1990) previously stated that the presence of such soluble surfactants can alter the hydrodynamic properties of the ocean surface and that the presence of these compounds can reduce gas transfer velocities even in the presence of breaking waves. The implications of this are that gas transfer between the ocean and overlying air is not purely a physical process but that surface chemistry, particularly in biologically productive regions, also plays an important role. Frew *et al.* (2004) previously confirmed this by demonstrating that

gas transfer velocities were more closely correlated to the mean square wave slope than to wind speed.

Martino *et al.* (2009) recently reported observing the production of the VOICs CH_2I_2, $CHClI_2$ and CHI_3 in seawater when exposed to ambient levels of gaseous ozone. The results within this study suggested that 1% ($\pm$ 0.3%) of the iodide oxidized by ozone reacts with organic matter in natural seawaters to form reactive VOIC. The production rates of these compounds were shown to be independent of the generation of biologically "fresh" DOM, but instead probably depend upon the presence of ubiquitous non labile DOM fractions such as FA. The production of VOIC can be explained by the haloform or a haloform type reaction, in which IOH (or I_2) reacts with DOC containing hydrogens α- to keto groups. This reaction has also been shown to occur during the disinfection of natural waters, producing a wide range of polyhalomethanes (Bichsel and Gunten, 1999; Hansson *et al.*, 1987).

3.7.1 The effect of aqueous DOM on ozone reactivity at the sea surface

Figure 3.25 shows the calculated mean surface resistances (r_s) of 10 µmol dm^{-3} iodide in PBS (pH 8, 20 mL) toward gaseous ozone (70 ppbv) over the aqueous DOC concentration range investigated (0 – 4.4 ppm). The experiment was conducted in duplicate to elucidate the effect of aqueous DOC concentrations on the rate of ozone deposition to the sea surface. The established *y* error bars on the r_s values in figure 3.25 are from the propagation of the quoted MFC error (2.5%), the ozone monitor error (2.5%) and the standard deviation of duplicate measurements. The established *x* error bars are from the propagation of volumetric errors during pipetting (2%) and glassware (2.5%).

The data would suggest a linear decrease in r_s of ~33 m s^{-1} per ppm of DOC extract added over the concentration range 0 – 4.4 ppm. Surface resistances were 5 - 10% lower at the range of typical DOC concentrations observed in seawater (1 – 2 ppm, Akkanen, 2002). This data is qualitatively in good agreement with the I_2 and aqueous I^- evolution data, figure 3.25, in that it suggests organic substrates within DOM react with ozone in seawater and that this reaction directly competes with the oxidation of I^- via ozone. However,

quantitatively explaining this observation is difficult due to the current lack of data on marine DOM characterization and subsequent kinetic studies of reaction with gaseous ozone.

It has previously been demonstrated that a surface organic microfilm exists at low wind speeds (Liss, 1983). The film is enriched with organic species such as DOM (Zhou and Mopper, 1997) of which the concentration is typically higher by a factor of 1 - 8 (Carlson, 1983). Other chemical species known to react with ozone, such as dimethyl sulfide (DMS) and alkenes, have previously been observed to be enriched in the surface layer, hence may play a significant role in ozone deposition to the surface ocean (Scwartz, 1992). Dimethylsufide is the most abundant sulfur species in sea water and is produced by phytoplankton (Andreae and Raemdonck, 1983). The average of previous measured surface concentrations in natural seawaters is 5.52 (0.04 - 316) nM (Kettle *et al.*, 1999). Ethene and propene are non-methane hydrocarbons produced directly by biological activity or photochemical degradation of DOM (Riemer *et al*., 2000). Riemer *et al.* (2000) previously observed 0.5 and 0.2 nM of ethene and propene in the surface of coastal seawaters within the Florida current. It is entirely possible that high fractions of both alkenes and DMS were extracted from seawater during the preparation of the DOC extract (section 2.7.5).

Using available second order kinetic rate constants, Chang *et al.* (2004) previously calculated ozone deposition rates of 1.5×10^{-4}, 1.1×10^{-4} and 1.7×10^{-3} cm s^{-1} attributed to propene, ethane and DMS respectively at their mean global concentrations. Assuming that these species were present within the seawater used to produce the DOC extract at the average concentrations specified (table 3.4), and that they were recovered with 100 % efficiency, these organic species alone would theoretically produce a combined ozone deposition velocity of $\sim 2.0 \times 10^{-3}$ cm s^{-1} at an aqueous DOC concentration of 1.12 ppm. Using linear regression in figure 3.25 this value is only ~25 % of the enhanced ozone deposition velocity, attributed to the presence of DOC (*aq*), observed within this study at a DOC concentration of 1.12 ppm (8.1×10^{-3} cm s^{-1}). The combined ozone deposition velocity of $\sim 2.0 \times 10^{-3}$ cm s^{-1} does not take into account gaseous ozone uptake by surface chlorophyll concentrations (Clifford and Donaldson, 2008), the impact of which would

depend upon the physical state of the chlorophyll (particularly whether it's associated or unassociated with phytoplankton and free at the ocean surface). Physical or chemical factors could still remain unaccounted for when considering ozone deposition within this system and highlights the need for the further characterization of marine DOM.

This experimental observation should be regarded with caution due to the high degree of scattering of the mean r_s values ($R^2 = 0.8$).The observed linear decrease in surface resistances shown in figure 3.25 should not be considered as quantitatively representing the situation in seawater as it is not known how representative the prepared DOC extract is of ubiquitous marine DOM.
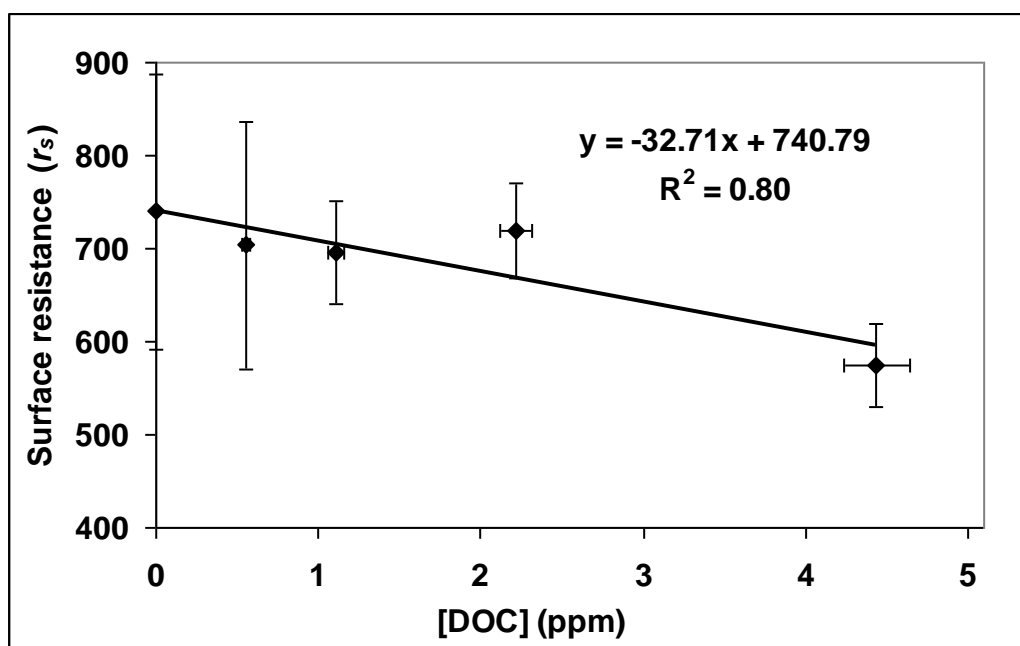
Figure 3.25 Measured gaseous ozone surface resistance values for 10 μmol dm^{-3} iodide in PBS (pH 8) at varying DOC concentrations.

3.7.2 Evolution of gaseous I_2 in the presence of aqueous DOM concentrations

Figure 3.26 shows the mean gaseous I_2 and aqueous I^- evolution on adding increasing amounts of concentrated DOC seawater extract to 10 μmol dm^{-3} iodide in PBS (pH 8 , 20 mL) during a 60 minute trap time. The experiment was conducted in triplicate to quantitatively investigate the effect increasing DOC concentrations in solution have on gaseous I_2 evolution from the surface layer via the I^- + O_3 interaction. The DOC

concentrations in solution were achieved by adding $20 - 160$ μl of an aqueous DOC extract (555 ppm) concentrated from seawater (sections 2.7.5 and 2.7.6) to the iodide in PBS (20 mL). The established *y* error bars on I_2 emitted in figure 3.26 are from the propagation of the quoted MFC error (2.5%), the calibration error and the established errors on the applied corrections (from figures 3.10 and 3.17). The *y* error bars on the concentrations of aqueous I^- lost represent the propagation of the calibration error and the standard deviation of replicate analyses.

The plot indicates that the amount of gaseous I_2 evolved from the iodide solution decreases exponentially on increasing the aqueous DOC concentration. The amounts of aqueous I^- lost, *via* oxidation by ozone, during the experiment exhibit a similar trend with increasing DOC concentration. The average amounts of gaseous I_2 trapped during the experiments account for 74 % ($67 - 79$ %) of aqueous iodine lost in the form of iodide, using EQ 3.38. The observed amounts of I_2 evolved from 10 μmol dm^{-3} iodide in PBS at typical seawater DOC concentrations ($1 - 2$ ppm, Akkanen, 2002) were between ~$60 - 80$ % of those observed in the absence of DOC, figure 3.26. These observed values are in generally good agreement with previous experimental data within this chapter that showed the rate of I_2 evolution from seawater containing 15 μmol $dm^{-3}[I^-]$ is ~20 - 40 % that of the PBS under identical conditions, figure 3.22. The discrepancies in these values are probably due to incomplete trapping of the complex range of organic species from sea water by the solid phase extraction device hence the DOC extract used within these experiments was not representative of that within natural seawater.
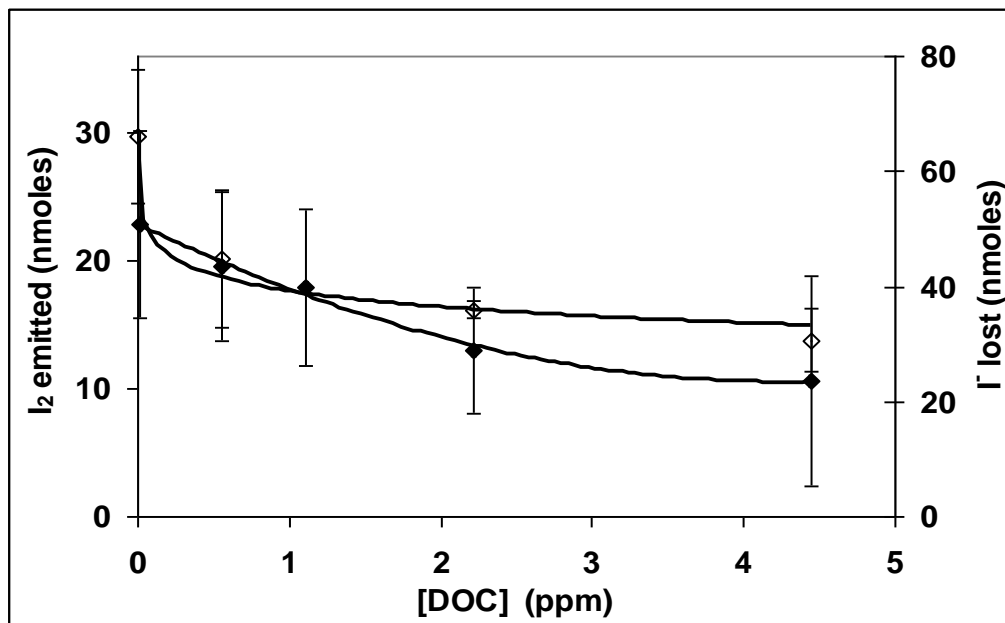
Figure 3.26 Gaseous I_2 and aqueous I^- evolution from 10 μmol dm^{-3} iodide in PBS (pH 8) at varying DOC concentrations in the presence of gaseous ozone. Filled diamonds, I_2 emitted; empty diamonds, aqueous I^- lost

These experiments clearly show a reduction in gaseous $I_{2(g)}$ evolution with increasing aqueous DOC concentrations. This could be caused by the increased competition for available ozone caused by reaction with organic species within DOC within the laminar layer, as supported by section 3.6.1, or direct loss of I_2/HOI via reaction with DOC (Bischel and Gunten, 1999). As the reaction of $[O_3(g)]$ in seawater is first order with respect to both $[I^-(aq)]$ (Sakamoto *et al.,* 2009; Hayase *et al*., 2010) and $[DOC (aq)]$, (Gershenzon *et al.,* 2001; Dowideit and von Sonntag, 1998; Broadgate *et al.,* 1997; Clifford *et al.,* 2008) it is the ratio of $[DOC (aq)]/[I^-(aq)]$ that is of importance. As the ratio of $[DOC (aq)]/[I^-(aq)]$ used in this experiment was ~ 50 times higher than observed naturally, this competitive reaction could be of even greater significance in marine waters in reducing I_2(g) emission. The observed decrease in I^- loss at higher DOC concentrations could also have resulted from a decrease in ozone deposition at the air-water interface due to the presence of soluble/insoluble surfactants (Frew *et al.*, 2004). It is possible that this phenomena is occurring in conjunction with the competition of ozone between $[DOC (aq)]$ and $[I^-(aq)]$ in reducing I_2 production in the laminar layer.

Table 3.5 shows an attempt to explain the observed data (figure 3.27) in terms of the ratios of [DOC (aq)]/[I$^-$$(aq)$] first order reaction rate constants (λ s^{-1}, EQ 3.34) with ozone in the experimental system**.** The concentration ranges of the compounds listed are based on DOC measurements previously conducted on the global ocean. Assuming the complete recovery of these organic compounds from seawater used for the DOC extract, the concentrations reflect their respective theoretical concentration ranges within PBS in this experiment. As quantitative determinations of phenol, p-cresol, p-methoxyphenol or salicyclic acid have not currently been conducted on seawater, an upper limit of 1 ppm was assumed.

As shown in table 3.5, a major potential DOC contributor to the reaction of O$_3$(g) in surface seawater is chlorophyll a (*Chl a*). Previous work by Clifford and Donaldson (2008) demonstrated that the reaction between ozone and free chlorophyll in solution significantly increases deposition velocity by up to a factor of 3 compared to iodide alone. The real impact of chlorophyll on ozone deposition will depend upon its actual physical state (either being associated with phytoplankton, or free at the ocean surface). The physical state of *Chl a* within the DOC extract was unknown, but for the purpose of this chapter *Chl a* concentrations were assumed to be free *Chl a* hence do not to reflect concentrations observed within the ocean.

Organic matter in atmospheric seawater/aerosol contain complex structured phenols (Leenheer *et al.,* 1995). Hayase *et al.* (2010) previously reported that the presence of aqueous phenol suppressed both I$_2$(g) and IO (g) emission in ozonised 5 mM NaI solutions. Under basic conditions, aqueous phenol (C$_6$H$_5$OH) can rapidly form phenolate (C$_6$H$_5$O$^-$) which reacts with gaseous ozone orders of magnitude faster than phenol, (1.4 x 10^9 mol dm^{-3} s^{-1}; Hayase *et al.,* 2010) comparable to I$^-$(aq). At pH 8 the [phenolate]/[phenol] ratio $\sim$ 0.1 suggests it could compete with the reaction of O$_3$(g) + I$^-$(aq) at millimolar concentrations at the air/water interface, hence was considered as a contributing factor to the reduction of I$^-$(aq) loss in this investigation (table 3.5). However, it was previously observed by Hayase *et al.* (2010) that both I$_2$(g) and IO(g) emission in their experiments was suppressed via rapid reaction with phenolate or its precursors.

Figure 3.27 shows the theoretical effect that reactions of $O_3(g)$ with DOC in surface waters have on $I^-(aq)$ loss to reaction with ozone. The linear regression represents the λ (s^{-1}) values calculated for the median concentration (6 x 10^6 mol dm^{-3}) of *Chl a* and mean concentrations of each other DOC compound previously observed in marine waters, with *y* error bars reflecting the upper and lower limits (table 3.5). The theoretical values can account for 67 – 110 % of the reduction in $I^-(aq)$ loss observed during the investigation. Ganzeveld *et al.* (2009) previously estimated λ values of ozone reactivity toward DOC in coastal surface seawaters to be in the order of 300 s^{-1}, approximately an order of magnitude smaller than the theoretical value λ calculated in this study, 2429 (139 – 3374)s^{-1}. This overestimation of the theoretical λ value is largely due to both the assumed phenolate/phenol concentrations (0.1 and 0.9 ppm respectively) in PBS, and that the physical state of *Chl a* was assumed to be unassociated with phytoplankton leaving it free to react with ozone at the gas/ liquid interface.

Figure 3.27 Observed and theoretical aqueous I^- evolution from 10 µmol dm^{-3} iodide in PBS (pH 8) at varying DOC concentrations in the presence of gaseous ozone. Empty diamonds, observed aqueous I^- lost; dashed line, theoretical values.

Compound	Molarity (10^{-9}mol dm^{-3})	k (mol^{-1}dm^3 s^{-1})	λ (s^{-1})
DMS[a]	20 - 400[g]	8.6 x 10^8	0.068 – 544
Ethene[b]	0.5[h]	1.8 x 10^5	1.8 x 10^{-4}
Propene[b]	0.2[h]	8.0 x 10^5	3.2 x10^{-4}
Isoprene[c]	0.05[c]	4.0 x 10^5	2 x 10^{-5}
Chlorophyll a[d]	2000 – 10,000[d]	6 x 10^7	120 – 1200*
Phenol[e]	9,540[1]	1.3 x 10^3	2.8 x 10^{-2}
Phenolate[e]	1,060[1]	1.4 x 10^9	1484
P-cresol[e]	9260[2]	3.0 x 10^4	0.56
P-methoxyphenol[e]	8056[2]	3.0 x 10^4	0.48
Salicylic acid[e]	7240[2]	3.0 x 10^4	0.43
TOTAL			2429 (139 – 3374)
Iodide	10,000	1.2 x 10^{9}[f]	12000

Table 3.5 Calculated reaction rate constants, λ, for DOC in seawater at 25°C.

[a] Gershenzon *et al.,* 2001.

[b] Dowideit and von Sonntag, 1998.

[c]Broadgate *et al.,* 1997.

[d]Clifford *et al.,* 2008.

[e]Hayase *et al*., 2010.

[f] Lui *et al.,* 2001

[g]Campos *et al.,* 1999.

[h] Kettle *et al.,* 1999.

[1] Calculated assuming 1ppm of phenol with phenolate/phenol ratio of 0.1 at pH 8.
[2] Calculated assuming 1ppm of each species.
* Calculated assuming *Chl a* concentrations were free to react at the surface of solution.

3.8 Conclusions

In order to better understand ozone deposition and subsequent I$_2$ evolution at the air-sea interface, their dependence on chemical enhancement and DOC concentration were thoroughly investigated. The work within this chapter provides evidence that the oxidation of I$^-$ at the seawater surface by atmospheric ozone is a viable source of I$_2$ to the MBL. This is consistent with previous field observations at the Cape Verde monitoring station (16.85°N, 24.87°W) where it was observed that the measured fluxes of VOIC were insufficient to account for the observed concentrations of IO, suggesting another iodine source within the region (Mahajan *et al.*, 2010; Jones *et al*., 2010).

In this laboratory work at seawater [I$^-$(aq)] of 15 μM, approximately 7 % of ozone deposited at the sea surface reacts with I$^-$(aq) forming I$_2$(g). In the environment, [I$^-$] is approximately 75 times lower, and both sea-air volatilization rates and the mixing rate of iodine species from the laminar layer to bulk seawater will be different.

It is important that the contribution of iodine from this source is investigated in order to fully understand the biogeochemical cycling of iodine. The work within this chapter suggests that gaseous I$_2$ evolution from the I$^-$ + O$_3$ reaction in the world's oceans are strongly constrained by the iodide and DOC content of the surface ocean, as well by physical processes such as frictional velocity and sea surface roughness. Due to the range of iodide (39 − 390 nM; Wong, 1976) and DOC (0.3 - 2.0 ppm; Akkanen, 2002) concentrations previously observed in the worlds oceans, it is likely that gaseous I$_2$ evolution from the O$_3$ + I$^-$ reaction in the surface ocean would vary significantly spatially. Therefore conclusions inferred from data within this chapter should be regarded as preliminary until confirmed by simultaneous open ocean ozone and I$_2$ flux measurements with complementary laboratory experiments coupling both biotic and abiotic interactions on I$_2$ dynamics in the surface ocean.

Chapter 4

Evidence for the emission of reactive halocarbons from open leads in sub-Arctic sea ice during the COBRA campaign.

4.1 Introduction

4.1.1 Tropospheric polar halogen chemistry

Polar Regions have a significant impact on the global atmosphere, influencing atmospheric and oceanic circulation as well as hosting unique chemical processes. The polar atmosphere is unique in that the region is dominated by sub-zero temperatures, stable stratification of the boundary layer, and unusual light conditions (Barrie *et al.*, 1988; Simpson, 2007). Recent research has suggested that halogens play an important role in the episodic destruction of tropospheric ozone in the Arctic environment during the onset of polar sunrise. Tropospheric ozone concentrations of ~ 30 - 40 ppbv have been observed to drop to near zero within a timescale of a day or less for periods of 1-10 days (Barrie *et al.*, 1988). Such ozone depletion events (ODEs) have most commonly been observed in late winter/early spring in the Arctic (Tarasick and Bottenheim, 2002) and August to October in the Antarctic (Jones *et al.*, 2006), when sunlight returns to high latitudes but temperatures are still low (-20ºC). The vertical distribution of ODEs typically extends from the surface to a height of 100 – 400 m, although previous ozone sonde data suggests this can vary from ~ 200 m to 1 km between early and late spring (Bottenheim *et al.*, 2002; Solberg *et al.*, 1996). The most severe and spatially extensive ground based observations of ODEs have been recorded at coastal sites within the frozen Arctic Ocean (Hopper *et al.*, 1998), however leads and polynyas are known to dynamically develop exposing the underlying seawater in this region. Although ODEs are believed to be initiated almost entirely over the ocean, depleted air masses can be transported to lower latitudes influencing oxidation chemistry on both a local and regional scale (Simpson *et al.*, 2007).

Previous measurements of ODEs during polar sunrise have coincided with enhanced amounts of filterable bromine within the marine boundary layer (MBL), suggesting that ODEs are caused by photochemical reactions involving brominated compounds (Barrie *et al.*, 1988). During the Polar Sunrise Experiments (PSE88, Barrie *et al.*, 1988; PSE92, Yokouchi *et al.*, 1994) conducted at Alert, Canada a strong negative correlation between gaseous ozone (O_3) and bromoform ($CHBr_3$) was observed, initially suggesting $CHBr_3$ photochemistry as the cause for O_3 depletion. However, this hypothesis was ruled out after absorption spectra of $CHBr_3$ suggested the photolytic lifetime of $CHBr_3$

under Arctic springtime conditions is ~ 100 days (Moorgart *et al.,* 1994) indicating insufficient reactive bromine could be photolytically produced from the typically low mixing ratios of $CHBr_3$ observed. It has since been suggested that halogens in the polar troposphere arise mainly from sea salt aerosol (Rankin *et al.*, 2002)*,* first year sea-ice (Wagner *et al.*, 2001; Freiβ *et al.,* 2004; Simpson, 2007), or other salty surfaces (Yang *et al.*, 2002). The resulting ODEs results from a catalytic ozone destruction mechanism involving halogen atoms that cycle between their atomic form and their oxides (Simpson *et al.,* 2007). Halogen radicals are photochemically produced from precursors such as X_2, XCl and XOH, as shown in section 1.2 (EQ 1.8 – 1.12).

4.1.2 Impacts of ODEs on Arctic chemistry

Tropospheric ozone is a significant greenhouse gas as well as being the precursor for most atmospheric oxidisers, such that it usually directly controls atmospheric oxidative potential. During ozone depletion events, ozone dominated oxidation pathways become less important and unique halogen oxidation pathways dominate. These halogen oxidation pathways alter the lifetimes of species, ultimately changing their fates in the environment. For example, halogens effectively oxidise gas phase mercury causing it to be deposited from the gas phase to the snow/sea-ice potentially increasing its bioavailability (Hylander and Goodsite, 2006). Mercury is a toxic, atmospheric pollutant of global importance which is emitted from both natural and anthropogenic sources. The dominant natural sources of mercury include forest fires, volcanoes and oceanic emissions whereas anthropogenic sources include coal power plants, medical activities, flooding and the production of fluorescent light bulbs, thermometers and switches (Mason *et al.*, 1994). The high vapour pressure and long atmospheric lifetime of mercury (6 – 24 months; Schroeder and Munthe, 1998) allows it to be transported in the form of gaseous elemental mercury (GEM, Hg^0) over long distances and it has been routinely observed within the MBL of the Arctic (Schroeder *et al.*, 1998). The unique chemistry of Arctic regions appears efficient in the oxidation and deposition of GEM and during polar springtime, rapid atmospheric mercury depletion events (AMDEs) have been observed to take place (Schroeder *et al.*, 1998; Slemr *et al.*, 2003).

Considerable research has been conducted over the last several years to elucidate the mechanisms behind these AMDEs, with a consensus that reactive bromine species

oxidise GEM in the Arctic MBL (and possibly the free troposphere) into reactive elemental mercury (REM) (Raofie and Ariya, 2004, 2006). Both Br and BrO are believed to play essential roles in AMDEs, however Br is suspected to be a more important oxidant in these reactions. Recent laboratory studies of I, Cl, I_2, Br_2, Cl_2, IO and ClO initiated reactions of GEM suggest that these reactions are unlikely to compete with Br oxidation pathways in the destruction of Arctic GEM (Ariya, 2004, 2006; Raofie and Ariya, 2006). REM species are more reactive than GEM and may deposit directly to snow/ice surfaces or onto particles as particulate absorbed mercury (p-Hg) (Lui *et al.,* 2001; Lindberg *et al.,* 2002). The currently proposed REM species and their production mechanisms are shown in EQ 4.1 to 4.4 (Calvert and Lindberg, 2003; Raofie and Ariya, 2004, 2006). However, the chemical speciation of both REM and p-Hg species remain unknown as existing analytical techniques are inadequate for their determination.

$$Br + Hg^0 \rightarrow HgBr \qquad\qquad\qquad\qquad (EQ\ 4.1)$$
$$BrO + Hg^0 \rightarrow HgO + Br \qquad\qquad\qquad (EQ\ 4.2)$$
$$BrO + Hg^0 \rightarrow HgBrO \qquad\qquad\qquad\quad (EQ\ 4.3)$$
$$BrO + Hg^0 \rightarrow HgBr + O \qquad\qquad\qquad (EQ\ 4.4)$$

Deposited mercury can re-enter the atmosphere through volatilisation and photo-reduction processes (Hylander and Goodsite, 2006). Any remaining mercury compounds in snow/sea-ice can enter the water cycle on the onset of melting during Arctic springtime and summer, causing bio-accumulation in both local wildlife and indigenous human populations. Previous estimates have calculated that spring-time mercury depletion events deposit between 50 and 300 tons of mercury to the Arctic over the period of one year (Schroeder *et al.*, 1998; Banic *et al.*, 2002; Ariya *et al.,* 2004). The effect of this mercury loading on indigenous human populations was previously investigated at the two Arctic settlements of Igloolik and Repulse Bay. It was found that up to 33% of the participants of Igloolik and 60% of Repulse Bay had levels of exposure above the minimal risk level (Oostdam *et al.*, 2005).

4.1.3 Halogen sources to the polar boundary layer

4.1.3.1 Saline sea-ice, snowpack and sea salt aerosol as a direct halogen source

Reactive halogen compounds are believed to be produced as a result of heterogeneous reactions on various surface types specifically including saline sea-salt aerosol, frost flower structures, saline snow or first year sea ice (FYI) surfaces (McConnell *et al*., 1992; Fan and Jacob, 1992; Foster *et al*., 2001; O'Dowd and Hoffman, 2005; Kalnajs and Avallone, 2006; von Glasow and Crutzen, 2007), as shown in figure 1.1 and EQ 1.30. The role of sea salt aerosol in halogen activation is discussed in section 1.3.2.

Saline snowpack and sea-ice surfaces are also considered possible sites of halogen activation. Snow is contaminated by salt driven by wind-transport of sea spray, vertical transport through sea ice and wind blown frost flowers. Previous measurements of high Br_2 and BrCl concentrations in the interstitial air of snow by mass spectroscopy are currently the most direct evidence of the role of the snowpack in halogen activation (Foster *et al.*, 2001; Spicer *et al.,* 2002). Avallone *et al.* (2003) have also shown enhanced BrO concentrations at the snow surface. Simpson *et al.* (2005) recently provided indirect evidence for the recycling of bromine on snow surfaces from the observation that many snow samples were depleted in bromide. A strong indication for the relevance of first year sea ice toward gaseous bromine emission are GOME satellite observations that showed that clouds of BrO were largely present over FYI but not over perennial sea ice (Wagner *et al.,* 2001). Similarly, both Freiß *et al.* (2004) and Simpson *et al.* (2006) previously demonstrated, using back trajectory analysis, that areas of FYI were correlated with high mixing ratios of BrO. The elevated BrO mixing ratios from air masses transecting regions of FYI are believed to reflect the higher sea ice salinities of younger ice columns.

Under typical polar weather conditions, it has been suggested that sea salt aerosol production from wind driven snow can be up to more than an order of magnitude more than from the open ocean (Hall *et al.,* 1998; Rankin *et al.*, 2002; Yang *et al.,* 2008). Loose snow overlying sea ice can accumulate sea salt through a combination processes including brine transport and sea salt deposition (Simpson *et al.,* 2007). If wind driven snow occurs over regions of contaminated snow, and there is sufficient availability of acidifying trace gases to titrate sea salt alkalinity, a bromine explosion is possible (Yang *et al.*, 2010*).*Since bromine in wind driven snow can be transported long distances, this

phenomenon can even contribute significantly to BrO in mid-lattitude regions (Yang *et al.,* 2010).

4.1.3.2 Frost flowers and derived aerosols as a source of reactive halogens

Frost flowers are vapour deposited dendritic crystals which form on brine surfaces, and have sharp angular features and a large surface area for gas exchange. Frost flowers usually form close to regions of open water due to their enhanced salinity caused by surface flooding. Figure 4.1 shows fresh frost flowers growing on newly formed seasonal sea ice in proximity to the coast of Kuujjuarapik during the COBRA campaign. This small frost flower field was observed within 1 km of the experimental site during the field campaign outlined in section 4.1.5. Previous estimates of frost flower surface areas are very high, leading to the assumption that they could be a direct source of bromine to the atmosphere (Rankin *et al.,* 2002). However, more recent estimates of the specific surface area (SSA) of fresh frost flowers have suggested values of ~200 cm^2/g, two orders of magnitude less than early estimates (Domine *et al*., 2005; Obbard *et al.,* 2009). Previous measurements of bromide/sodium ratios in fresh frost flowers showed that bromide is not measurably depleted when compared to sodium (Simpson *et al.,* 2005). Also, past measurements of frost flowers indicate that their pH are typically too alkaline (pH > 6.5) to support catalytic bromine explosion chemistry (Kalnajs and Avallone, 2006). Both the *in-situ* and laboratory observations of the physical and chemical properties of frost flowers suggest that frost flowers are unlikely to contribute significantly to atmospheric halogen concentrations via direct gas emission. However, to date, this remains an area of further work.

Wind driven derived aerosol potentially produced from frost flowers contain high concentrations of aqueous bromide (Barrie *et al.,* 1988) and high acidity (Sander *et al.*, 2006). This enhancement in aqueous bromide concentration and acidity could occur by the scavenging of HBr, the termination product of the bromine explosion, by these particles. Theoretically, this particulate bromine could then be recycled to gaseous bromine following transport to higher altitudes or different geographical locations. Supporting field measurements include ground-based and aircraft measurements of high BrO column densities in the free troposphere (Honninger *et al.,* 2004; McElroy *et al.,* 1999). As the lifetime of Br$_2$ and BrO (BrO$_x$ family) is only a few hours in the absence of

bromine recycling, these observed gaseous BrO column densities observed in the free troposphere would have to have been transported within this lifetime or be the product of recycling on transported aerosol. Despite this evidence for bromine recycling on aerosols, most ODEs and AMDEs have been observed at ground level, which could suggest a ground based flux of either halogens or their precursors initiating these auto-catalytic mechanisms.

Recent laboratory and field observations of frost flowers (Obbard *et al.,* 2009; Roscoe *et al.,* 2011) suggest their direct effect on sea salt mobilization and halogen chemistry may be less than previously estimated due to their high surface stability even when subjected to high wind speeds ($\leq$ 12 m/s). However, frost flowers may still provide a significant role in sea salt mobilisation. For instance, under low humidity conditions, significant frost flower dehydration may occur making parts of the frost flower more fragile and susceptible to wind destruction generating aerosol (Roscoe *et al.,* 2011). Similarly, frost flowers may provide an indirect source of salinity to wind blown surface snow which can later be remobilized (Obbard *et al.,* 2009).
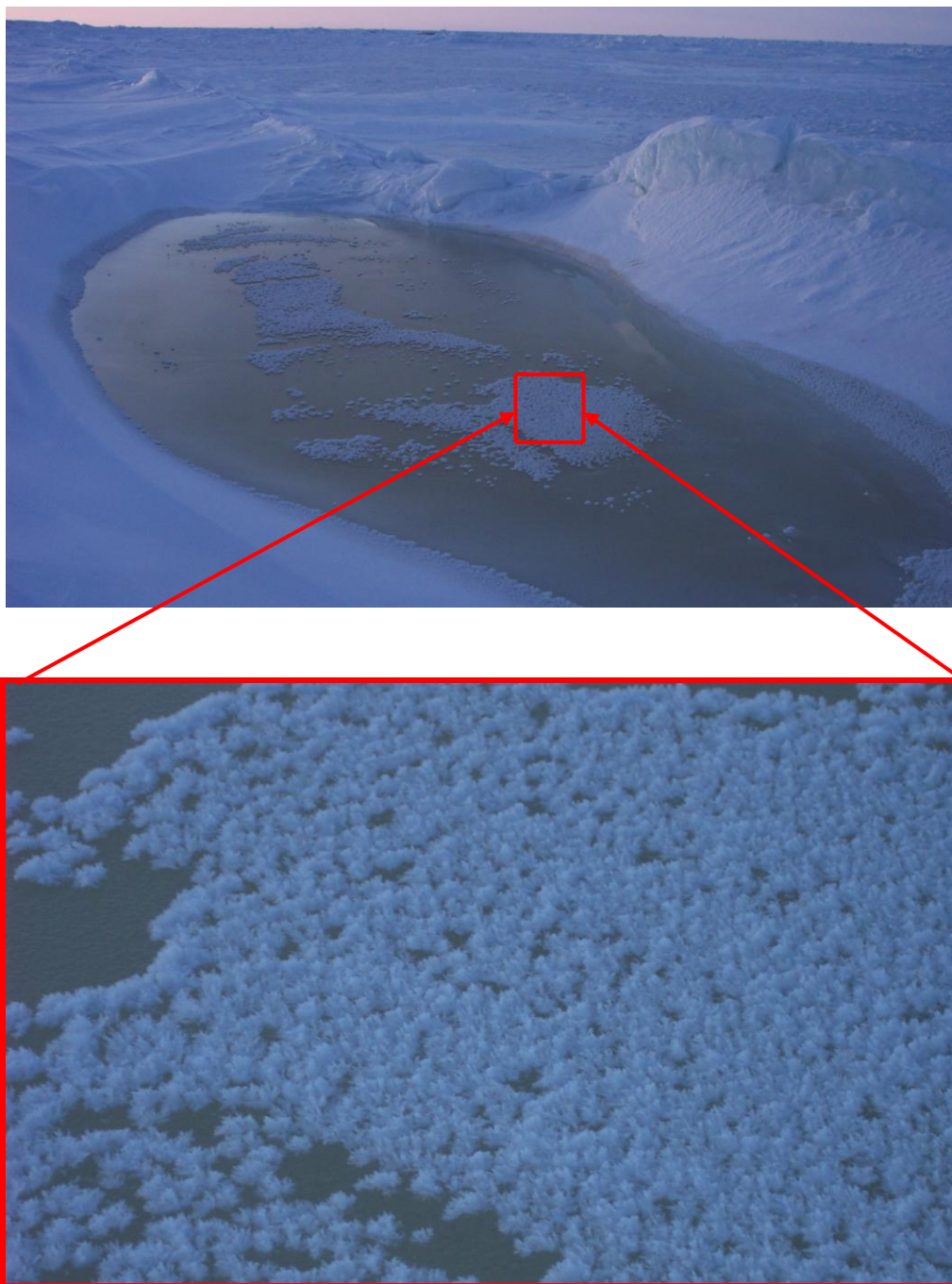
Figure 4.1 Evidence of frost flower growth on newly formed sea ice in the Kuujjuarapik region of Hudson Bay, Canada (February, 2008).

4.1.4 Sources of VSLHs

Very short lived halogenated organics (VSLHs) are a group of short lived mono-, di and tri- halogenated organics which are believed to be a major source of iodine to the MBL and may play a role in the initiation or termination in reactive halogen chemistry in polar regions. Most of the organobromine compounds are believed to be produced by macro and microalgae, particularly diatomaceous ice algae previously observed in both the ocean and in colonies on the underside of sea-ice (Reifenhauser and Heumann, 1992

and Schall *et al.*, 1994). These findings also correlate with those of Sturges and Shaw (1993) who previously observed bromoform ($CHBr_3$) venting from leads in Arctic sea-ice.

During winter within polar regions, biological activity is focussed at the surface and on the underside of the ice sheet on the ice covered ocean. Previous measurements in the Arctic have demonstrated that numerous diatom species are capable of producing poly halogenated methanes including $CHBr_3$, CH_2I_2 and CH_2ICl (Schall and Heumann, 1993). However, *in-situ* determinations of these compounds within the boundary layer have been observed to peak over a broad winter period, and do not correlate with measured blooms of marine biota despite halocarbon loss rates being taken into account (Yokouchi *et al.*, 1996).

Previous field measurements also suggest a significant abiotic source of halocarbons in polar regions. The mono-halogenated organics CH_3Br, CH_3I and C_2H_5I have been measured in the near surface Arctic snowpack where the concentrations were found to be 3-10 times higher than the overlying ambient air, indicating this surface as a direct halocarbon source (Swanson *et al.*, 2002). This proposed source involves the production of alkyl radicals from the photolysis of carbonyl compounds, which exist as high concentrations of dissolved organic carbon (DOC) found in snow (Yang *et al.*, 2002). These alkyl radicals are then free to react with iodine, produced from the oxidation of iodide by OH radicals present in high concentrations within the quasi liquid layer of the snowpack (QLL).

The shorter lived di and tri-halomethanes (CH_2I_2, CH_2IBr and CH_2ICl) have recently been observed in air that had passed over Hudson Bay during polar sunrise (Carpenter *et al.*, 2005). The absence of local leads over the bay coupled with the extremely short atmospheric lifetime of CH_2I_2 indicated production occurred on the snowpack/sea-ice surface rather than from emissions from any underlying ice-algae. The previous abiotic mechanism does not explain the production of di- and tri-halomethanes. Carpenter *et al.* (2005) instead proposed that high levels of dissolved HOBr and HOI react with dissolved organic material (DOM) present in the quasi liquid layer (QLL), as shown in equation 1.29 (section 1.3.1). Such haloform reactions of HOI with DOM have also previously been observed in natural waters (Hansson *et al.*, 1987). Halogenation of

compounds containing hydrogens α- to keto groups is both acid and base catalysed and leads to production of RX, RX_2 and RX_3 with relative amounts depending upon reactant conditions.

4.1.5 The COBRA Campaign

As part of the International Polar Year associated impact of COmbined Bromine and Iodine Release on the Arctic atmosphere (COBRA) project, a field campaign took place on the eastern coast of Hudson Bay, Canada (Figure 5.4; 55.28°N, 77.77°W), from 12/02/08 – 7/3/08 (Figures 4.2 and 4.3). The geographical location of this region is shown in figure 5.3. Throughout the field campaign sea-ice covered the majority of the Hudson Bay region with only minor, temporary leads and polynyas dynamically forming, intermittently exposing the underlying seawater surface. The experimental site was located on the land/sea-ice boundary north of the town of Kuujjuarapik. The central objectives of COBRA were to:

- further develop the understanding of the role of iodine (in concert with bromine) in Arctic gas phase photochemistry, aerosol production and evolution
- investigate the relative/combined roles of frost flowers, older sea-ice/snow pack, sea salt aerosol and biological sources in releasing halogens to the Arctic atmosphere
- increase understanding of the temporal and spatial variability of halogen-related ozone and mercury depletion events in the Arctic
- develop improved models of Arctic chemistry and emissions and their effect and feedbacks on regional/global atmospheric chemistry and climate

The campaign built on previously collected *in-situ* measurements and supporting data from the same field station in March 2004 (Carpenter *et al*., 2005). An International consortium of institutions contributed toward the project, the Universities of York, Leeds, Manchester, Leicester, East Anglia, Cambridge, British Antarctic Survey (BAS) and from the University of Cork, Ireland. A complete list of the measurements made during the COBRA campaign are listed in table 4.1.

Measurements	Technique	Institute
I_2/IO/BrO/OIO. OH, HO_2.	LP-DOAS, MAX-DOAS FAGE	University of Leeds
O_3, NO, NO_2, CO, VSLHs	ANNOX, Aerolaser TD-GC/MS	University of York
Aerosol number-size distributions (3-10μm) size segregated particle fluxes. Meteorological measurements	UHSAS, CPCs and SMPS	University of Manchester
Total gaseous mercury*, mercury speciation and O_3*	Mercury Tekran 1130,1135 ozone TECO	Environment Canada
Temperature, ozone profiles, height of boundary layer. Chemical, physical and biological characteristics of ice.	Met. Sonde on tethered kite/balloon BET method for specific surface area, ion chromatography, microscope analysis and chlorophyll assays	British Antarctic Survey

Table 4.1 Measurements made during COBRA by contributing institutions.
* These were longterm measurements routinely carried out at the field station (Environment Canada).

Whilst many measurements of short lived brominated organics in both air and water have been conducted (Carpenter *et al*., 2005) there are very few data sets with the simultaneous measurement of both bromocarbons and iodocarbons and even fewer including di-halomethanes. The aim of this chapter is to contribute to this existing limited dataset of Arctic VSLH measurements in the MBL and investigate their sources, including the potential roles of various surface types.

Figure 4.2 Kuujjuarapik Centre d'Etudes Nordiques.

Figure 4.3 Containers at the COBRA experimental site on the east coast of Hudson Bay.

4.2 Experimental

4.2.1 Site and Sampling Details

The Kuujjuarapik field station is run by the Canadian Centre d'Etudes Nordiques, and is equipped with research laboratories (with existing long term O_3 and Hg measurements), a weather station and living quarters (figure 4.2). In addition to the existing research

facilities, a 20' laboratory container was positioned directly on the coast which contained a suite of analytical instrumentation for comprehensive *in-situ* field measurements (Figure 4.3). Located on the adjacent sea ice, ~ 150 metres from the coast a micrometeorological (MET) station (University of Manchester) conducted continuous wind speed, wind direction and temperature measurements at the site.

Two Perkin Elmer Autosystem XL Gas Chromatographs each connected to a Perkin Elmer Turbomass Mass Spectrometer (GC-MS) were used for air and seawater and ice meltwater sampling of VSLHs during COBRA. The system which resided in the experimental container was set-up with a thermal desorption - gas chromatograph - mass spectrometry detector (TD-GCMS) for the pre-concentration and analysis of halogenated organics in air. The second system resided in the research laboratory at the Kuujjuarapik field station. This second system had a purge and trap (P&T) arrangement for volatilising VSLHs from sea water and ice samples prior to pre-concentration and analysis via automated thermal desorption (ATD)-GC/MS. A full description and analysis of the VSLHs in seawater and sea-ice sampled within the Hudson Bay region in included in section 5.4.

The sample inlet was situated directly next to the experimental container at a height of 3.6 m above ground level using a 10 m MICROMET tower, Figure 4.4. Samples were taken at 100 ml min^{-1} for 30 minutes every hour. The entire length of Teflon sample line was covered with electrical tape for the duration of the campaign to reduce any photolytic degradation of halocarbon species during sampling.
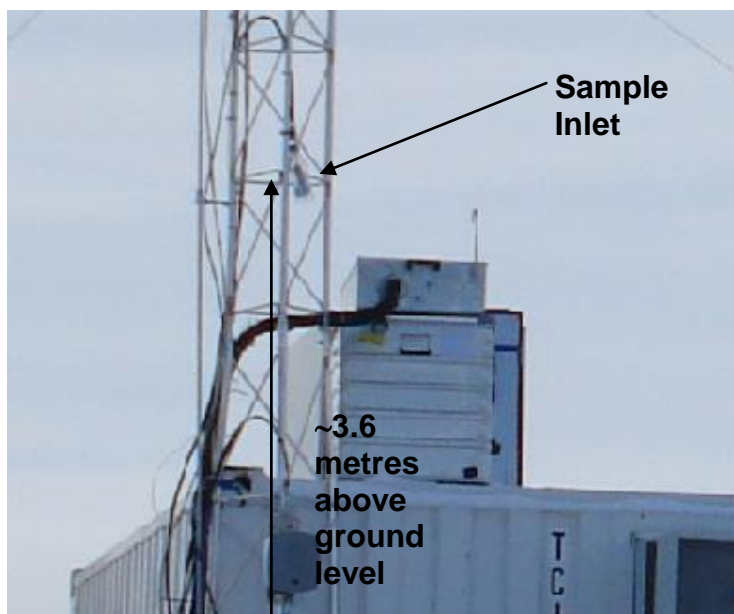
Figure 4.4 Online air sample inlet used for VSLH sampling at experimental site.

4.2.2 Online air VSLH measurements

Approximately hourly in situ measurements of 3 L sample volume were made of VSLHs at the experimental container site using a TD-GCMS. Air was sampled using a 10 m PFA Teflon sample line (0.5" i.d), which collected ambient air from outside the container using a large capacity diaphragm pump, and dried to remove as much moisture as possible prior to "trapping". The first stage used an "in house built" Nafion box dryer, consisting of Nafion tubing drawn through molecular sieve and self indicating silica gel (0.5-2.0 mm diameter) contained in a gas tight container, to remove bulk moisture from the sample stream. The second stage involved using a counter current flow Nafion dryer (Permapure.inc) to remove any remaining residual moisture. A stainless steel T-piece (1/2 to 1/4") was situated upstream of the diaphragm pump and was connected to an metal bellows pump (Aerospace Ltd) via ~ 1 m of 1/4 " PFA Teflon tubing. The metal bellows pump supplied sample air to the online trapping system at 100 ml min^{-1} via ~ 1 m of 1/8" PFA Teflon tubing. Samples were then pre-concentrated on an air monitoring trap (Perkin Elmer) held at -30°C. After collecting the desired volume on the cold trap, the trap underwent flash heating to 350°C at a rate of 40 °C sec^{-1} and was purged with helium to thermally desorb the halogenated organics and introduce them to the GC in a narrow band. Subsequent TD zones (valve and transfer line) were heated to 200 - 250°C to prevent analytes of interest from condensing before reaching the GC column. The VSLHs were resolved

chromatographically using a CP-Porabond Q capillary column (section 2.5). A detailed description of the operation of the Perkin Elmer TD-GC/MS hardware can be found in sections 2.1 – 2.5.

4.2.3 Online air measurements calibration and normalisation

The VSLH online air measurements obtained at the experimental site were internally standardised against carbon tetrachloride (CCl_4) within the troposphere. Carbon tetrachloride is a stable gaseous compound (global atmospheric lifetime of $\sim34 \pm 5$ years; Allen *et al.,* 2009) observed at relatively high concentrations in the atmosphere. Due to the lack of rapid tropospheric removal mechanisms, CCl_4 is typically present in the troposphere at mixing ratios of ~100 pptv (Allen *et al.,* 2009). Due to its long term stability and uniform distribution within the MBL, CCl_4 can be directly used as a measure of instrument sensitivity over time, making it an ideal *in-situ* internal standard for air analyses. The use of such an *in-situ* internal standard during on-line air analysis was essential during the COBRA campaign due to the high variability of instrument sensitivity over the analysis period.

Figure 4.5 shows the high variability of instrument sensitivity during the analysis period of the container GC-MS (figure 4.4), with CCl_4 responses over the analysis period ranging between 725 x 10^3– 195 x 10^4 peak areas, RSD 21.3%. The instrument sensitivity during the online air analysis period (19th – 28th of February) is weakly anti-correlated to ambient air temperature (measured from a MET station positioned on the sea ice $\sim$ 150 metres from the experimental container site, University of Manchester). During overnight analysis it was common for the experimental container internal temperatures to drop from $\sim 25°C$ to $< 10°C$ (James Dorsey, personal communication). It is possible that such instrument temperature changes could be the cause of such sensitivity variation. The Perkin Elmer Clarus 600 Mass Spectrometer is recommended to operate at ambient temperatures between 10 - 28°C with a temperature variability, usually caused by direct sunlight or temperature gradients, that does not exceed $\pm 1°C$ per hour (Clarus 600 hardware manual). If temperature variability exceeded these limits the electronic components which control the ionisation source filament current of the GC/MS could be affected. This would ultimately alter source emission and instrument sensitivity. A possible solution for future deployments of this type of instrument in

polar regions would be to include an independent temperature regulating fan heater within the mass spectrometer housing to maintain the temperature of its electronics.

Alternatively, the varying moisture content of the sampled air could have influenced ionisation efficiency within the electron ionisation source of the mass analyser. This is less likely however due to the low dew point (-26°C → -41°C) hence specific humidity of the ambient air sampled, and its pre-treatment with a Nafion dryer (section 2.1) during the analysis period.
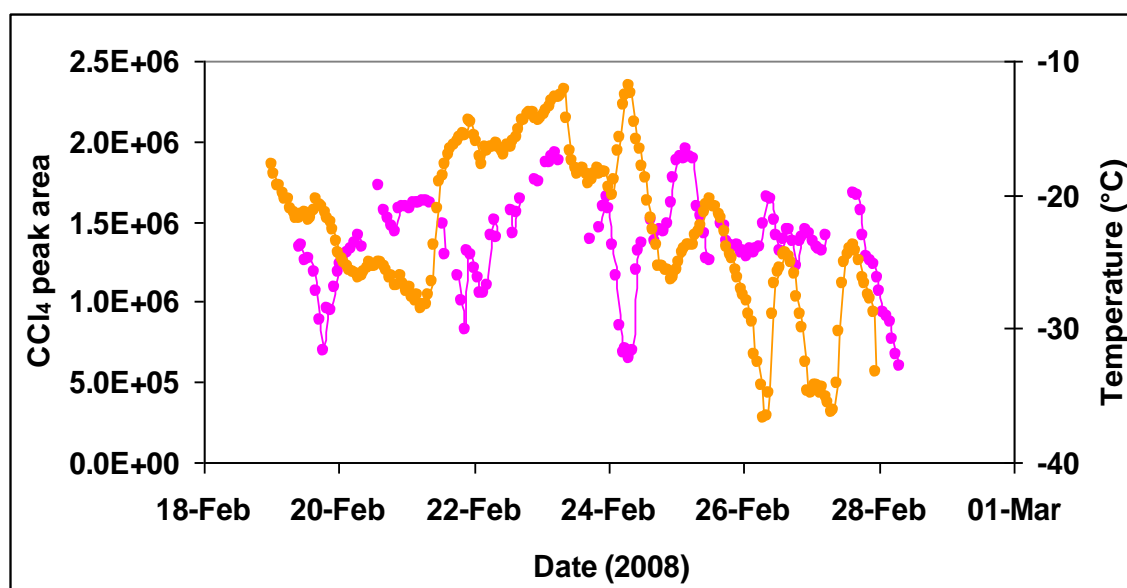
Figure. 4.5 Variation of the CCl_4 internal standard response (pink) and ambient temperature (orange) during the 16 day online air testing period at the experimental container site.

The TD-GC/MS and ATD-GC/MS were calibrated in the field against a VSLH external gas standard 200 mL (~ every two days), as described in section 2.6.1. The concentrations of VSLH gases in this standard were determined pre and post campaign by a VSLH permeation oven (Wevill and Carpenter, 2004), as discussed in section 2.6.4. The ratio of the VSLH / CCl_4 responses were then calculated and plotted over the analysis period, figure 4.6. The calculated ratios were within 20% RSD over the 10 day analysis period, indicating that the method of VSLH normalisation described in section 2.6.8 was an acceptable approach.
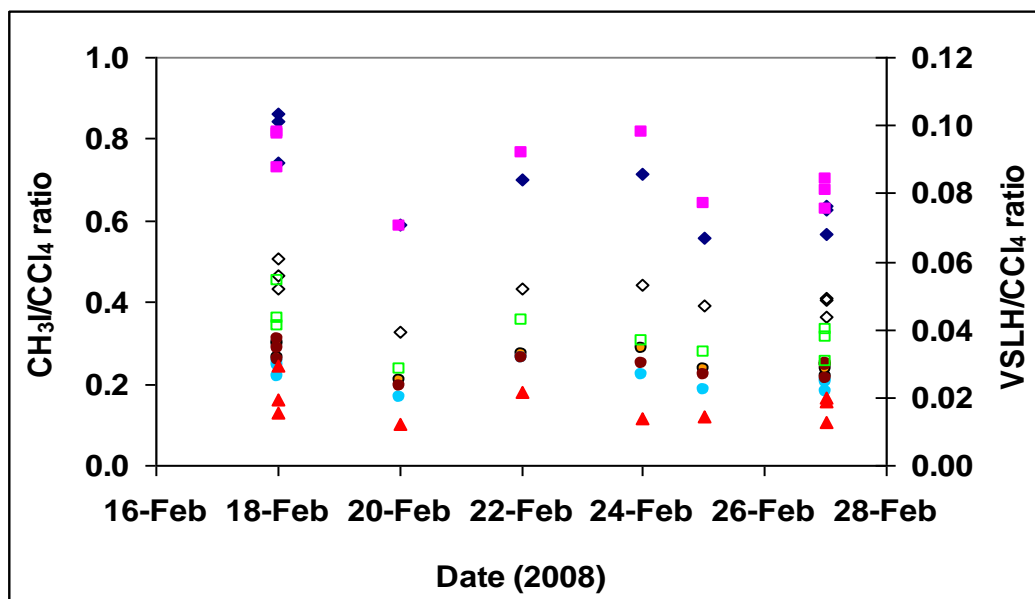
Figure. 4.6 VSLH (external gas standard)/online air CCl$_4$ ratio over analysis period. Dark blue diamonds, CH$_3$I; filled pink squares, C$_2$H$_5$I; empty black diamonds, CH$_2$Br$_2$;empty green squares, CHBr$_3$;filled light blue circles, CH$_2$ICl;filled brown circles, 2-C$_3$H$_7$I; filled orange circles, 1-C$_3$H$_7$I; filled red triangles, CH$_2$IBr.

4.2.4 Air mass classification using calculated back trajectories

Throughout the campaign, three dimensional 5 day back trajectories were calculated using the NOAA HYSPLIT model (hybrid single-particle Lagrangian integrated trajectory) model (Evans, M; School of Earth and Environment, University of Leeds). Back trajectory analyses were calculated every 6 hours during 19th – 27th February. More frequent back trajectory analyses were not attainable due to the lack of sufficient meteorological data of the Hudson Bay region during the analysis period. The arrival point for the air mass back trajectories was over the town of Kuujjuarapik at 1000 mb. From the back trajectory data, air masses were comprehensively grouped into 4 classifications dependent upon their behaviour prior to online air analysis. Type A refers to air masses which have been identified as passing directly polynyas, within the MBL. Type B refers to air masses which predominantly (>80%) pass over the sea-ice/snowpack of Hudson Bay. Type C refers to air masses which have passed over a distant polynya (~ 1000 km) located northwest of Hudson Bay. Type D refers to air masses passing over a local lead (~ 40 km) north of the experimental site. The formation of polynyas and leads were identified within the Hudson Bay region using a combination of satellite techniques (section 4.3.4).

Figure 4.7 shows typical examples of these grouped trajectory types, note trajectory types A and B are crossing identified regions of leads/open water, section 4.3.4. Despite the high sea ice coverage observed in Hudson Bay during the campaign, up to 73% of air masses analysed (during the period 19th – 27th February) transected regions of open water such as polynyas and leads, figure 4.8.
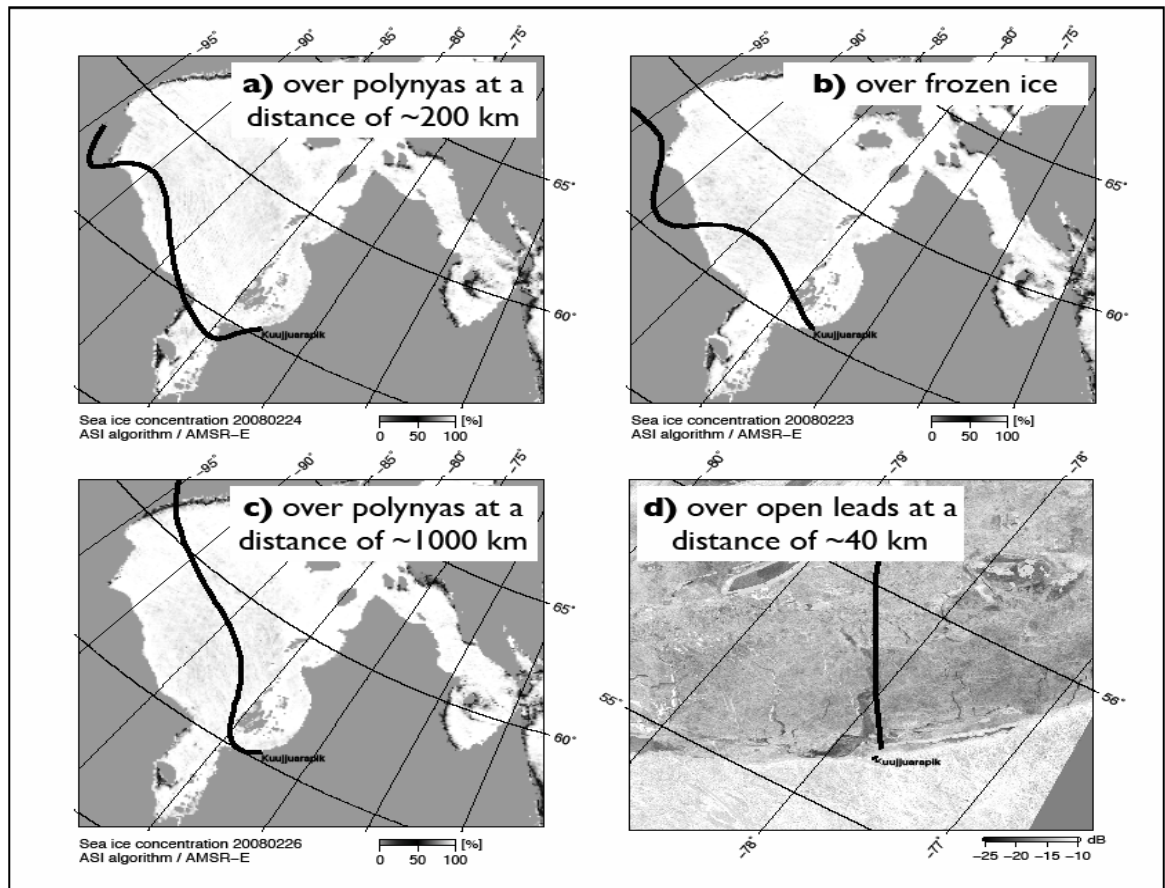
Figure 4.7 Air mass classification types from NOAA HYSPLIT model.

A = Air mass passes over polynyas with transit time of 14 – 17 hours.

B = Air mass passes over region of predominantly sea-ice/snowpack surface.

C = Air mass passes over region with polynyas with transit time <72 hours.

D = Air mass passes over local leads with a transit time of < 1 hour.

Figure adapted from Mahajan *et al.,* 2010.
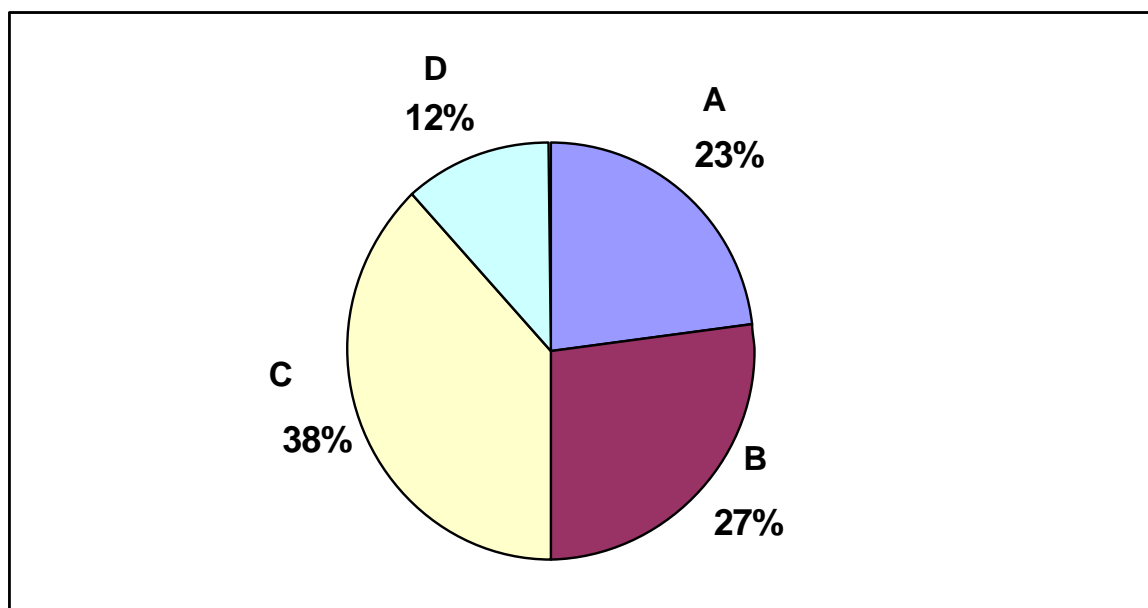
Figure 4.8 Air mass classifications sampled at the experimental container site during 19th – 27th February.

A = Air mass passes over polynyas with transit time of 14 – 17 hours.

B = Air mass passes over region of predominantly sea-ice/snowpack surface.

C = Air mass passes over region with polynyas with transit time <72 hours.

D = Air mass passes over local leads with a transit time of < 1 hour.

4.3 Results

4.3.1 Meteorological conditions during COBRA campaign

The shallow polar boundary layer (PBL) within polar regions limits the dispersion of reactive compounds produced at the surface/air interface, and meteorology plays a dominant role in the occurrence of ODE and AMDEs. From the perspective of surface chemistry, the PBL can be defined as the depth of the lower atmosphere through which surface emissions can be vertically mixed. The PBL is usually considered to be stable, particularly during winter and spring. It is capped by a temperature inversion and weak vertical mixing is experienced within this layer. Exceptions are regions with open leads or polynyas where the surface temperature is elevated close to freezing point through significant heat and vapour fluxes from the surface ocean (Lupkes *et al.,* 2007). These warmed air masses rapidly convect vertically up to altitudes of a few thousand meters causing the efficient transport of both heat and chemical species from the PBL into the free troposphere. Similarly, the passage of synoptic systems (essentially warm and cold

fronts) are associated with the destabilisation of PBL temperature inversions, allowing advection/entrainment of species between these layers. Under ODE conditions this can lead to the entrainment of O_3 and bromine transport to the free troposphere. Such phenomena could be the cause of previously observed BrO concentrations in the polar free troposphere (McElroy *et al.,* 1999).

Figures 4.9 and 4.10 show the meteorological data collected from the University of Manchester meteorological station adjacent to the experimental container site. Approximately 40% of the measured wind directions between the 19th to the 27th February were from a south-south westerly to a north-north easterly (230 – 30 ºN) direction, from incoming air masses immediately crossing Hudson Bay. Air masses of wind directions between 20 - 120° N (land mass) were not observed at the experimental site and the majority of air sampled during the analysis period was predominantly from a north westerly direction between the 19th and 27th of February (figure 4.10). The ambient air temperature observed during the analysis period was highly variable with a mean temperature of -22ºC (-12 to -38ºC). The decline in ambient air temperature observed on the 23rd (~ 8 °C) and 24th (~14 °C) correlates with the passage of cold frontal systems identified from synoptic surface pressure charts (NOAA, Appendix 4.2 to 4.4). No other synoptic events were identified within proximity to the experimental site during the analysis period.

Observed wind speeds at the experimental site seemed independent of wind direction, probably largely due to the absence of topography in the local region. A mean wind speed of 5.1 m s^{-1} (3 – 9 m s^{-1}) was observed during the analysis period. Interestingly a low wind speed period was observed between the 25th – 27th of February, with average wind speeds of 2.5 m s^{-1} (0 – 6 m s^{-1}).
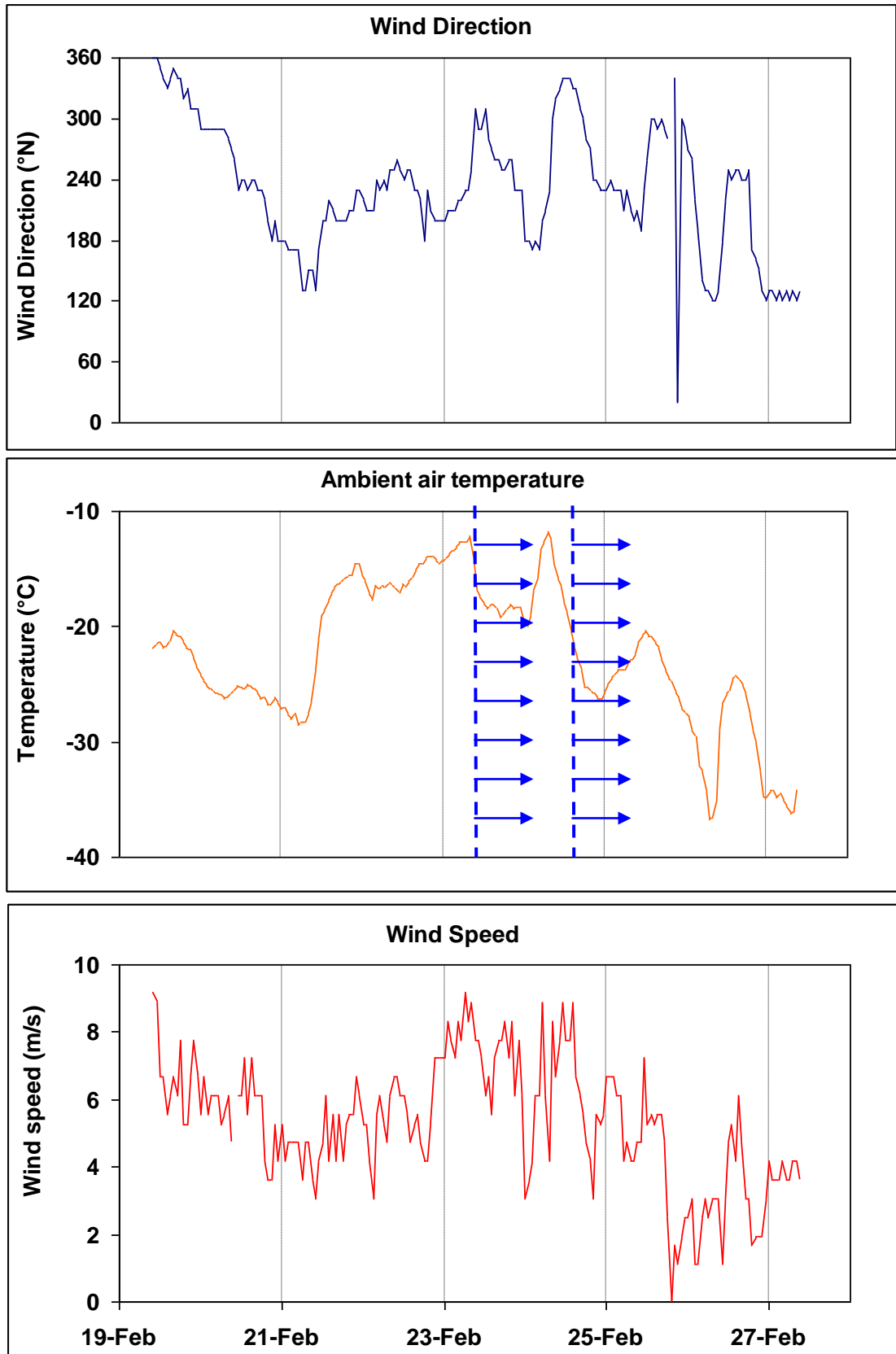
Figure 4.9 Meteorological data from MET station adjacent to experimental containers. Top, wind direction (°N); middle, ambient air temperature (°C), identifying periods cold fronts pass over experimental site; bottom, wind speed (m s^{-1}).
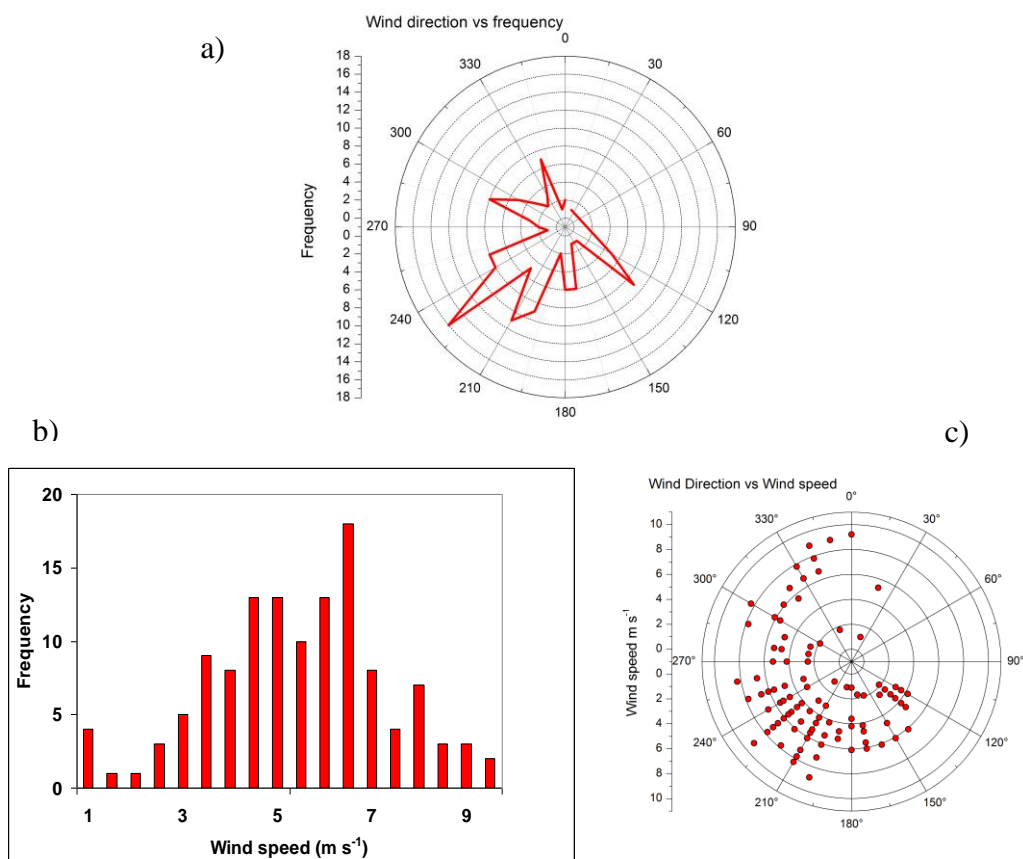
Figure 4.10 Plots of a) wind direction against frequency (1° binned), b) wind speed against frequency (0.25 m s^{-1} binned) and c) wind direction against wind speed (1° binned) during the 19th to 27th of February.

4.3.2 Ambient air determinations of poly-brominated organics

Figure 4.11 shows the time series for ambient air measurements of the poly-brominated organics bromoform ($CHBr_3$) and dibromomethane (CH_2Br_2). Maximum bromocarbon concentrations observed during the analysis period were 2.25 pptv and 0.83 pptv for $CHBr_3$ and CH_2Br_2 respectively. Calculated instrument limits of detection (LoD) during the period were 0.02 pptv ($CHBr_3$) and 0.26 pptv (CH_2Br_2). As can be seen from the time series of these compounds CH_2Br_2 and $CHBr_3$ weakly positively correlate with one another suggesting that they originate from the same or a co-located source. Linear correlation coefficients (R^2 values) between these compounds were 0.35 during the analysis period of the 19th to the 27th of February (figure 4.12).

147

Elevated mixing ratios for these compounds are present towards the beginning (19th – 20th February) and end of the analysis period (24th-27th February). To illuminate possible source regions of these brominated organics, local wind direction was used as a proxy for air mass history, figure 4.12. Mixing ratios of both CH_2Br_2 and $CHBr_3$ are generally centralised with respect to wind direction showing no correlation with wind direction. The measured mixing ratios of $CHBr_3$ were slightly elevated in the north westerly (clockwise) sector of the polar plot, which corresponds to a peak in concentrations on the 19th of February.
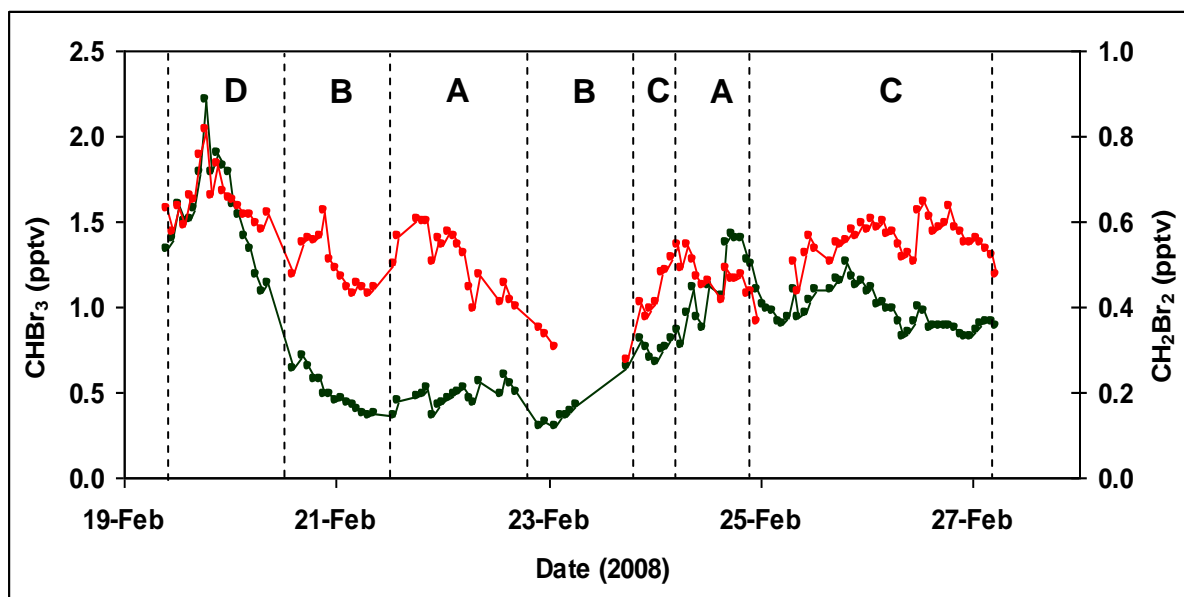
Figure 4.11 Time series for poly-brominated methanes with air mass classifications. Green, $CHBr_3$; red, CH_2Br_2.
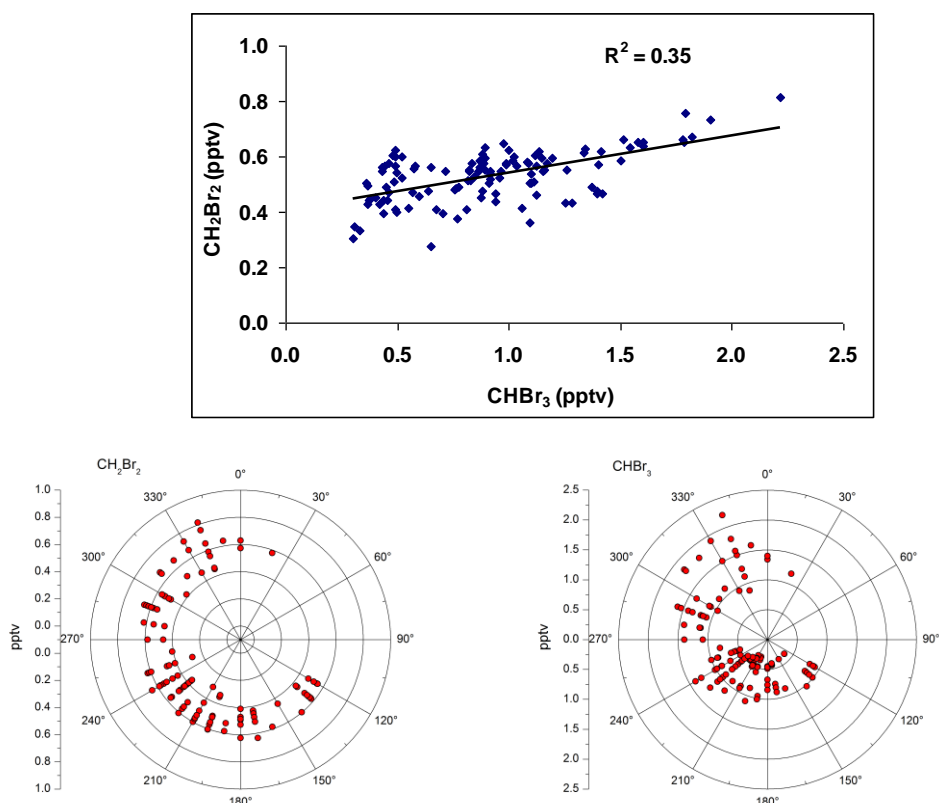
Figure 4.12 Correlation and polar plots of poly-brominated organics. Top, Correlation plot of ambient air CH_2Br_2 vs $CHBr_3$. Bottom, polar plots of poly-brominated organic ambient air concentrations against wind direction.

4.3.3 Ambient air determinations of mono-iodinated and poly-halogenated organics

Figures 4.13 and 4.14 show the time series for ambient air measurements of the mono-iodinated organics; Iodoethane (C_2H_5I), 2-Iodopropane ($2\text{-}C_3H_7I$), 1-Iodopropane ($1\text{-}C_3H_7I$) and iodomethane (CH_3I) and the polyhalogenated organics; chloroiodomethane (CH_2ICl) and bromoiodomethane (CH_2IBr) respectively, observed during the analysis period 19th – 27th of February. Maximum iodocarbon concentrations observed during the analysis period were 3.83 pptv (CH_3I), 1.50 pptv (C_2H_5I), 2.59 pptv ($2\text{-}C_3H7I$), 0.31 pptv ($1\text{-}C_3H_7I$), 0.17 pptv (CH_2ICl) and 0.08 pptv (CH_2IBr). Calculated instrument LoDs during the period were 0.15 pptv (CH_3I), 0.02 pptv (C_2H_5I), 0.03 pptv ($2\text{-}C_3H7I$), 0.02 pptv ($1\text{-}C_3H_7I$), 0.01 pptv (CH_2ICl) and 0.02 pptv. Di-iodomethane (CH_2I_2) was below the GC/MS LoD (0.05 pptv) during the entire analysis period.

As can be seen from the time series, all the mono- and poly- halogenated organics positively correlate with one another suggesting that they originate from the same or a co-located source. Linear correlation coefficients (R^2 values) between each VOIC were considerably high, ranging from 0.70 to 0.86 during the analysis period of the 19th to the 27th of February (figure 4.15).

When comparing the time series of the mono-iodinated organics (figure 4.13) and the poly-halogenated methanes (figure 4.14) to that of the poly-brominated methanes (figure 4.11) no clear correlation between the data sets seems apparent. An explanation for this could be that either the compounds originate from alternate sources or could be an effect of the longer lifetimes of the trace gases CH_2Br_2 (2 – 3) weeks and $CHBr_3$ (2 - 3 months).

Figure 4.16 shows VOIC air concentrations with respect to wind direction (ºN). The majority of the VOIC mixing ratios determined are highly centralised within the polar plots which show the range of background air concentrations during the analysis period. Elevated air concentrations for all the VOIC measured were observed in the north-westerly (clockwise) south-westerly sectors of the polar plots. VOIC air concentrations from the north-westerly sector correspond to an observed peak in concentrations on the 19th of February, whilst those in the south westerly sector both correspond to peaks in concentrations observed on the 22nd and 24th of February, figures 4.13 and 4.14. This observation could initially suggest two dominant sites of VOIC emissions within the region.
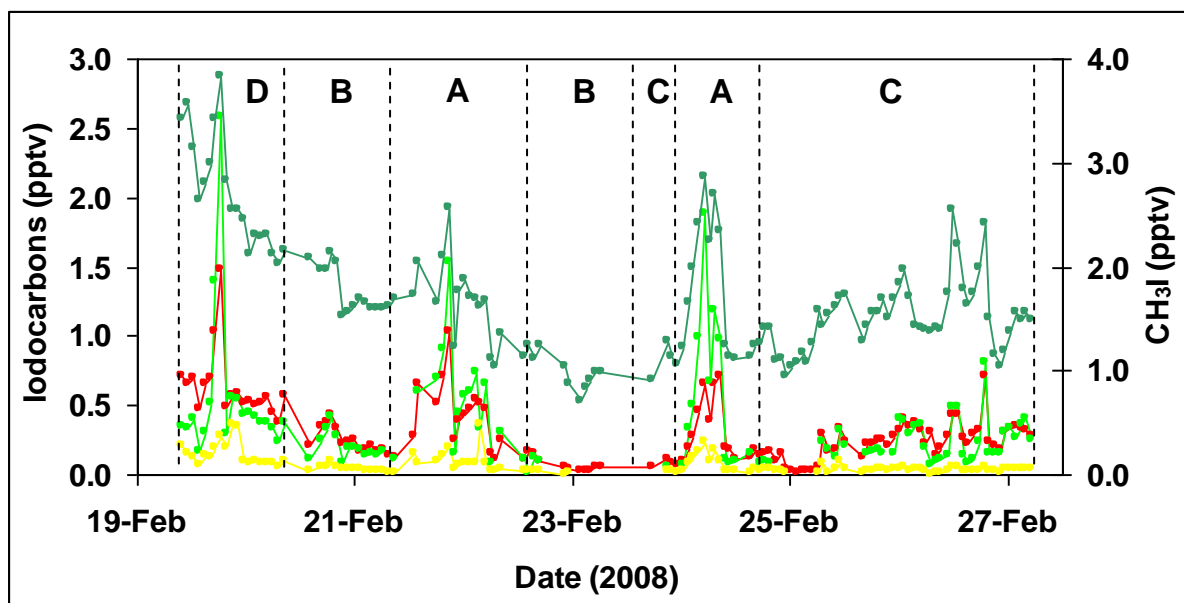
Figure 4.13. Time series for mono-iodinated organics with air mass classifications. A, air mass transects region with large leads with transit time < 24 hours; B, air mass transects region with polynyas with transit time < 72 hours; C, air mass passes over region of predominantly ($\geq$ 80%) sea-ice/snowpack surface. Dark green, CH_3I; red, C_2H_5I; light green, $2-C_3H_7I$; yellow, $1-C_3H_7I$.
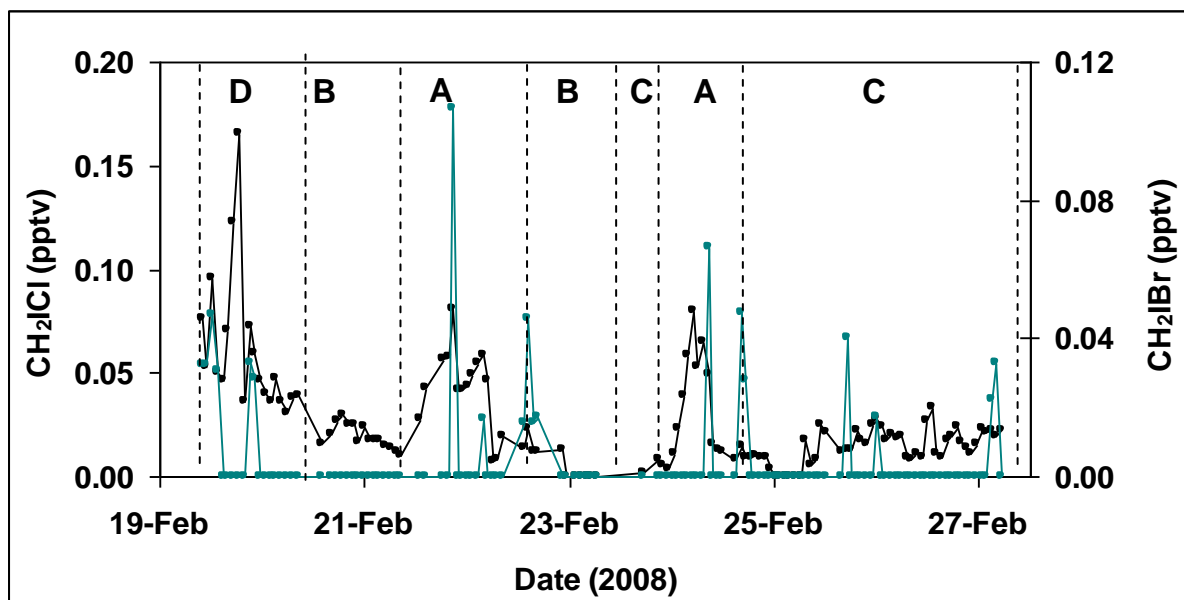
Figure 4.14. Time series for poly-halogenated organics with air mass classifications. A, air mass transects region with large leads with transit time < 24 hours; B, air mass transects region with polynyas with transit time < 72 hours; C, air mass passes over region of predominantly ($\geq$ 80%) sea-ice/snowpack surface. Black, CH_2ICl; blue, CH_2IBr.
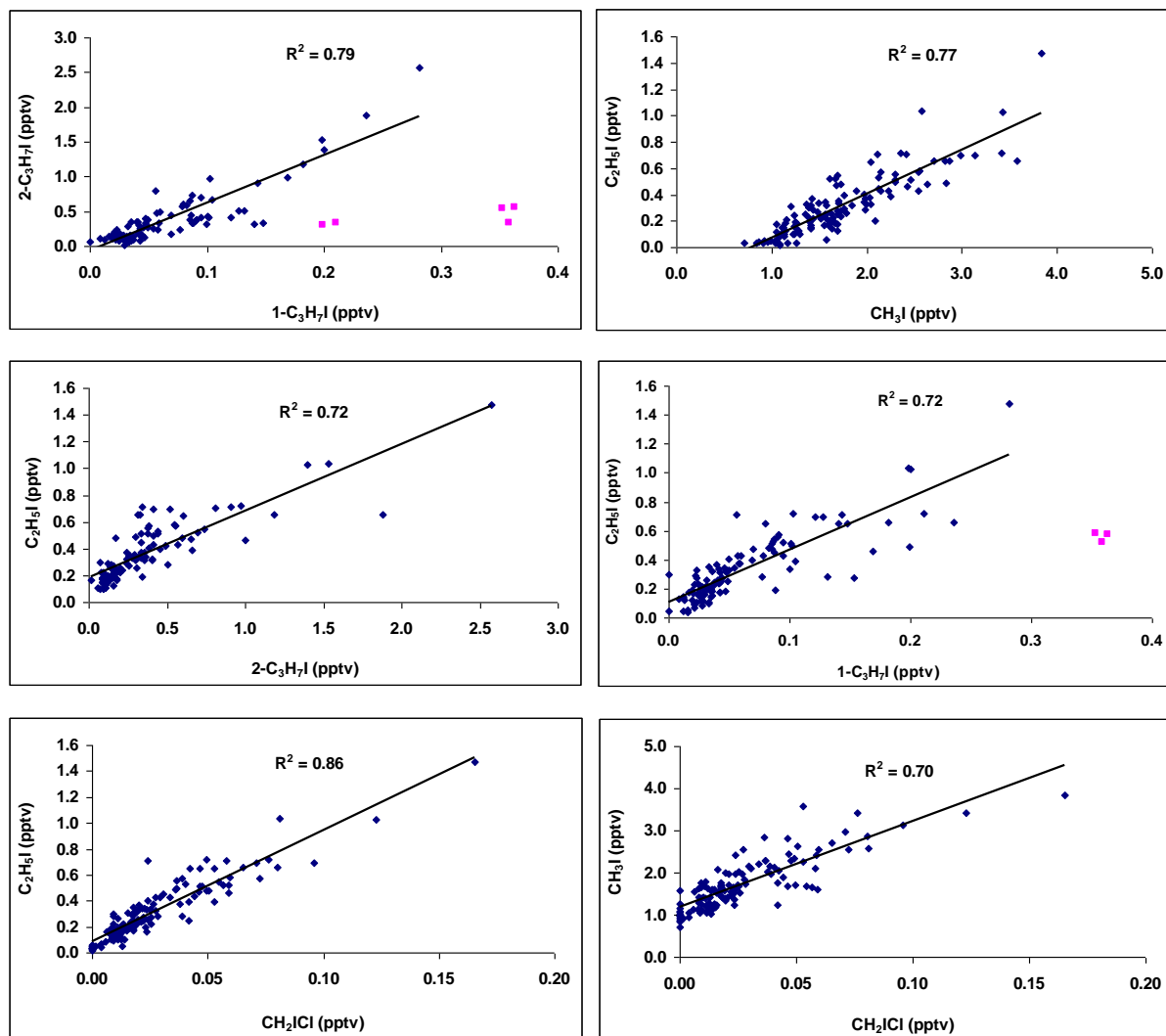
Figure 4.15 Correlation plots of ambient air VOIC concentrations during 19th to 27th of February. Pink data points are air concentrations excluded from linear regression line.
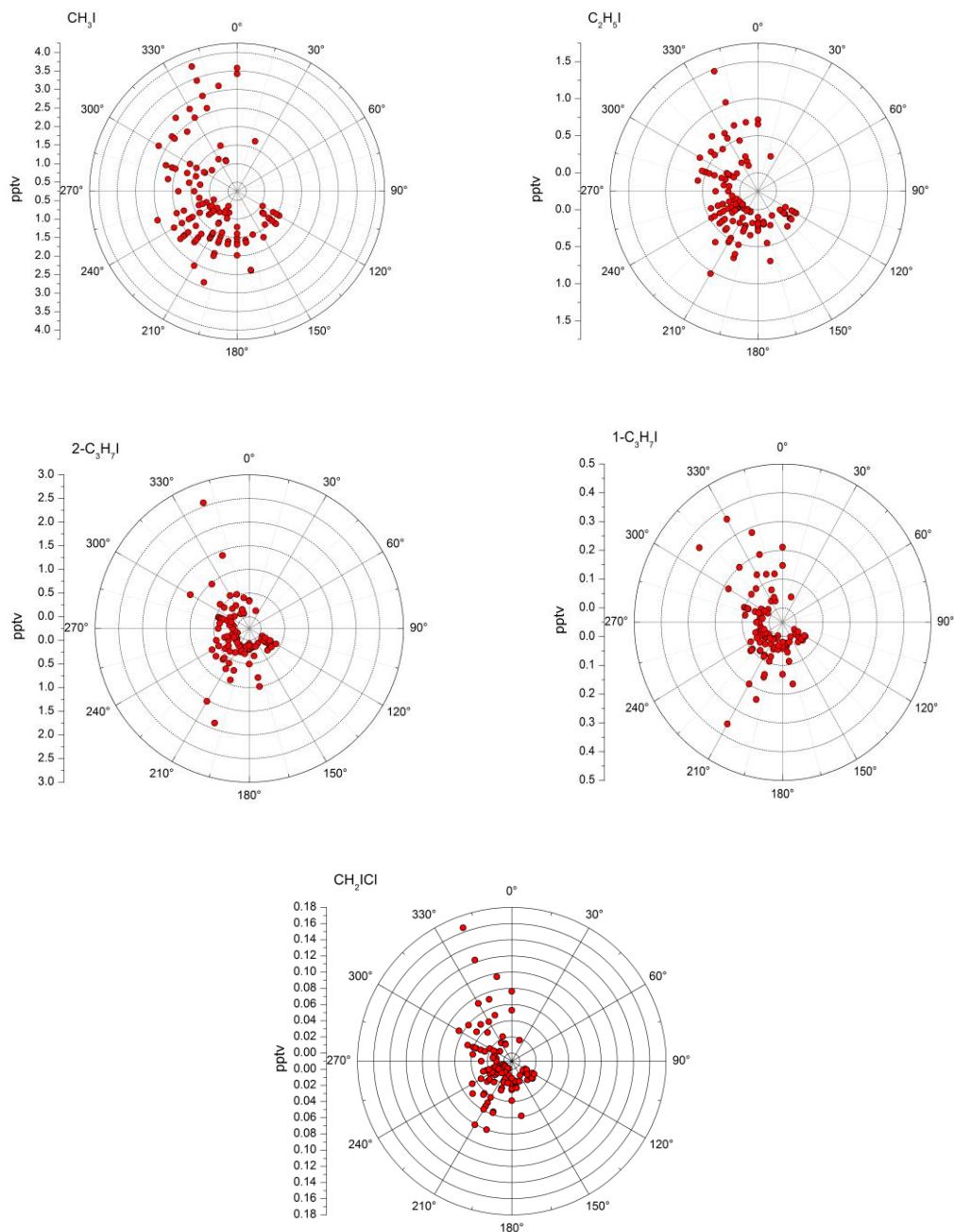
Figure 4.16 Polar plots of VOIC ambient air concentrations against wind direction (1° binned).

4.3.4 Determination of air mass histories

Although local wind direction is a useful guide for ascertaining air-mass origin it is an over simplification of the meteorological situation. An improved diagnosis of air mass history can be achieved from examining calculated back-trajectories with respect to surface type. Air mass back trajectories were calculated using the NOAA HYSPLIT model and grouped into 4 distinct classifications using a combination of surface satellite

imaging techniques (section 4.2.4). The combination of NASA's Advanced Synthetic Aperture Radar (ASAR) imaging satellite in wide swath mode (75 m resolution, 3 day temporal resolution) and the Advanced Microwave Scanning Radiometer (AMSR-E) imaging satellite (5 km resolution, 1 day temporal resolution) were used in concert during the sampling period to identify regions of sea ice, open leads and regions of open water over Hudson Bay. These were then compared with calculated 5 day back trajectories of the region to determine whether the air masses sampled transected bodies of open water during their history (section 4.2.4).

Spring is a common period for the observation of open leads due to ocean currents or wind stress on ice sheets. Leads and polynyas can occupy up to 12% of the Arctic sea ice area (Eicken, 2008). Whilst the formation of polynyas in Hudson Bay occurred on several occasions during the analysis period, the formation of open leads only occurred once during the analysis period in the region immediately north of the experimental site. As can be interpreted from figure 4.17, a region of large open leads develops ~ 40 km north from the experimental site (Mahajan *et al.,* 2010) over a 3 day period on the 19th of February and completely dissipates within another 3 days. Similarly, a 15 - 20 km wide polynya can be observed to develop 200 – 250 km directly to the west of Kuujjuarapik. Figure 4.19 is an AMSR-E image from the 24th of February which shows the formation of a large polynya on the north west of Hudson Bay. This region of open water is first observed on the 22nd of February and does not dissipate until the 27th of February, figures 4.18 and 4.19. Calculated back trajectories during this period transect this polynya continuously from midday of the 24th onwards which would suggest this as a possible source of the elevated poly-brominated methanes during this period (figure 4.11). As the inferred transit time between the polynya and the experimental site is ~ 72 hours, elevated VOIC air concentrations were not observed during this period (figures 4.13 and 4.14).

The presence of these leads (figure 4.17) and polynya (figure 4.18 and 4.19) coincides temporally with the peaks in mono-iodinated and poly-halogenated organic air concentrations observed on the 19th, 22nd and 24th of February (figures 4.13 and 4.14). On comparison of calculated back trajectories for the time period within the location of these large leads and polynya, it is evident that the trajectories directly transect these

open water regions (figures 4.20 and 4.21). Air mass transit times of ~ 1 hour and 14 – 17 hours were inferred from the calculated 5 day back trajectories for elevated VOIC air concentrations observed on the 19th and 22nd – 24th of February, respectively.

16th February

19th February

22nd February
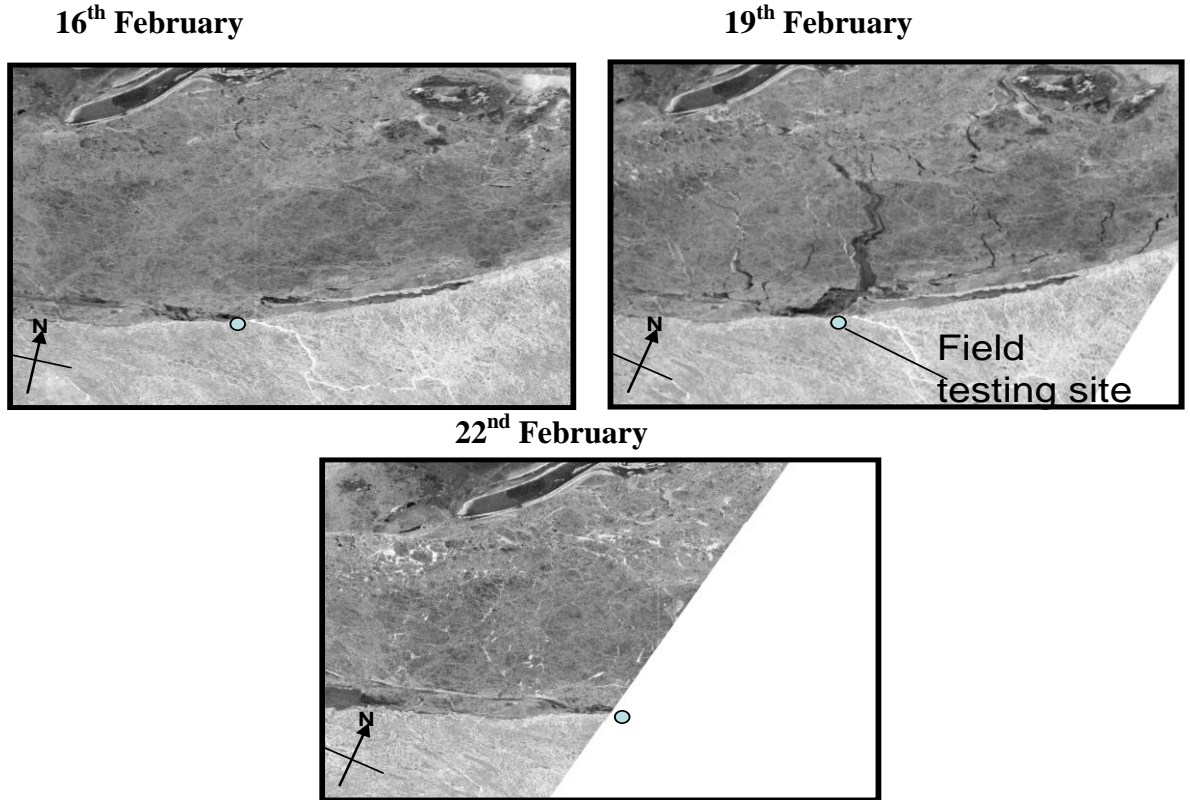
Figures 4.17 ASAR images depicting the formation of large leads directly north of the experimental site on the 19th of February.
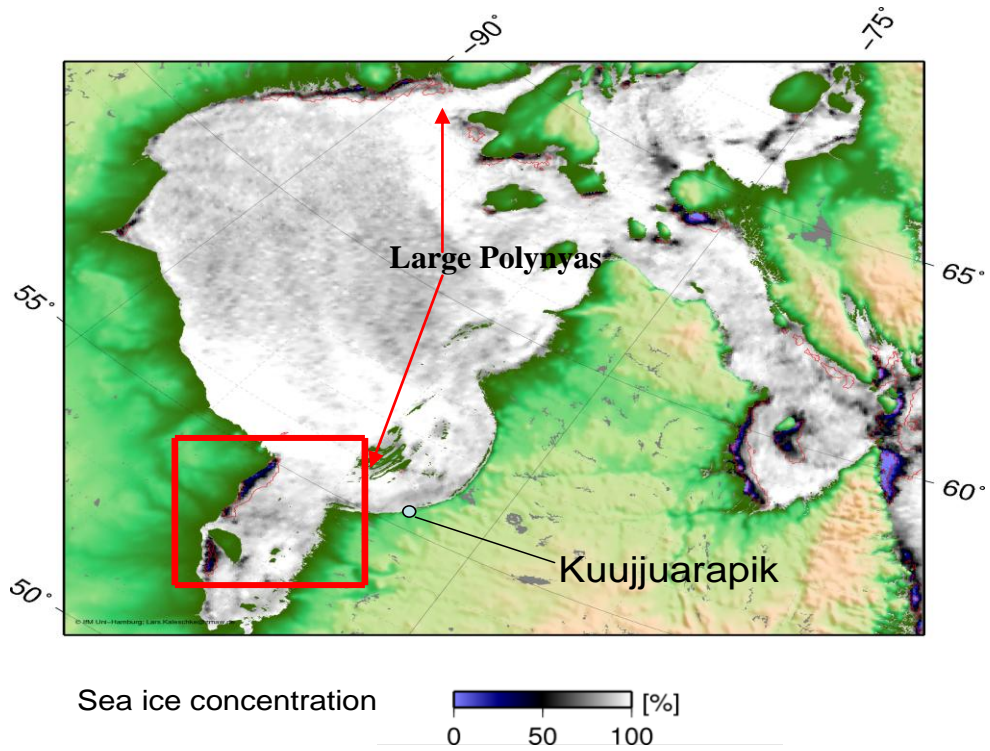
Figure 4.18. AMSR-E image of Hudson Bay region between the 24th and the 25th of February. The highlighted geographic region above is shown in greater detail in figure 4.19.
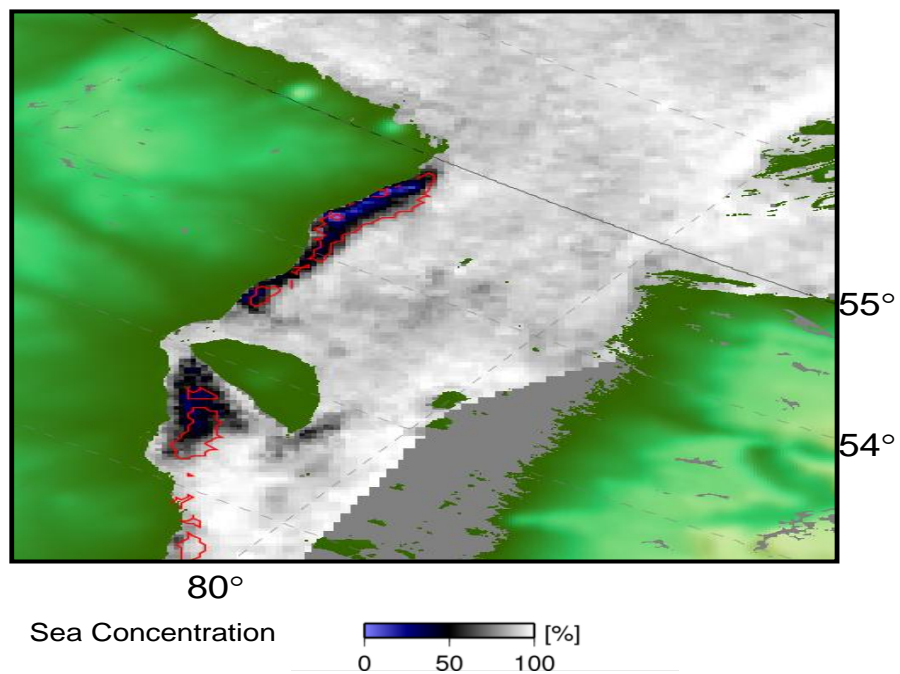
Figure 4.19 AMSR-E enhanced image of back trajectory region in Hudson Bay between the 24th to the 25th of February.
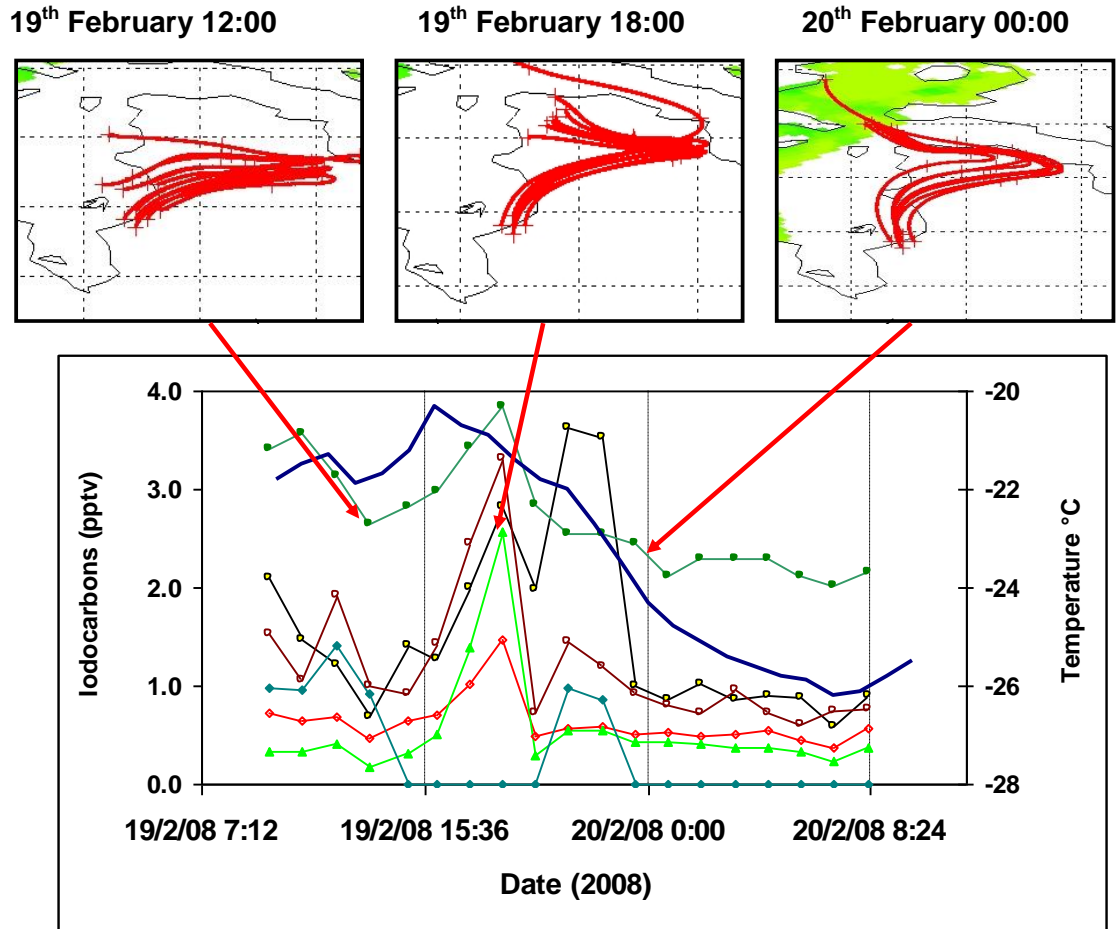
Figure 4.20 NOAA HYSPLIT back trajectories for 19th February and how they correlate to VOIC concentrations and temperature (°C) over the 24 hour period. [C_2H_5I], red; [$2-C_3H_7I$], light green; [CH_3I], dark green; [$1-C_3H_7I$] x 10, black; [CH_2ICl] x 20, brown; [CH_2IBr] x 30, light blue; temperature, dark blue.
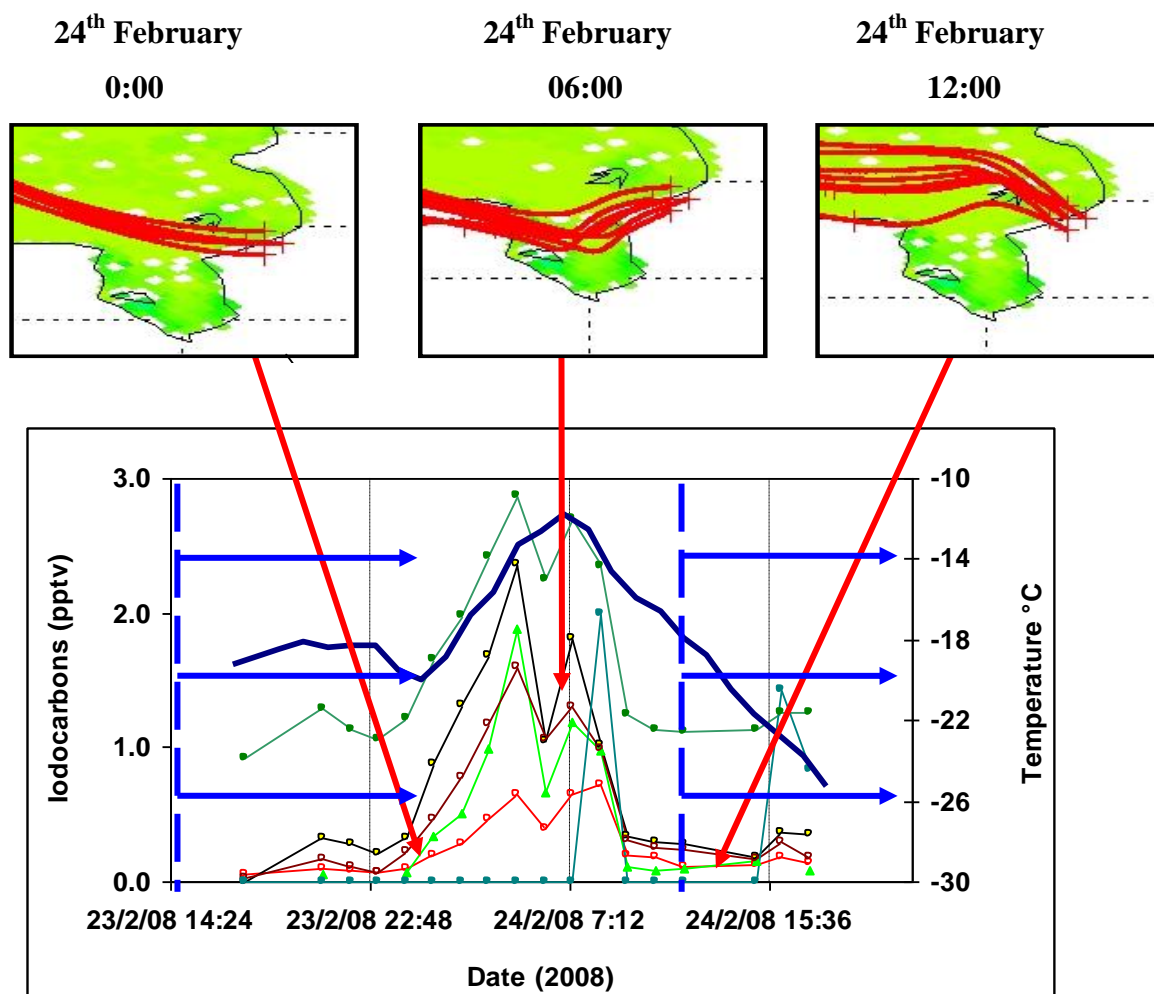
Figure 4.21 NOAA HYSPLIT calculated back trajectories for 24th February and how they correlate to VOIC concentrations and temperature (°C) over the 24 hour period. [C_2H_5I], red; [2-C_3H_7I], light green; [CH_3I], dark green; [1-C_3H_7I] x 10, black; [CH_2ICl] x 20, brown; [CH_2IBr] x 30, light blue; temperature, dark blue. Blue dashed lines represent periods when cold frontal systems were observed to pass over experimental site (Appendix 4.2 to 4.4)

4.3.5 Statistical analysis

A statistical analysis was carried out on the VOIC time series to evaluate whether significantly higher concentrations were observed in air masses transecting regions of open water. Statistical testing using the two tailed Mann-Whitney U test was carried out on two datasets created by binning the measured VOIC concentrations during air mass classifications A and D ([VOIC]$_{water}$) and B and C ([VOIC]$_{seaice}$).

The Mann-Whitney U test is a non-parametric test that can be used to test the null hypothesis (H_0) that two samples originate from the same population or, alternatively that the observations in one sample are statistically significantly different than observations in the other (termed the alternative hypothesis, H_1). The Mann-Whitney U test was chosen to test the H_0 VOIC concentrations were not statistically significantly different during air mass classifications A and D compared to B and C. This H_0 essentially describes a situation in which elevated VOIC concentrations in air masses transecting open water regions (within transit times of < 24 hours) was due to chance. Statistical analysis was carried out on CH_3I, C_2H_5I, $2\text{-}C_3H_7I$, $1\text{-}C_3H_7I$ and CH_2ICl using EQ 4.5 and 4.6, where T is the sum of the group mixing ratios and N is the sample size of groups A ($[VOIC]_{water}$; $N = 9$) and B ($[VOIC]_{seawater}$; $N = 17$) respectively. The U parameters for groups A and B were then compared to critical values for Mann-Whitney U to assess at what confidence limit, if any, H_0 could be rejected.

$$U_A = N_A N_B + \frac{N_A(N_A +1)}{2} - T_A \qquad \text{(EQ 4.5)}$$

$$U_B = N_A N_B + \frac{N_B(N_B +1)}{2} - T_B \qquad \text{(EQ 4.6)}$$

As shown in table 4.2, the H_0 was rejected for C_2H_5I, $2\text{-}C_3H_7I$ and $1\text{-}C_3H_7I$ at a confidence limit of $\geq 95\ \%$. This statistically proves the alternative hypothesis that these VOICs were observed at higher mixing ratios during periods of air masses transecting open water (within transit times of < 24 hours), suggesting that leads and polynyas were the dominant regional sources for these compounds during the analysis period.

CH_3I and CH_2ICl were not statistically different between $[VOIC]_{water}$ and $[VOIC]_{seaice}$ at $\geq 90\%$ confidence limit. For CH_3I, this is probably due to the relatively high background mixing ratios of CH_3I observed during the campaign (1.56 ± 0.44 pptv) leading to a % difference in mean $[VOIC]_{water}$ and $[VOIC]_{seaice}$ of only 20%, table 4.2. For CH_2ICl, this is most likely influenced by the very short atmospheric lifetime of this compound.

VOIC	Lifetime (days-noon)	Mean [VOIC]$_{water}$ (pptv)	Mean [VOIC]$_{seaice}$ (pptv)	Difference (%)	Statistical confidence (%)
CH$_3$I	6	1.96 ± 0.92	1.56 ± 0.44	20.3	< 90
C$_2$H$_5$I	3.5	0.46 ± 0.42	0.23 ± 0.13	50.5	≥ 95
2-C$_3$H$_7$I	1.2	0.74 ± 0.79	0.26 ± 0.17	64.4	≥ 95
1-C$_3$H$_7$I	0.5	0.09 ± 0.08	0.04 ± 0.03	51.5	≥ 95
CH$_2$ICl	0.14	0.05 ± 0.04	0.02 ± 0.01	66.3	< 90

Table 4.2 Mean [VOIC] air on transecting regions of open water or predominantly sea ice and the degree of confidence at which their statistically different.

4.3.6 Influence of leads/polynyas in sea ice on atmospheric surface temperature

Leads and polynyas can occupy up to 12% of the Arctic sea ice area (Gloersen and Campbell, 1991), providing a significant source region for sea salt aerosols, water vapour and latent heat to the PBL. Water vapour emitted from leads exerts a major control on radiative effects through cloud formation as well as inducing significant growth of aerosol particles, altering their composition and gas phase partitioning effects (Piot and von Glasow, 2007). Previous model estimations suggested sensible and latent heat fluxes from open leads in polar regions of 300 Wm^{-2} and 45 Wm^{-2}, respectively (Piot and von Glasow, 2007). The contribution of leads and polynyas is greatest during clear skies during cold regimes, when the surface temperature difference between open leads and snow covered sea ice can be up to 40 K, causing a strong temperature gradient to exist which induces strong vertical convection in the boundary layer. Due to increased evaporation, the specific humidity above such an open lead is predicted to be an order of magnitude higher than over snow covered sea ice, 2.5×10^{-3} kg H$_2$O kg^{-1} air compared to 2.2×10^{-4} kg H$_2$O kg^{-1}air (Piot and Glasow, 2007).

During each period of elevated VOIC mixing ratios observed during the COBRA campaign, an observable increase in ambient air temperature of between ~ 1 – 8 ºC was observed. This correlates with peaks in VOIC responses on the 19th (figure 4.18), 22nd (Appendix 4.1) and the 24th (figure 4.19) of February. A possible explanation for this is that an increase in temperature (i.e. through the passage of a synoptic system such as a warm front) is directly influencing the positive flux of VOICs from these leads/polynyas or surrounding snowpack through increased volatilisation. On the

analysis of synoptic surface pressure charts of the region (NOAA), only two frontal systems were observed passing over Hudson Bay (23rd and 24th of February) during the analysis period. Interestingly the peak in ambient air temperature observed on the 24th of February (figures 4.9 and 4.21) correlates with the passage of these two bracketing cold frontal systems through the experimental site (Appendix 4.2 to 4.4). An alternative hypothesis is that heat is convected from these leads/open water regions during the flux of VOICs. If the latter is true, then potentially temperature could be used as a tracer for trace gas emissions from or around leads and polynyas.

The maximum effect of open leads within sea ice on atmospheric temperature has previously been investigated using a 1D atmospheric model coupled to a snow/sea-ice model (Lűpkes *et al*., 2008). With this model approach, it was clearly demonstrated that air (10 metres) and surface temperatures are strongly dependent upon sea ice coverage, and wind speed. The results demonstrate that as Arctic sea ice coverage decreases from 100% to 95% (i.e. during the formation of polynyas) mean air temperature (10 metres) adjacent to the sea ice opening increases by 5 K during a 12 hour period and ~ 14 K during a 2 day period. This model observation would initially support the conclusion that the increases in air [VOIC] and temperature are caused by emissions from leads and polynyas. However, it is not known how much of an effect air mass transit time would have on air temperature, particularly in those air masses which transected the polynya 200 – 250 km away from the experimental site (14 – 17 hours).

4.3.7 Oceanography of leads and polynas in sea ice

Leads and polynyas in pack ice have long been considered important to the thermodynamics of polar regions (Badgley, 1966). The amount of ice formation in leads and polynyas is of the same order of magnitude as that formed under perennial sea ice and, due to brine rejection, accounts for a major fraction of the salt input to the Arctic mixed layer (Eicken, 2008). This affects the surrounding ocean because it is a strong density source to the mixed layer water column. As dense brine is rejected during the refreezing of leads and polynyas, dense water sinks under the lead. This forms a cellular convection pattern within the mixed layer depth with less saline seawater flowing in from directly under the surface of sea ice and the dense water flowing away from the lead (figure 4.22). This cellular convection pattern in the mixed layer is characterised by velocity perturbations (velocity jets) immediately below the sea ice (0 – 0.5 metres) and

at the base of the mixed layer (1 - 5 cm s^{-1}). However, this can only occur during low geostrophic under ice currents (less than ~ 5 cm s^{-1}; Morrison *et al.,* 1992). During high geostrophic currents the mixed layer is fully turbulent and this cellular convection may not occur, rather the rejected brine is simply mixed into surface water column. This phenomena is not only important when considering latent heat fluxes from leads/polynyas but could also potentially influence trace gas emissions to the MBL.
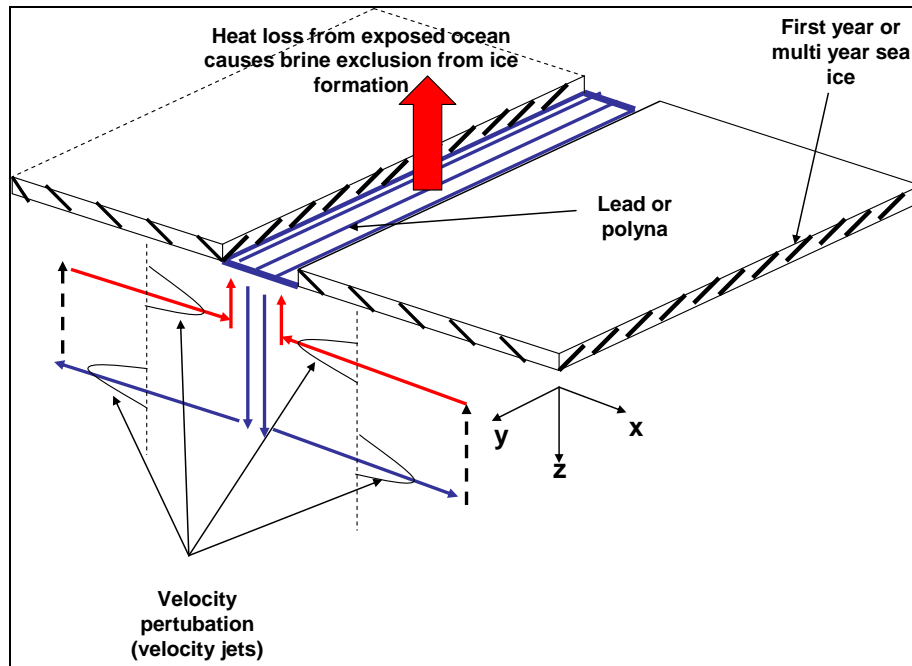
Figure 4.22 Illustration of the cellular convection circulation induced by a winter lead in the absence of rapid ice motion. Figure adapted from Morison *et al.* 1992.

Diatoms inhabit both the microstructure and the underside of sea ice in Arctic regions (Garrison and Buck, 1989). The production of brominated and iodinated organics by these organisms is well established (Sturges *et al.,* 1992; Tocarzyk and Moore, 1994), via enzymes active in the oxidative metabolism of the cell (Moore *et al.,* 1996). Subsequent volatilisation of these halogenated compounds can occur if the surface layer of the ocean becomes supersaturated. It is therefore feasible to conceive that the observed peaks in VOIC air concentrations are produced by such diatoms present in the underlying skeletal layer of the ice, which are then transported to the open water of the lead due to a combination of thermal gradients between the sea-surface layer and the overlying air.

The cellular convection circulations described cause velocity perturbations below sea ice which converge at the surface of the lead/ polynya. During low geostrophic currents (< 5 m/s), this phenomena has the potential to entrain trace gases produced by microalgal colonies on the underside of the sea ice toward the open lead, rapidly replenishing those lost to the MBL through sea-air exchange. Although the horizontal distribution of these cellular convection circulation cells beneath the sea ice is not known (Morrison *et al.,* 1992), this phenomena clearly has the potential to enhance trace gas emissions from leads and polynyas in sea ice and remains an area for further work. Conversely high geostrophic currents (> 5 m s) towards leads/polynyas can directly replenish aqueous trace gas concentrations directly under the sea ice opening. In both extremes, the presence of under ice lateral flows have the potential to enhance heat and mass sea-air exchange from within the water column depending on the size of the sea ice opening. Loose *et al.* (2009) previously experimentally investigated the relationship of the gas exchange rate (*k*) with sea ice fractional coverage (*f*) using the conservative dissolved tracers O_2 and SF_6. Originally *k* was expected to increase proportionally to *f* (1:1). However, the authors observed in each experiment that the determinations for *k* were consistently clustered above this 1:1 relationship suggesting under ice lateral flows were enhancing the emission of dissolved trace gases, particularly at high *f*.

4.3.8 Observed effects of brominated organics on surface ozone

Figure 4.23 shows ozone plotted against bromoform mixing ratios during the analysis period (19th – 27th of February). Ozone mixing ratios were relatively stable (~ 37 ppbv) between the 19th and 24th of February. On the 24th of February at 18:30, a small ODE was observed in which ozone mixing ratios dropped to ~ 20 ppbv from background levels over ~ 9 hours. Similarly, an extensive ODE was observed between the 25th and 26th of February in which ozone mixing ratios dropped to near zero (1.9 ppbv) over ~ 24 hours.

Based on 5 day air mass back trajectory calculations and satellite observations, sections 4.2.4 and 4.3.4, sampled air masses were observed to transect a region of open water on the north west of Hudson Bay (~ 1000 km away) from midday of the 24th of February to the end of the analysis period. This correlates well with enhanced $CHBr_3$ and CH_2Br_2

mixing ratios during this period. As the calculated transit time of air masses between the polynya and the experimental site was $\sim$ 72 hours, this would imply that O_3 depletion may also have occurred in transit during the same time period.

Bromoform mixing ratios are anti-correlated to ozone concentration throughout the period, particularly during the ODE's (figure 4.24). This phenomena was first observed during the Polar Sunrise Experiment 1988 (PSE88, Barrie *et al.* 1988) at Alert, Canada and has been observed on several field campaigns since. Initially this data would suggest that the production and photolysis of bromoform is directly depleting ozone. However, bromoform photochemistry as a cause for tropospheric ozone depletion has previously been ruled out (Moortgat *et al*., 1993; Simpson *et al.,* 2002), due to the compound's low mixing ratios and long photolytic lifetime under Arctic springtime conditions. This could however suggest a link between organic and inorganic bromine production within the region.

Direct Br_2 emission and wind derived aerosol from the surface seawater of the polynya and adjacent frost flower fields/saline sea ice surfaces could have contributed to ozone depletion within the sample air mass during this 72 hour period. Sea ice in proximity to regions of open water usually have enhanced salinity due to surface flooding, facilitating the formation of frost flowers (Simpson *et al.,* 2005). Wind derived aerosol produced from frost flowers contain high concentrations of aqueous bromide (Barrie *et al.,* 1988) and high acidity (Sander *et al.*, 2006), and are currently believed to be the predominant surface on which halogen activation occurs. This enhancement in aqueous bromide concentration and acidity could occur by the scavenging of HBr, the termination product of the bromine explosion, by these particles. Theoretically, this particulate bromine could then be recycled to gaseous bromine during transit to the experimental site.

Additional organic and inorganic halogens produced and emitted from the surface sea ice during transit may also have contributed to the observed ODEs. Surface wind speeds (Manchester met station) were observed to drop from background velocities of $\sim$ 6 m s^{-1} to 2 and 0.2 m s^{-1} during ODEs observed on the 24th and 25th of February, respectively (figure 4.25). Reduced wind speed periods induce a stable PBL situation, confining

trace gases in the boundary layer, and potentially increase sea ice – air contact times. Such phenomena could have caused greater amounts of gaseous HOBr uptake (EQ 4.22) into the QLL of sea ice surfaces during transit causing catalytic gaseous Br_2 emission into the sampled air mass before reaching the experimental site (Barrie *et al*., 1988). However, as comprehensive Br_2 and BrO measurements were not conducted during the analysis period this hypothesis cannot be confirmed.
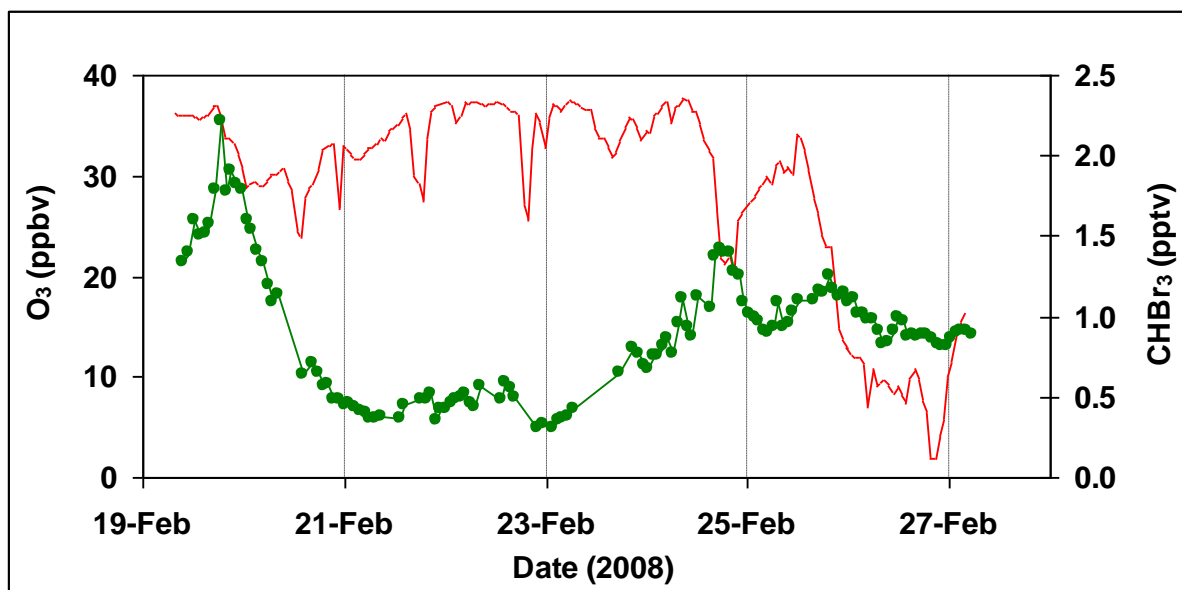
Figure 4.23 Time series of bromoform and ozone mixing ratios during the 19th – 27th of February. Red, ozone mixing ratios (ppbv); green, bromoform mixing ratios (pptv).
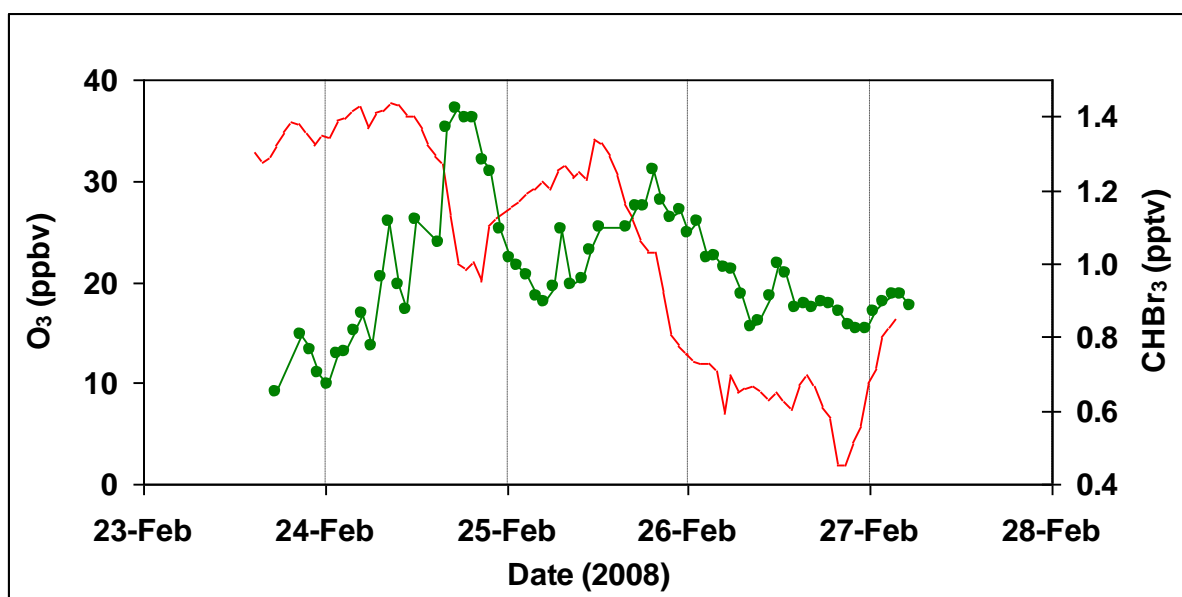
Figure 4.24. Time series of bromoform and ozone mixing ratios during the 23rd – 27th of February. Red, ozone mixing ratios (ppbv); green, bromoform mixing ratios (pptv).
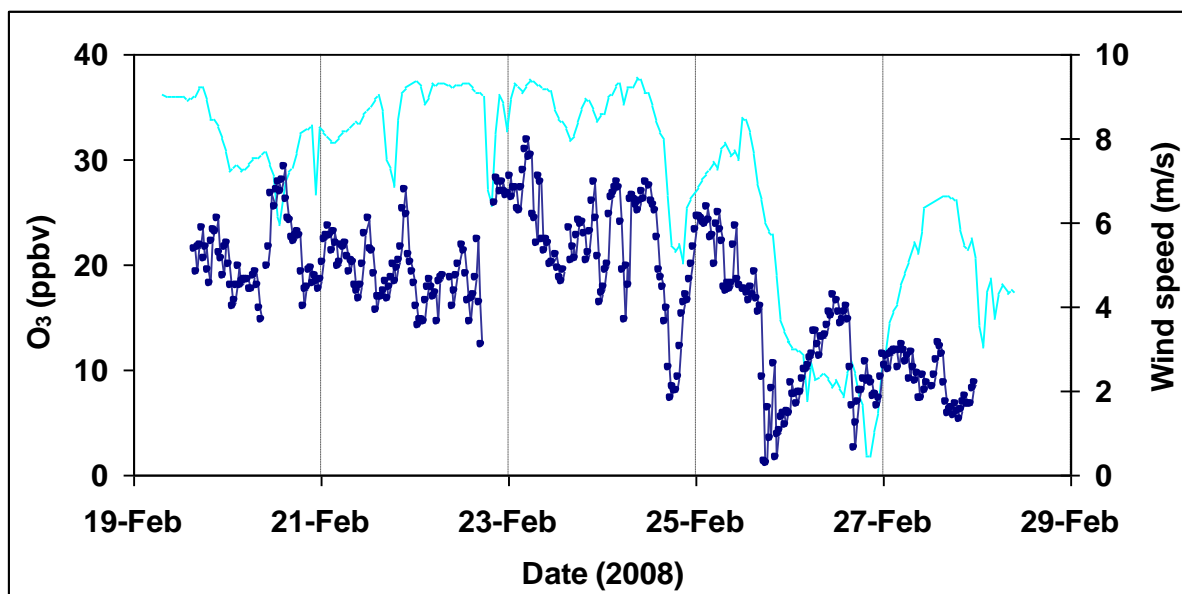
Figure 4.25 Ozone mixing ratios over analysis period against wind speed. Light blue, ozone mixing ratios (ppbv); dark blue, wind speed (m s^{-1}).

4.3.9 Observed effects of VOICs on MBL composition

Measurements of IO were conducted for 11 days using the long path differential optical absorption spectroscopy (LP-DOAS) operated by the School of Earth and Environment (University of Leeds). Further information on IO measurements made during the campaign are discussed in Mahajan *et al.* (2010). Figure 4.26a shows ozone mixing ratios observed during the analysis period and Figure 4.26b shows IO observations above the LoD of the LP-DOAS instrument ($\sim 1 - 1.5$ pptv; Mahajan *et al.* 2010). The maximum IO mixing ratio observed during the campaign was 3.4 ± 1.2 pptv. Neither IO nor VOICs (figure 4.26c) were observed ubiquitously during the campaign, in fact IO was never observed above the LoD during the night. Both IO and VOIC concentrations measured during this study depend strongly on the history of the air mass, indicating that the emissions from polynyas are their primary source as neither were detected in air masses passing over ice or land. The highest IO concentrations $3.1 - 3.4$ pptv were observed in air masses passing over a polynya 200 - 250 km away (figures 4.16 and 4.17). An interesting observation is that in the air mass transecting the lead on the 19th of February (figures 4.15 and 4.18), elevated concentrations of VOIC were observed during the daytime whereas IO was not observed above the detection limit.
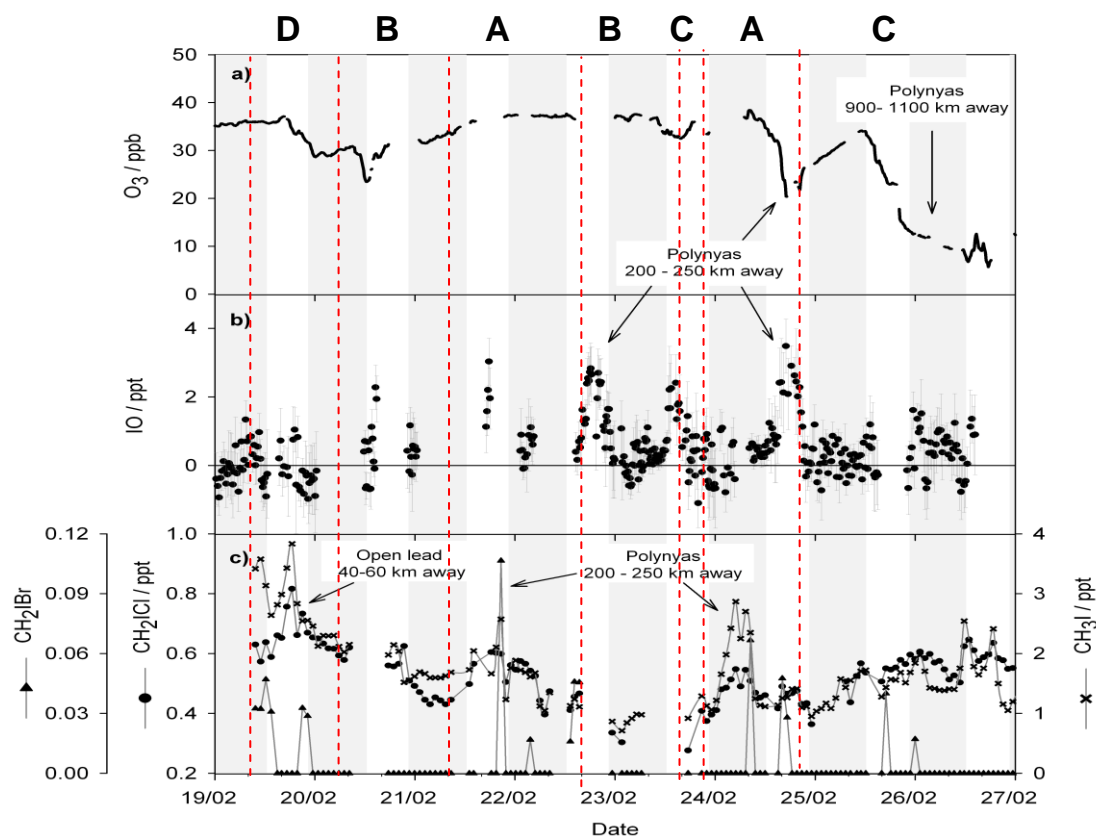
Figure 4.26 Time series of ambient air O_3, IO and VOIC mixing ratios and air classifications. a) O_3 mixing ratios (ppb); b) IO mixing ratios (pptv); c) VOIC mixing ratios (pptv). CH_2IBr, triangles; CH_2ICl, circles; CH_3I, squares. Vertical white and black regions show day and night periods. Figure adapted from Mahajan *et al.* (2010).

Mahajan *et al.* (2010) used a one-dimensional Tropospheric Halogen Chemistry Model (THAMO, Saiz Lopez *et al.,* 2008) to study the impact of VOIC concentrations on the formation of IO and their impact on the oxidising capacity of the PBL with respect to O_3 during the COBRA campaign. Direct VOIC fluxes were not determined from leads/polynyas during the campaign, hence the model initialisation flux was tuned to reproduce the VOIC air concentrations observed at the experimental site. Fluxes of 1.4 nmol m^{-2} d^{-1} (CH_2I_2), 2870.1 nmol m^{-2} d^{-1} (CH_2IBr), 71.7 nmol molecule m^{-2} d^{-1} (CH_2ICl), and 286.9 nmol m^{-2} d^{-1}(CH_3I) were required to reproduce both daytime and night time levels observed on the 24th of February. Fluxes of C_2H_5I, 2-C_3H_7I and 1-C_3H_7I were not taken into account due to their relatively low mixing ratios observed during the campaign. The use of THAMO helped explain several interesting observations within the dataset, figure 4.26.

During the 19th of February, enhanced VOIC mixing ratios were observed during the daytime, but IO was not observed above the LP-DOAS LoD. Airmass back trajectories during this period suggest a small region of leads (figure 4.17) 1 – 4 km wide $\sim$ 40 km north of the experiment site that may be influencing air mass composition. Such leads are likely to contribute lower VOIC concentrations from lead venting due to low sea-air contact times. This observation is correlated with the THAMO runs which predict only a 10 min sea-air contact time is necessary to produce the observed VOIC concentrations at the tuned flux rates. Interesting THAMO only predicts IO mixing ratios of $\sim$ 1 pptv arriving at the experimental site on the 19th of February, below the established LoD of the LP-DOAS, in good agreement with the observed data.

During the 24th of February back trajectory analysis predicts a $\sim$ 14 hour transit time between the polynya and the experimental site and a $\sim$ 1 hour sea-air contact time over the 15 $-$ 20 km width of the opening. Following an initial 1 hour VOIC pulse and a 14 hour transit time, the THAMO model predicts 0.06 pptv and 0.08 pptv of CH$_2$IBr and CH$_2$ICl, in agreement with the night time concentrations of 0.06 pptv CH$_2$IBr and 0.08 pptv CH$_2$ICl observed at the experimental site at 0300 hours on the 24th of February. Additionally, CH$_2$I$_2$ mixing ratios were predicted to be under the upper limit of 0.05 pptv, as confirmed from the observations. Similarly the THAMO model predicts that high levels of IO would not be observed during the night due to the absence of VOIC photolysis, again confirmed by the observations. Figure 4.26 shows elevated IO mixing ratios, anti-correlated to ozone, on the 24th of February. The decrease in ozone concentrations of $\sim$ 10 ppbv cannot be explained by the presence of IO alone. THAMO predicts the loss of only $\sim$ 1.6 ppbv of ozone during this period from iodine chemistry. Instead we suggest that significant concentrations of BrO could have been present within the air mass causing greater ozone losses due to halogen oxide cross reactions. Using THAMO for the 24th of February, if IO (3.1 pptv) is present within the same airmass as high BrO mixing ratios (25 pptv; Honninger *et al.,* 2004) the overall ozone destruction rate would be $\sim$ 2 ppbv hr^{-1} (Mahajan *et al.*, 2010). This is over 3 times the effect of BrO alone (0.62 ppbv hr^{-1}), producing a net ozone loss of $\sim$ 28 ppbv ozone during transit from the polynya.

On the 26th of February sampled air masses had a transit time of ~ 72 hours from the polynya over ~ 1000 km away (Figure 4.18). During this period, THAMO predicts that any VOIC emitted from this lead would be permanently lost through photolysis explaining why elevated levels were not observed during the 25th – 26th of February. Similarly THAMO predicts that all IO generated from VOIC photolysis would be lost to iodine oxide particle (IOP's) formation within 24 hours (Saunders *et al.,* 2010), explaining why IO was not observed above the LoD during this period. However, during this period high BrO mixing ratios of 25 - 30 pptv were measured in the MBL using multi axial differential optical absorption spectroscopy (MAX DOAS; Oetken, H. *unpublished data*), figure 4.27, which most likely caused the observed ozone loss (~ 0.9 ppbv hr^{-1}) during the large ODE.
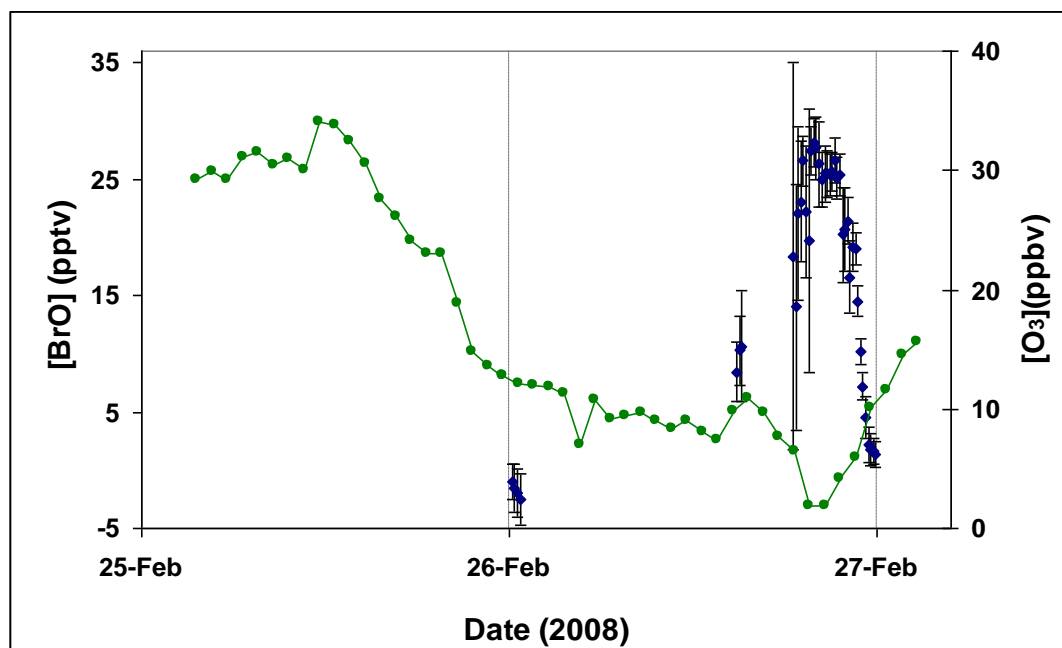
Figure 4.27 BrO measurements conducted via MAX DOAS during the ODE (Oetken, H. *unpublished data*). Filled blue diamonds, [BrO] (pptv); filled green circles, [O$_3$] (ppb).

Higher levels of IO are predicted around the large polynyas, with mixing ratios typically peaking at ~ 11 pptv at 10 metres in altitude, 1 hour after the initial VOIC pulse. As the IO is confined to the prescribed PBL within the model (101 ± 51 m; Mahajan *et al.* 2010), the corresponding column density would be considerably lower than the satellite LoD (1.7 x 10^{12} molecules cm^{-2}) for a single measurement. This is consistent with the

current lack of satellite based IO observations within Arctic regions (Schonhardt *et al.*, 2008).

4.4 Conclusions

To the author's knowledge, the work herein contains the first in direct evidence of VOIC emission from leads and polynyas within the Arctic. Elevated mixing ratios of halogenated organics and halogen oxides were observed in the sub-Arctic MBL suggesting that the presence of bromine in concert with iodine can play an important role in the region. Calculated air mass back trajectories indicate high IO and VOIC mixing ratios were associated with air masses transecting polynyas in Hudson Bay (Mahajan *et al.,* 2010). The observations suggest that the dominant source of IO within the MBL is the photolysis of VOIC emitted from these polynyas in the sea ice and that observed levels of IO greatly accelerate bromine catalyzed ozone depletion of ozone. However, due to the short atmospheric lifetimes of these IO precursors, iodine chemistry in concert with bromine is predicted to occur only on a local scale.

Direct VOIC fluxes were not determined from leads/polynyas during the campaign, hence the THAMO initialisation flux was tuned to reproduce the VOIC air concentrations observed at the experimental site (Mahajan *et al.,* 2010). This tuned sea-air flux of VOIC from the polynya is considerably higher than previously observed in the open ocean (Jones *et al.*, 2010; Hughes *et al.,* 2009).

Calculated sea-air fluxes (table 5.3) were determined to assess the validity of the tuned fluxes used in the THAMO. This was achieved using VOIC concentrations previously observed in the open ocean (Jones *et al*., 2010; Hughes *et al.*, 2009) and mean concentrations in air between 18th – 28th February during the COBRA campaign, (section 5.4.8, EQ 5.22). Under ice turbulence in the proximity of openings in sea ice may not be dominated by wind driven mixing and geostrophic currents (section 4.3.6). The amount of gas exchange through leads/polynyas is not solely dependent upon wind-speed scaling as used for the open ocean (Nightingale *et al.,* 2000), hence gas flux is not a linear function of *f* (Loose *et al.,* 2009; 2011). Loose *et al.* (2009) previously experimentally determined that a power law relationship exists between sea-air gas exchange rate (k_w) and sea ice coverage. During typical partial sea ice cover experience during winter (*f* ∼ 0.1; Tanning and Fanning, 1991) sea-air gas exchange rates were

predicted to be a factor of ~ 4.3 times higher than linear scaling would suggest. Using EQ 5.22, this enhanced exchange rate was taken into account to calculate the theoretical sea-air flux of VOIC occurring at the polynyas/leads during COBRA, table 4.3.

VOIC	Typical seawater-air flux (nmol m^{-2} d^{-1})[a]	Calculated theoretical sea-air flux from leads/polynyas (nmol m^{-2} d^{-1})[b]	Tuned sea-air flux used in THAMO (nmol m^{-2} d^{-1})[c]	Flux from surface sea ice (nmol m^{-2} d^{-1})[d]
CH_3I	41.3 ± 5.8	179.0 ± 25.1	286.9	0.15 ± 0.02
C_2H_5I	1.33 ± 0.2	5.8 ± 0.9	0	0.04
CH_2ICl	2.7 ± 0.3	11.7 ± 1.3	71.73	< LoD
$1-C_3H_7I$	1.2 ± 0.2	5.2 ± 0.9	0	0.02
CH_2IBr	3.9 ± 0.5	16.9 ± 1.5	2870.1	0.04 ± 0.01
CH_2I_2	10.8 ± 1.4	46.8 ± 4.2	1.4	< LoD

Table 4.3 Comparison of calculated VOIC fluxes from sea ice openings during COBRA with THAMO initialisation fluxes.

[a] Calculated using VOIC concentrations previously observed in the open ocean (Jones *et al.*, 2010; Hughes *et al.*, 2009), EQ 5.22.

[b] Calculated assuming an increase in gas exchange rate of ~ 4.3 at $f \sim 0.1$ (Loose *et al.,* 2009).

[c] Mahajan *et al.* (2010).

[d] Fluxes calculated using the calculated VOIC concentrations in the upper 2.4 cm of brine, EQ 5.24. Assumes an ambient air temperature of -3ºC and that the brine percolation threshold of the upper sea ice was met.

The theoretical VOIC fluxes of CH_2ICl and CH_2IBr were considerably lower than those used as the initialisation flux for the THAMO, whereas the CH_3I flux was similar. Fluxes of CH_2I_2 , C_2H_5I and $1-C_3H_7I$ from leads however have the potential to be much higher than considered in THAMO. VOIC fluxes from the sea ice surface are unlikely to have significantly contributed to the mixing ratios observed at the experimental site, table 5.3. The data shown in Table 4.3 suggests that the overall VOIC sea-air fluxes required by THAMO to reproduce IO levels are rather higher than can be expected. This could mean that additional sources are required, or that iodine activation/recycling on sea salt aerosol is more efficient than in the model, and/or that recycling on sea ice surfaces maintains elevated IO mixing ratios during transit. This highlights the need of further field investigation as there is currently a lack of direct VOIC flux measurements from leads and polynyas in polar regions.

Previous observations have suggested a decline in sea ice thickness and an increase in the frequency of occurrence of polynyas and leads in the Arctic over recent decades (Lindsay and Zhang, 2005; Parkinson and Cavalieri, 2008). Assuming that iodine species are emitted from regions of open water in sea ice, the measurements within this chapter and the corresponding model results (Mahajan *et al.,* 2010) indicate that iodine chemistry could potentially play a larger role in the Arctic environment in the future.

Chapter 5

Gas diffusion through columnar sea ice: Implications for halocarbon fluxes in the seasonal sea ice zone.

5.1. Introduction

As discussed in Chapter 4, future fluxes of halogens to the atmosphere may be enhanced (Mahajan *et al*., 2010) as sea-ice continues to thin and retreat, predominantly from sea-air exchange from open water within the ice-pack. As sea-ice becomes warmer and thinner, an additional potential route is through increased bulk diffusive gas transport through the porous microstructure of thinner, warmer sea ice (Loose *et al.*, 2009; Loose *et al.*, 2011). Oceanic emission of VOIC is widely believed to be the dominant atmospheric source of iodine, which has both microalgal (Hughes *et al.*, 2008) and photochemical sources (Richter and Wallace, 2004) within the open ocean (as discussed in section 1.3). During periods of first year ice coverage, oceanic VOIC emissions are considered to be "capped" by this overlying ice layer (McPhee *et al.*, 1996). Recent research suggests that fluid transport and gas transfer in sea-ice may result in a redistribution of such atmospherically important trace gases from the surface ocean to the overlying atmosphere (Saiz Lopez and Boxe, 2008; Golden *et al.*, 1998). The likely significant changes to the emissions of halogens and their impacts on Arctic climate through atmospheric composition are currently unknown.

5.1.1 Sea ice formation

Seawater above its freezing point cooled at the sea/air interface will experience thermohaline convection (overturning of colder, denser surface waters with warmer, lighter waters at depth) until the entire upper water layer is at its freezing point. At this point ice crystals form throughout the upper water layers and are kept in suspension until a surface layer of slush builds, reducing wind stress and thermohaline mixing. The ice crystals in this surface ice layer take the shape of small ice platelets which are intertwined into aggregates called frazil ice (Eicken*,* 2008; Weeks and Ackley, 1986). Typical crystals are ~5 to 50 mm in length and less than a millimetre thick. Following further freezing and consolidation of this frazil ice layer (typically ~5 cm thick) the microstructure of the underlying ice layers alters as layer upon layer of ice is added to the bottom of the ice sheet through quiescent growth of columnar ice (Eicken, 2008). This layer consists of vertically elongated prismatic crystals that are typically several centimetres in diameter and tens of centimetres in length (Weeks and Ackley, 1986, Tyshko *et al.*, 1997).

During the action of seawater freezing, dissolved ions and gases are excluded from the ice crystal structure (Richardson, 1976). The exclusion of salt from these crystals produces a hyper-saline brine which carves a structure within sea ice that is porous to both water and gas (Loose *et al.*, 2011), facilitating brine transport. The bulk of this hypersaline brine resides in the intra crystalline layers whose vertical connectivity is predicted to underpin the development of the brine permeability (Golden *et al.*, 2007). This phenomenon is attributed as being responsible for several important processes including: sea ice production from the freezing of flooded surfaces, convection enhanced thermal transport, an input of both freshwater and brine into the ocean and the transport of nutrients and enzymes. The latter is essential for the survival of *in-situ* micro-organisms, from the upper ocean through the sea ice column (Weeks and Ackley, 1986 and Thomas and Dieckmann, 2003).

5.1.2 Sea ice dynamics

Sea-ice is a complex multiphase medium consisting of pure ice crystals, brine and air inclusions, the sizes of which vary significantly with temperature and bulk salinity. Columnar sea ice exhibits a transition in its fluid transport properties at a critical brine volume fraction (p_c) of between 5 – 5.4 %. This is known as the percolation threshold (Cox and Weeks, 1975; Petrich *et al.*, 2006). Below this value, the ice is considered impermeable to fluid transport whereas above this value seawater and brine are mobile through the ice. Brine volume is critically related to both temperature (T) and salinity (S) (Frankenstein and Garner, 1967) by "the rule of fives", which states that p_c corresponds to a critical temperature T of ~ -5 °C for a salinity (S) of 5 psu (Golden *et al.*, 2007). Evidence supporting this theory includes observations of the exponential decrease of the permeability of sea-ice to sea water as the surface temperature decreases from -3 °C to -12 °C (Ono and Kasai, 1985), and the dissipation of brine gravity drainage for a brine volume fraction (p) $\leq$ 5% (Weeks and Ackley, 1986; Cox and Weeks, 1975).

5.1.3 Nutrient exchange through sea ice

In abiotic systems, *in-situ* ice concentrations of inorganic nutrients (such as nitrate, nitrite, ammonia, phosphate and silicate) will change proportionally to the salinity change (Thomas and Papadimitriou, 2008). Major ions such as sodium, potassium, magnesium,

chloride, sulphate and calcium within different ice types and age follow a similar trend. However, in biologically active sea ice columns nutrient depletion and even exhaustion events are observed as would be expected due to the desalination from gravity drainage processes (section 5.3.2) and uptake by organisms (Dieckmann *et al.*, 1991).

An important factor influencing nutrient concentrations in sea ice, hence microalgal biological production rates, is their rate of exchange and vertical transport with the underlying seawater. This is dictated by the sea ice percolation threshold, hence brine channel fractional connectivity. Nutrient depletion has rarely been reported as a biological growth limiting factor in the skeletal layer of sea ice (lower few cms) as sea- ice exchange is readily possible at this depth. This is due to the relatively high salinities and temperatures observed within this ice layer which allow the percolation threshold to be met. Krembs *et al.* (2002) established that, even though nutrient exchange rates were ~100 times smaller in the skeletal ice layer than in sandy sediments, this rate of exchange was still sufficient to satisfy typical algal nutrient demands. Previous work (McMinn *et al.*, 1999) on both perennial and seasonal sea ice during winter suggests that the rates of nutrient transport decrease away from the ice-water interface. In this work nutrient depletion and algal growth limitation was observed at distances of 5 - 10 cm from the ice-water interface. Alternatively, in porous summer sea-ice, where ice-water nutrient exchange is postulated to extend deeper into the bulk ice, large concentrations of microalgae have previously been recorded (Thomas *et al.*, 1998, Kennedy *et al.*, 2002).

5.1.4 Biogeochemistry of sea ice

During winter within polar regions, biological activity is believed to be focussed at the surface and on the underside of the ice sheet on the ice covered ocean (Sturges *et al*., 1997). Previous incubation studies have demonstrated phytoplankton, including several diatom species, are capable of producing both volatile organic bromine compounds (VOBC) and VOIC (Tokarczyk and Moore, 1994; Moore and Tokarczyk, 1996). The significance of phytoplanktonic VOBC and VOIC production in surface waters is of global significance as they have an ocean wide distribution, unlike macrophytes which are largely confined to the coastal zone. However, previous halocarbon determinations within the polar boundary layer

have been observed to peak over a broad winter period, and do not correlate with measured blooms of marine biota despite halocarbon loss rates being taken into account (Yokouchi *et al.*, 1996).

Previous work on unialgal diatom cultures, which are ubiquitous in the Arctic Ocean, by Moore *et al.* (1996) confirmed the presence of both iodoperoxidase and bromoperoxidase enzymes which are known to facilitate halocarbon production. It was observed that the particular bromoperoxidase enzyme present was capable of oxidizing both I^- and Br^- by H_2O_2, generating an enzyme bound electrophilic halogen. Whereas the iodoperoxidase enzyme was only capable of oxidizing I^- by H_2O_2 (as discussed in section 1.3) both VOIC and VOBC production is diatom species-dependent and is largely explained by their ability to synthesis the haloperoxidase enzymes required for the biogenically driven haloform reaction.

5.1.5 Sea ice radiative transfer and its effect on the photic zone

Biological production in the marine environment is influenced by a combination of radiative flux, nutrient availability and grazing pressure. Radiative backscatter, reflection and absorption within the sea ice/snow canopy reduces radiative flux to the mixed layer by a factor ranging between 50 and 1000, dependent upon the age of the ice and relative thickness (Perovich, 1990). Excluding seasonal variations, the radiative fluxes into sea ice depend on the characteristics of snow cover and on absorption within the ice, dependent upon sea ice microstructure and by the concentration and distribution of photosynthetic pigments. The amount of incident light scattered back from the snow/ice cover, as measured in albedo, is controlled by both snow thickness and sea ice microstructure, specifically the presence of gas and brine inclusions and salt precipitates therein. The number of brine inclusions acting as incident light scatterers correlates with the thickness of the ice cover, such that a pronounced increase in ice albedo is observed at higher ice thicknesses.

Light attenuation within the deposited snowpack is dependent upon a number of site specific conditions. Long wave radiation is typically absorbed, whereas visible and ultra-

violet radiation is scattered by individual snow grains. In the upper few centimetres of the snowpack, incident light is backscattered and upwelling radiation escapes (Kuhn and Siogas, 1978). The actinic flux within the upper snowpack is dependent upon the incident angle of irradiance, the solar zenith angle and the homogeneity of the snowpack.

Oceanic emissions of trace gases in the polar seasonal sea ice zones have the potential to perturb atmospheric chemistry and climate (as discussed in sections 1.1 and 1.2), however considerable uncertainty exists when quantifying their sources now and in the future. The aim of this investigation was to obtain a better understanding of the mechanisms of sea - air gas exchange in ice-bearing waters and to assess the impact of temperature-dependent sea ice microstructure evolution on the bulk diffusive gas transport of VOICs through sea ice.

5.2. Experimental

5.2.1 Experimental chamber

A total of 5 freezing experiments were conducted in a programmable temperature-controlled (-60 ℃ to 50 ℃) WIR19-60HS environmental chamber in the physics department at the University of Leeds, UK. A 233 L stainless steel tank (l × w × h = 118 × 66 × 30 cm, figures 5.1 and 5.2) was used within the chamber to conduct experiments at -3 ℃ and -14 ℃, with either artificial seawater and sea-ice or pure water and ice (section 5.2.2). Two Rule 360 bilge pumps were fixed to the bottom of the tank and used to mix the tank. To promote mixing within the tank, these bilge pumps were orientated so that their jets impacted each other to maximize turbulence whilst minimizing circulation in the tank. This was done by fixing the pumps to a stainless steel baseplate using HDPE brackets (figure 5.2). The water volume within the tank was flushed through the pumps every ~5 mins, so that compete mixing should take place in 25 – 35 minutes (Loose *et al.*, 2011). Despite this a minimum of ~ 7 hours were allowed for thorough mixing. A third bilge pump was used to circulate water through a length of heated insulated Teflon tubing (1" diameter) used for discrete halocarbon and salinity sampling. This sample line was heated to ~4 ℃ and continuously re-circulated to prevent freezing. Internally heated/insulated stainless steel housings were used to protect the sample line when in contact with the

artificial sea ice. Stainless steel has a greater thermal conductivity than ice, causing more rapid heat transfer and freezing around the exterior of the housings. The effect of freezing around the stainless steel housings eliminates the possibility for gas ventilation through sea ice adjacent to the housing (Loose *et al.,* 2011). Discrete salinity measurements were made in triplicate every ~ 1.5 hours using both a handheld refractometer (Omega, RFH201) and handheld conductivity meter (Omega, CDH-90), calibrated daily against a 5 point salt solution (Hobby Marin salt) calibration curve. Within the tank, the ice and overlying air temperature was measured hourly with a depth resolution of 12 mm using an in house 35 point thermistor array and Matlab R2009 software. Ice depth was controlled by a flexible silicone rubber heating mat (OMEGALUX®), capable of supplying a heat transfer of 2.5 W in^{-2}. This was adhered to the bottom of the tank and worked automatically in conjunction with the thermistor array and Matlab R2009 software to maintain water temperatures in the tank. The final ice thickness measurements using the thermistor array were compared to the observed ice depth at the end of the experiment. The thermistor array measurements were ± 0.6 cm of the final ice depth. Under ice water pressure within the tank was minimized by using two air compressible devices which were submerged and fixed to the bottom of the tank during all experiments, figure 5.2. These devices were vacuum sealed in air tight polypropylene grip tight bags (RAJAGRIP®) to minimize the leaching of organic material from the air compressible devices into the surrounding water. Artificially generated winds were produced (3 m s^{-1} ± 0.5) over the tank during each experiment using a 500 mm axial fan, logged using a standard cup anemometer and Matlab 2009 software, and a purpose built wind chamber around the water tank.
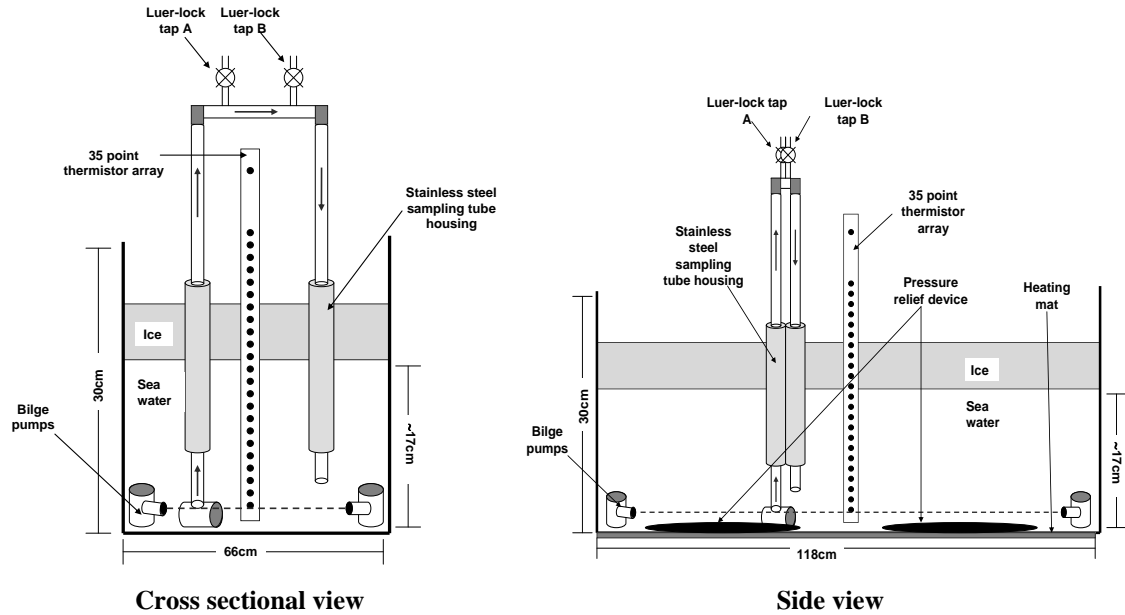
Figure 5.1 Configuration of the set-up in the experimental chamber tank
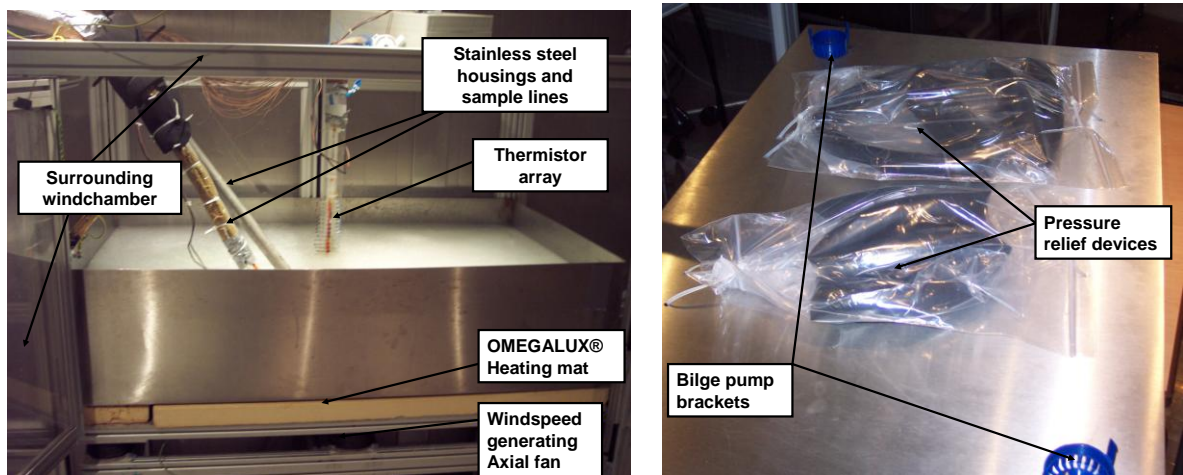
Figure 5.2 From left to right, images showing experimental set up and pressure relief devices employed.

5.2.2 Experimental procedure

The initial salt composition of seawater during the action of freezing can significantly influence sea ice microstructure (Weeks and Ackley, 1986). Therefore it was important that the artificial seawater used in these experiments was representative of typical salt contents observed in the ocean. Hobby Marin Salt additive was chosen for the seawater experiments as it is currently one of the best products available to accurately simulate typical seawater

trace element compositions required in modern aquariums. Figure 5.3 compares the trace element composition of the artificial seawater used to natural marine waters using the concentration x 10^3 parts per thousand (ppth) of each constituent expressed on a log scale. Once mixed the solution has a 4.5% total mass difference in trace elements to typical global seawater concentrations, (Turekian, 1968). The majority (4.2%) of this mass difference arises due to the presence of rubidium, barium, selenium and fluoride added to improve the health of marine organisms within the aquarium (Siedel, 2010).

The artificial seawater was prepared by mixing Milli-Q water (15 MΩ, 140 L) with the aquarium sea salt additive. All seawater experiments were carried out using a sea salt additive concentration of 36 ± 0.1 g per dm^3 in MilliQ water to obtain salinities between 33 − 35 psu, validated using both the handheld refractometer and conductivity meter. Milli-Q water was used in isolation for the freshwater control experiments.

Prior to each experiment, the experiment tank, bilge pumps and tubing were cleaned with a 10% H_2O_2 aqueous solution followed by de-ionised water to minimize bacterial growth. The solution was initially heated within the experimental tank to 60 °C and sparged with nitrogen (zero grade, BOC) for ~ 1 hour to remove any volatile compounds dissolved in solution. The experiments were initiated by setting the temperature of the experimental chamber to the ice growth temperature, allowing the experimental bath to cool until a layer of artificial sea ice was generated over the surface water. Once the ice layer was established, the chamber temperature was altered to the experimental temperature and allowed to equilibrate for 24 hours. The flexible rubber heating mat was activated to maintain the ice thickness for the duration of the experiment. A total of 3 experiments were conducted in artificial seawater, experiments 1, 2 and 3 (see Table 5.1) in order to elucidate the impact of both temperature and different ice growth rates on brine microstructure and hence gas fluid transport through the media. Experiment 1 was conducted at -14 °C and experiments 2 and 3 were conducted at -3 °C with different freezing rates.

Once the ice layer had been established, the VOICs CH_3I (99%, Sigma Aldrich), C_2H_5I (99%, Sigma Aldrich), 2-C_3H_7I (99%, Sigma Aldrich), 1-C_3H_7I (99%, Sigma Aldrich) were added as a concentrated solution dissolved in 100 mL of Milli-Q water *via* a gas-tight glass syringe (50 mL, Samco) to Luer-lock tap B. The bilge pumps were activated and the entire solution was allowed to mix thoroughly for ~7 hours. The pumps remained active for the experiment duration to ensure thorough VOIC mixing and prevent any stratification within the water column. The resultant under-ice bulk artificial seawater concentrations were compound dependent and were within the range $25 - 210$ nmol dm^{-3}. To minimize the possibility of algal growth and due to the photo-labile nature of the compounds investigated, all experiments were conducted under dark conditions. This involved closing all chamber sample ports and covering the main observation window with aluminium foil. Fluorescent lights within the cold chamber were only operated during ice sampling at the end of each experiment.
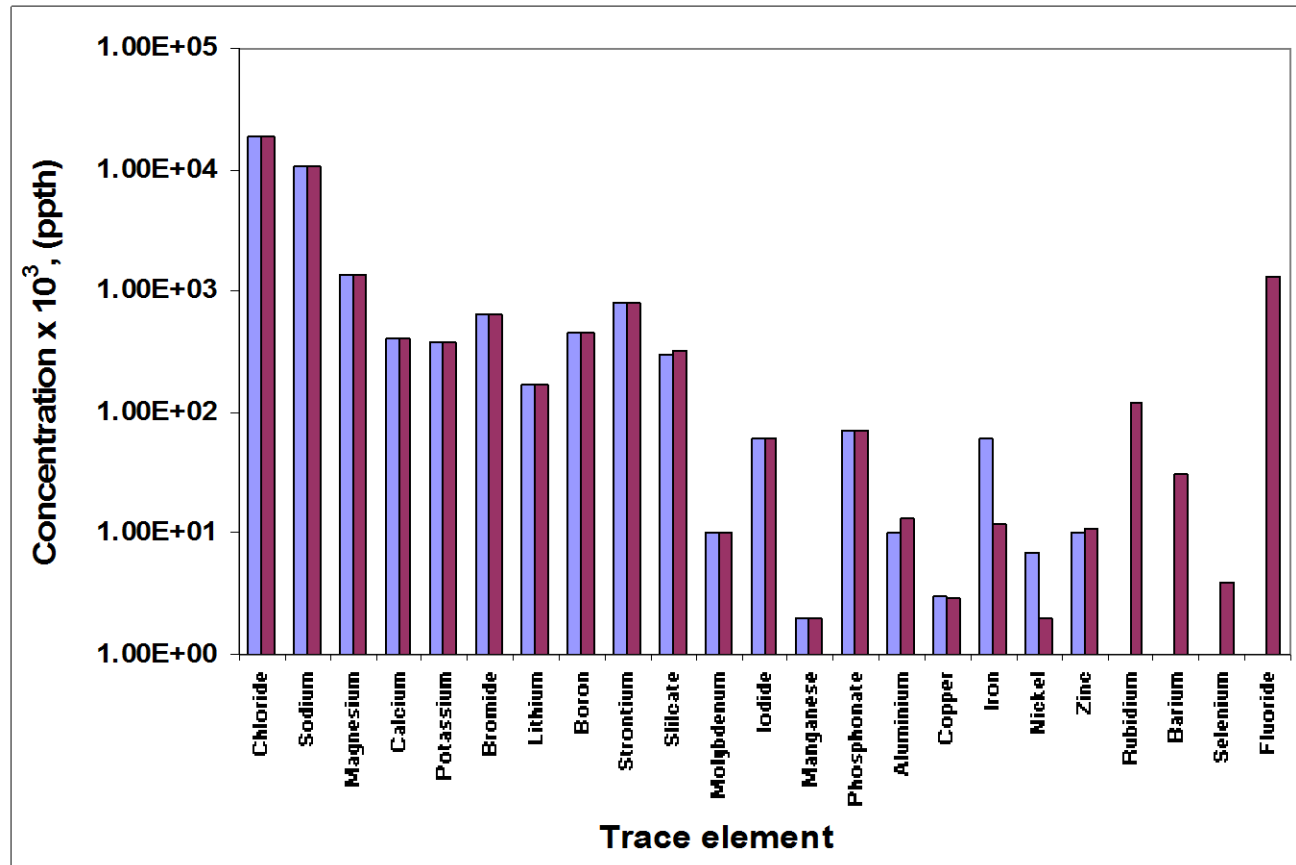
Figure. 5.3 Comparison of Hobby Marin Salt additive and typical seawater trace element compositions.

Purple bars, natural global seawater concentrations (Turekian, 1968); red bars, Hobby Marin Salt additive solution concentrations (Siedel, 2010).Values on y axis are the trace element concentrations x 10^3 ppth expressed on a log scale.

Experiment	Ice growth temperature (ºC)	Experimental temperature (ºC)	Ice growth duration (hrs)	Ice growth rate (cm s^{-1})[c]	Initial ice depth (mm)
1	-14	-14	34	3.68×10^{-5}	45[a]
2	-14	-3	39	4.20×10^{-5}	60[b]
3	-5	-3	150	1.30×10^{-5}	70[b]
4*	-14	-3	24	9.26×10^{-5}	60[b]
5*	-14	-14	24	9.72×10^{-5}	40[a]

Table 5.1 Experimental conditions for artificial sea-ice experiments

[*] Experiments 4 and 5 are freshwater experimental controls; 1 - 3 are artificial seawater experiments.

[a] ice thickness was not maintained for the duration of the experiment, final observed ice depth was 80 and 84 mm for experiments 1 and 5, respectively.

[b] ice thickness was maintained for duration of experiment, final ice depth was the same as initial.

[c] Ice growth rates were calculated for ice growth periods only.

5.2.3 Aqueous VOIC *in-situ* losses

The most significant loss mechanism for VOICs within tropical and mid-latitude seawater, excluding photolysis and volatilisation to the overlying atmosphere, is through chlorination and hydrolysis. Chlorination and hydrolysis reactions are strongly temperature-dependent and at low temperatures the dominant fraction of the chemical destruction occurs by the action of hydrolysis (Jones and Carpenter, 2007). Chemical destruction rates of CH_3I, C_2H_5I and $1\text{-}C_3H_7I$ in saline solutions occur via S_N2 reactions and were calculated using EQ 5.1, where as $2\text{-}C_3H_7I$ proceeds via an S_N1 mechanism and was calculated using EQ 5.2 (Jones and Carpenter, 2007). VOIC total lifetimes were determined using the established temperature dependent hydrolysis (k_H), chlorination (k_c) and observed rate (k) constants for each compound (Jones, 2006; Jones and Carpenter, 2007).

$$k_{total} = k_c[\text{Cl}^-] + k_H[\text{H}_2\text{O}]$$

$$\text{VOIC}_{\text{lossrates}} = k_{total} \, [\text{VOIC}] \qquad\qquad (\text{EQ 5.1})$$

$$2\text{-C}_3\text{H}_7\text{I}_{\text{lossrate}} = k[2\text{-C}_3\text{H}_7\text{I}] \qquad\qquad (\text{EQ 5.2})$$

Where k_{total} is the total loss rate constant attributed to hydrolysis and chlorination and

VOIC$_{\text{lossrate}}$ and $2\text{-C}_3\text{H}_7\text{I}_{\text{lossrate}}$ are the amounts of each compound lost (mol dm^{-3} s^{-1}).

VOIC total lifetimes in seawater under experimental conditions (-1.86°C, 34 ppth) were calculated as approximately 13 months, 12 months, 8 months and 5 months for CH_3I, $\text{C}_2\text{H}_5\text{I}$, $1\text{-C}_3\text{H}_7\text{I}$ and $2\text{-C}_3\text{H}_7\text{I}$ respectively. VOIC lifetimes within the brine channels (at typical brine conditions of 80ppth and -3°C) were calculated as approximately 12 months, 14 months, 8 months and 7 months for CH_3I, $\text{C}_2\text{H}_5\text{I}$, $1\text{-C}_3\text{H}_7\text{I}$ and $2\text{-C}_3\text{H}_7\text{I}$ respectively. Calculated VOIC losses from simultaneous hydrolysis and chlorination over the duration of the experiments in seawater were between 3.8 – 9.2% of the losses measured during the experiments. These aqueous *in-situ* losses are taken into account in the following flux determinations (sections 5.2.7, and 5.2.8).

Experiments 4 and 5 were freshwater (ice-capped) control experiments designed to elucidate any wall losses of VOICs within the chamber, Table 5.1. These experiments were initially conducted using milli-Q water for the experimental temperatures to ascertain the rate of VOIC deposition to the walls of the stainless tank over the time period of the experiments. No measurable loss within solution was observed, within established error, for any of the compounds during the experimental periods.

5.2.4 Aqueous under-ice VOIC sampling

Aqueous sample aliquots were collected ~hourly for a minimum of 40 hours through Luer lock tap A, figure 1, using gas tight glass syringes (20 mL, Samco) for subsequent salinity and VOIC analysis. Salinity analysis was carried out by allowing the aqueous aliquots to equilibrate to room temperature prior to salinity determination using the handheld conductivity meter (section 5.2.1). VOIC analysis was immediately carried out using purge

and trap thermal desorption gas chromatography mass spectrometry (P&T TD-GC/MS). The seawater sample (40 mL) was introduced to a heated gas tight vessel (~70 °C) where nitrogen (zero grade, BOC) was used to sparge residual volatiles from the liquid into the gas phase (40 mL min^{-1}) for 20 minutes (as described in section 2.2). The purge and trap sparging efficiencies for CH_3I, C_2H_5I, $2-C_3H_7I$ and $1-C_3H_7I$ were observed to be ~ 100 % under the sampling conditions utilised (Jones, 2006). The resultant sample gas was dried using both a Nafion membrane molecular sieve box dryer and counter current flow Nafion dryer (150 mL min^{-1} zero grade N_2, BOC) in series. Subsequent pre-concentration and quantitative determination was carried out using a Perkin Elmer, Clarus 600 TD-GC/MS, as described in sections 2.1 and 2.5.

During the sea water experiment conducted at an experimental chamber temperature of -14 ºC (experiment 1), the ice depth was observed to increase from 40 – 80 mm using the 35 point thermistor array and hence the water volume decreased throughout the experiment. VOIC concentrations within the water were corrected to account for this concentration effect (section 5.3.1). The remaining seawater experiments conducted at -3 °C (experiments 2 and 3) showed no evidence of ice growth during the analysis period, suggested via the 35 point thermistor array and the long-term salinity measurements of the underlying water (section 5.3.2). Hence no correction for water volume was carried out for these experiments.

5.2.5 Artificial ice and brine VOIC sampling

Aliquots of artificial sea-ice were sampled using a stainless steel hand corer (L x i.d. = 20 cm x 5 cm, British Antarctic Survey) at ice depth increments of 1.2 cm to a maximum depth of 4.8 cm at the end of each experiment. Upon sampling the ice was introduced to gas tight glass syringes, whilst taking care to minimise headspace within the barrel. No effort was made to separate residual brine during sampling, hence these ice aliquots consisted of both bulk sea ice and residual brine. The ice was thawed (2 - 8 °C) under dark conditions and the resulting melt water VOIC concentration determined as outlined in section 5.2.4. Following ice coring, aliquots of brine were sampled from the relevant ice depth directly into a gas tight glass syringe and thermally equilibrated (2 - 8 ºC) under dark

conditions prior to VOIC analysis, as in section 5.2.4. Both ice melt water and brine salinities were determined at each ice depth using the handheld refractometer. This was preferred over the conductivity meter due to the relatively small volumes of brine and ice melt water sampled from each depth.

5.2.6 Internal standardization and external calibration

All data was internally standardized against a deuterated halocarbon standard mixture containing CD_3I, C_2D_5I, $2\text{-}C_3D_7I$ in nitrogen (10 ppb, 99% purity, CK gases) using a continuous restricted flow set-up (section 2.6.9). Sample gas and deuterated standard gas flow-rates into the TD adsorbent trap were maintained at 50 mL min^{-1} and 20 mL min^{-1}, respectively, for the duration of the analysis. Internally standardized data was externally calibrated at the end of the experimental period against a VOIC gas standard which itself was calibrated against an in house gas permeation oven, as outlined in section 2.6.4.

5.2.7 VOIC fluxes calculated from a consideration of the molar balance

Seawater-air VOIC fluxes were estimated by carrying out a molar balance on the experimental system. For experiments 2 (fast ice growth) and 3 (slow ice growth), the net flux of VOICs from the water to the air above was calculated from the difference between the absolute number of moles lost from the underlying water over the duration of the experimental period and the amount measured within the volume of the ice column at the end of experimental period. These calculations assume a homogenous VOIC distribution at each ice depth analysed and that the concentrations in ice at the end of the experimental periods were representative of steady state conditions. For experiment 1 (-14ºC) the net flux of VOICs from the water to the air above was calculated from the number of moles lost from the underlying water after 24 hours. At this point steady state conditions were observed to be established from loss rates in the underlying water, figure 5.23. Absolute molar quantities of VOIC in brine throughout the ice column were calculated, taking into account *p* and both sea ice and brine densities. The *p* values in ppth were calculated using equation EQ 5.3, empirically derived by Frankenstein and Garner (1967), where *S* is the bulk ice salinity (*psu*) and θ is the ice temperature (ºC). This equation does not account for salt precipitation within the hypersaline brine.

$$p = S\left(\frac{45.917}{\theta}\right) + 0.930$$ (EQ 5.3)

The net fluxes calculated in this way were compared to calculations of the flux from the quasi liquid layer (QLL), as described below.

5.2.8 Calculation of VOIC fluxes from the QLL to air

Within the sea-ice brine channels, the local flux of VOICs is related to the concentration gradient, as deduced from the diffusion coefficients D in brine (EQ 5.5, Wilke and Chang, 1955) and the concentration gradient within the surface brine channels according to Ficks first Law of diffusion. The measured concentration gradient within the surface brine is multiplied by the volumetric factor (V) which takes into account the VOIC concentration effect between the brine channels and surface *QLL*, EQ 5.4. The volume of the *QLL* was calculated using equations EQ 5.9, EQ 5.10 and EQ 5.11, taking into account the sea ice thicknesses of each experiment, surface ice densities, and assuming mass fractions of liquid water in sea-ice at 270 K and 259 K of 2×10^{-2} and 5×10^{-3}, respectively (Conklin and Bales, 1993).

$$Flux = -D\left(\frac{dC_{brine} \times V}{dz}\right)$$ (EQ 5.4)

The diffusivity of a solute in a liquid solvent can be calculated by a number of established methods. Whilst it is believed that the method of Tyn and Claus (1975) is likely to produce the most accurate D values (Polling *et al.*, 2001), it requires empirical data which is currently not available for the VOIC trace gases studied. As a compromise, the method of Wilke and Chang (1955) was chosen for this study as it best reflected the available empirical and experimental data available for each species, as shown in EQ 5.5, where T is temperature (K), Φ is the unitless association factor of the solvent (2.6 for water), M_s is the relative molecular mass of the solvent, n_w is the dynamic viscosity of solution (cP, 10^{-3} kg m^{-1} s^{-1}), and V_b is the liquid molar volume of the gas at it's boiling point (cm^3 mol^{-1}) as calculated using the Schroeder additive method (Johnson, 2010).

$$D = \frac{7.4 \times 10^{-8} \times T \times \sqrt{\Phi \times M_s}}{n_w \times V_b^{0.6}}$$ (EQ 5.5)

The term n_w is calculated using the temperature and salinity dependent viscosity scheme of Laliberte (2007), equation EQ 5.6, which requires seawater composition expressed as mass fractions of component solutes. The term w_w is the mass fraction of water in solution (calculated from experimental salinity measurements), n_s is the temperature corrected dynamic viscosity of pure water (cP, 10^{-3} kg m^{-1} s^{-1}). For each solute in solution, w_i is the mass fraction and n_i is the dynamic viscosity attributed to each component solute (cP, 10^{-3} kg m^{-1} s^{-1}). The mass fractions of component solutes are the fraction of each solute as a proportion of the solution's total salinity. This was derived from the standard seawater definition of Millero *et al.* (2008). Note, only the principal solutes NaCl, KCl, CaCl$_2$, MgCl$_2$ and MgSO$_4$ were taken into account.

$$\ln(n_w) = w_w \times \ln(n_s) + \sum w_i \times \ln(n_i)$$ (EQ 5.6)

The temperature dependent dynamic viscosity of pure water, at atmospheric pressure was calculated using EQ 5.57 (Laliberte, 2007) where T is the temperature of solution (K).

$$n_s = T + \frac{246}{(0.05594 \times T^2) + (5.2842 \times T) + 137.37}$$ (EQ 5.7)

The n_i values were calculated according to EQ 5.8 where v_1 to v_6 are empirically derived constants for each common solute in seawater (Laliberte, 2007). Using these parameterisations, temperature and salinity dependent viscosity values for seawater can be calculated.

$$\ln(n_i) = \frac{v_1 \times (1 - w_w)^{v_2} + v_3}{(v_4 \times T + 1) \times \ln[v_5(1 - w_w)^{v_6} + 1]}$$ (EQ 5.8)

189

The volumetric factor (V) was determined from the surface sea-ice brine volume (V_{brine}, cm^3cm^{-2}) and QLL volume (V_{QLL}, cm^3cm^{-2}) *via* equation EQ 5.9. The V_{brine} was determined per unit of cross sectional area (A, cm^2) of surface sea-ice using p values. The V_{QLL} was determined per unit of A (cm^2) by taking into account the calculated theoretical QLL thickness (cm), EQ 5.10. The quasi-liquid layer thickness (QLL, cm) of the surface sea ice could be determined *via* equation EQ 5.11, taking into account sea ice thickness (S_h, cm) and assuming the mass fractions of liquid water in sea-ice (m_f) at 270 and 259 K were 8 x 10^{-1} and 3 x 10^{-2} respectively (Conklin and Bales, 1993).

$$V = V_{brine} / V_{QLL} \qquad\qquad\text{(EQ 5.9)}$$

$$V_{QLL} = A \times 1 \times QLL \qquad\qquad\text{(EQ 5.10)}$$

$$QLL = S_h \times A \times m_f \qquad\qquad\text{(EQ 5.11)}$$

5.2.9 Calculation of VOIC gas transfer velocities

The gas transfer velocity of a species is usually expressed as a function of wind speed (m s^{-1}), or more specifically wind speed at 10 m above water level. The most commonly used parameterisation for studies of such open ocean trace gas exchange are outlined in Duce *et al*. (1991), Liss (1974) and Nightingale *et al*. (2000). However, such open water gas transfer parameterisations are unsuitable for sea/sea-ice/air gas exchange. The experimental surface QLL-air ($k_{QLL \rightarrow air}$) and ice-air ($k_{ice \rightarrow air}$) gas transfer velocities were determined for each species from the molar balance inferred flux using EQs 5.12 and 5.13, the assumed concentration in the QLL ($C_{brine} \times V$) and observed concentrations in the sea-ice (C_{ice}). The effective sea-ice-air gas transfer velocities ($k_{sea \rightarrow ice \rightarrow air}$) for each species were determined from the molar balance inferred flux using EQ 5.14, where C_w (mol dm^{-3}) is the average measured seawater concentration during each experiment.

$$k_{QLL \rightarrow Air} = \left(\frac{Flux}{C_{brine} \times V} \right) \qquad\qquad\text{(EQ 5.12)}$$

$$k_{ice \to Air} = \left(\frac{Flux}{C_{ice}} \right)$$

(EQ 5.13)

$$k_{Sea \to ice \to Air} = \left(\frac{Flux}{C_w} \right)$$

(EQ 5.14)

5.2.10 Calculation of mass diffusion lengths

The mass diffusion length (L_d, cm) through the sea-ice was calculated from the species dependent diffusion coefficients in brine using EQ 5.15. This value is an upper limit of vertical diffusion through sea-ice which assumes 100% brine channel fractional connectivity. If L_d is longer than the ice thickness, the VOIC concentration gradient in the sea-ice should be essentially linear and independent of time (steady state equilibrium). Alternatively if L_d is shorter than the ice thickness, the VOIC concentration gradients in sea-ice can differ within the media and are highly time dependent (dynamic equilibrium). L_d values were calculated for experiment 1 (-14 °C experiment) using calculated diffusion coefficients at 42 mm, where significant VOIC vertical transport was observed. L_d values for experiments 2 (slow ice growth) and 3 (fast ice growth) were calculated using calculated surface diffusion coefficients. In each experiment, L_d values exceeded the measured sea ice thicknesses suggesting that vertical brine transport through the sea-ice was independent of time and in a steady state condition, table 5.2.

$$L_d = \sqrt{4Dt}$$

(EQ 5.15)

5.2.11 Sea water and sea ice sampling during the COBRA campaign

A number of discrete sea/sea-ice melt water samples were collected from the Hudson Bay region and analysed during the course of the COBRA campaign (chapter 3). Salinity and VOIC determinations were carried out in duplicate using a handheld refractometer (OMEGA$^{®}$) and the purge and trap set-up linked to the ATD-GC/MS, as described in sections 2.1, 2.2 and 2.5, respectively.

Two ice cores were sampled adjacent to the Manitounuk Sound region within Hudson bay (figure 5.4) at core positions 1 (N55.340°, W77.721°) and core positions 2 (N55.369°, W77.723°) by using a purpose built hand corer (L × i.d = 110 × 20 cm, British Antarctic Survey) up to a maximum depth of 120 cm. Sea ice at core positions 1 and 2 were sampled on the 9th and the 6th of March 2008 respectively. Once a section of sea ice was cored, the pressure difference below and above the ice caused the underlying seawater to rapidly fill the void left by coring. The under ice seawater samples were sampled from within this core void into gas tight syringes (~40 mL) and covered in aluminium foil. We gratefully acknowledge H. Atkinson (British Antarctic Survey) for assistance in both seawater and ice core sampling.

The ice cores were transported to Kuujjuarapik field station (55.30°, 77.73°) within the ice corer and immediately transferred into gas tight syringes (~ 40 mL) upon arrival. The mean ambient temperatures during the sea ice/water sampling and transport periods, for cores 1 and 2, were -20.1. and -21.0°C respectively. All subsequent ice cores were allowed to thaw between 5 – 10 °C for ~ 8 hours prior to VOIC and salinity determination. All aqueous samples were analysed within 24 hours of sampling.
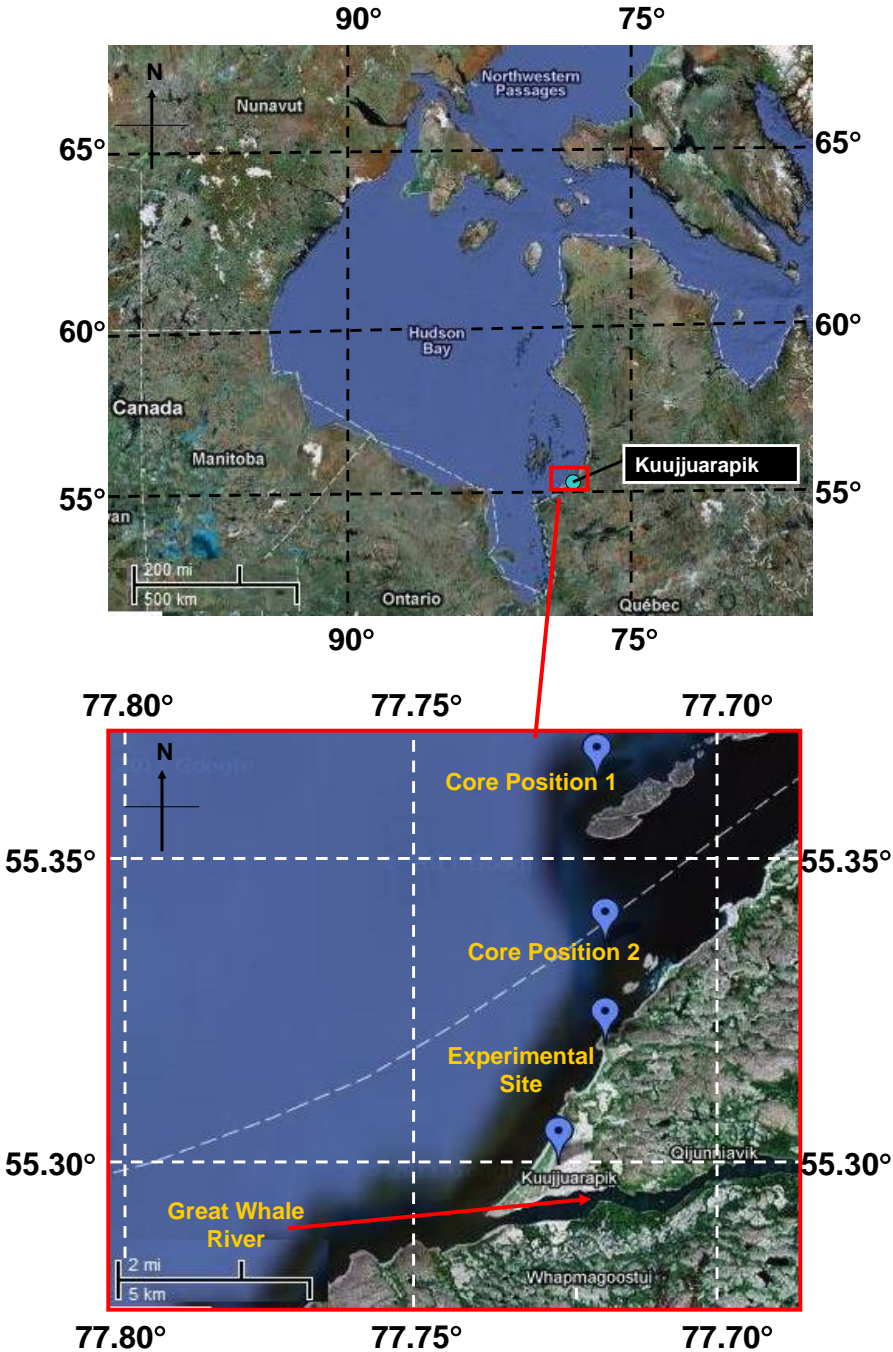
Figure 5.4 Study area showing the locations of the experimental site and sea ice coring positions.

5.3. Results and Discussion

5.3.1 Temperature distributions in Leeds chamber artificial sea ice

Measured sea ice temperature depth profiles were used to infer sea ice thickness and determine temperatures with ice depth for the duration of each experiment. The sea ice thicknesses inferred from the temperature depth profiles were compared to observed sea ice thicknesses at the end of each experiment and were within the thermistor array sea ice depth error (± 0.6 cm).

Inferred sea ice thicknesses at the end of each experiment were 8.0, 6.0 and 7.0 cm for experiments 1, 2 and 3, respectively (table 5.1). Sea ice growth during the experimental periods of experiments 2 (fast ice growth) and 3 (slow ice growth) were considered to be at steady state (zero ice growth). This was inferred on comparison of their sea ice temperature depth profiles at the beginning (t_0), at the mid point ($t_{0.5}$) and end (t_{end}) of each experiment, figures 5.5 and 5.6. However, during experiment 1 (-14°C experiment) the thermistor sea ice temperature depth profiles suggested significant ice growth during the experiment period inferring sea ice depths of 4.6 ± 0.6, 6.5 ± 0.6 and 8.0 ± 0.6 cm for t_0, $t_{0.5}$ and t_{end} respectively, figure 5.7.

During sea ice growth, hypersaline solution is continuously rejected from the ice column to the underlying water, as discussed in section 5.3.2. VOICs are also expelled from the sea ice within this hypersaline solution which causes a considerable concentration effect in the underlying seawater. As gravity drainage into the underlying seawater dissipates at ~ <-5°C (Weeks and Ackley, 1986; Cox and Weeks, 1975), theoretically any enhancement in seawater salinity will be a direct effect of brine rejection due to sea ice growth. Therefore relative sea ice depth can be inferred using the evolution of seawater salinity during the experiment. This was achieved by scaling the ice depth at t_{end} with the change in seawater salinity for the duration of experiment 1.

The VOIC concentrations in the underlying seawater were corrected against ice depth inferred from the thermistor array. However, the inferred sea ice depths for the duration of

experiment 1 using both the thermistor array and change in seawater salinity were within established errors, figure 5.8. The established errors are 0.1% (as quoted by manufacturer) and 0.6 cm for the conductivity meter and thermistor array, respectively. Corrected and uncorrected VOIC data for experiment 1 is included in the Appendix (Appendices 5.1 to 5.4).

Approximately linear temperature gradients were measured within sea ice during each experimental period. This phenomena has previously been observed in seasonal sea ice, during the winter season of 1977-78 (Nakawo and Sinha, 1981) and is expected to exist throughout the season. Nakawo and Sinha (1981) collected a substantial volume of data on sea ice characteristics, including sea ice growth rates, at Eclipse Sound (lat 72.7° N, long 78.0° W), Baffin Island, Canada during February to April 1978. The authors derived an empirical calculation using this data for the determination of temperature gradients in seasonal sea ice, EQ 5.16, where a growing ice sheet of thickness h_i (cm), subjected to an air-ice interface temperature T_a (°C), with a sea ice melting point of T_m (°C) produces the temperature gradient (G_i).

$$G_i = \frac{T_m - T_a}{h_i}$$
(EQ 5.16)

Calculated temperature gradients using EQ 5.16 for chamber experiments 1, 2 and 3 were 1.53, 0.20 and 0.17 °C cm^{-1} respectively. These calculated temperature gradients were in generally good agreement with the observed values herein (determined from the thermistor array) at t_{end} which were 0.95± 0.04, 0.27± 0.18, 0.25± 0.03 °C cm for experiments 1, 2 and 3 respectively. The observed temperature gradients for experiments 2 and 3 (-3 °C experiments) were also in relatively good agreement with the values of Nakawo and Sinha (1981) who measured seasonal consolidated sea ice G_i values of between 0.09 – 0.175 °C cm^{-1}. This agreement between experimental and observed seasonal sea ice values is of importance as ice temperature gradients essentially determine ice growth velocities which in turn affects the microstructure of sea ice, as discussed in section 5.3.2. This agreement between the growth rates of the Arctic and ice chamber sea ice, coupled with the similarity

in trace element compositions between the artificial used and global seawater (figure 5.3), would suggest that the sea ice grown within these experiments is abiotically representative of freshly formed ice in the seasonal sea ice zone.
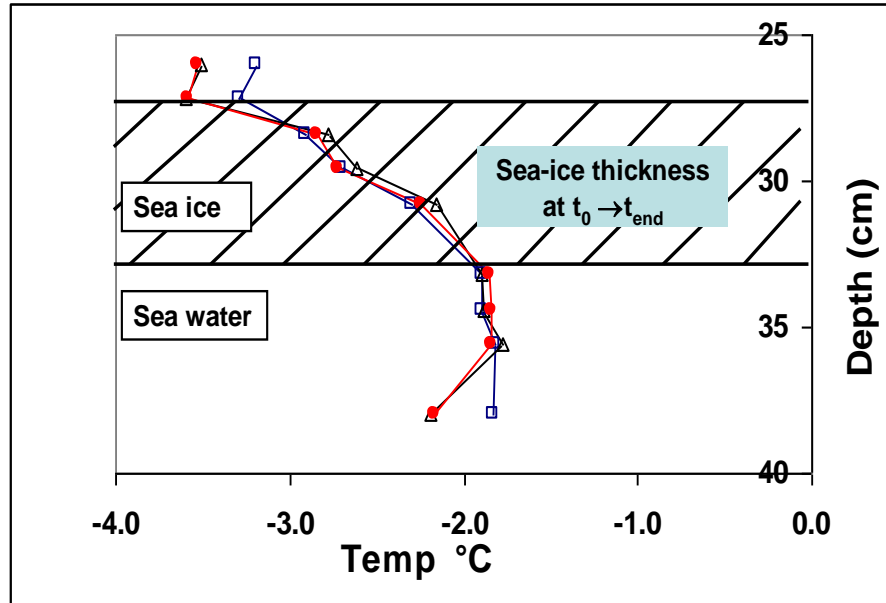
Figure 5.5 Sea ice temperature gradients during experiment 2 (fast ice growth). Empty blue squares, t_0; empty black triangles, $t_{0.5}$; filled red diamonds, t_{end}.
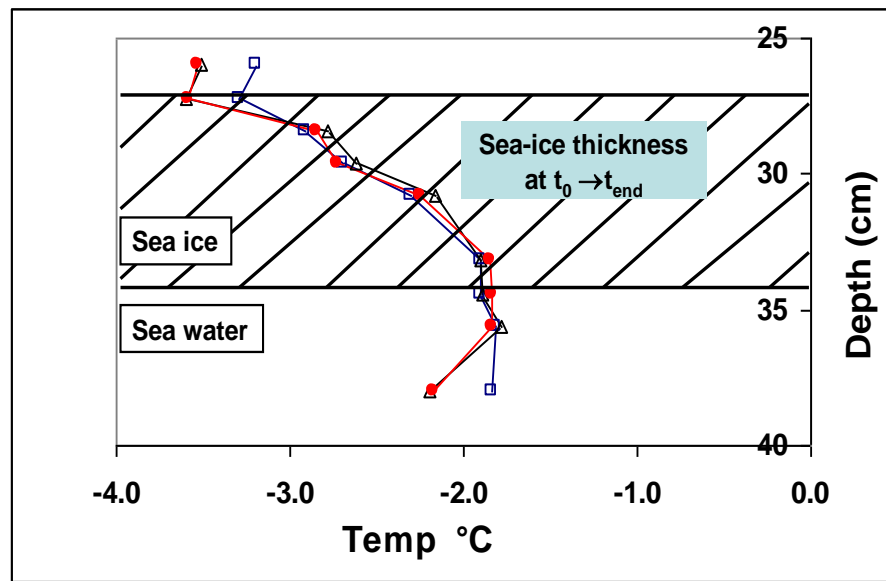
Figure 5.6 Sea ice temperature gradients during experiment 3 (slow ice growth). Empty blue squares, t_0; empty black triangles, $t_{0.5}$; filled red diamonds, t_{end}.
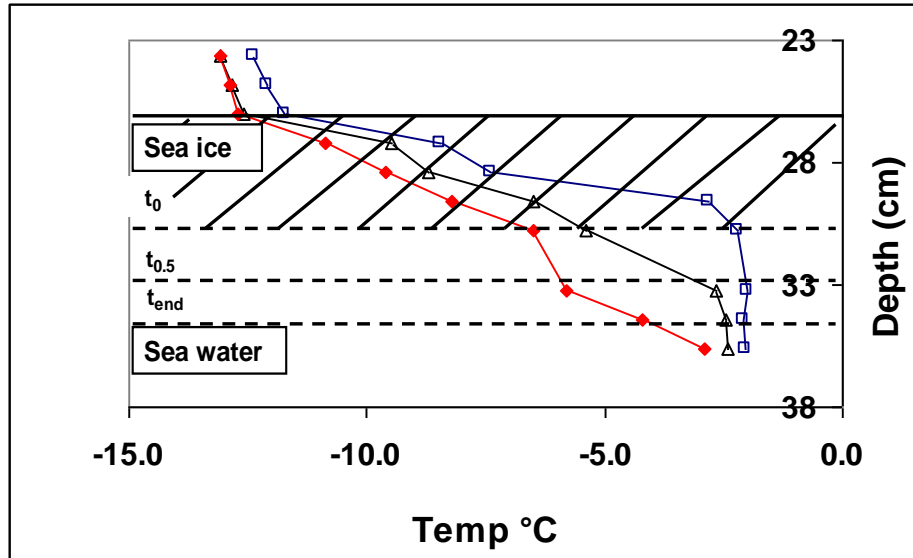
Figure 5.7 Sea ice temperature gradients during experiment 1 (-14°C experiment).
Empty blue squares, t_0; empty black triangles, $t_{0.5}$; filled red diamonds, t_{end}.
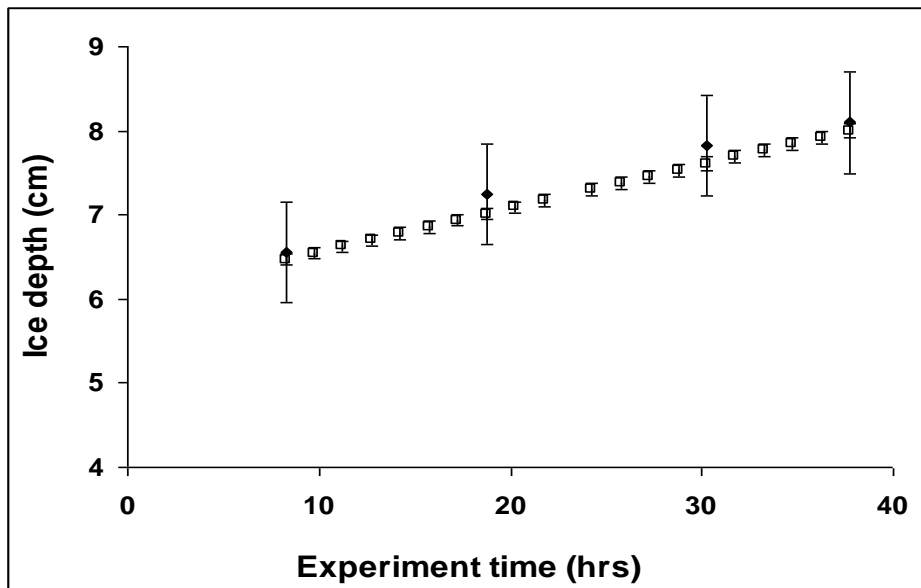
Figure 5.8 Sea ice depth inferred from the thermistor array and seawater salinity change. Filled diamonds, thermistor inferred depth; empty squares, salinity inferred depth. Error bars represent a 0.6 cm thermistor and 0.1% salinity error.

5.3.2 Distribution of salinity in sea ice

Sea ice generally consists of a crystal lattice array of small ice platelets which grow vertically from the ice water interface producing what is commonly referred to as the

skeletal layer. During freezing, salt ions and other solutes are rejected from the ice crystal lattice producing a hypersaline solution along the ice grain boundaries. As the platelets elongate and broaden over time, ice bridges form between adjacent peaks, trapping inclusions of brine. It's due to this mechanism of platelet array growth that brine inclusions are dominantly vertically orientated with characteristic spacings, and extend all the way up through the ice sheet as seen in columnar ice. Brine inclusions shrink as temperature decreases, as brine salinity must increase to maintain freezing equilibrium with the surrounding ice, and *vice versa* for warming. This is accomplished by the freezing and melting of pure water into and from the surrounding ice lattice hence influencing the p_c (Light *et al.*, 2003). Eventually, the ice layer is entrained into the floe interior and the ice platelets join up as brine is lost to gravity drainage. This causes a consolidation of the ice layer into lower porosity sea ice, such as that observed in aged first year or perennial sea ice. Previous measurements of the vertical salinity in seasonal sea ice during the growth season suggest that rapid desalination (25 to 7.8± 0.8 *psu*) from brine drainage can occur throughout the ice column within 1 week of the initial ice formation (Nakawo and Sinha, 1981). Thereafter, desalination processes accounted for a 0.5 *psu* loss in ice salinity per month during an average ambient temperature of -30 °C (temperature ranged between -20 to -40 °C). No such rapid desalination of the sea ice columns were observed in this study up to a maximum of 10 days.

This initial distribution of salt between the ice and the underlying water is affected by several brine drainage processes. Several sea ice desalination processes exist but during ice growth only gravity drainage and brine expulsion are of quantitative importance. Gravity drainage is essentially convective brine transport within the ice column, induced by thermal gradients. As growing sea ice is cooled by the overlying ambient air, the density profile of brine within the ice column is unstable and likely to result in convective exchange. In this action, cold, dense brine within the upper ice is exchanged with warmer, less dense brine/seawater from lower ice layers. This process continually expels brine into the underlying seawater over time. As pressure gradients associated with gravity drainage are small, the rate of this convective brine exchange is strongly dependent upon the

temperature gradients through the ice, brine channel pore size and fractional connectivity (Eicken, 2008).

Brine expulsion is a particularly important desalination process during ice formation. During sea ice growth the sea-ice interface advances into seawater during freezing, and rejected salt ions are concentrated in solution at its leading edge. The majority of this brine is ultimately consolidated as brine inclusions within the ice column during freezing or is transported into the bulk sea water *via* either convective transport or molecular diffusion. The amount of brine consolidated within the ice is dependent upon both under-ice turbulence and the time spent exposed at this leading edge, the latter essentially dependent upon ice growth rate. Another form of brine expulsion is caused by significant changes in consolidated sea ice volume with temperature which causes a pressure build up in isolated brine inclusions. This pressure build up is said to create micro-fractures intersect both brine channel networks and isolated brine inclusions into which the brine is ejected, the rates of which would be independent of sea ice permeability (Eicken 2008).

Of considerable importance when considering the sea ice substructure is how the dimensions of the incorporated ice platelets exhibit an exponential dependence on growth velocity. Nakawo and Sinha (1981) previously demonstrated this for seasonal Arctic sea ice where reduced ice growth velocity was observed to correlate with an increase in brine spacing. Brine spacing is typically of the order of several tenths of a millimetre in ice in the seasonal ice zone (Eicken, 2008). Zotikov *et al.* (1980) previously observed brine channel spacings in the order of several millimetres in perennial sea ice grown at velocities of several centimetres a year. The reduction in overall brine volume within the ice column from such enhanced brine channel spacing could potentially effect $k_{sea \rightarrow ice \rightarrow air}$ transfer rates of dissolved gases by reducing the number of available channels for vertical transport. It is therefore of critical importance to consider sea ice growth rates when conducting laboratory ice studies (section 5.3.1).

Sea ice grown in the absence of turbulence exhibits the typical crystal lattice lamellar structure described, whereas ice grown in turbulence exhibits a grain sub-structure which

delineates brine channels potentially reducing the overall porosity of the ice column (Weeks and Lorgren, 1967; Eicken 2008). All ice growth in this study was conducted without the presence of external currents to maximise ice porosity under each condition investigated. Following ice growth, under ice turbulence was generated to minimise stratification of VOICs within the water column which could impact their respective flux rates through the sea ice.

The most important factor controlling seasonal sea ice salinity is the segregation of sea salt ions at the ice-water interface during ice formation. This salt segregation is controlled by the salt segregation coefficient (k_{eff}) which is proportional to ice growth rate (v), EQ 5.17 and EQ 5.18 (Cox and Weeks, 1980). Newly grown sea ice initial salinity ($S_{i,0}$) can then be calculated using k_{eff} and the salinity of the seawater (S_w, ~ 32-35 *psu*) as described by Weeks and Ackley (1986), EQ 5.19. Limitations in this approach to accurately deriving k_{eff} is that its assumes a planar rather than a platelet ice-water interface. A platelet ice-water interface would typically produce higher k_{eff} values, (Eicken, 2008) hence the calculated values herein are to be used carefully.

$$k_{eff} = \frac{0.26}{0.26 + 0.74 \exp(-7243v)} \qquad v > 3.6 \text{ x } 10^{-5} \text{ cm s}^{-1} \qquad \text{(EQ 5.17)}$$

$$k_{eff} = 0.8925 + (0.0568 \times \ln v) \qquad 3.6 \times 10^{-5} \geq v \geq 2.0 \times 10^{-6} \text{ cm s}^{-1} \qquad \text{(EQ 5.18)}$$

$$S_{i,0} = k_{eff} \times S_w \qquad \text{(EQ 5.19)}$$

Using equations EQ 5.17 – EQ 5.19, the calculated k_{eff} values were 0.34, 0.36 and 0.25 for experiments 1, 2 and 3 respectively. The calculated $S_{i,0}$ values of the surface ice (top 1.2 cm) were 10.9, 11.5 and 8.0 *psu* for experiments 1, 2 and 3, respectively. Measured salinities at this sea ice depth at t_{end} were approximately 2 − 3 times higher than these calculated initial salinity values.

Figures 5.9, 5.10 and 5.11 show sea ice salinities with depth for the seawater experiments 1, 2 and 3, respectively. Errors on the *x* axis represent the propagation of the refractrometer error (0.1%, as quoted from the manufacturer) and an arbitrary 5% sampling error. Errors on the y axis reflect the ice depth sampled to generate each data point.

For each experiment, sea ice salinities increase linearly with depth as has previously been observed for young columnar sea ice grown in a large ice tank during the INTERICE experiments (Haas, 2000). The INTERICE experiments are analogous to the experiments in this study as they were also conducted over similar timescales (5 days) and temperatures (-2 to -10°C) to the experiments herein and as such were not subject to substantial gravity brine drainage. In this study*,* the observed linear increase in sea ice salinities with depth, coupled with the measured salinities being considerably higher than $S_{i,0}$ values, could indicate that the increasing underlying bulk seawater salinities observed during ice growth for each experiment (figures 5.12, 5.13 and 5.14 for experiments 1, 2 and 3 respectively) are affecting the relative amount of salt consolidated within the ice column. This increase in bulk seawater salinity at t_{end} $(35 - 47\ psu)$ is caused by the continual brine expulsion into the seawater from the newly formed sea ice. Assuming a constant ice growth rate, hence k_{eff} value, enhanced seawater salinities would lead to an increased consolidation of salt into the sea ice and a higher sea ice salinity, EQ 5.19.

Neither ice core exhibits the characteristic C shaped ice salinity distribution observed previously in Arctic seasonal sea ice (Sturges *et al.*, 1997). This is likely due to the relatively short time scales used during the ice chamber experiments, hence providing little opportunity for gravity brine drainage. The measured brine salinities of each experiment were anti-correlated to temperature, decreasing approximately linearly with sea ice depth, as shown in figures 5.9, 5.10 and 5.11. This characteristic profile of brine salinity is due to both the temperature dependence of brine density and brine enrichment through the ice column. Brine salinity increases as temperature decreases to maintain freezing equilibrium with the surrounding ice which is accomplished by the freezing and melting of pure water into and from the surrounding ice lattice, causing brine enrichment. The increase in brine salinity is both temperature and time dependent, which is shown when comparing the brine

salinity of the experiments. Experiment 1, conducted at -14 °C, has brine salinities ~ 2 - 3 times higher than either of those conducted at -3 °C. Also the measured brine salinities during experiment 3 were ~ 1.5 times higher than those measured during experiment 2 which reflects their respective ice growth and experimental duration at -3 °C of 225 and 138 hours, respectively.
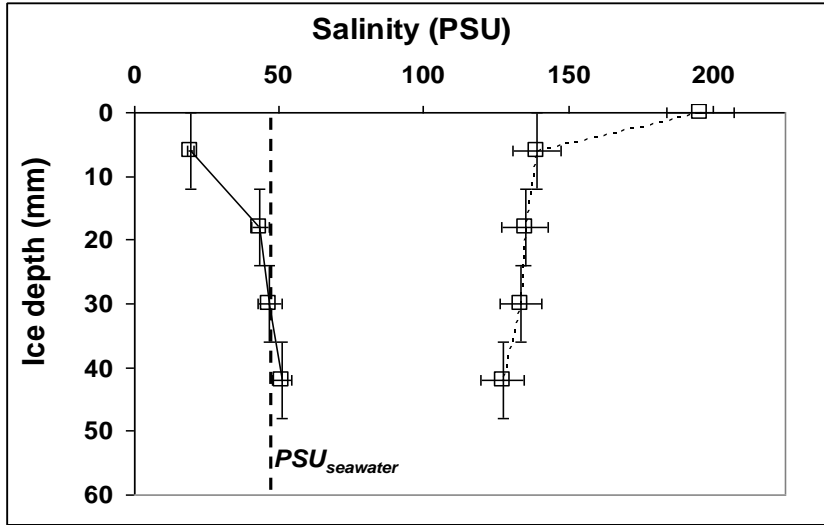
Figure 5.9 Measured sea ice and brine salinity plotted against ice depth during experiment 1 (-14°C). Empty squares and solid line, sea ice salinity; empty squares and dotted line, brine salinity. Dashed line represents measured underlying seawater salinity during ice sampling, $t_{end.}$
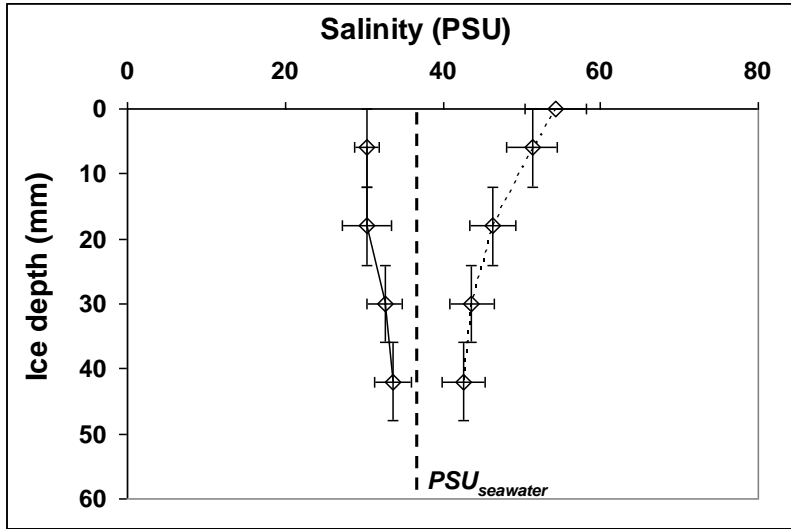
Figure 5.10 Measured sea ice and brine salinity plotted against ice depth during experiment 2 (fast ice growth -3 °C). Empty diamonds and solid line, sea ice salinity; empty diamonds and dotted line, brine salinity. Dashed line represents measured underlying seawater salinity during ice sampling, $t_{end.}$
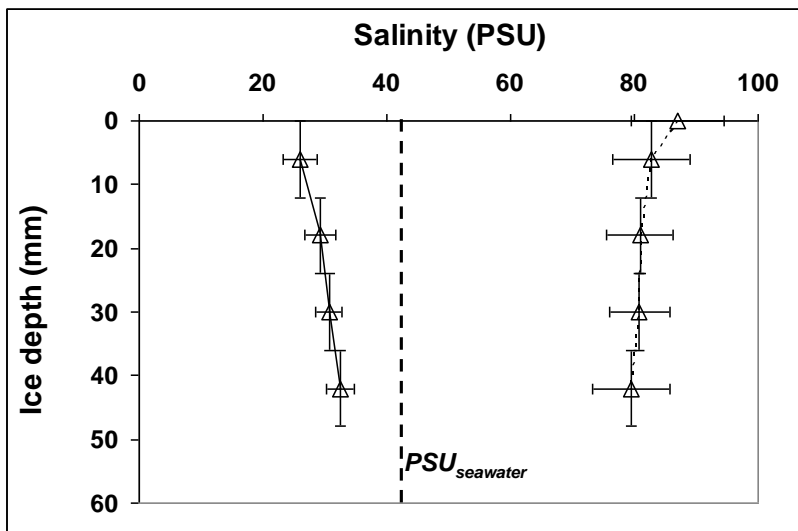
Figure. 5.11 Measured sea ice and brine salinity plotted against ice depth during experiment 3 (slow ice growth -3 °C). Empty triangles and solid line, sea ice salinity; empty triangles and dotted line, brine salinity. Dashed line represents measured underlying seawater salinity during ice sampling, $t_{end.}$

5.3.3 Evolution of artificial seawater salinity

The salinity of the underlying seawater was periodically monitored during each experiment (as described in section 5.2.2). Figures 5.12, 5.13 and 5.14 show the measured underlying seawater salinities during each experiment. Regions marked as A, B and C on the plots refer to the ice growth, ice temperature equilibration and experiment periods, respectively. Salinity enhancement of the underlying seawater was observed due to brine rejection during sea-ice growth periods (section 5.3.2). This phenomenon is not observed in the environment due to the rate that the expelled brine is mixed and transported into the underlying bulk seawater, but is clearly observed in each experiment due to the limited underlying seawater volumes present. The salinity of the underlying seawater of the experiment conducted at -14 °C (experiment 1), figure 5.11, increases linearly with respect to time. This is in good agreement with the expected change according to ice depth measurements made using the thermistor array during the experimental period (± 2%), figure 5.8.

Both seawater experiments conducted at -3 °C, figures 5.13 and 5.14, (experiments 2 and 3) show no appreciable change in the underlying water salinity during experimental periods, suggesting no brine rejection from new ice formation was taking place. This is in good agreement with the thermistor array inferred depths during this period as shown in figures 5.5 and 5.6. The data also suggests that measurable *in-situ* gravity brine drainage did not occur during either of their experiment periods, due to the short timescales investigated. However, immediately after the ice growth period, the initial seawater salinity in experiment 3 was ~ 10 *psu* higher than in the other experiments, possibly due to both brine exclusion and additional gravity brine drainage occurring over the 150 hr ice growth period, figure 5.14 (Weeks and Ackley, 1986; Cox and Weeks, 1975). This is consistent with the fact that the calculated brine volume in experiment 2 is higher, figure 5.15.
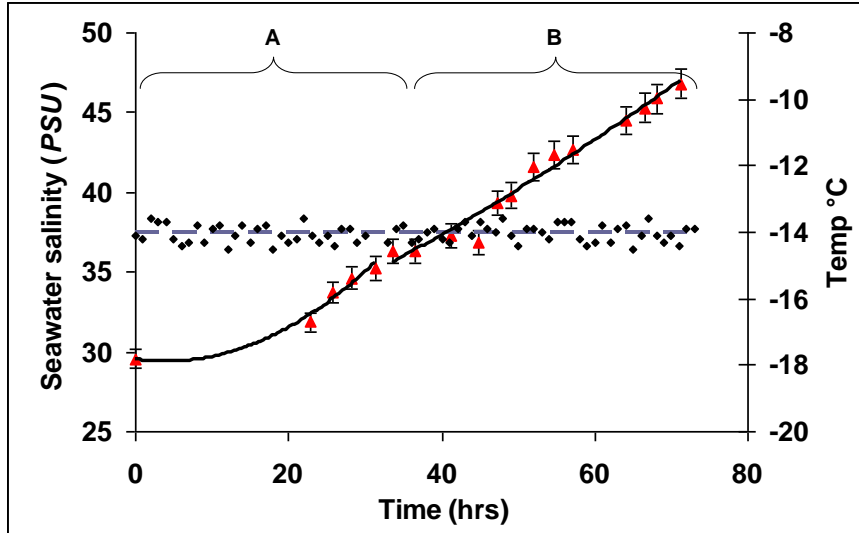
Figure 5.12 Underlying seawater salinities during experiment 1. Black diamonds, measured ambient chamber temperature (°C); grey dashed line, chamber temperature set point; red triangles, seawater salinities (*psu*). A is the ice growth period, B is the experiment period.
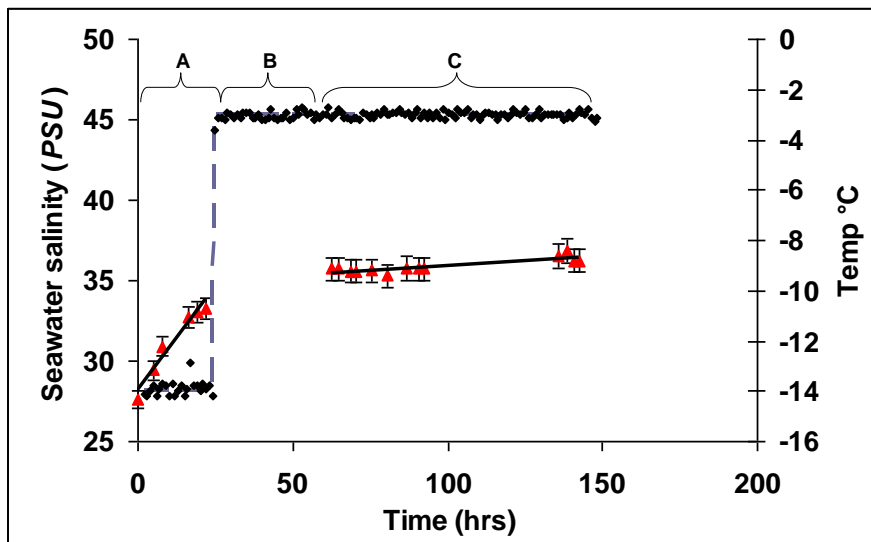
Figure 5.13 Underlying seawater salinities during experiment 2. Black diamonds, measured ambient chamber temperature (°C); grey dashed line, chamber temperature set point; red triangles, seawater salinities (*psu*). A is the ice growth period, B is the ice temperature equilibration period and C is the experiment period.
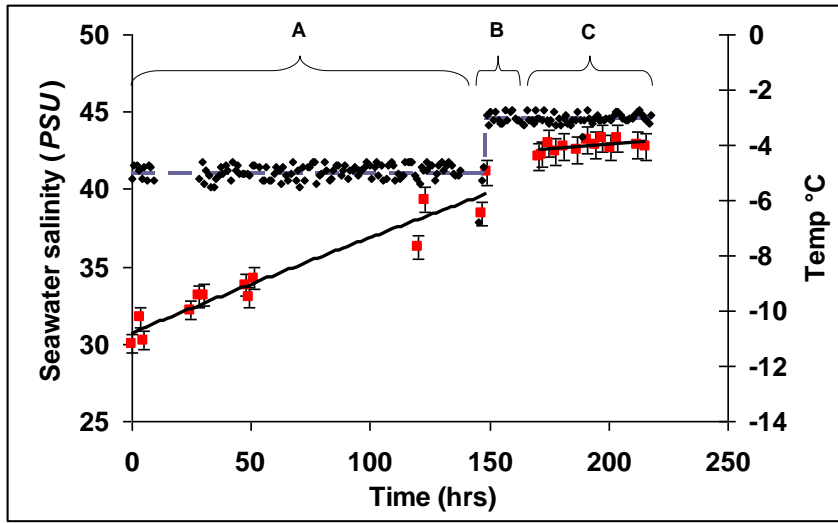
Figure 5.14 Underlying seawater salinities during experiment 3. Black diamonds, measured ambient chamber temperature (°C); grey dashed line, chamber temperature set point; red squares, seawater salinities (*psu*). A is the ice growth period, B is the ice temperature equilibration period and C is the experiment period.

5.3.4 Calculated VOIC diffusion coefficients and brine volumes through sea-ice

Figures 5.15 and 5.16 depict the calculated *p* values and the mean VOIC brine diffusion coefficients for each experiment through the top 4.2 cm of the sea ice. The *x* axis error in figure 5.15 is the thermistor error (± 0.5 °C) at each ice depth. Calculated *p* errors ranged from 2.7 -12.0 % and 16.8 - 20.0 % for experiments conducted at a chamber temperature of -14°C (experiment 1) and -3 °C (experiments 2 and 3) respectively. The x axis error in figure 5.16 is the error as quoted by Wilke and Chang (1955) (±10%). Errors on the y axis in both figures reflect the ice depth sampled to generate each data point.

Both the calculated *p* values and calculated mean VOIC diffusion coefficients (*D*) in brine for each experiment strongly correlate with sea ice temperature, increasing linearly with ice depth. This is due to the temperature dependence of the calculated *p* values and the VOIC diffusion coefficients within the sea ice microstructure, EQ 5.3 and 5.5 respectively. The calculated surface brine diffusion coefficients of the experiments conducted at -3 °C (between $5.3 - 8.1 \times 10^{-5}$ cm^2 s^{-1}) are ~ 4.5 times greater than those calculated at -14 °C (*D* between $1.3 - 1.5 \times 10^{-5}$ cm^2 s^{-1}). All calculated diffusion coefficients are in good agreement with previously determined values for O_2 and SF_6 in laboratory sea-ice under

similar conditions (3 – 20 x 10^{-5} cm^2 s^{-1}, for sea ice grown at seawater salinities of 33 -35 *psu* and temperatures of -5 °C to -20 °C (Loose *et al.*, 2011).
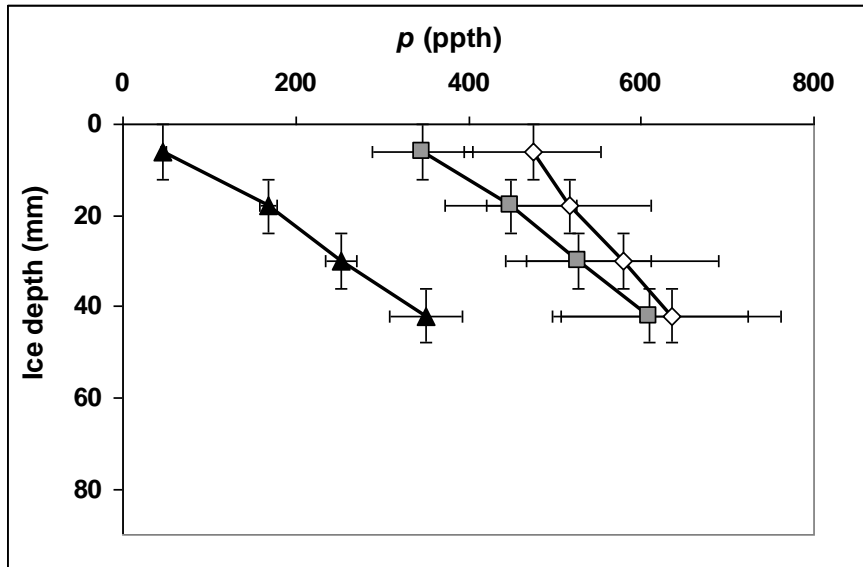
Figure 5.15 Calculated *p* values against sea-ice depth for the three artificial seawater experiments. Black triangles, experiment 1 (-14ºC); empty diamonds, experiment 2 (-3°C fast ice growth); grey squares, experiment 3 (-3°C slow ice growth). Brine volumes calculated using EQ 5.5 (Frankenstein and Garner, 1967).
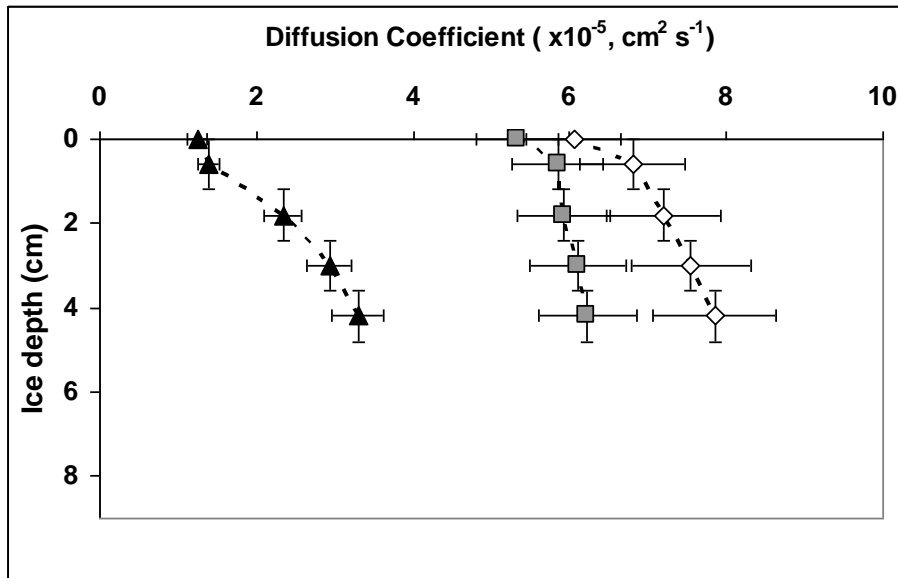
Figure 5.16 Calculated VOIC diffusion coefficients in brine against sea-ice depth for the three artificial seawater experiments. Black triangles, experiment 1 (-14ºC); grey squares, experiment 3 (-3°C slow ice growth); empty diamonds, experiment 2 (-3°C fast ice growth). Diffusion coefficients calculated using EQ 5.5 (Wilke and Chang, 1955). Diffusion coefficients at an ice depth of 0 cm represent calculated values in surface brine.

5.3.5 Depth resolved VOIC concentrations within sea ice

Analysis of the VOIC concentrations in both the sea ice and brine were carried out after each experiment to confirm their permeation through the ice column, as shown in Figures 5.17 and 5.18, respectively. The sea ice and brine concentrations (nmol dm^{-3} melt water and brine, respectively) are plotted along with the under-ice water concentrations at t$_{end}$ for each VOIC. The established x axis errors for the sea ice and fresh ice (section 5.3.6) experiments were 9.0 %, 10.5 %, 8.5 % and 8.6 % for CH$_3$I, C$_2$H$_5$I, 2-C$_3$H$_7$I and 1-C$_3$H$_7$I, respectively. These errors were propagated from an arbitrary 5 % sampling error and the standard deviations of the regression lines of the VOIC permeation rates and the internal standard corrected VOIC calibration curves, both of the latter were required for external calibration. The observations can be explained in terms of VOIC diffusion rates through the brine channels coupled with their fractional connectivity.

Fractional connectivity is defined as the proportion of brine inclusions intersecting both the upper and lower ice surfaces required for sea/ice/air gas transfer. Recent studies carried out on saline solutions using dual model analysis and X-ray Computed Tomography (CT) imaging at 100 – 1000 μm length scales (Pringle *et al*., 2007 and Light *et al*., 2003) suggest that the fractional connectivity of vertical brine inclusions is influenced by *p*, and hence, ultimately, temperature. The data illustrated that at a temperature of -18 °C and *p* of 2.2 %, many disconnected brine inclusions were detectable without any vertical percolating path from the lower to the upper surface. At a temperature of -4 °C, *p* of 8.8 %, the brine inclusions were vertically elongated with "shunts" or "necks" connecting them, and the vertical percolation path was well connected through the ice. In other work (Golden *et al.*, 2007), X-ray CT was again used to investigate the thermal evolution of inclusion morphology and fractional connectivity. Fractional connectivities of ~50 % and ~1 % were observed at -3 °C and -14 °C respectively, through an ice thickness of 0.8 cm at a salinity of 9.3 ppth.

Additionally, lateral brine channel connectivity can form at higher *p* values by the formation of thin pores between brine inclusions. Such connectivity has been observed in land-fast first year sea ice and lab based measurements above *p* values of 8 - 10 % (Ingham

et al., 2008; Pringle *et al.*, 2007). All p_c values measured within the ice column for the artificial seawater experiments in this study were above this value, excluding those within the top 1.2 cm for experiment 1 (47 ppth), suggesting relatively high degrees of both lateral and vertical brine connectivity throughout, figure 5.15. It is this thermal evolution of both vertical and lateral brine channel connectivity, and the diffusion coefficients (D) of compounds therein, which is believed to be the determining factor for the observations within this study.

Both experiments conducted at an experimental temperature of -3 °C exhibited similar VOIC concentration gradients within the ice. Both the VOIC concentrations in ice and p values throughout the ice column suggest that the sea – ice percolation threshold is met, hence the brine networks within are permeable to vertical transport through the column. This is supported by the VOIC concentrations in brine which are up to ~ 4 times higher than those in the equivalent volume of ice melt-water throughout the ice column. The VOIC concentration gradients within the brine were similar to those within the sea-ice, and during experiment 3 (-3 ºC slow ice growth) reach concentrations at 4.2 cm depth which are comparable to those of the under-lying water.

Whether the micro-structural evolution and subsequent gas transport properties of sea ice during warming or cooling processes is reversible or associated with significant hysteresis effects is currently of considerable interest when considering sea ice transport properties. This phenomena is addressed using the experiments conducted at -3 °C (experiments 2 and 3) which were conducted under identical experimental conditions except for the temperatures in which the sea ice was grown (table 5.1). The ice grown during experiment 3 (slow growth) was generated over 150 hours at a temperature of -3 °C (ice growth rate of 1.30 x 10^{-5} cm s^{-1}) and that of experiment 2 (fast growth) was over 24 hours at -20 °C and conditioned for 15 hours at -3 °C (ice growth rate of 4.20 × 10^{-5} cm s^{-1}), Table 5.1. Despite the same final temperature, p values were ~ 20 % higher using the faster ice growth regime. This is due to both gravity brine drainage and the effects that slower ice growth rates have on sea ice microstructure (section 5.3.2). Slower ice growth velocities cause increased brine

spacing and decreased brine consolidation and hence lower *p* values per unit volume, as described in section 5.3.2 (Nakawo and Sinha, 1981).

The calculated *p*/VOIC ratios throughout the ice column for experiment 2 (fast ice growth at -3 ºC) were 11.0 ± 0.9, 22.8 ± 4.2, 63.0 ± 7.0, 70.7 ± 12.0 for CH_3I, C_2H_5I, $2\text{-}C_3H_7I$ and $1\text{-}C_3H_7I$ respectively. The calculated ratios throughout the ice column were $\sim 30 - 55$ % higher during experiment 3 (slow ice growth). A possible explanation for this is that the vertical and lateral fractional connectivity of brine channels within the ice column which underwent fast growth (experiment 2) are not as high as those generated at the slower growth rate (experiment 3). Despite the sea ice in experiment 2 having a greater *p* value than the sea ice in experiment 3, it is possible that the ice microstructure has undergone an irreversible change during it's growth at -14 °C in that much of its brine resides within isolated inclusions within the ice, unable to contribute to the connectivity of the brine channel network and influence rates of diffusion. Alternatively, following the growth of the fast grown sea ice at -14 °C (experiment 2), the temperature equilibration period of the ice column at -3 °C (~24) hours may have been insufficient for any precipitated salts within the brine channels to dissolve into solution. In which case, these precipitated salts could theoretically have physically reduced sea ice permeability by restricting brine channels which would have otherwise contributed to vertical brine transport, as previously observed by Light *et al.* (2003).

The experiment carried out at a temperature of -14 °C (experiment 1) exhibits a very different vertical profile for both *p* values and VOIC concentrations to those conducted at -3°C (experiments 2 and 3). The concentrations of each compound within the upper 2.4 cm are negligible. This trend is supported by the *p* value within the upper 1.2 cm (4.7 %) which is below the percolation threshold. The upper ice is effectively impermeable to brine migration and exhibits a "capping effect" for the transport of volatiles to the overlying air. A similar phenomena was previously observed during the ANFLUX experiment in the eastern Weddell Sea where most of the sea ice layer remained below the critical temperature for percolation and the top 5 cm exhibited this "capping effect" (Golden *et al.,* 1998).
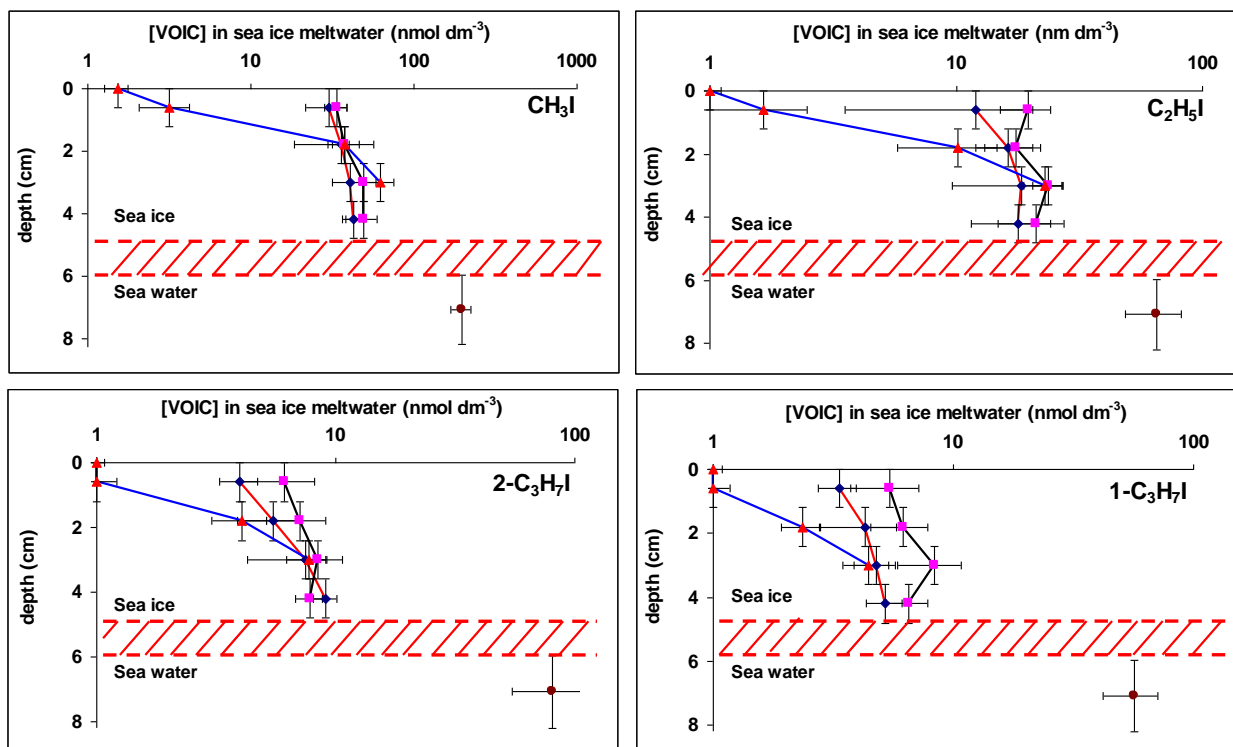
Figure 5.17 Depth profile of VOIC concentrations (nmol dm^{-3} of bulk sea ice meltwater). Red triangles, experiment 1, pink squares, experiment 3, blue diamonds, experiment 2, brown circles, seawater concentrations. The y error bars on seawater concentrations at bottom of plots reflect the standard deviation of ice depths between the experiments. Shaded area represents bulk sea ice depths not sampled.
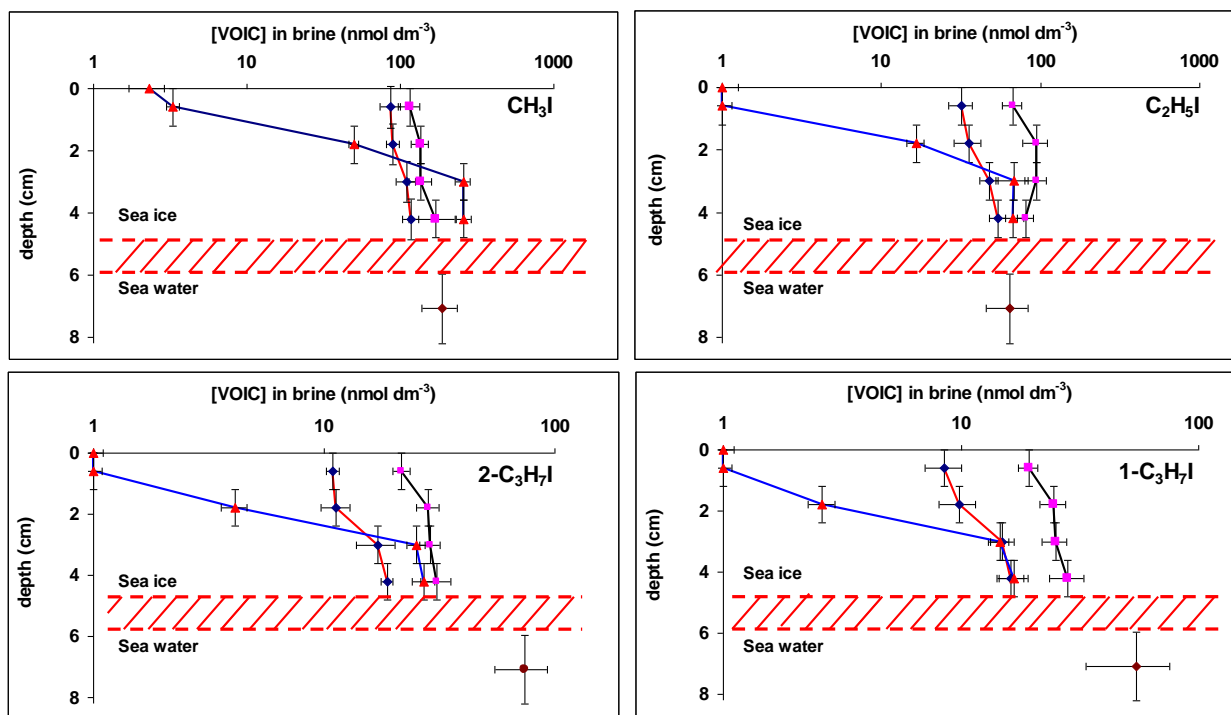
Figure 5.18 Depth profile of VOIC concentrations (nmol dm^{-3} of brine). Red triangles, experiment 1 (-14°), pink squares, experiment 3 (-3ºC slow ice growth) blue diamonds, experiment 2 (-3ºC fast ice growth), brown circles, seawater concentrations. The y error bars on seawater concentrations at bottom of plots reflect the standard deviation of ice depths between the experiments. Shaded area represents bulk sea ice depths not sampled.

Figures 5.19, 5.20 and 5.21 show a comparison of the VOIC sea ice concentrations and *p* corrected VOIC concentrations in brine against ice depth for experiments 1, 2 and 3 respectively. The *p* corrected brine VOIC concentrations were calculated by multiplying the brine volume fraction by the measured VOIC concentrations in brine for each ice depth. The established errors on the *x* axis were propagated from an arbitrary 10% sampling error, the depth dependent thermistor error, the standard deviations of the regression lines of the VOIC permeation rates and the internal standard corrected VOIC calibration curves. These *x* axis errors ranged between ± 26 -31% and ±13 -21% for experiments conducted at -3ºC and -14°C respectively.

The sea ice VOIC concentrations and brine corrected VOIC concentrations were equivalent within error for each experiment in the upper ice column (1.2 – 2.4 cm). This confirms not only the reliability of the VOIC concentrations determined in the ice/brine and the calculated *p* values within this depth, but that the VOICs resided in the brine within the sea

ice microstructure during sampling. In the lower ice column (3.0 – 4.2 cm), the *p* corrected VOIC brine concentrations were consistently higher than measured VOIC sea ice concentrations. The calculated brine volumes used were calculated using EQ 5.3 (Frankenstein and Garner, 1967) and represent the total fraction of brine per unit volume of sea-ice. Quantities of brine can be present within isolated pockets within the sea ice microstructure which would not contribute to the vertical transport of VOICs, hence contain negligible VOIC concentrations (section 5.3.2). This correction does not take into account such isolated brine pockets hence the *p* corrected brine concentrations would typically be overestimated, as observed. This overestimation increases with *p* and reflects the increase in non-quantifiable error associated with sampling ice and brine at increasing depth during the experiment. An arbitrary 10% sampling error is included on the propagated ice and brine *x* errors at all depths to account brine and ice mixing during sampling.
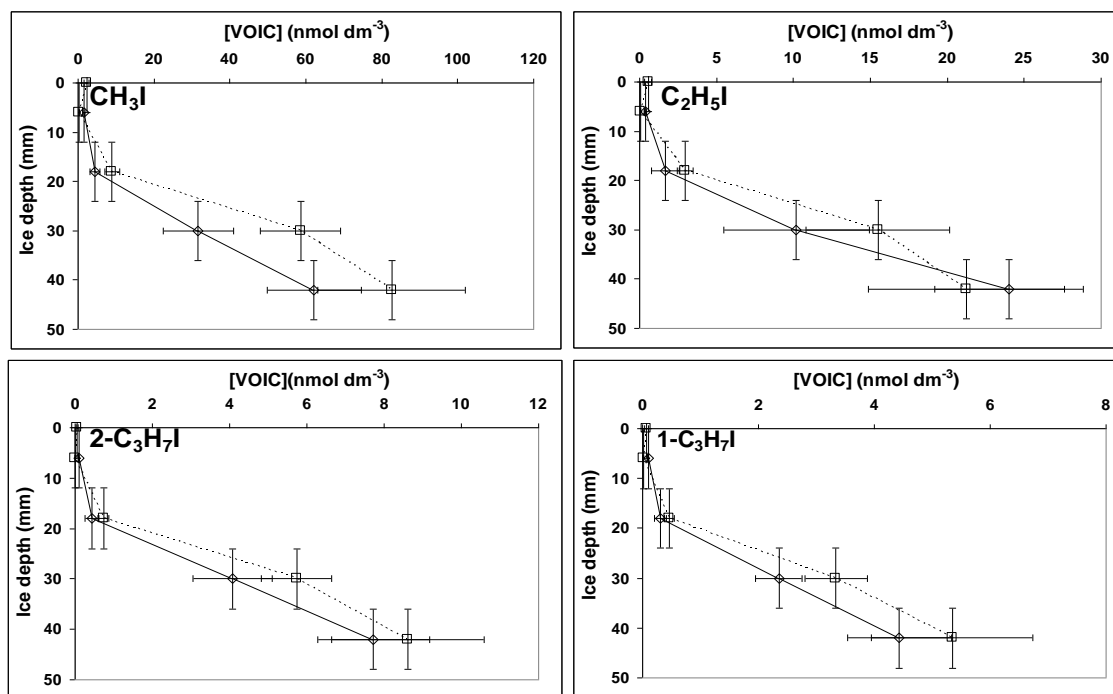
Figure 5.19 Measured VOIC concentrations in sea ice and p_c corrected brine through the ice column for experiment 1 (-14°C). Filled line, measured [VOIC] in sea ice; dashed line, *p* corrected [VOIC] in brine.
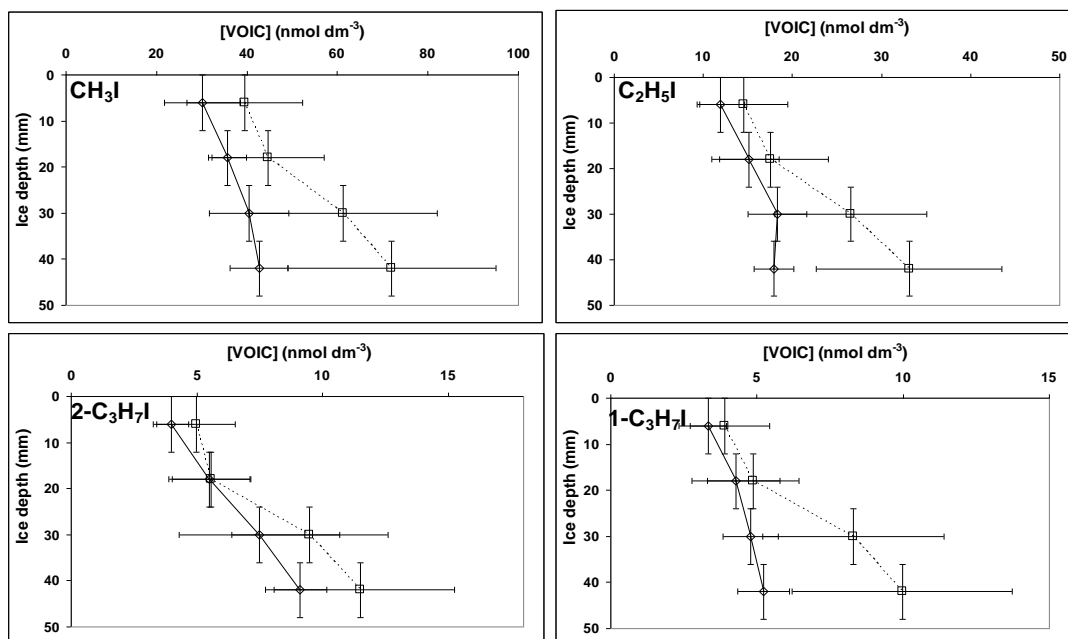
Figure 5.20 Measured VOIC concentrations in sea ice and *p* corrected brine through the ice column for experiment 2 (-3ºC fast ice growth). Filled line, measured [VOIC] in sea ice; dashed line, *p* corrected [VOIC] in brine.
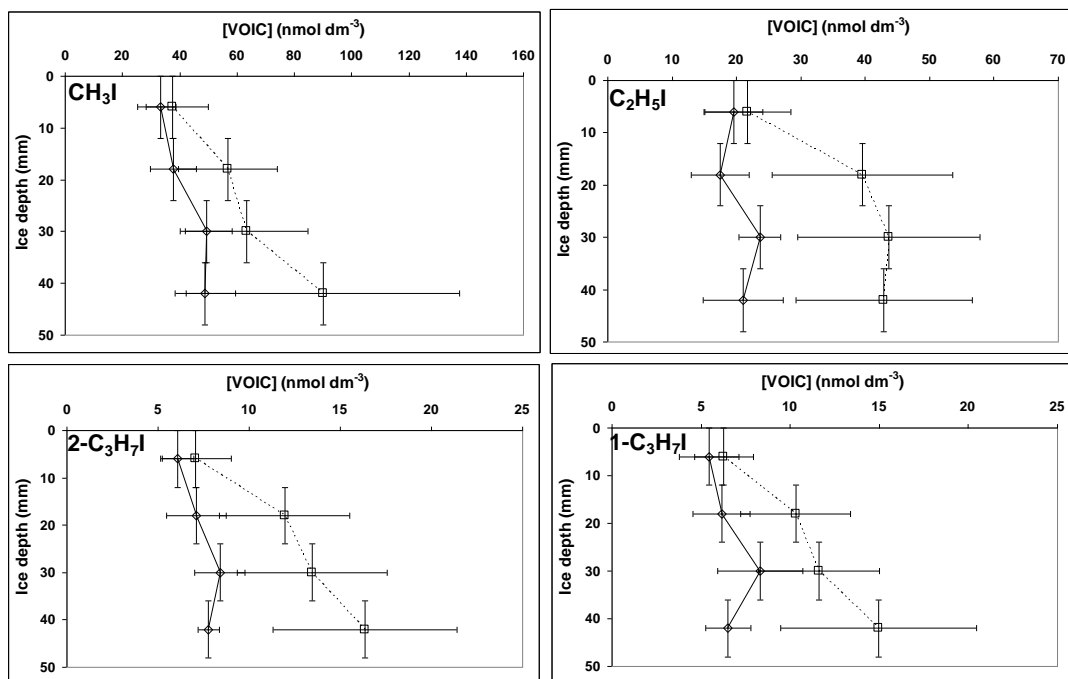
Figure 5.21 Measured VOIC concentrations in sea ice and *p* corrected brine through the ice column for experiment 3 (-3ºC slow ice growth). Filled line, measured [VOIC] in sea ice; dashed line, *p* corrected [VOIC] in brine.

5.3.6 Depth resolved VOIC concentrations in fresh ice

Figures 5.22 and 5.23 show VOIC concentrations within the fresh ice columns for the control experiments conducted at both -3 °C (Experiment 4) and -14 °C (Experiment 5) respectively. The VOIC concentrations in fresh ice are compared to the underlying freshwater concentrations observed prior to the addition of the aqueous mixed VOIC standard (section 5.2.2). The calculated x axis errors for these experiments were the same as they were for the sea ice experiments, section 5.3.5. The negligible VOIC concentrations present within the fresh ice were comparable to those within the Milli-Q water before the introduction of the mixed aqueous VOIC standard. The data provided no evidence for the vertical transport from the underlying water which was in good agreement with the underlying fresh water loss VOIC rates determined during the experiment; refer to Appendix, 5.13 to 5.20. Both data sets support the well established assumption that a brine channel network is required for vertical gas transport through ice (Golden *et al.*, 1998).

The VOIC profiles within fresh ice suggested significant surface enhancements for each compound (top 0 – 24 cm) during both experiments. As these freshwater experiments were conducted under dark conditions, in the absence of salt (freshwater ~ 0.0 *psu*) *in-situ* abiotic VOIC production within the surface ice layer is unlikely to be the explanation. The most plausible explanation for this observation is instead the direct scavenging of VOICs (or residual organisms within the tank which biogenically produce them) from the water column by dense frazil ice during the onset of freezing.

A mechanism previously used to explain surface enhancements of chemical concentrations and organisms in young first year sea ice is that of frazil ice scavenging (Eicken, 2008). Frazil ice crystals form on particles suspended within the water column and particles also adhere to them as they form and rise to the sea surface. This mechanism of scavenging from the water column during frazil ice formation can be considered as primary filtration. Previous studies of brine and sea ice suggest that the major frazil ice scavenging mechanism is through primary filtration, but that ice nucleation and resulting chemical concentration should not be ruled out (Ackley, 1982; Garrison *et al.*, 1983). Secondary filtration could possibly occur in which Langmuir circulation (Stavn 1971, Bainbridge,

1957) provides the likely mechanism. Langmuir circulation aggregates frazil ice in converging circulation cells (Martin, 1981). These aggregated surface frazil ice crystals could act as a filter for suspended organisms transported within these cells, leading to their enhancement in the surface ice layer.

The surface enrichment factors ([VOIC] surface ice/[VOIC] freshwater) averaged 3.36 ± 2.82 (n = 4) and 2.28 ± 1.80 (n = 4) for experiments conducted at -3 °C (experiment 4) and -14°C (experiment 5) respectively, figures 5.22 and 5.23. These enrichment factors are in good agreement with the laboratory studies of Garrison et al (1983). During these experiments the diatoms *Nitschia sp.* and *Chaetoceros neogracile* were cultured from the Antarctic pack ice and used as a proxy for frazil ice scavenging in an ice generation chamber where ice was grown at -20°C. Chlorophyll a enrichment factors of 1.8 ± 0.9 were observed in the sea ice of these experiments. There was no indication that the resulting chlorophyll a enrichment factors had any dependence upon the concentration of the initial algal suspensions, organisms used, the duration of the experiment run or the amount of frazil ice formed. Instead the relative quantities scavenged from the water column were assumed to be dependent upon the depth at which frazil ice forms, hence the distance it must travel before it can become consolidated at the ice surface.

The depth at which natural frazil ice is generated is not well established but it has been suggested that frazil ice formation and transport from thermohaline convection in polar regions can extend to tens of metres below the sea surface (Foster and Weiss, 1989). It seems likely that the frequency of encounters between suspended algal cells and frazil ice crystals would be higher in nature, hence this filtration effect would be significantly enhanced. This goes someway toward explaining previous field observations of Arctic seasonal sea ice in which surface Chl a concentrations were significantly higher in the ice surface layer than the remaining ice column (Sturges, 1997).
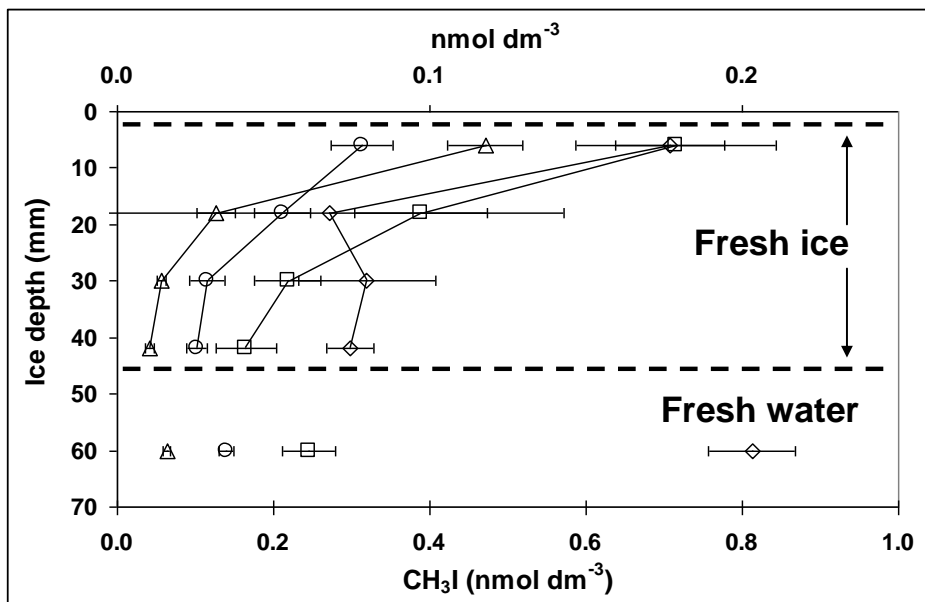
Figure 5.22 VOIC concentrations measured within fresh ice during experiment 4 (-3°C). Empty diamond, CH_3I; empty squares, C_2H_5I; empty triangles, $2-C_3H_7I$; empty circles, $1-C_3H_7I$.
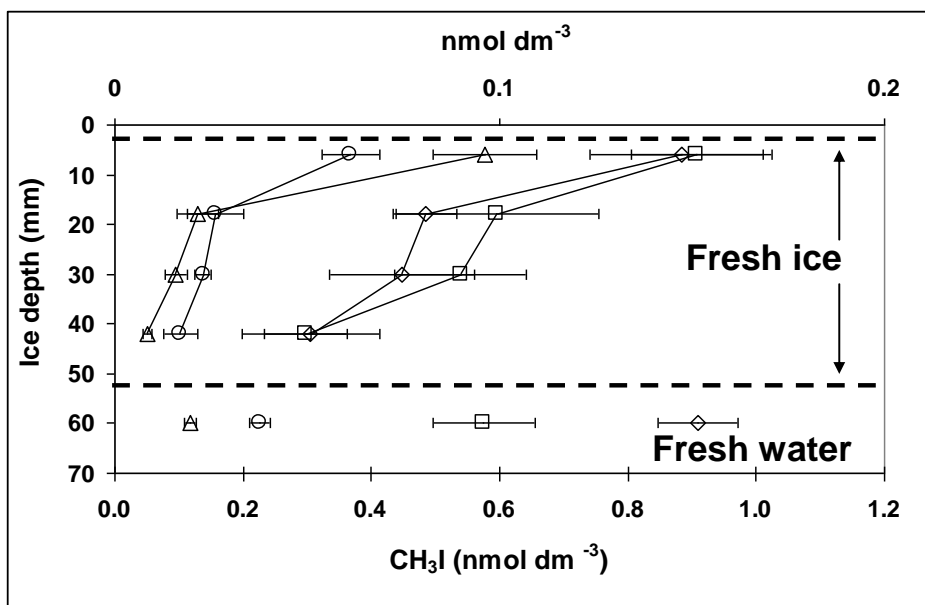
Figure 5.23 VOIC concentrations measured within fresh ice during experiment 5 (-14°C). Empty diamond, CH_3I; empty squares, C_2H_5I; empty triangles, $2-C_3H_7I$; empty circles, $1-C_3H_7I$.

5.3.7   Under-sea ice VOIC concentration evolution

Figure 5.24 illustrates VOIC loss rates from artificial seawater at the different temperatures investigated over their experimental periods. The propagated errors for these experiments

were 4.0 %, 7.8 %, 3.3 % and 3.6 % for CH_3I, C_2H_5I, $2\text{-}C_3H_7I$ and $1\text{-}C_3H_7I$, respectively. The errors for VOIC loss rates for the experiments were propagated from the standard deviations of the regression lines of the VOIC permeation rates and the internal standard corrected VOIC calibration curve, both of which were required for external calibration. Refer to Appendix 5.1 to 5.12 for raw data.

A significant difference in the profiles of loss rates from the underlying seawater is observed at the two temperatures investigated, due to differing fractional connectivity and hence vertical transport rates through the sea ice. The loss rates from the seawater experiment conducted at -14 °C, experiment 1, shows that an initial rapid loss of all VOIC concentrations occurs from the seawater, which plateaus over time. This suggests an incomplete brine network within the ice column, the result of which is that the VOICs are lost from the water until a steady state is reached in the brine channels. This observation is consistent with the ice core and brine data described previously (section 5.3.5).
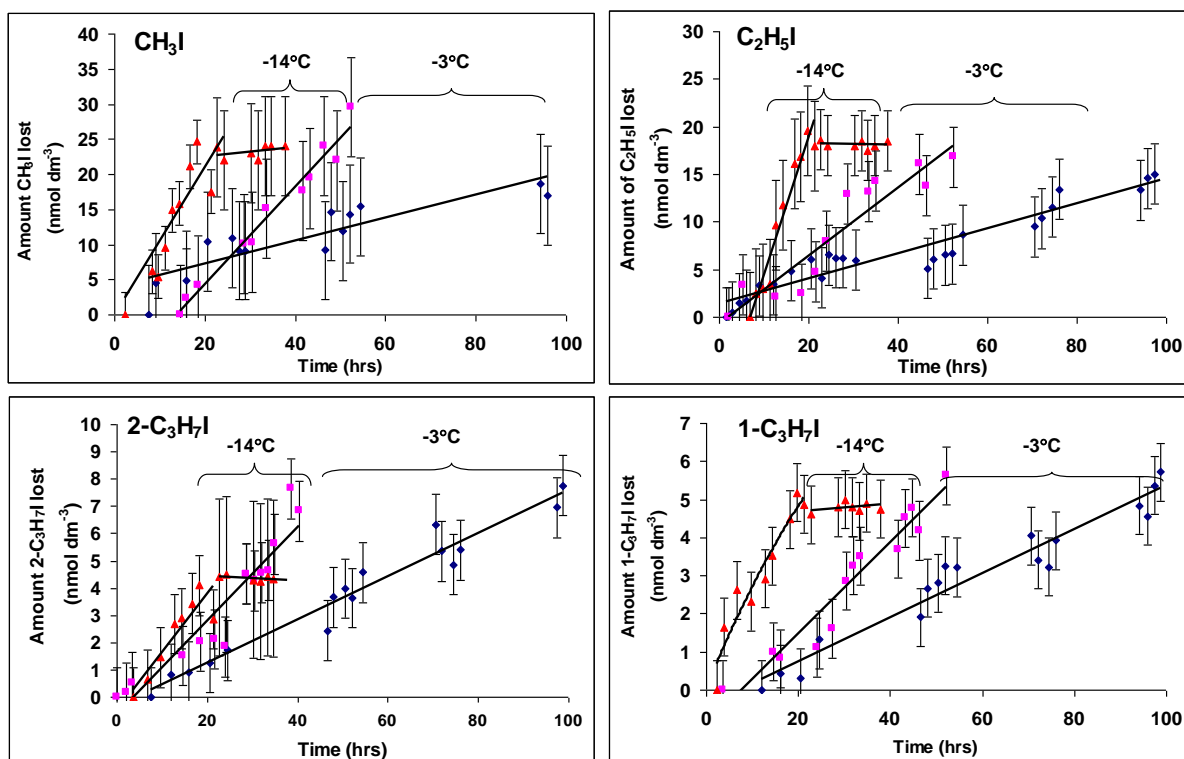
Figure 5.24 Normalised losses in under-ice aqueous halocarbon concentrations (nmol dm^{-3}) for the experimental conditions investigated. Pink squares, experiment 3 (slow ice growth); blue diamonds, experiment 2 (fast ice growth); red triangles, experiment 1 (-14°C).

218

5.3.8 Calculated diffusive fluxes from the QLL to air

Table 5.2 shows fluxes inferred from the molar balance of the experimental system (section 5.2.7) and the diffusive fluxes calculated from surface brine VOIC concentrations (section 5.2.8). Molar balance inferred fluxes were effectively zero within experimental error for all VOICs during the -14 °C investigation (experiment 1). The fluxes inferred from the molar balance during experiment 2 (-3 ^{o}C fast ice growth rate) were 733.2 ± 322.7, 575.6 ± 354.2, 245.0 ± 109.5, and 191.8 ± 80.7 nmol m^{-2} d^{-1} whereas the calculated diffusive flux values were 1222.3 ± 249.6, 552.9 ± 207.7, 278.0 ± 109.5 and 233.6 ± 80.7 nmol m^{-2} d^{-1} for CH_3I, C_2H_5I, 2-C_3H_7I and 1-C_3H_7I, respectively. The fluxes inferred from the molar balance during experiment 3 (-3 ^{o}C slow ice growth rate) were 1222.3 ± 249.6, 552.9 ± 207.7, 278 ± 109.5, and 233.6 ± 80.7 nmol m^{-2} d^{-1} whereas the calculated diffusive flux values were 703.1 ± 322.7, 575.6 ± 354.2, 245.0 ± 109.5 and 191.8 ± 80.7 nmol m^{-2} d^{-1} for CH_3I, C_2H_5I, 2-C_3H_7I and 1-C_3H_7I, respectively.

Both the VOIC flux rates inferred from the molar balance and the calculated diffusive fluxes for each experiment were in good agreement with one another when considering the established margins of error for each VOIC. The diffusive flux rates for each VOIC species are generally slightly lower than those inferred from the molar balance calculation. Such a contrast is expected as the calculated diffusive flux rates assume the concentration gradient across the QLL is the same as that of the brine in the upper ice, and as such offer a lower limit of VOIC flux rates. The calculated diffusive flux represents a lower limit, since the relative concentration gradient in the QLL maybe greater than in the surface brine, because of turbulent losses from the QLL to the air above.

Of the experiments carried out at -3 ^{o}C, experiment 3 (slow ice growth) exhibited much faster (by ~ factor of two) VOIC loss rates from the water than experiment 2 (fast ice growth). This is consistent with the higher concentrations (~ factor of two) of VOICs in ice and brine in the slow ice growth experiment, as discussed, and can be explained by the differing ice microstructures in each scenario. The microstructure of the ice column within experiment 2 (fast growth) has possibly undergone significant hysteresis effects during ice growth in that a higher fraction of the brine resides within isolated inclusions within the ice,

unable to contribute to the connectivity of the brine channel network and influence rates of VOIC diffusion.

Transfer velocities ($k_{ice \to air}$ and $k_{QLL \to air}$) were inferred for each VOIC by dividing the experimental molar balance flux of each species by the [VOIC] in the surface ice (C_{ice}) and the [VOIC] in the QLL (C_{QLL} x V), respectively (EQ 5.13 and 5.11, respectively). Calculated $k_{ice \to air}$ values and $k_{QLL \to air}$ at -3 °C were between $2.4 \times 10^{-2} - 6.17 \times 10^{-2}$m d^{-1} and $2.3 \times 10^{-3} - 6.2 \times 10^{-3}$m d^{-1}, respectively. $k_{sea \to ice \to air}$ transfer velocities were inferred for each VOIC by dividing the experimental molar balance flux of each species by the [VOIC] in the underlying water (C_w) (EQ 5.12). Calculated $k_{sea \to ice \to air}$ values at -3 °C were between 4.2×10^{-2} and 1.2×10^{-1} m d^{-1} which were in relatively good agreement with previous values determined for CO_2 (1.4×10^{-1} m d^{-1}, Loose *et al.* 2011). At -14 ºC, the surface brine channels are not connected as shown by the fact that there was no loss from the underlying water after the initial 24 hours of the experiment (Figure 5.24) nor appreciable concentrations in surface ice/brine (Figs 5.17 and 5.18). Therefore no gas transfer velocities could be inferred for the experiment at -14 °C as the inferred flux from the molar balance was effectively zero, table 5.2.

5.3.9 Comparison of sea-ice-air to sea-air fluxes

Assuming that the VOIC diffusive transfer velocities determined in our experiments are representative of those operating in the polar environment, we can compare them to open water gas exchange to estimate the relative importance of consolidated sea-ice-air and open lead sea-air fluxes. Hypothetical seawater-air transfer velocities in the absence of ice (k_w) were calculated using the Nightingale parameterisation and a typical wind speed of 7 m s^{-1} (Nightingale *et al.*, 2000). The calculated $k_{sea \to ice \to air}$ values inferred from the molar balance at -3 ºC were between 0.1 and 0.2% of these k_w values.

Previous studies estimate fractional ice coverage (*f*) in the seasonal sea ice zone to typically range between 90% (*f* ~ 0.1) during the winter and < 70% (*f* > 0.3) during summer months (Tanning and Fanning, 1991). Hypothetical k_w values were determined for *f* ~ 0.1 by linearly scaling the k_w values in the absence of sea-ice to 10%. The average $k_{sea \to ice \to air}$

values inferred by the molar balance at -3 ºC represented 1.0 %, 2.1 %, 1.7 % and 2.1 % of $f \sim 0.1$ k_w values for CH_3I, C_2H_5I, $2\text{-}C_3H_7I$, $1\text{-}C_3H_7I$ respectively. These values offer an upper limit for VOIC diffusion through newly grown first year sea-ice at surface temperatures above the percolation threshold, not taking into account *in-situ* losses or the chemical and biogenic production of VOICs within the brine network.

VOIC	Mass diffusion length (Ld) cm[a]	Calculated diffusion coefficient (D) within sea-ice[c] (cm^2 s^{-1})	Flux calculated from molar balance[d] (nmol m^{-2} d^{-1})	Diffusive flux through surface sea ice[e] (nmol m^{-2} d^{-1})	Sea-ice to air transfer velocity[f] ($k_{seaice\to air}$) m d^{-1}	QLL to air transfer velocity[f] ($k_{QLL\to air}$) m d^{-1}
Experiment 1						
(-14ºC) CH_3I	4.1 ± 0.4[b]	$1.3 \times 10^{-5} \pm 0.1$	122.8 ± 462	0.5 ± 0.1	0.0	0.0
C_2H_5I	4.5 ± 0.5	$1.5 \times 10^{-5} \pm 0.2$	-18.5 ± 383	0.1 ± 0.1	0.0	0.0
$2\text{-}C_3H_7I$	4.1 ± 0.5	$1.4 \times 10^{-5} \pm 0.1$	16.7 ± 133	0.03 ± 0.01	0.0	0.0
$1\text{-}C_3H_7I$	4.1 ± 0.5	$1.4 \times 10^{-5} \pm 0.1$	16.2 ± 92	0.03 ± 0.01	0.0	0.0
Experiment 2						
(-3ºC fast ice						
growth) CH_3I	9.2 ± 0.9	$6.9 \times 10^{-5\pm} \pm 0.7$	733.2 ± 322	755.1 ± 52	2.4×10^{-2}	2.3×10^{-3}
C_2H_5I	10.1 ± 1.0	$8.1 \times 10^{-5} \pm 0.8$	575.6 ± 354	643.5 ± 82	4.8×10^{-2}	5.0×10^{-3}
$2\text{-}C_3H_7I$	9.76 ± 1.0	$7.7 \times 10^{-5\pm} \pm 0.8$	245.0 ± 109	217.6 ± 17	6.1×10^{-2}	5.0×10^{-3}
$1\text{-}C_3H_7I$	9.76 ± 1.0	$7.7 \times 10^{-5} \pm 0.8$	191.8 ± 80	$214.3. \pm 15$	5.7×10^{-2}	6.2×10^{-3}
Experiment 3						
(-3ºC slow ice						
growth) CH_3I	7.39 ± 0.7	$5.3 \times 10^{-5} \pm 0.5$	1222.3 ± 249	703.1 ± 48	3.7×10^{-2}	3.6×10^{-3}
C_2H_5I	8.03 ± 0.8	$6.3 \times 10^{-5} \pm 0.6$	552.9 ± 207	217.9 ± 28	2.8×10^{-2}	2.8×10^{-3}
$2\text{-}C_3H_7I$	7.89 ± 0.8	$6.0 \times 10^{-5} \pm 0.6$	278.0 ± 109	133.8 ± 11	4.6×10^{-2}	4.4×10^{-3}
$1\text{-}C_3H_7I$	7.89 ± 0.8	$6.0 \times 10^{-5} \pm 0.6$	233.6 ± 80	130.6 ± 10	4.3×10^{-2}	4.1×10^{-3}

Table 5.2 Experimentally determined VOIC fluxes, transfer velocities and calculated hypothetical diffusion coefficients.

[a]Mass diffusion length from initialisation of experiment to end .

[b]Tabulated errors represent 1 σ estimated uncertainties calculated from propagating the RSDs of the VOIC permeation rates, the calibration curve and internal standard precision.

[c]Compound-specific diffusion coefficients calculated for brine solution in upper 1.2 cm of ice.

[d]Molar balance represents the VOIC loss rate over the experimental period. Fluxes for experiment 1 were calculated from point steady state had been established.

[e]Fluxes calculated using the VOIC concentration gradients in the upper 2.4 cm of brine.

[f]Gas transfer velocity values calculated using EQ 5.12 and EQ 5.13 respectively.

5.4   Physico-chemical characteristics of Hudson Bay sea ice

The Hudson Bay region in eastern Canada is a small enclosed region of the Atlantic ocean which is characterised by a 1.2×10^6 km^2 sea surface area and an average depth of 128 m. The surrounding drainage area of Hudson Bay, comprising some 4×10^6 km^2, provides a major source of freshwater to the Bay. The relative proportions and mixing characteristics of the continental freshwaters and the marine waters advected from the Atlantic Ocean determine the general characteristics of biological production in Hudson Bay (Legendre *et al.*, 1981).

During COBRA, two ice cores were sampled on the coast of Kuujjarrapik in proximity to the Manitounuk Sound region, as outlined in section 5.2.11. Within this region water mass characteristics are greatly influenced by the intrusion of brackish fresh water from the plume of the Great Whale River, figure 5.4. Such changes in seawater salinity not only impact *in-situ* biological production but also sea ice microstructure during formation (section 5.2).

5.4.1 Salinity distribution through Hudson Bay Sea ice

Previous salinity measurements of the under ice seawater adjacent to the Great Whale River estuary (figure 5.4) during March 1978 were between ~0.5 – 1.0 *psu* (Legendre *et al.*, 1981), considerably lower than those observed in open ocean seasonal ice zones. During COBRA, mean under ice seawater salinity measurements conducted adjacent to the experimental site at core position 2 (9th of March 2008) and ~7 km into the bay at core position 1 (6th of March 2008) were 5.3 ± 0.8 and 20.4 ± 3.0 psu respectively. This difference in seawater salinity between the Great Whale River estuary and waters in the Bay reflects the mixing of the continental freshwaters and marine waters in the region. Reduced seawater salinities during sea ice formation causes reduced salt consolidation within the sea ice microstructure during growth (section 5.3.2), which was observed when comparing the sea ice salinity at the two sites.

The salinity distributions through the Hudson Bay sea ice at both core positions 1 and 2 (figures 5.25 and 5.26 respectively) both exhibit similar profiles with salinities decreasing with depth. The measured salinities, from surface sea ice to the bottom, ranged between 7.5 ±0.8 − 2.8 ±0.3 and 2.8 ±0.3 − 0.8 ± 0.09 psu (to 1 sig fig) for core positions 1 and 2, respectively.

Nakawo and Sinha (1981) previously measured consolidated seasonal sea ice G_i values of 0.09 − 0.17 °C cm^{-1} which were generally in good agreement with that measured during the ice chamber experiment 3 (0.25 °C cm^{-1}, slow growth rate -3°C experiment). Therefore, assuming that the growth rate of the sea ice within the Hudson Bay region was similar to that measured during experiment 3 at a temperature of -3 °C (1.3 x 10^{-5} cm s^{-1}, table 3.1), a k_{eff} of 0.25 can be inferred (section 5.3.1 and 5.3.2). Assuming the mean underlying water salinities observed at core position 1 on the 6th of March 2008 (20.4 ± 3.0) *psu* were the same as those during sea ice formation, a newly grown sea ice salinity (S_i) of 5.1 ± 0.8 was calculated using EQ 5.19 (Cox and Weeks, 1980), figure 5.25. This is in good agreement with the observed mean sea ice salinitiy measured at core position 1 (4.0 ±1.4). Similarly, assuming the mean underlying water salinities observed at core position 2 on the 9th of March 2008 (5.3 ± 0.8) *psu* were the same as those during sea ice formation, a S_i of 1.3 ± 0.2 was calculated (figure 5.26), which was in good agreement with the observed mean sea ice salinitiy (1.8 ±0.8).

Neither sea ice core exhibits the characteristic C shaped salinity distribution observed previously in Arctic seasonal sea ice (Sturges *et al.*, 1997). In the lower ice column, this is probably due to a loss of brine during sampling. In figure 5.25, the measured sea ice salinities are consistently lower than the calculated S_i values except for that measured at an ice depth of 2.5 cm. This could be attributed to *in-situ* gravity brine drainage. Previous work by Nakawo and Sinha (1981) in which a decrease in seasonal sea ice salinity of ~0.5 *psu* per month during an average ambient temperature of -30 °C was measured supports this assumption. The measured salinity of the surface sea ice (upper 2.5 cm) is higher than the S_i, likely due to the presence denser frazil ice in the upper several centimeters of the ice column and salt expelled to the surface layer during initial ice formation (Eicken, 2008).

The sea ice salinity distributions within the Hudson Bay sea ice (figures 5.25 and 5.26) are inversed to those observed in the artificial sea ice during the ice chamber experiments. This highlights the significance of gravity brine drainage in natural sea ice and the effect it has on sea ice microstructure with respect to the age of the ice column.
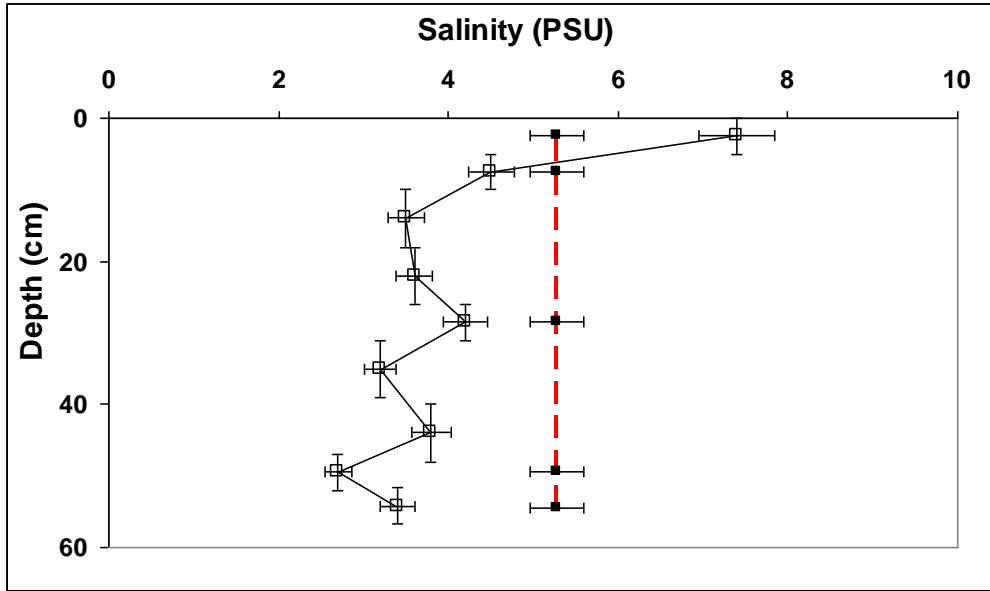
Figure 5.25 Measured and calculated sea ice salinities at core position 1. Empty squares, measured values. Filled squares, calculated values.
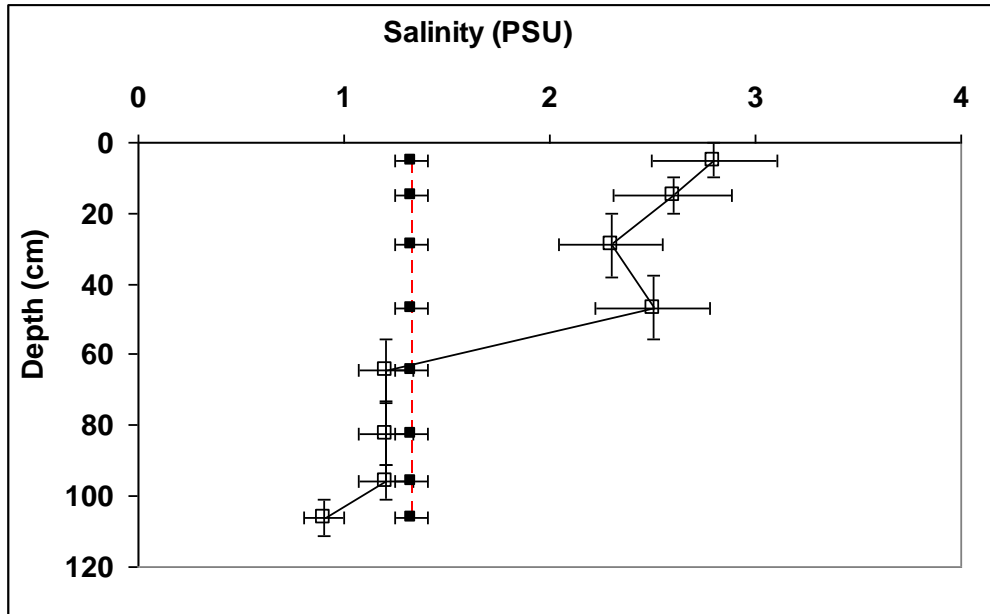
Figure 5.26 Measured and calculated sea ice salinities at core position 1. Empty squares, measured values. Filled squares, calculated values.

5.4.2 Nutrient exchange through Hudson Bay sea ice

When considering the sea-ice sampled during the COBRA campaign, it is possible that nutrient depletion within the sea ice column could have contributed to limited algal growth and the low *Chl a* concentrations measured. However, as the nutrient concentrations were not determined in either sea ice or the underlying seawater during this campaign, it is difficult to conclude with any confidence that nutrient depletion was the direct cause of the low *Chl a* concentrations observed. Nutrient exchange at the ice-water interface and through the Hudson Bay ice columns can be inferred from the calculated brine volumes. These brine volumes were calculated by assuming an extrapolated linear thermal gradient existed through the sea ice between the air-ice interface (-20.1 and -21.0°C for core positions 1 and 2 respectively) and the ice-water interface (-1.85°). This phenomena has previously been observed both in the work contained in this chapter (section 5.3.1) and in seasonal sea ice in the Arctic (Nakawo and Sinha, 1981). The overlying snow thickness measured prior to sampling (~3 cm) was not taken into account but at this thickness is assumed to produce a negligible thermal inertia effect. Brine volume was calculated using these extrapolated temperature values and the measured sea ice salinities through the ice column (figure 5.27) using EQ 5.3.

Figure 5.27 shows the calculated brine volume through the sea ice sampled at core positions 1 and 2. The established errors on the x axis reflect both an arbitrary 10% sampling error and 1% measured salinity error (as quoted by manufacturer). The y errors show the range of ice depths sampled for each data point.

The calculated brine volumes for both ice cores were considerably lower than the established sea ice percolation threshold of 50 – 54 ppth (Golden *et al.,* 1998), excluding that of core 1 at a depth of 56 cm. These calculated values suggest that nutrient exchange did not occur throughout the upper ice column, which could have caused a nutrient deficiency leading to an inhibition in algal growth rates. The data suggests that nutrient exchange could only have occurred on the underside of the sea ice at core position 1. These values are in good agreement with figure 5.28 for core 1 which shows a significant increase

in *Chl a* concentrations at this ice depth, possibly suggesting that nutrient deficiency was not a growth limiting factor in the lower ~ 5 - 10 cm of sea ice.
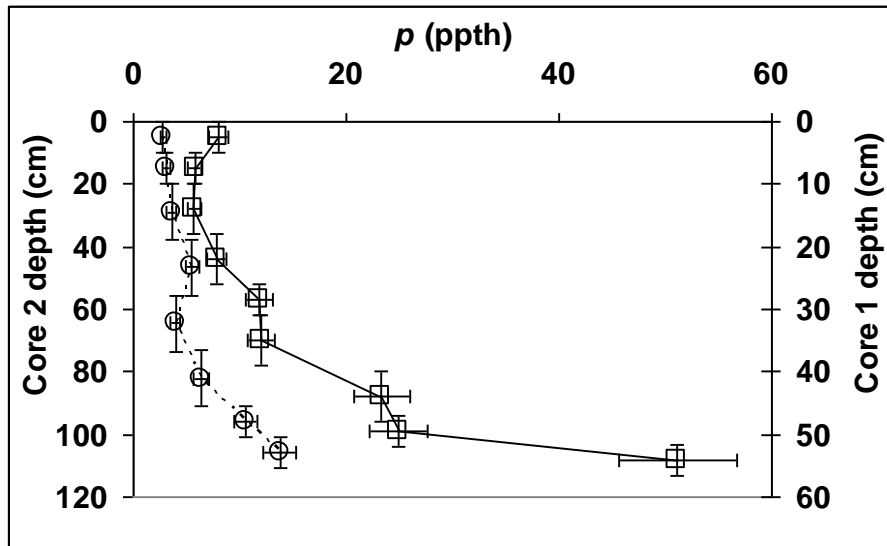
Figure 5.27 Calculated brine volumes through sea ice sampled from Manitounuk Sound. Empty squares, core position 1. Empty circles, core position 2.

5.4.3 Chlorophyll a distributions within Hudson Bay

Figure 5.28 shows the *Chl a* concentrations through sea ice for core positions 1 (total depth ~ 60 cm) and 2 (total depth~ 115 cm), as described in section 2.7.7. The calculated *x* errors were 18%, determined from the propagation of the spectrophotometric error and an arbitrary 10% sampling error. The *y* errors reflect the range of depths each datapoint represents. The *Chl a* concentrations increase with ice depth in the upper ice column with mean concentrations of 53 ± 42 and 369 ± 304 ng dm^{-3} for the sea ice at cores at positions 1 and 2, respectively. Both cores also exhibit substantially higher *Chl a* concentrations on the underside of the sea ice of 2491 ± 448 and 1250 ± 225 for cores 1 and 2 respectively. The *Chl a* concentrations measured in the sea ice during COBRA were considerably lower than those observed previously in Arctic seasonal sea ice. Sturges *et al.* (1997) previously reported sea ice *Chl a* concentrations at Resolute Bay in the Canadian Arctic that ranged between ~1 - 20 mg dm^{-3} through the bulk ice and 200 mg dm^{-3} at the skeletal layer. These *Chl a* concentrations are ~ $10^2 – 10^4$ times higher than the values reported herein.

The spatial distribution of *Chl a* within the underlying seawater in the Hudson Bay region was also investigated during the COBRA campaign. Measurements were conducted close to the experimental site and at core positions 1 and 2 on the 25th of February and the 6th of March respectively. *Chl a* concentrations of 207.2 ±37.3, 247 ±44.6 and 335 ±60.3 ng dm^{-3} were measured in the seawater at the experimental site, and core positions 2 and 1 respectively. The data suggests that the *Chl a* concentrations were dependent upon the freshwater mixing as *Chl a* concentrations increased with distance from the Great Whale River. This supports the work of a previous study (Legendre, 1996) in which it was concluded that salinity has a significant effect on the algal populations within the Bay.

In south eastern Hudson Bay, the salinity of the under ice water and lower ice column is controlled throughout the year by the hydrographic conditions of the fresh water plume supplied by the Great Whale river (Ingram *et al.*, 1981; Legendre *et al.*, 1996). The Great Whale river plume transports freshwater, chemical substances and heat from the river into the estuary and into the bay. The salinity of the plume is hydrographically controlled by the rate of discharge of the river; eg influenced by the rate of snow melt within its drainage basin. Previous work in an analogous estuarine region to that of southeastern Hudson Bay (Saroma-ko lagoon, Japan) suggested that the low salinity water discharged from the river caused a reduction in the photosynthetic activity of ice algae and consequently led to a decrease in Chl a concentrations (Taguchi *et al.*, 1997). Similarly, previous work within southeastern Hudson Bay (Legendre *et al*., 1996) suggested that salinity, and not nutrients, are the primary limiting factor for the development of ice algae within the region. Poulin *et al.* (1983) observed that the biodiversity of ice algae, within Hudson Bay, decreased with lower salinities. This study suggests that salinity could directly influence the taxonomic composition of ice algae as cryophilic algae are generally stenohaline and not tolerant to low salinities. Thus it could be hypothesized that salinity may influence the biomass of ice algae through osmotic or other physiological effects. These physiological effects could be a combination of the effect of low salinities on the sea ice surface available for colonization, which may have a direct effect on the colonization efficiency of ice algae, and the thickness of the sea ice, which also influences the irradiance at the bottom of the ice (Poulin *et al.,* 1983).

As ice algae in southeastern Hudson Bay are exposed to low salinity water throughout the year, the ice algae are subjected to both osmotic damage and physiological effects reducing their photosynthetic activity and growth rates. This phenomena influences the *Chl a* concentrations in the underlying seawater, hence their concentrations within sea ice from scavenging and consolidation during sea ice formation (section 5.3.2). This explains why the *Chl a* concentrations within sea ice at both core positions were $\sim 10^2 - 10^4$ times lower than those previously measured in higher salinity (~ 35 *psu*) seawater bearing seasonal sea ice zones (Sturges *et al.*, 1997). The relatively low *Chl a* concentrations within the sea ice can be explained by a combination of osmotic stress, induced at low salinities in seawater prior to sea ice formation, and the possibility of nutrient deficiency within the brine channel network limiting algal productivity. However, although a lack of nutrient exchange through the ice column is implied by the low brine volumes observed through both cores (figure 5.28), the possibility that nutrient deficiencies within the sea ice are limiting algal productivity can not be confirmed as nutrient concentrations in sea ice were not determined.
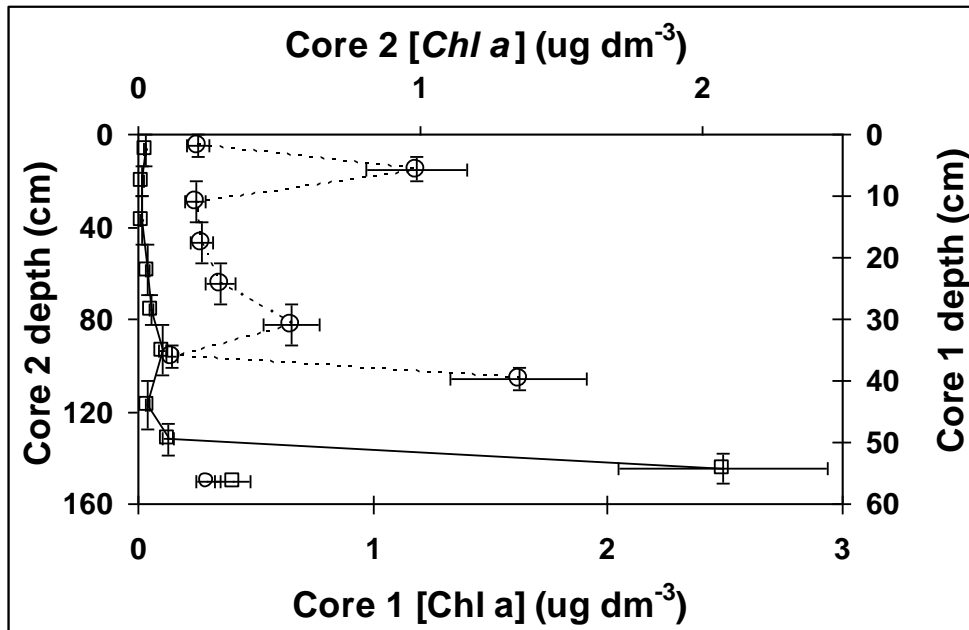
Figure 5.28 Chlorophyll distributions through sea ice.

Empty squares, core position 1;empty circles, core position 2.

Bottom data points reflect under ice *Chl a* concentration in seawater.

5.4.4 Biogenic VOIC production

The polyhalogenated organic compounds ($CHBr_3$, CH_2Br_2, CH_2I_2 and CH_2ICl) were previously shown to be produced by the marine diatoms *Nitschia sp, Nitschia arctica and Porosira glacialis* grown in laboratory cultures (Moore *et al.*, 1996). In contrast CH_2IBr was only produced in the cultures *Nitschia sp* and *Porosira glacialis.* Further testing revealed that all these species of diatoms possessed the bromoperoxidase enzyme to which the organisms iodinating and brominating ability was attributed. A culture of *Navicula sp* also produced CH_2I_2 and CH_2ICl, but no $CHBr_3$ or CH_2Br_2. This was attributed to the absence of a bromo-peroxidase enzyme and the presence of an iodo-peroxidase enzyme within the algal tissue. Moore *et al.* (1996) noted that the production rates of the poly-halogenated organics were considerably higher at higher illuminations, with no significant production occurring under dark conditions for any of the compounds investigated. This phenomenon is likely to be related to the increased production of H_2O_2 during photosynthesis. While different organisms have different patterns of H_2O_2 production (Hakkinen *et al.,* 2004), it is consistent with current theory that photosynthetic organisms would all have enhanced H_2O_2 production under increased radiance (Cooper *et al.*, 1989).

In Moore *et al's* (1996) diatom incubations study, the biogenic production of the mono-iodinated compounds (CH_3I and C_2H_5I) was observed only in the *Nitschia sp* culture held at higher illumination in which the concentration reached up to 10 times the control levels. Under similar conditions the culture *Porosira glacialis* produced CH_3I concentrations only a few times above the control level. Neither CH_3I or C_2H_5I would be expected to be linked to haloperoxidase enzyme activity however as mono-halogenated organics are not formed from the resultant haloform reaction. However, the biogenic formation of mono-halogenated organics is believed to occur in the presence of halide methyl transferase enzymes. Wuosmaa and Hagner (1990) previously reported a mechanism involving a methyl chloride transferase enzyme, which catalyzes the methylation of halide ions in seawater. Subsequent work yielded CH_3I from incubations of I^- and organic substances in the presence of the methyl transferase enzyme (Itoh *et al.*, 1997).

5.4.5 Abiotic production of halogenated organic compounds

Previous work by Moore and Zafiriou (1994) suggests a photochemical production mechanism of mono-halogenated organics (RX) from alkyl radicals, formed from the photolysis of dissolved organic matter (DOM), recombining with iodine atoms. DOM and detritus are known to be readily scavenged and consolidated in sea ice during its formation (section 5.3.2) with dissolved organic concentrations (DOC) within seasonal sea ice typically reaching in excess of 100 μm dm^{-3} (Thomas *et al.*, 1995). The primary competing reaction of this abiotic mechanism of VOIC formation is the reaction of the alkyl radical with molecular oxygen (O_2). However the sea ice and overlying snow of these aqueous phase reactions are likely to reduce the O_2 content available for such competing reactions.

Keppler *et al.* (2000) describes a terrestrial production mechanism of RX in organic rich soils involving the synchronous oxidation of 2-methoxyphenol by ferrihydrite and the nucleophillic substitution of the methyl group by halide. This reaction is specific for all of the mono-iodinated organics in question as C_2H_5I and $2/1$-C_3H_7I are generated by using ethoxyphenol and propoxyphenol respectively. This RX production mechanism could be of specific importance within Hudson Bay due the large amount of continuous freshwater drainage that occurs from the surrounding terrestrial ecosystems into the Bay. Such drainage is likely to contribute to the transport of alkoxylated phenolic structures and minerals from terrestrial soils into the Bay, where they can be scavenged during sea ice formation.

Hansson *et al.* (1987) previously described the abiotic production of poly-halomethanes in natural waters via the haloform reaction. The haloform reaction is not biologically or photo-chemically mediated, hence reaction rates are dependent upon pH, temperature, halide and DOM concentrations. However, these variables were not determined within sea ice during the COBRA campaign, therefore it is difficult to interpret how the production rates of poly-halogenated organics would vary throughout the sea-ice column.

5.4.6 VOIC and VOBC lifetimes in Hudson Bay sea ice

The total lifetimes of VOICs and VOBCs had to be considered in both cores 1 and 2 of the sea ice in order to determine the importance of any *in-situ* production as a regional source to the marine boundary layer. The primary loss mechanism of VOICs and VOBCs in the atmosphere is through photolysis (section 1.3, table 1.1). Photolysis lifetimes of these compounds in sea ice is strongly influenced by snow cover, age, consolidation and thickness of the overlying snow layer. The overlying snow thickness was measured at core positions 1 and 2 immediately prior to sampling and consisted of ~1 cm of loose wind driven snow and ~2 - 2.5 cm of aged consolidated snowpack. The topography of the snowpack immediately surrounding the points of sampling consisted of wind driven snow depths of 1 - 10 cm, which were observed to change over a timescale of days. As solar irradiance was not measured through either the snowpack or sea ice prior to sampling, it is difficult to infer *in-situ* photolysis lifetimes for the VOICs and VOBCs measured.

Rowland and Grannas (2011) recently carried out irradiance measurements through the Arctic seasonal snowpack at Barrow Alaska using actinometer films. These measurements established that UV-A light is strongly attenuated near the snowpack surface, with 90 - 100% of the surface intensity lost within the first 5 cm of aged consolidated snow. This 10% discrepancy in light intensity was an experimental artefact attributed to either light leakage from the side of the sample snow trench, disruption of the snowpack during slide placement or the accidental exposure of the actinometer films during repackaging. Therefore, when considering the sea ice sampled at both core positions in the Hudson Bay region during COBRA, it is possible that almost all of the incident UV radiation was attenuated within the snowpack and did not reach the underlying sea ice surface.

Following the assumption that photolytic VOIC losses were negligible in the lower ice column, secondary *in-situ* loss mechanisms were considered, namely hydrolysis and chlorination (Jones *et al.*, 2007). The VOIC concentrations measured in sea ice represent the concentrations within the hypersaline solution in the intercrystalline inclusions within the ice microstructure. In order to calculate the total loss rates for these compounds within these environments, both the brine salinities and VOIC concentrations through the sea ice

column had to be estimated. Brine salinities were estimated using the calculated brine volumes (figure 5.27) and sea ice salinities (figures 5.25 and 5.26) at each depth whereas brine VOIC concentrations were scaled according to the brine volume. Figure 5.29 shows the estimated brine salinities through sea ice for core positions 1 and 2. The established errors on the *x* axis reflect an arbitrary 10% sampling error whereas the *y* errors show the range of ice depths sampled for each data point.

The total VOIC lifetimes for CH_3I, and $1\text{-}C_3H_7I$ as a function of sea ice depth were calculated using EQ 5.1. VOIC hydrolysis and chlorination temperature dependent rate constants (k_H *and* k_c respectively) were extrapolated from previous relationships established by Jones (2006). Calculated total lifetimes attributed to hydrolysis and chlorination losses in the surface sea ice were between 4.2 – 3.8 and 28.7 years for CH_3I and $1\text{-}C_3H_7I$ respectively. Calculated total lifetimes decreased significantly with sea ice depth due to the temperature dependence of VOIC hydrolysis and chlorination and the higher temperatures inferred toward the ice-water interface, tables 5.3 and 5.4. However, at the CH_3I concentrations observed, in the lower ice column at core position 2 the calculated total lifetimes due to hydrolysis and chlorination were still in excess of 1 year. As the seasonal sea ice cover in the Hudson Bay region typically lasts ~ 6 - 7 months (Legendre *et al.*, 1996) the *in-situ* VOIC total lifetimes throughout the sea ice column are considerably higher than the duration of the sea ice.
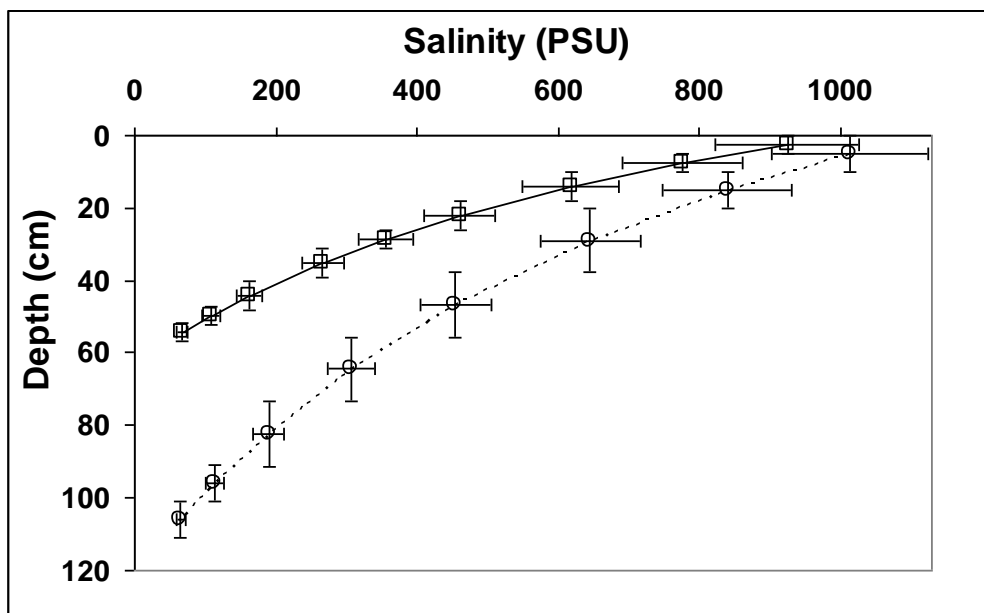
Figure 5.29 Estimated brine salinities through Hudson Bay sea ice. Empty squares, core position 1; empty circles, core position 2.

VOIC	Temperature (K)	Ice depth (cm)	k_H (dm^3 mol^{-1} s^{-1})	k_c (dm^3 mol^{-1} s^{-1})	Total lifetime (years)
CH$_3$I	254	2.5	5.28×10^{-11}	5.81×10^{-10}	3.8
	255	7.5	8.09×10^{-11}	1.24×10^{-9}	2.0
1-C$_3$H$_7$I	254	2.5	1.61×10^{-10}	3.18×10^{-11}	28.7
	255	7.5	2.30×10^{-10}	7.86×10^{-11}	8.5

Table 5.3 Calculated total VOIC lifetimes and chemical destruction rate constants in sea ice at ice core position 1.

VOIC	Temperature (K)	Ice depth (cm)	k_H (dm^3 mol^{-1} s^{-1})	k_c (dm^3 mol^{-1} s^{-1})	Total lifetime (years)
CH$_3$I	253	5	4.8×10^{-11}	4.9×10^{-10}	4.2
	263	64.5	1.53×10^{-10}	3.85×10^{-9}	1.3
	270	106	3.26×10^{-10}	1.48×10^{-8}	1.0

Table 5.4 Calculated total VOIC lifetimes and chemical destruction rate constants in sea ice at ice core position 2.

5.4.7 Distribution of halogenated organics through Hudson Bay sea ice

Figures 5.30 5.32, 5.33, 5.35 and 5.31, 5.34, 5.36, 5.38 show VOBC, and VOIC profiles through sea ice for core positions 1 and 2, respectively (see figure 5.4 for geographical locations). The measured VOIC/VOBC seawater concentrations at core position 2 on the 6th of March 2008 were 21.1, 0.11 and 3.21 pmol dm^{-3} for CH_3I, CH_2Br_2 and $CHBr_3$ respectively. These seawater concentrations are considerably lower ($\sim 30 - 100\%$) than those measured in the open ocean previously (Jones *et al.*, 2010; Hughes *et al.*, 2009). This demonstrates the effect reduced biological activity (caused from sea ice cover) and reduced algal densities (caused by osmotic stress from fresh water mixing) potentially have on biogenic VOIC production within the region. The data points at an ice depth of 65 and 140 cm for core positions 1 and 2, respectively, represent the measured VOIC/VOBC concentrations in the underlying seawater.

Due to the low diatom cell numbers that are inferred from the *Chl a* concentrations measured within the Hudson Bay sea ice, figure 5.28, both the VOBCs and VOIC concentrations were too high to be explained by their *in-situ* biogenic production by diatoms alone. Moore *et al.* (1996) stated that during an incubation study of the most productive arctic diatom species (*Nitschia sp*) the CH_3I to *Chl a* ratios were in the order of 17 pmol CH_3I mg dm^{-3} *Chl a*. Assuming that the conditions in this incubation study were representative of those in the upper sea ice of Hudson Bay and that the *Chl a* concentrations measured were only from *Nitschia sp*, the measured CH_3I concentrations in the upper sea ice were 10^3-10^5 orders of magnitude higher than can be explained by these biological production rates, as shown in figure 5.30.

Similarly the measured VOIC and VOBC concentrations in the Hudson Bay sea ice cannot be explained by vertical transport from the underlying seawater as the brine volume fraction through out the ice column is below the critical percolation threshold ($5 - 5.4\%$, Cox and Weeks, 1975; Petrich *et al.*, 2006), excluding that of the lower $5 - 10$ cm of sea ice sampled at core position 1 (figure 5.27). As vertical VOIC transport through sea ice from the underlying seawater was not possible at the time of sampling (figure 5.27) and the measured *Chl a* concentrations in the ice column infer negligible VOIC production rates,

only *in-situ* abiotic production and/or scavenging and consolidation of VOIC from the underlying seawater during ice formation can explain the observed concentrations.

Due to the large calculated lifetimes of the VOICs in the sea ice (tables 5.3 and 5.4), assuming that hydrolysis and chlorination were the only loss mechanisms, the VOIC concentrations measured could also have been attributed to a combination of ice scavenging and consolidation processes during sea ice formation during October to November 2007. This was investigated using the salt segregation coefficient (k_{eff}) of initial ice formation outlined earlier, EQ 5.19 (Weeks and Ackley, 1986). The k_{eff} values of the Hudson Bay ice column were calculated using the mean measured salinity of the underlying seawater at core positions 1 (20.4 ± 3.0 *psu*) and 2 (5.1 ± 0.8 *psu*) using S_i (EQ 5.20). k_{eff} values between 0.16 − 0.35 and 0.17 − 0.53 were calculated for the sea ice sampled at core position 1 and 2 respectively, which is in good agreement with the k_{eff} values calculated during the ice chamber experiments discussed in this chapter (section 5.3.2.2). Using these k_{eff} values, the expected VOIC concentrations consolidated in sea ice (VOIC$_i$) can be estimated from their respective concentrations in seawater during ice formation using EQ 5.21. As the VOIC concentrations in Hudson Bay seawater during ice formation were not measured, their measured concentrations in the under ice seawater on the 6th March 2008 and previously reported surface concentrations in the polar oceans (Jones *et al*., 2010; Hughes *et al.*, 2009) were used.

This approach estimates the concentrations of VOIC$_i$ attributed to segregation and consolidation from the underlying seawater during ice formation. As the VOIC concentrations are scaled with measured sea ice salinity, they also take into account losses through gravity brine drainage from the point of ice formation. However, there are several limitations to this approach that need to be considered. Firstly, the approach assumes that the segregation of VOIC from seawater during initial ice formation is equal to that of ubiquitous sea salt. Secondly, we assume that the rates of VOIC loss from the sea ice column due to gravity brine drainage are equal to the loss in sea ice salinity. To our knowledge, no previous study, either in the field or in the laboratory, has been carried out to investigate these factors. Thirdly, we assume that the measured seawater salinities reflect

those during ice formation, when in fact the salinity is dependent on influx of fresh water from terrestrial sources and subject to change both spatially and seasonally. A further limitation in deriving k_{eff} is that it assumes a planar rather than a platelet ice-water interface. A platelet ice-water interface would typically produce higher k_{eff} values, (Eicken, 1998) hence the calculated values herein are to be used with care.

$$k_{eff} = S_i \times S_w \qquad\qquad\qquad\qquad\qquad (EQ\ 5.20)$$

$$VOIC_i = k_{eff} \times C_w \qquad\qquad\qquad\qquad\qquad (EQ\ 5.21)$$

The mono-iodinated volatile organic compounds generally exhibited elevated concentrations in the upper sea ice which decreased with depth. Measured concentrations in the upper 5 cm of sea ice at core positions 1 and 2 reached 36.5 - 23.0 and 2.0 pmol dm^{-3} for CH_3I and $1\text{-}C_3H_7I$ respectively. The latter was not detected in sea ice above the LoD of the instrument at core position 2. In the surface ice column (upper 10 cm), the estimated concentrations of CH_3I and $1\text{-}C_3H_7I$ attributed to scavenging during ice formation (assuming no *in-situ* photolytic losses) were ~ 40 ± 10% and ~ 15 ± 10% of those measured respectively. Given this discrepancy, a plausible explanation for these enhanced VOIC concentrations in the sea-ice surface layer is through abiotic photochemical production.

Generally the concentration profiles of the poly-halogenated organics (CH_2IBr, CH_2Br_2 and $CHBr_3$) measured in the Hudson Bay sea ice were anti-correlated to those measured for the mono-iodinated compounds, with an increase in concentration with sea ice depth (figures 5.33 - 5.38). Measured concentrations in the upper 5 cm of sea ice were between 0.0 - 9.1, 6.5 - 9.7 and 0.9 - 1.2 pmol dm^{-3} for CH_2IBr, $CHBr_3$ and CH_2Br_2 respectively. Significant brine drainage is likely to have taken place in the lower sea ice column during sampling of core 1. This could explain why significantly lower VOIC concentrations were observed in the lower ~ 10 cm of the ice column, figures 5.33, 5.35 and 5.37. The estimated concentrations of CH_2IBr attributed to scavenging during ice formation through out the ice column (assuming no *in-situ* photolytic losses) were ~ 25 ± 10%, (figure 5.33) similar to

those of the mono-iodinated organics. Alternatively, $CHBr_3$ and CH_2Br_2 concentrations attributed to scavenging during ice formation were $110 - 160 \pm 50$ % and 200 ± 140 % of the measured concentrations in sea ice respectively (figures $5.35 - 5.36$ and $5.37 - 5.38$ respectively).

Given that previous work on the seasonal snowpack at Barrow Alaska (Rowland and Grannas, 2011) suggests as little as 0 - 10% of incident UV radiation is penetrating the consolidated snowpack to the underlying sea ice, coupled with the large calculated hydrolysis/chlorination lifetimes of VOICs in sea ice (tables 5.3 and 5.4) the observed VOIC/VOBC distributions in sea ice can largely be explained through scavenging and consolidation during ice formation.
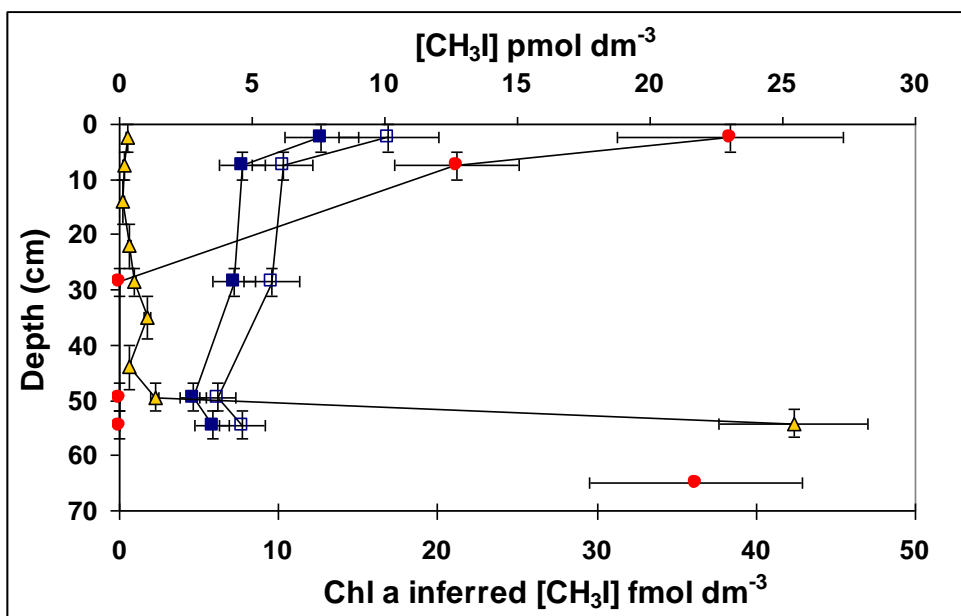
Figure. 5.30 CH_3I concentrations through sea ice (Core 1). Red circles, measured concentrations; yellow triangles, *Chl a* inferred concentrations; filled blue squares, $VOIC_i$ concentrations inferred from measured seawater concentrations; empty blue squares $VOIC_i$ concentrations inferred from seawater concentrations in literature (Jones *et al.*, 2010). Lower data point represents measured underlying seawater CH_3I concentrations.
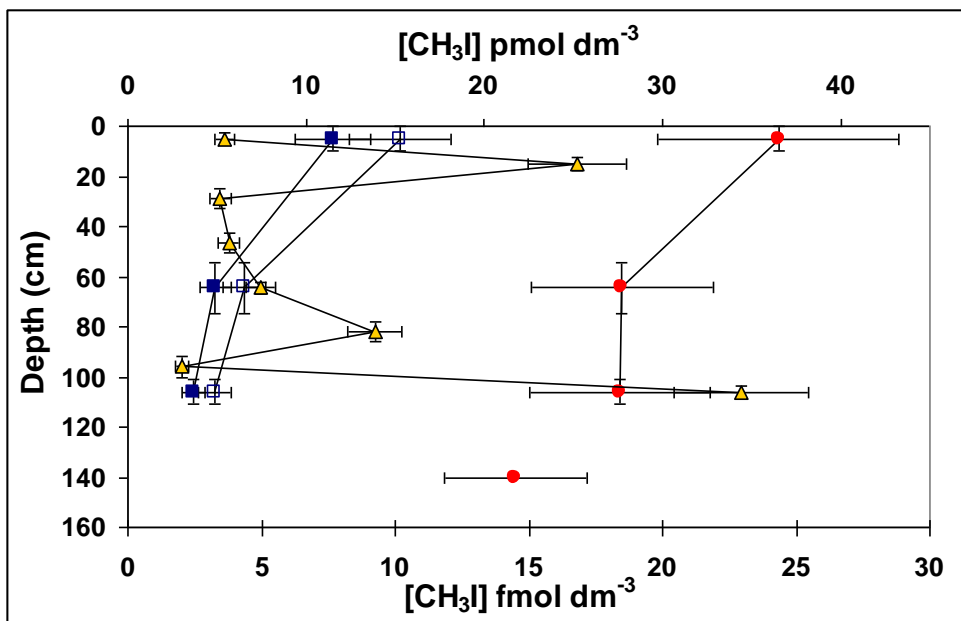
Figure. 5.31 CH_3I concentrations through sea ice (Core 2). Red circles, measured concentrations; yellow triangles, *Chl a* inferred concentrations; filled blue squares, $VOIC_i$ concentrations inferred from measured seawater concentrations; empty blue squares $VOIC_i$ concentrations inferred from seawater concentrations in literature (Jones *et al.*, 2010). Lower data point represents measured underlying seawater CH_3I concentrations.
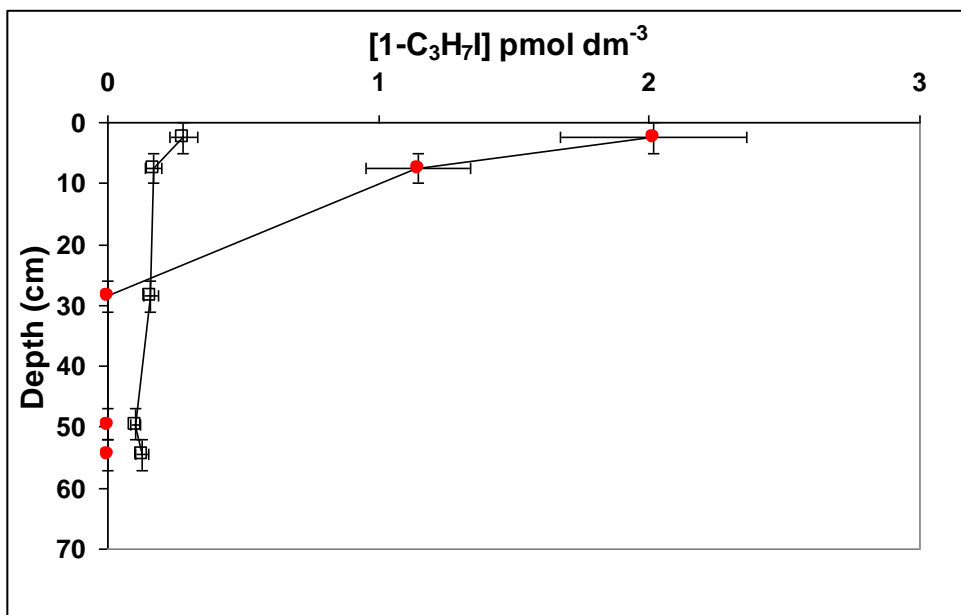
Figure. 5.32 $1\text{-}C_3H_7I$ concentrations through sea ice (Core 1). Red circles, measured concentrations; empty blue squares, $VOIC_i$ concentrations inferred from seawater concentrations in literature (Jones *et al.*, 2010).
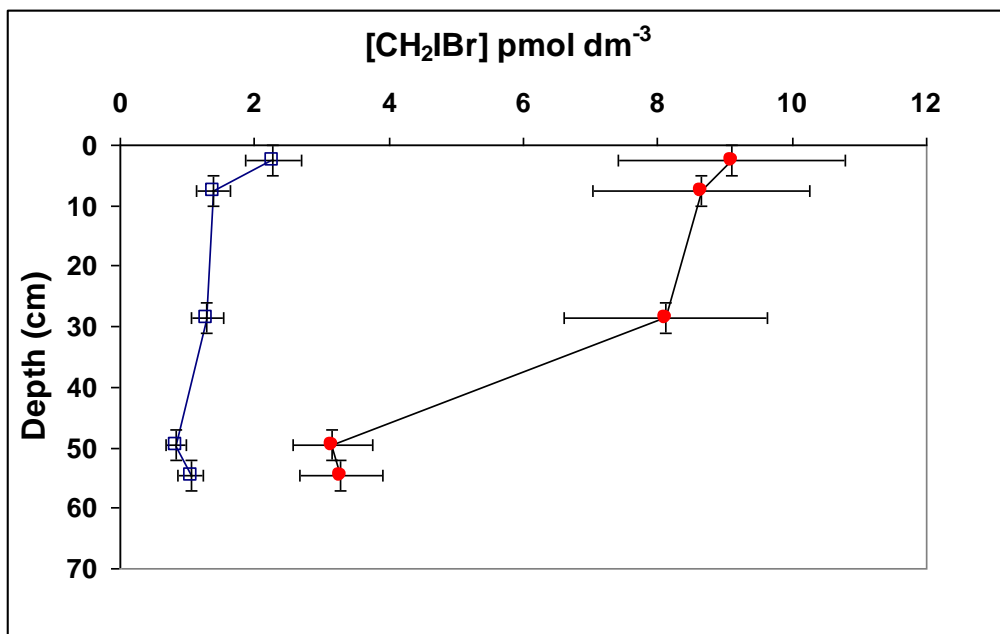
Figure. 5.33 CH$_2$IBr concentrations through sea ice (Core 1). Red circles, measured concentrations; empty blue squares, VOIC$_i$ concentrations inferred from seawater concentrations in literature (Jones *et al.*, 2010).
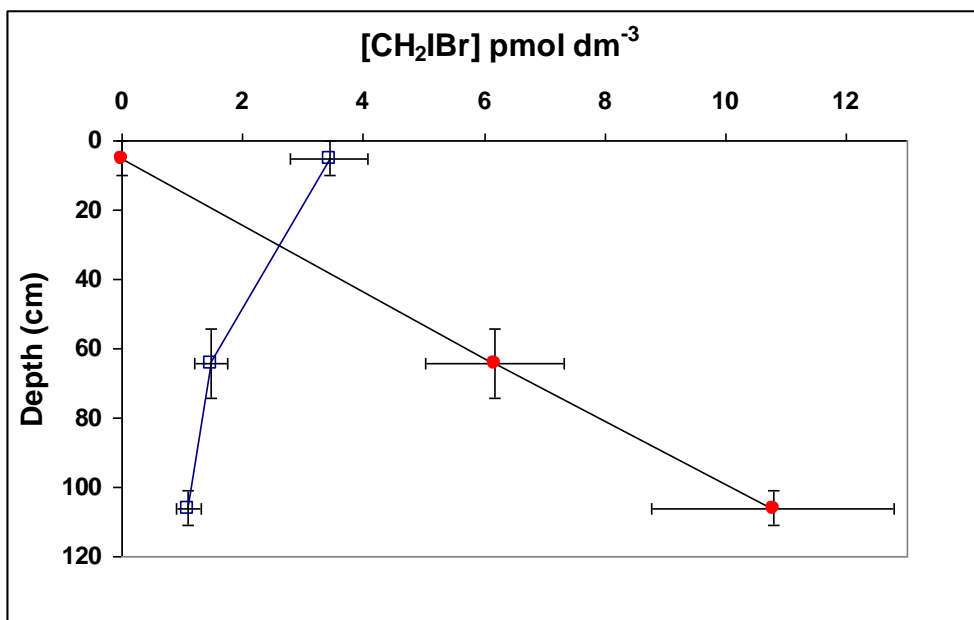
Figure. 5.34 CH$_2$IBr concentrations through sea ice (Core 2). Red circles, measured concentrations; empty blue squares, VOIC$_i$ concentrations inferred from seawater concentrations in literature (Jones *et al.*, 2010).
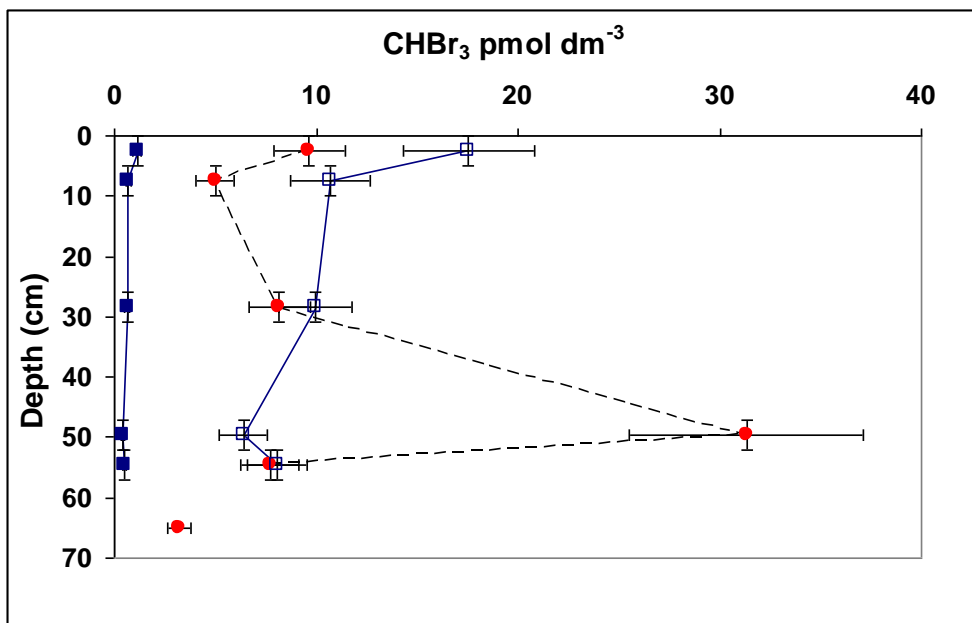
Figure. 5.35 CHBr$_3$ concentrations through sea ice (Core 1). Red circles, measured concentrations; filled blue squares, VOIC$_i$ concentrations inferred from measured seawater concentrations; VOIC$_i$ concentrations inferred from seawater concentrations in literature (Hughes *et al.*, 2009). Lower datapoint represents measured underlying seawater concentrations.
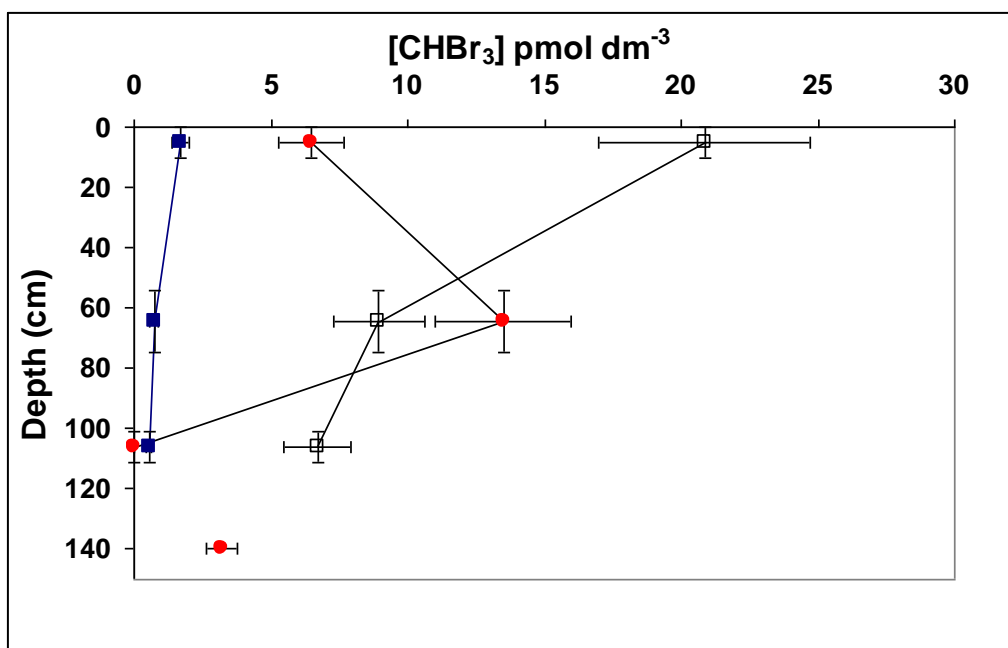
Figure. 5.36 CHBr$_3$ concentrations through sea ice (Core 2). Red circles, measured concentrations; filled blue squares, VOIC$_i$ concentrations inferred from measured seawater concentrations; VOIC$_i$ concentrations inferred from seawater concentrations in literature (Hughes *et al.*, 2009). Lower datapoint represents measured underlying seawater concentrations.
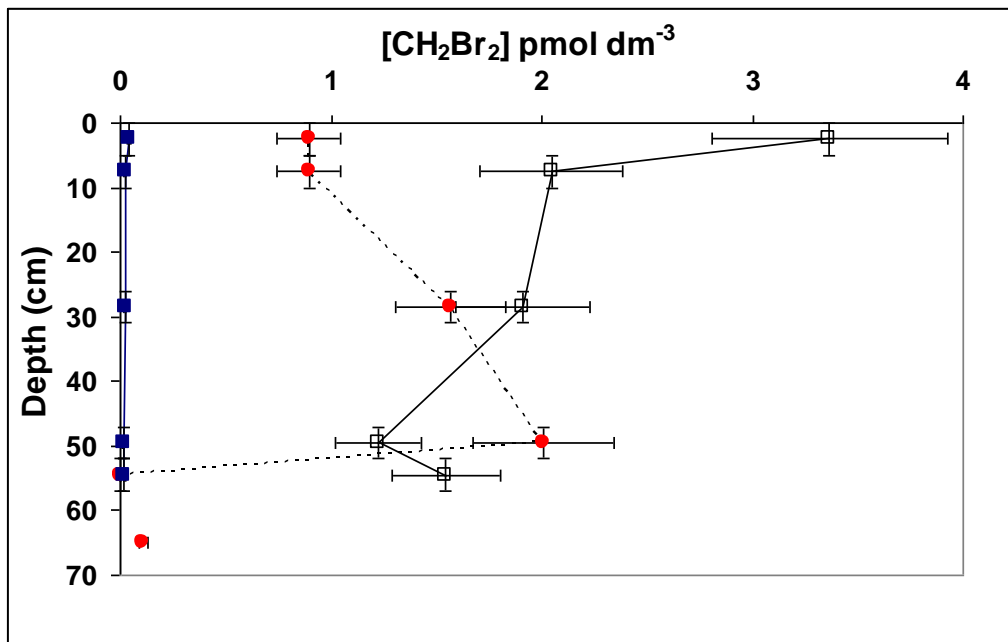
Figure. 5.37 CH_2Br_2 concentrations through sea ice (Core 1). Red circles, measured concentrations; filled blue squares, $VOIC_i$ concentrations inferred from measured seawater concentrations; $VOIC_i$ concentrations inferred from seawater concentrations in literature (Chuck *et al.*, 2004). Lower datapoint represents measured underlying seawater concentrations.
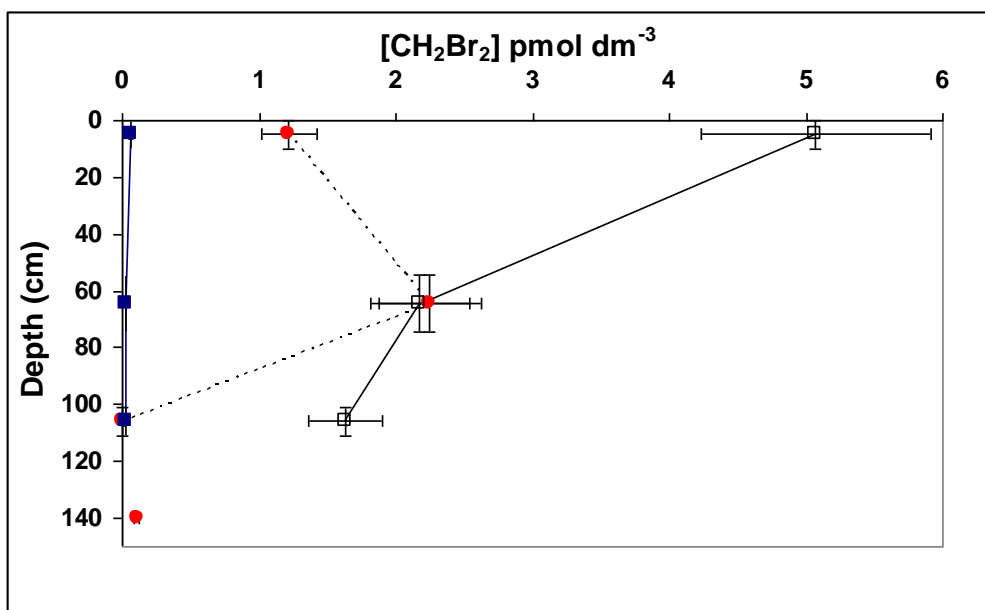
Figure. 5.38 CH_2Br_2 concentrations through sea ice (Core 2). Red circles, measured concentrations; filled blue squares, $VOIC_i$ concentrations inferred from measured seawater concentrations; $VOIC_i$ concentrations inferred from seawater concentrations in literature (Chuck *et al.*, 2004). Lower data point represents measured underlying seawater concentrations.

5.4.8 Comparison of sea-ice-air to sea-air fluxes within Hudson Bay

The hypothetical k_w values calculated in section 5.3.9 were used to determine the flux of VOIC from the waters of Hudson Bay in the absence of sea ice and during partial sea ice coverage ($f \sim 0.1$ and $f > 0.3$). Hypothetical k_w values were determined for $f \sim 0.1$ and $f > 0.3$ by scaling the k_w values to 10 and 30 %, respectively. Fluxes were determined using VOIC and VOBC C_w values previously observed in the open ocean (Jones *et al.*, 2010; Hughes *et al.*, 2009) and mean concentrations in air (C_a) between 18th – 28th February during the COBRA campaign (chapter 3), (EQ 5.22).

The VOIC and VOBC concentrations in the surface brine, C_{brine}, of the Hudson Bay sea ice were calculated using the calculated surface brine volume, p_c, (0.8%) and the measured C_{ice} values at a depth of 2.5 cm for core position 1, EQ 5.23. This calculation assumes that the measured C_{ice} completely resided in brine within the sea ice. VOIC and VOBC fluxes from Hudson Bay sea ice were determined using the k_{QLL} values calculated during the fast ice growth at -3°C (experiment 2), table 5.5, EQ 5.24. Using this value, VOIC/VOBC fluxes will only occur at air/ice interface temperatures $> \sim -5°C$. The k_{QLL} determined for $1\text{-}C_3H_7I$ during experiment 2 was used to calculate fluxes for CH_2Br_2 and $CHBr_3$ as these compounds were not included in the chamber investigation section (5.2.1). The flux values and gas transfer velocity values calculated are tabulated in table 5.5.

$$Flux = k_w \times (C_w - \frac{C_a}{H})$$ (EQ 5.22)

$$C_{brine} = \frac{100}{p_c \times 10} \times C_{ice}$$ (EQ 5.23)

$$Flux = k_{QLL} \times ((C_{brine} \times V) - (\frac{C_a}{H}))$$ (EQ 5.24)

Assuming that the k_{QLL} used was representative of seasonal sea ice, the calculated VOIC and VOBC fluxes from the surface sea ice in Hudson Bay were between $0.01 - 1.5$ % of

the calculated fluxes from the seawater in the absence of sea ice. The calculated surface sea ice flux values were 3.7, 15.1, 0.1, 0.7 and 10.3 % of the calculated fluxes from partial sea ice cover assumed during winter ($f \sim 0.1$, Tanning and Torres 1991) for CH_3I, $1\text{-}C_3H_7I$, CH_2Br_2, $CHBr_3$ and CH_2IBr respectively (table 5.5). This data supports the ice chamber data herein (section 5.3) suggesting that the flux of volatile gases from bodies of open water (such as leads or polynyas) within seasonal sea ice zones are more significant than those from the sea ice surface.

The ratios of the calculated surface sea ice and partial sea cover fluxes (at $f \sim 0.1$) are significantly higher in the Hudson Bay region than observed during the ice chamber experiments. The ice chamber experiments were conducted under abiotic dark conditions and only take into account diffusive vertical transport of VOIC through newly grown sea ice and their subsequent exchange with air. Arctic seasonal sea ice is a complex media in which competing *in-situ* abiotic, biogenic and photo-chemical VOIC production and destruction mechanisms exist. The higher flux ratios of sea ice exchange in Hudson Bay demonstrate the effect these processes have on halocarbon concentrations in the upper ice column and their concentrations within the boundary layer.

The VOIC/VOBC *QLL* $\rightarrow$ *air* fluxes from the Hudson Bay sea ice are likely to be lower than those calculated herein due to lower surface sea ice salinities observed when compared to the ice chamber experiments. Also the calculated fluxes do not take into account the effect of consolidated snow cover and are dependent upon VOIC/VOBC replenishment in the surface sea ice. However, these values offer an upper limit for VOIC and VOBC flux from the seasonal sea ice in the Hudson Bay region for surface temperatures above the percolation threshold at the surface sea ice concentrations measured.

VSLH	Calculated seawater to air transfer velocity k_w (m d^{-1})[a]	Calculated C_{brine} of sea ice (nmol dm^{-3})[c]	Calculated seawater-air flux (nmol m^{-2} d^{-1})	Calculated seawater-air flux at f = 0.1 (nmol m^{-2} d^{-1})	Calculated seawater-air flux at f = 0.3 (nmol m^{-2} d^{-1})	Flux from surface *QLL* (nmol m^{-2} d^{-1})[d]
CH₃I	4.2 ± 0.4[b]	2.89 ± 0.61	41.3 ± 5.8	4.1 ± 0.6	12.4 ± 1.8	0.15 ± 0.02
1-C₃H₇I	4.4 ± 0.4	0.25 ± 0.07	1.3 ± 0.2	$0.1 \pm 2 \times 10^{-2}$	$0.4 \pm 5 \times 10^{-2}$	$0.02 \pm 3 \times 10^{-4}$
CH₂Br₂	4.5 ± 0.5	0.11 ± 0.03	42.8 ± 5	4.3 ± 0.5	12.8 ± 1.5	$0.6 \times 10^{-2} \pm 0.1$
CHBr₃	3.9 ± 0.5	1.21 ± 0.25	153.1 ± 18.4	15.4 ± 1.8	46.0 ± 5.4	0.11 ± 0.01
CH₂IBr	4.6 ± 0.5	1.14 ± 0.22	3.9 ± 0.5	$0.4 \pm 5 \times 10^{-2}$	1.2 ± 0.2	0.04 ± 0.01

Table 5.5. Sea/ice-air VOIC/VOBC transfer velocities, and fluxes at an ambient air temperature of -3°C.

[a] Gas transfer velocity values calculated using Nightingale *et al.* (2000) parameterisation for the open ocean.

[b] Tabulated errors represent 1 σ estimated uncertainties calculated from propagating the RSDs of the VOIC permeation rates, the calibration curve and internal standard precision.

[c] Calculated VOIC/VOBC concentrations in brine in upper ice column (2.4 cm) using EQ 5.23.

[d] Fluxes calculated using the calculated VOIC concentrations in the upper 2.4 cm of brine (EQ 5.24).

5.5 Discussion

5.5.1 Advantages and limitations of ice tank experiments

Laboratory experiments conducted in artificial ice tank environments have several significant advantages when compared to field investigations. Within an artificial ice tank, air and water temperatures are easily measured and controlled and replicate measurements are possible, all of which is difficult to achieve in the field. As the majority of sea-ice measurements are conducted using destructive sampling techniques, a sea ice area with homogenous properties is advantageous when conducting time dependent experiments. Whilst this is readily achievable in an indoor tank, natural sea ice is known to be highly spatially variable, depending largely upon its history (Eicken, 2008).

Limitations of laboratory experiments conducted in artificial ice tank environments also have to be considered. As artificial ice tank studies are conducted over small temperature gradients, associated growth rates can be much higher than for naturally formed sea ice, influencing microstructure (section 5.3.2). This is because only relatively small ice thickness can be generated, hence the temperature inertia/insulating thermal effect of the overlying sea ice layers observed within natural sea-ice are not observed. Also it is inherently difficult to observe the micro structural evolution of sea ice columns with

respect to time in artificial ice tanks, due to the extensive operational costs usually involved with such facilities.

Another important limitation in the ice tank experiments conducted is that they do not take into account the effect of naturally occurring biochemical processes within the sea ice microstructure and how these influence vertical transport rates. Of recent interest is the role of exopolymeric substances (EPS) on dissolved gas vertical diffusion rates through the brine channel network. The formation of EPS by algae and bacteria is reportedly stimulated by changes in temperature, salinity, inorganic nutrients as well as the irradiance levels (Decho, 1990; 2000).   Diatoms are well known producers of EPS, mainly polysaccharides, and are likely the major contributor to EPS loading in sea ice. High concentrations of EPS have previously been measured in winter Arctic sea ice, which were closely correlated with DOC concentration and bacterial cell density (Krembs, 2002). The suspected effect of EPS within the brine of sea ice is that it will increase the viscosity of brine and hence the properties with regard to diffusive transport of ions and gases through the matrix EQ 5.4. Hence the diffusion coefficients determined from ice tank measurement herein, table 5.2, are reported as upper values for the abiotic conditions investigated.

5.5.2 Conclusions

Sea-ice strongly retards sea-air gas transfer of climate relevant trace gases from the polar oceans. The laboratory experiments herein are a reproduction of seasonal sea-ice under temperature conditions which are typical of late winter to early spring where the air temperature is considerably colder than the water temperature (Loose *et al.*, 2009, 2011). The laboratory and field data within this study suggests that sea-ice permeability and subsequent vertical gas transport rates through sea-ice are dependent upon the media's micro-structural evolution with temperature. The data herein supports previous publications which suggest that the ocean f alone is insufficient when constraining gas transfer velocities (Golden *et al.*, 2007).

The diffusion of VOICs through sea-ice provides a very small flux pathway for gas transport during periods of consolidated ice cover. The calculated VOIC $k_{sea \rightarrow ice \rightarrow air}$ values

herein, suggest that halocarbon gas transport from leads and polynyas during the winter ($f \sim$ 0.1) is at least $\sim$ 60 times greater than that observed from diffusion through the sea-ice microstructure at -3ºC. This supports previous data that has suggested gas ventilation takes place primarily through leads and fractures in the ice (Loose *et al*., 2011).

Assuming 100% brine channel fractional connectivity and the average diffusion coefficient during the -3°C experiments (*D* of 5 x 10^{-5} cm^2 s^{-1}) the timescale of diffusion is 30 – 50 hours for a sea-ice thickness of 50 mm. For a first year sea-ice thickness of 500 mm at the same air temperature the timescale of diffusion is ~145 days. This has significant implications for *in situ* VOIC losses within the brine from chlorination, hydrolysis and photolysis processes and it is unlikely that measurable concentrations of the species investigated would survive vertical transport from the underlying seawater to the surface sea ice QLL. However, both abiotic and biogenic *in situ* VOIC production in the brine channels, particularly in the upper ice column, could still contribute significantly to sea ice/air fluxes.

Since sea-ice strongly retards sea-air gas transfer of climate relevant trace gases from the polar oceans, rapid Arctic sea-ice loss has global atmospheric and climatic implications for perturbed sea-air gas transport (Gabric *et al*., 2005). However, warming and thinning of sea-ice is also expected to substantially increase its gas permeability (Delille *et al*., 2007). During warming, the formation of air-filled pore networks within sea-ice, caused by gravity brine drainage (Delille *et al*., 2007), could lead to vertical gas diffusion rates considerably greater than those measured within this study. Predicted future sea-ice warming and thinning (Holland *et al*., 2010) also has the potential to influence biogenic trace gas production in sea-ice by increasing nutrient availability and grazing pressure through exchange and vertical transport with the underlying seawater (Golden *et al*., 1998; Thomas and Dieckmann, 2003; Zhang *et al*., 2010; Loose *et al.,* 2011). The future impact of potentially increased biogenic trace gas production within sea-ice combined with increased gas diffusion through melting sea ice requires further study.

Appendix
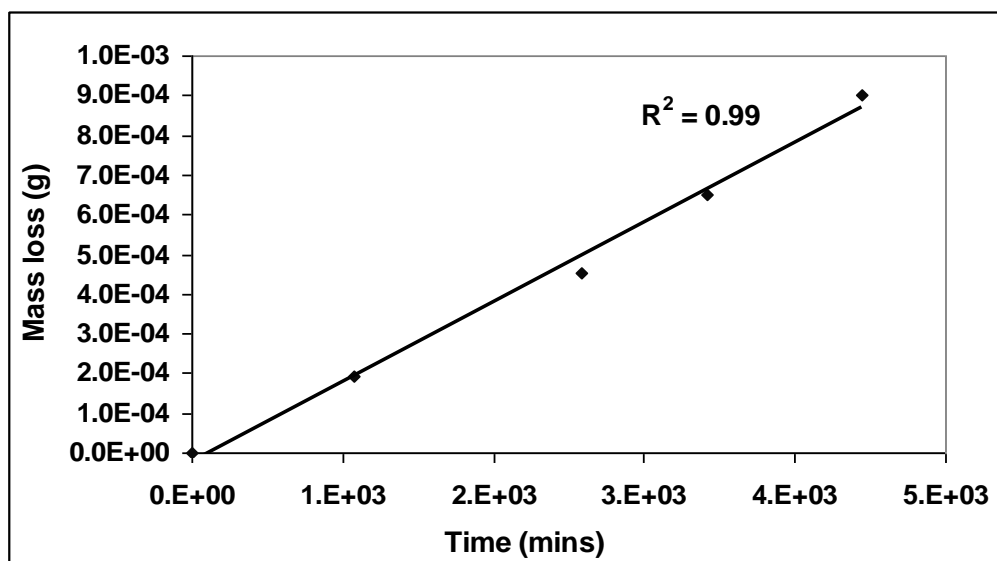
Appendix 3.1 Plot of I_2 permeation tube mass change over time, used to calculate permeation rates at 30°C.
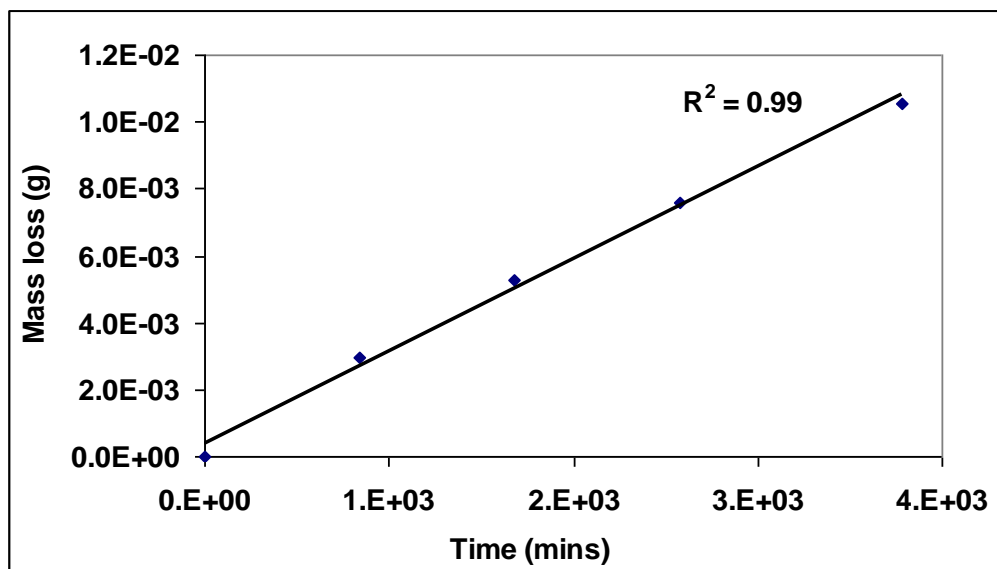
Appendix 3.2 Plot of I_2 permeation tube mass change over time, used to calculate permeation rates at 60°C.
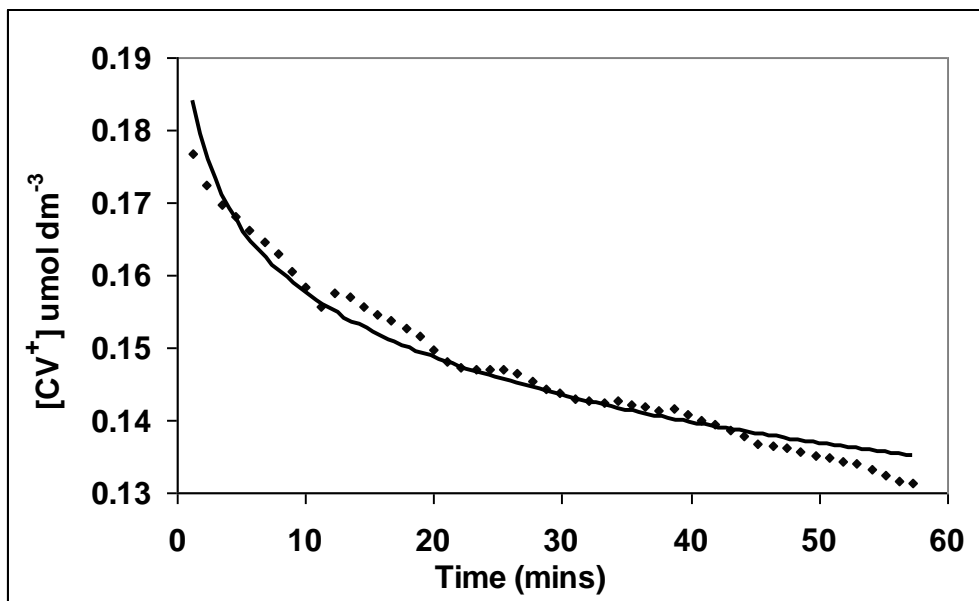
Appendix 3.3. CV^+ stability in hexane as a function of time.
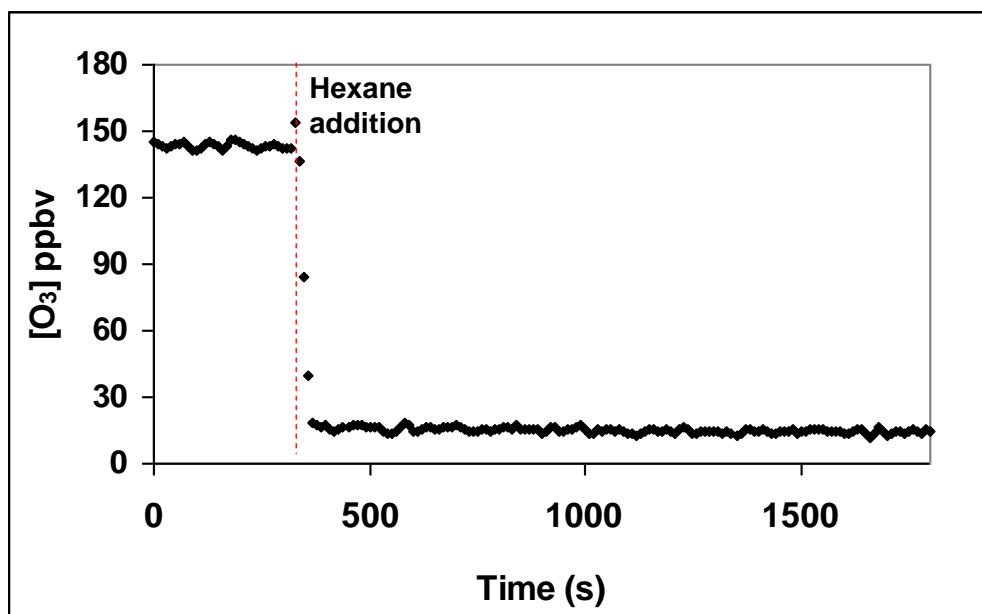
Appendix 3.4. Gaseous ozone trapping in hexane.
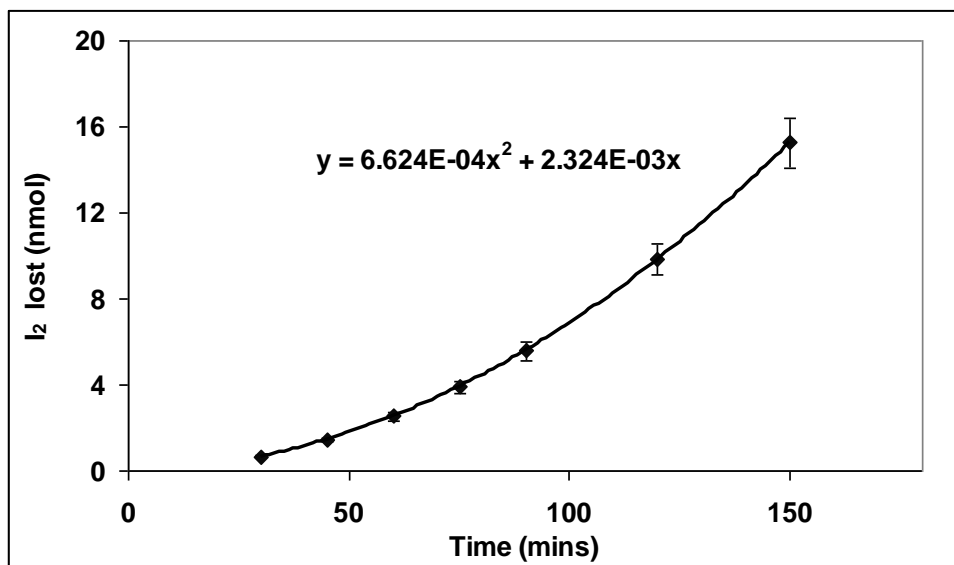
Appendix 3.5 I_2 lost from the $I_2 + O_3$ reaction in hexane as a function of time.
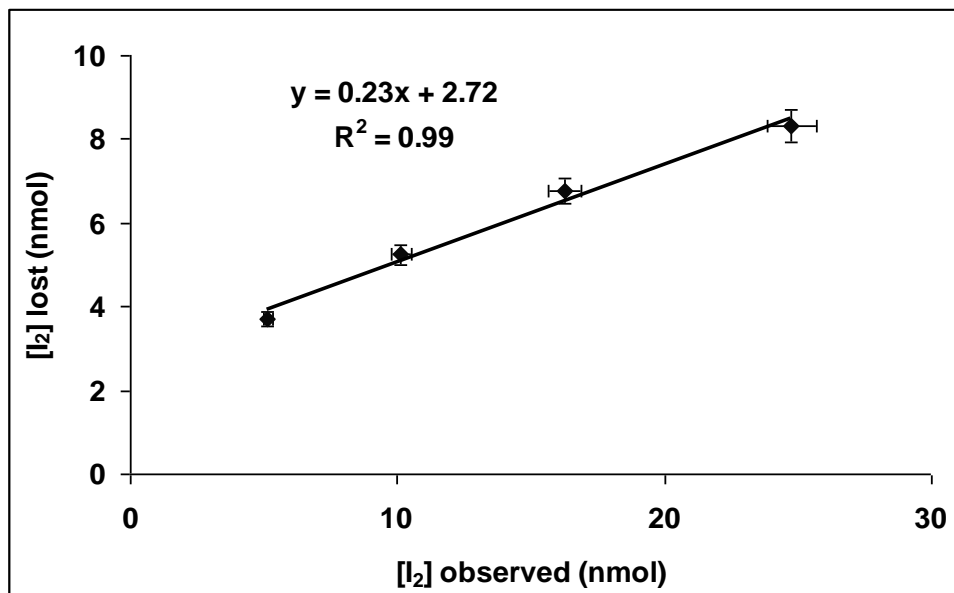
Appendix 3.6 I_2 lost from the $I_2 + O_3$ reaction in heaxne as a function of gaseous I_2 concentration.
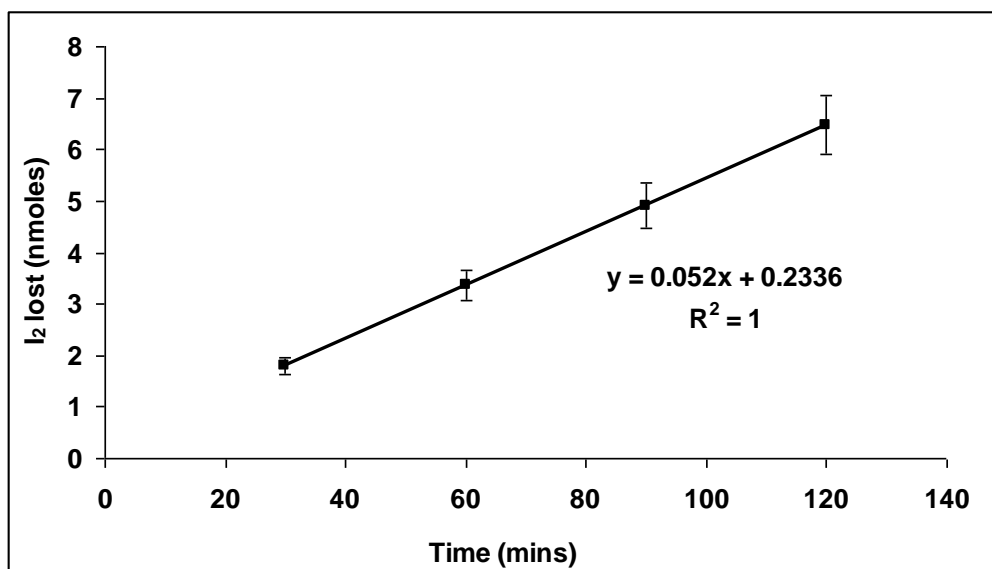
Appendix 3.7 I_2 loss attributed to wall losses as a function of time.
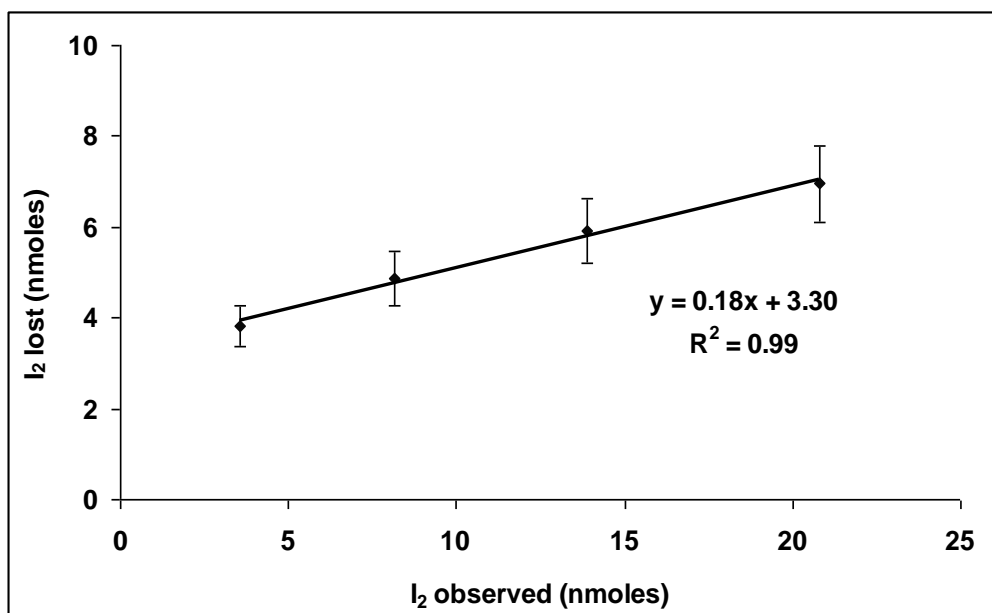
Appendix 3.8 I_2 loss attributed to wall losses as a function of gaseous $[I_2]$.
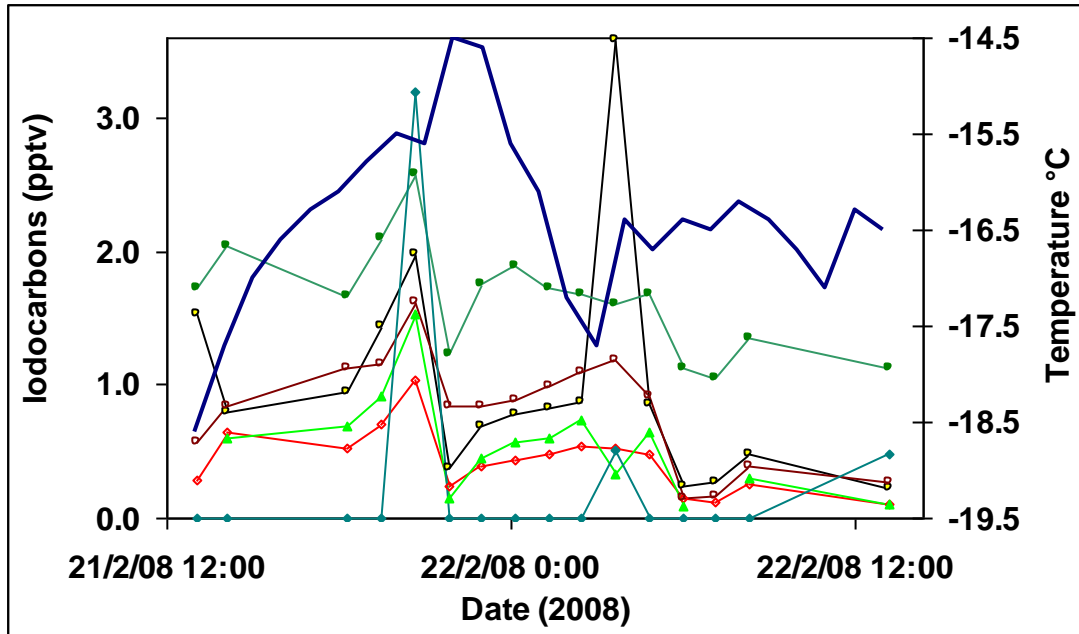
Appendix 4.1 VOIC concentrations and temperature (°C) over the 24 hour period (21st-22nd February). [C$_2$H$_5$I], red; [2-C$_3$H$_7$I], light green; [CH$_3$I], dark green; [1-C$_3$H$_7$I] x 10, black; [CH$_2$ICl] x 20, brown; [CH$_2$IBr] x 30, light blue; temperature, dark blue.
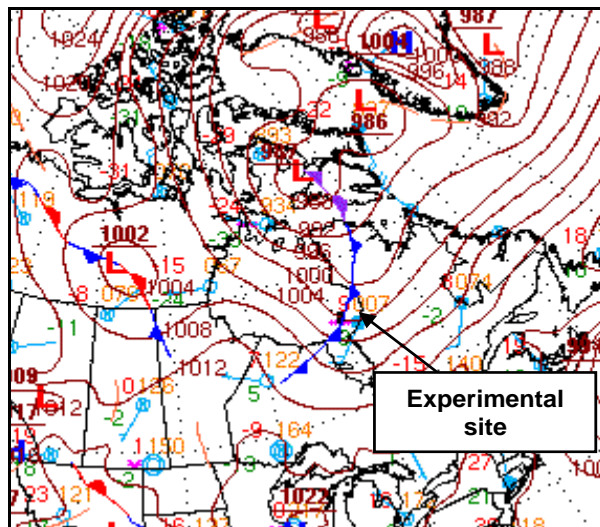
Appendix 4.2 Surface pressure chart of Hudson Bay on 23rd February 12:00 hrs (NOAA).
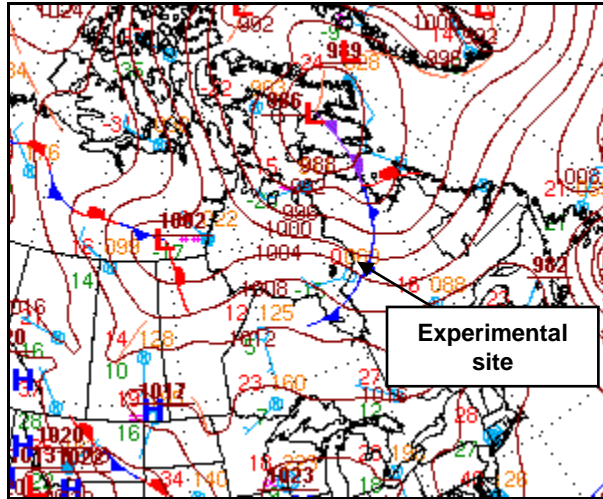
Appendix 4.3 Surface pressure chart of Hudson Bay on 23rd February 18:00 hrs (NOAA).
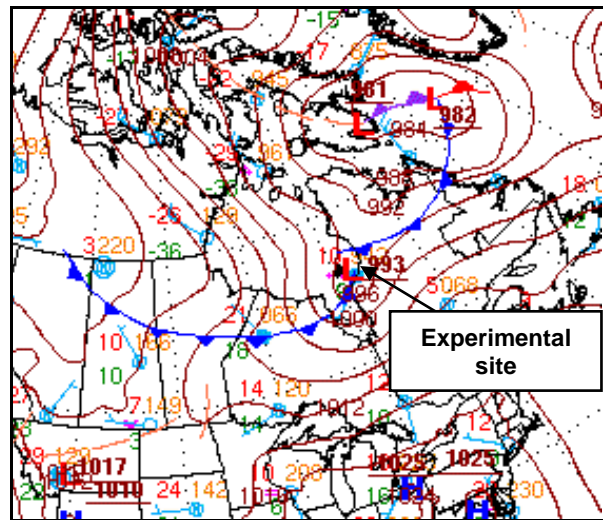
Appendix 4.4 Surface pressure chart of Hudson Bay on 24th February 12:00 hrs (NOAA).
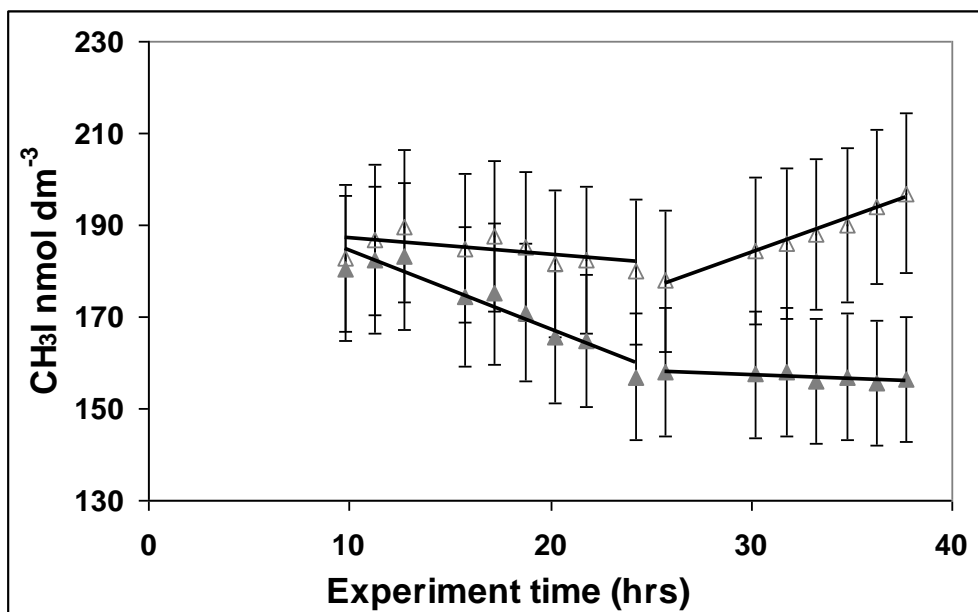
Appendix 5.1 CH$_3$I observed and corrected artificial seawater concentrations during experiment 1.Empty triangles, uncorrected data; Filled triangles, sea ice depth corrected data.
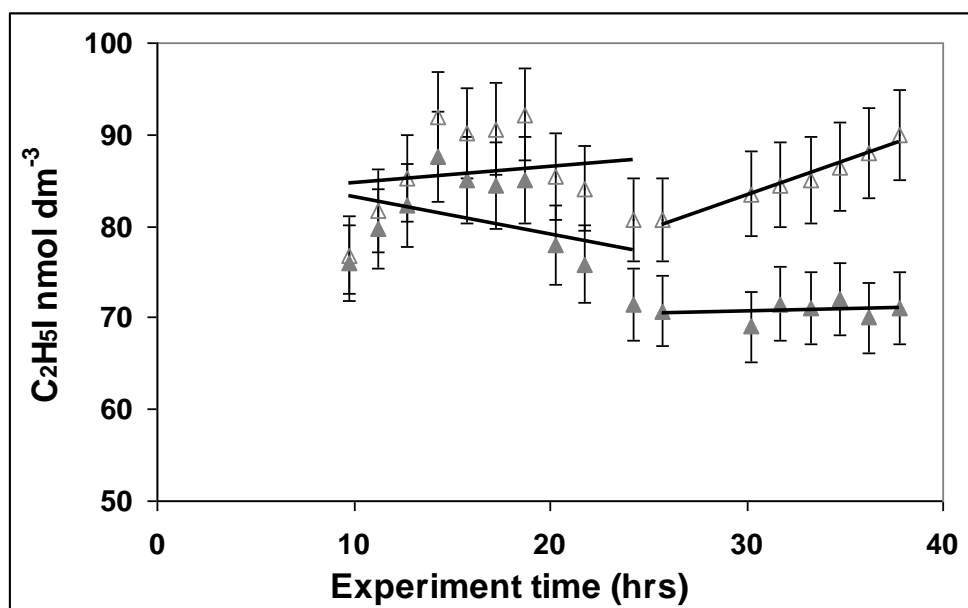
Appendix 5.2 C$_2$H$_5$I observed and corrected artificial seawater concentrations during experiment 1. Empty triangles, uncorrected data; filled triangles, sea ice depth corrected data.
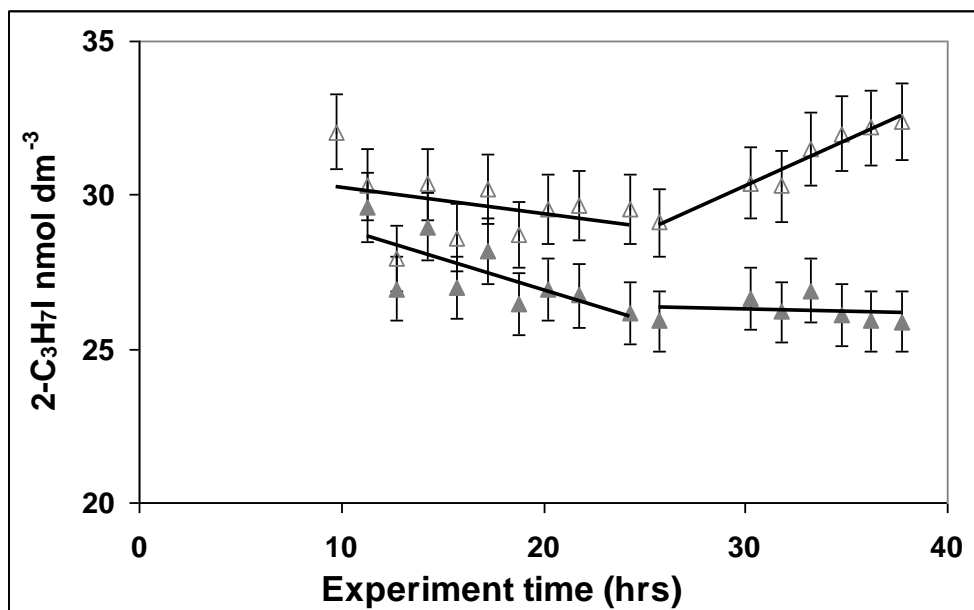
Appendix 5.3 2-C_3H_7I observed and corrected artificial seawater concentrations during experiment 1. Empty triangles, uncorrected data; Filled triangles, sea ice depth corrected data.
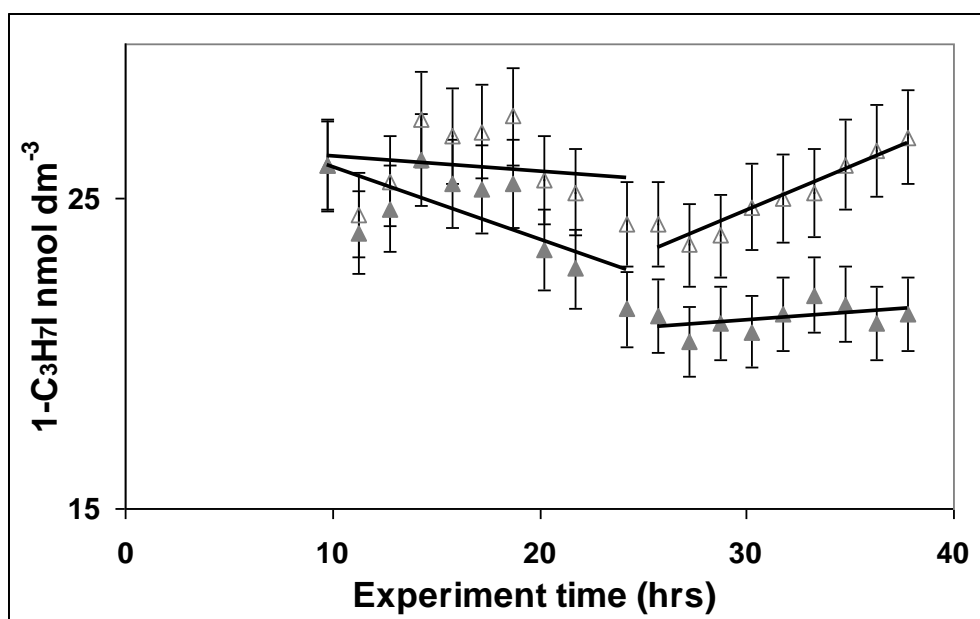
Appendix 5.4 1-C_3H_7I observed and corrected artificial seawater concentrations during experiment 1. Empty triangles, uncorrected data; Filled triangles, sea ice depth corrected data.
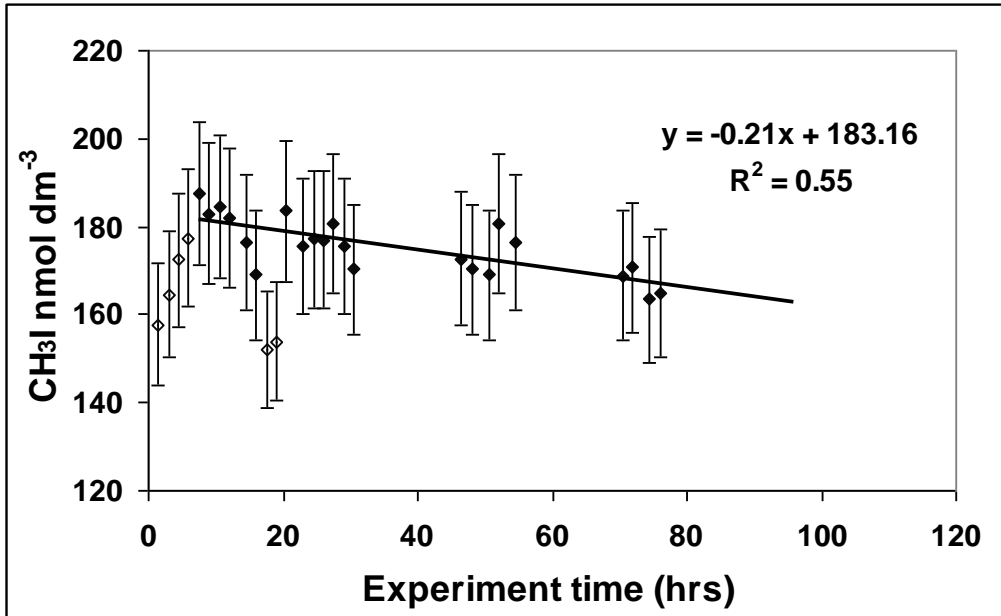
Appendix 5.5 CH$_3$I concentrations observed in artificial seawater during experiment 2. Empty diamonds, excluded data; Filled diamonds, included data.
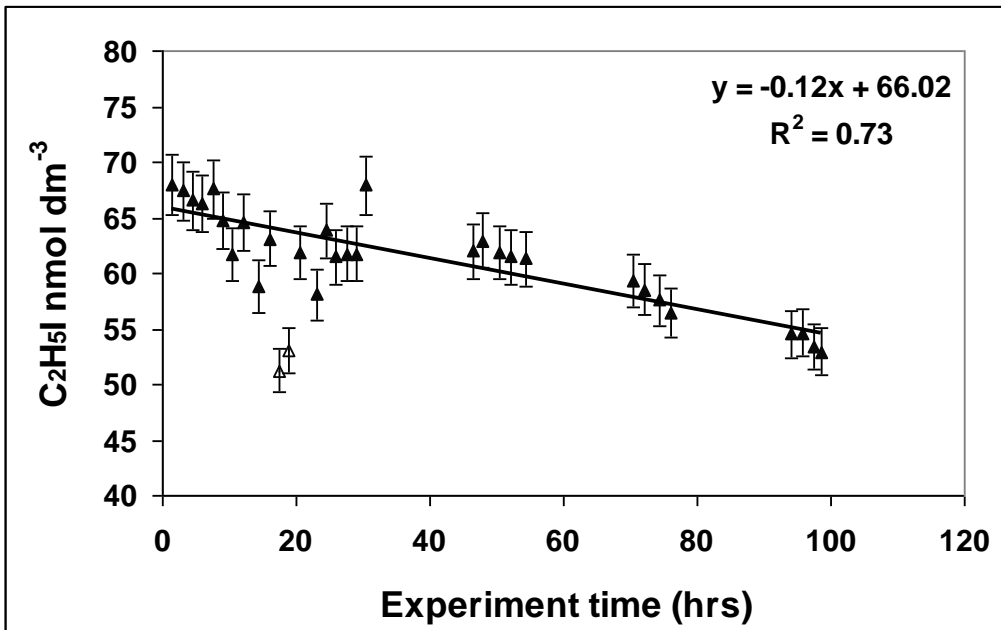
Appendix 5.6 C$_2$H$_5$I concentrations observed in artificial seawater during experiment 2. Empty triangles, excluded data; filled triangles, included data.
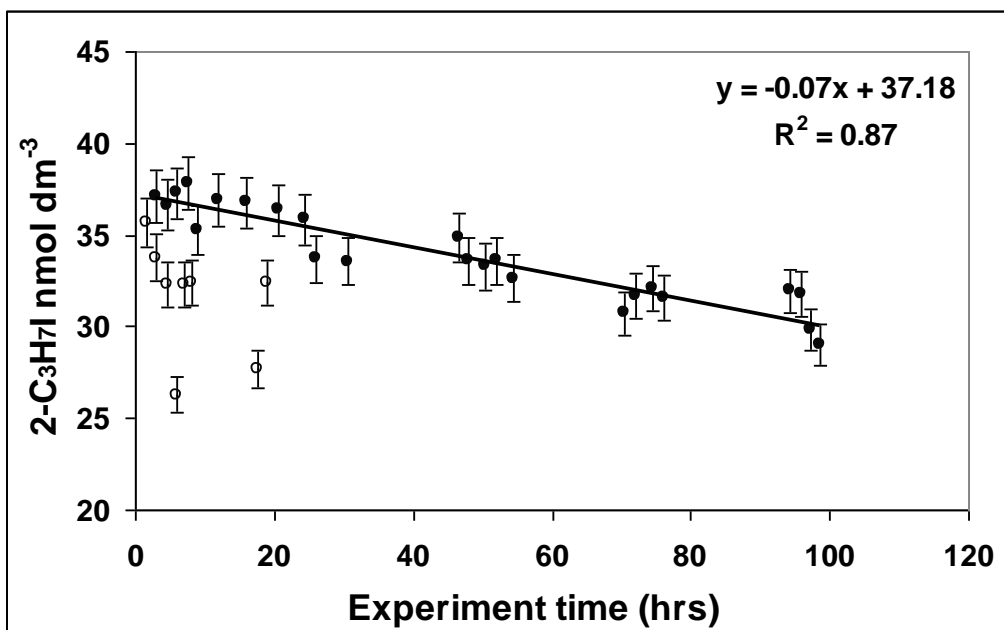
Appendix 5.7 2-C_3H_7I concentrations observed artificial seawater during experiment 2. Empty circles, excluded data; filled circles, included data.
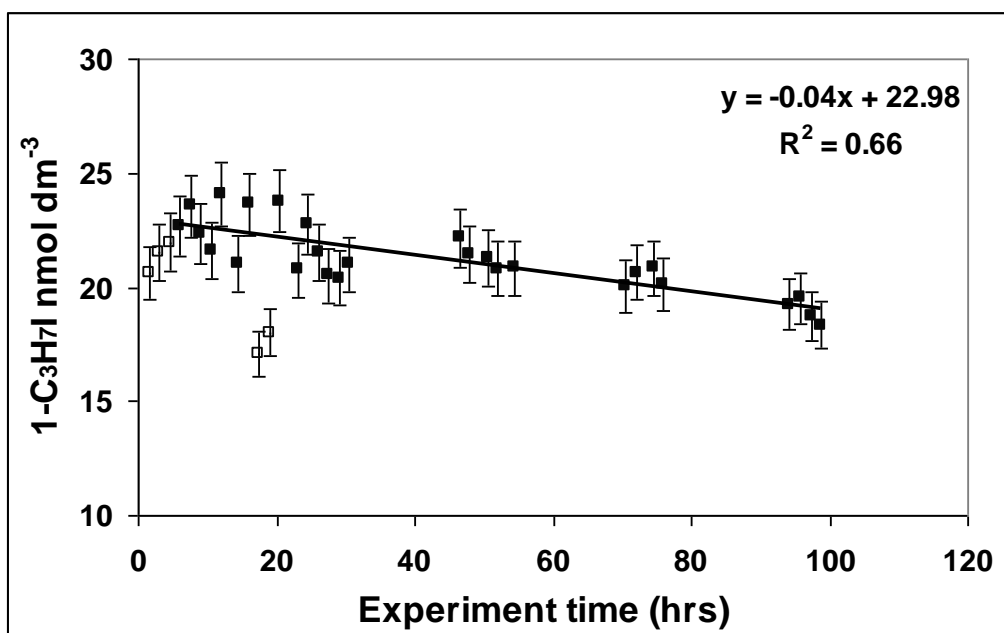
Appendix 5.8 1-C_3H_7I concentrations observed in artificial seawater during experiment 2. Empty squares, excluded data; filled squares, included data.
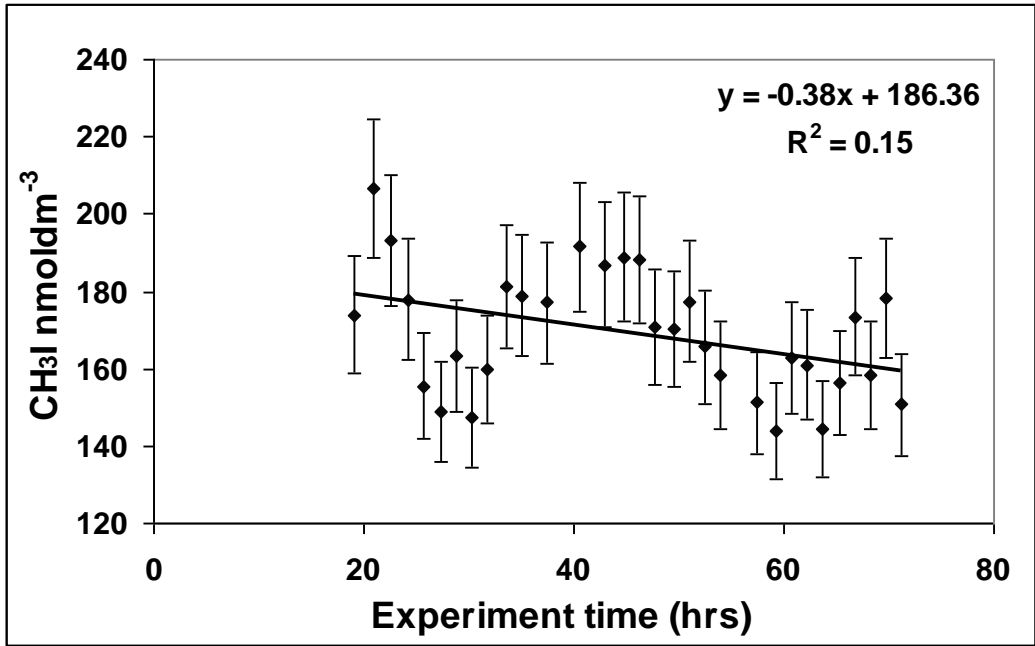
Appendix 5.9 CH$_3$I concentrations observed in artificial seawater during experiment 3.
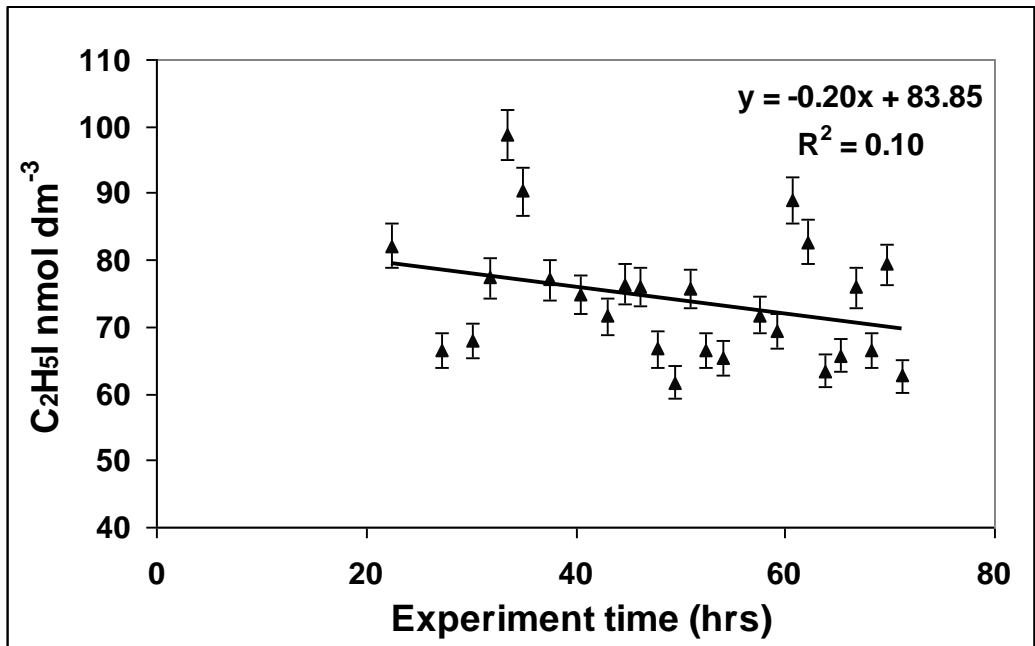
Appendix 5.10 C$_2$H$_5$I concentrations observed in artificial seawater during experiment 3.
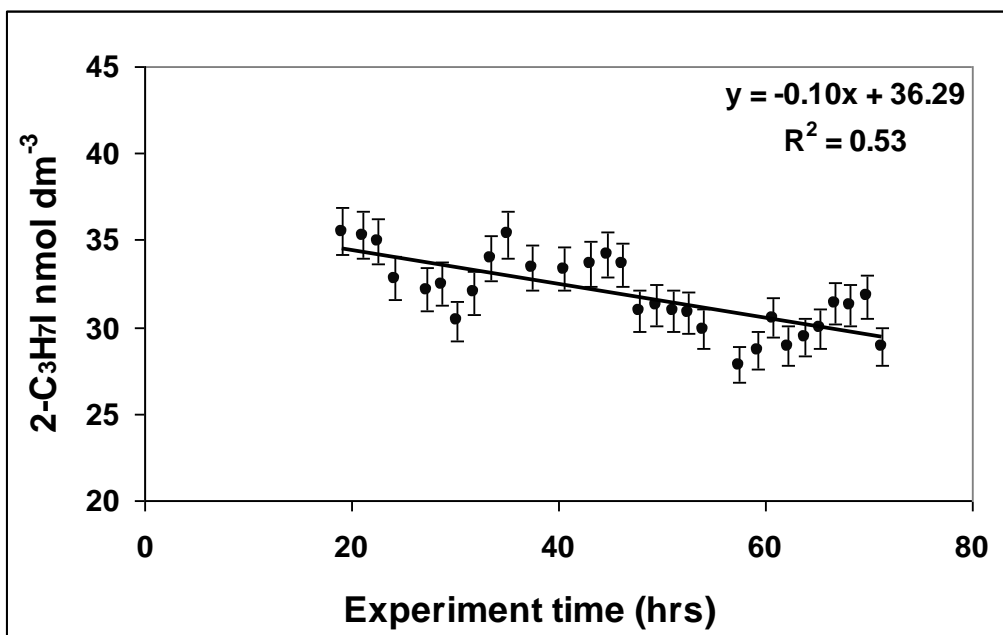
Appendix 5.11 2-C_3H_7I concentrations observed in artificial seawater during experiment 3.
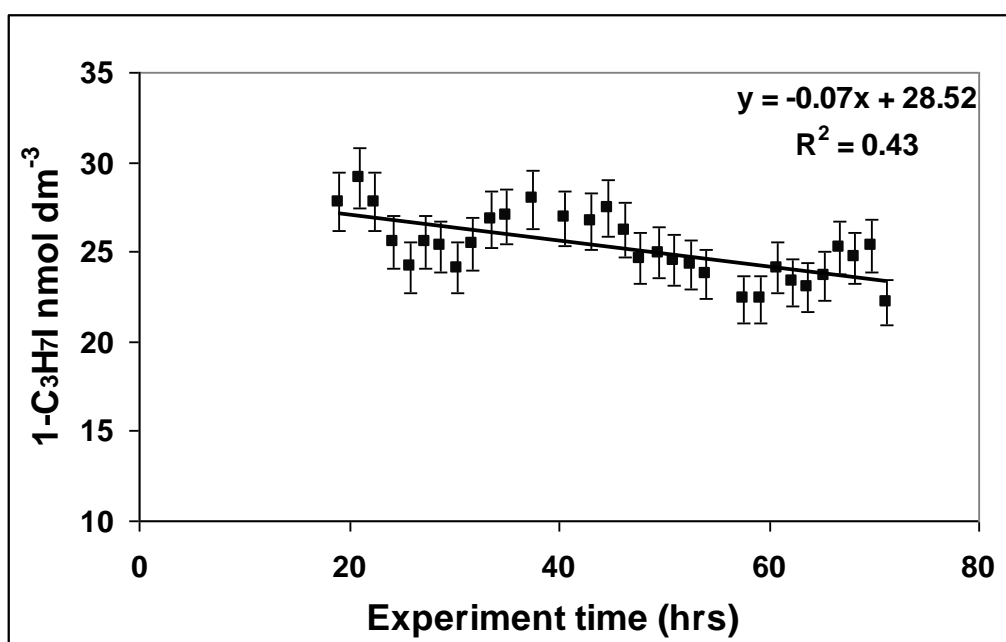
Appendix 5.12. 1-C_3H_7I concentrations observed in artificial seawater during experiment 3.
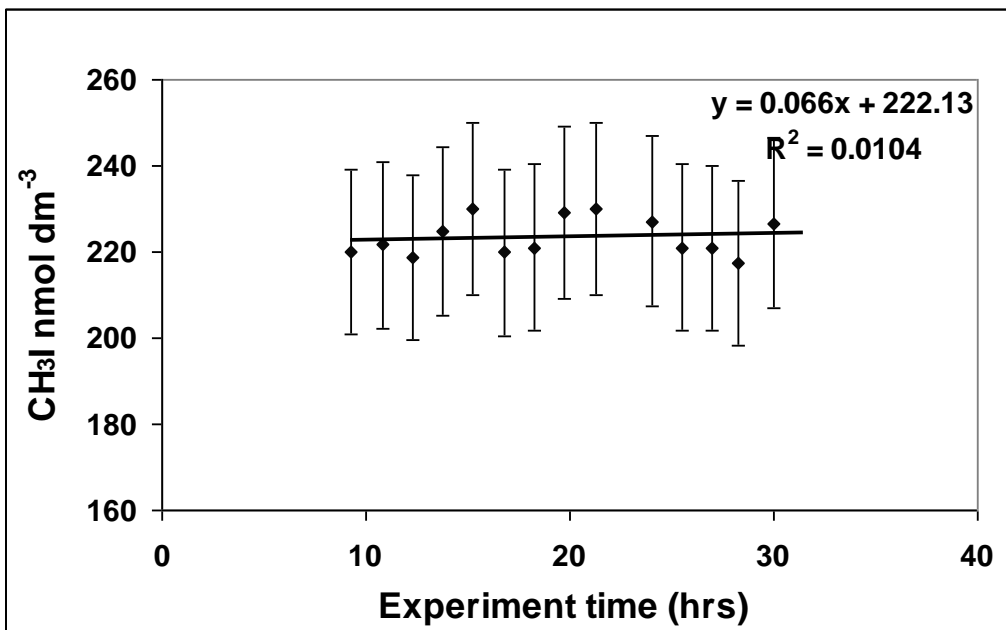
Appendix 5.13. CH$_3$I concentrations observed in freshwater during experiment 4.
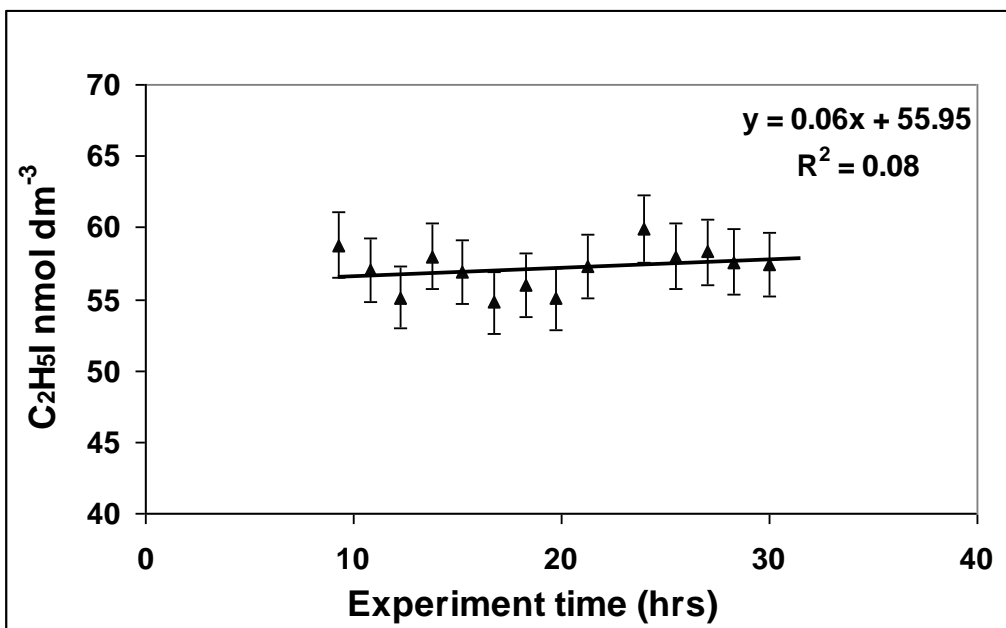
Appendix 5.14 C$_2$H$_5$I concentrations observed in freshwater during experiment 4.
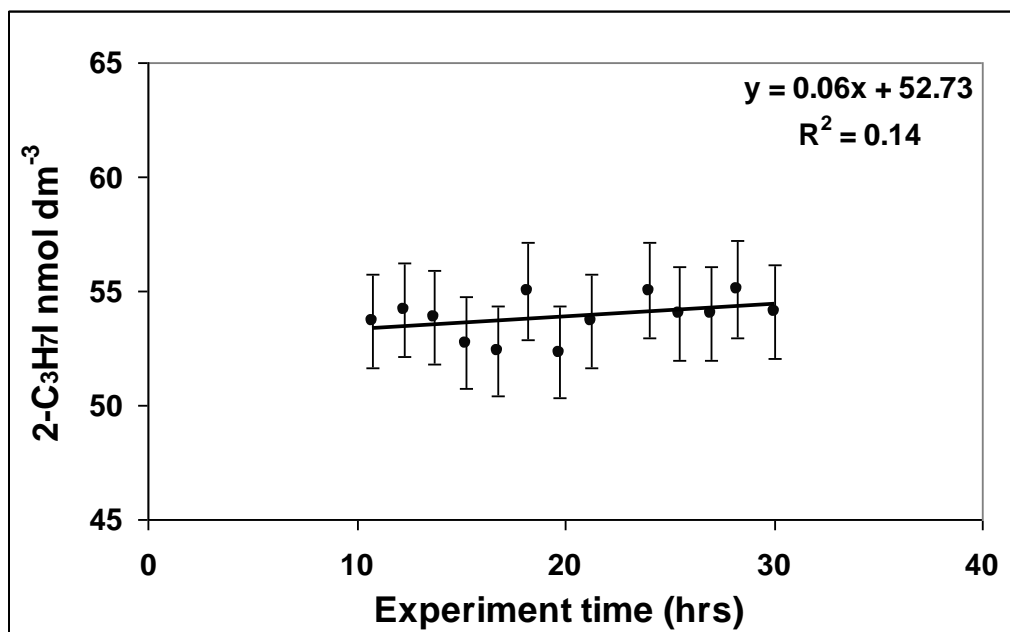
Appendix 5.15 2-C_3H_7I concentrations observed in freshwater during experiment 4.
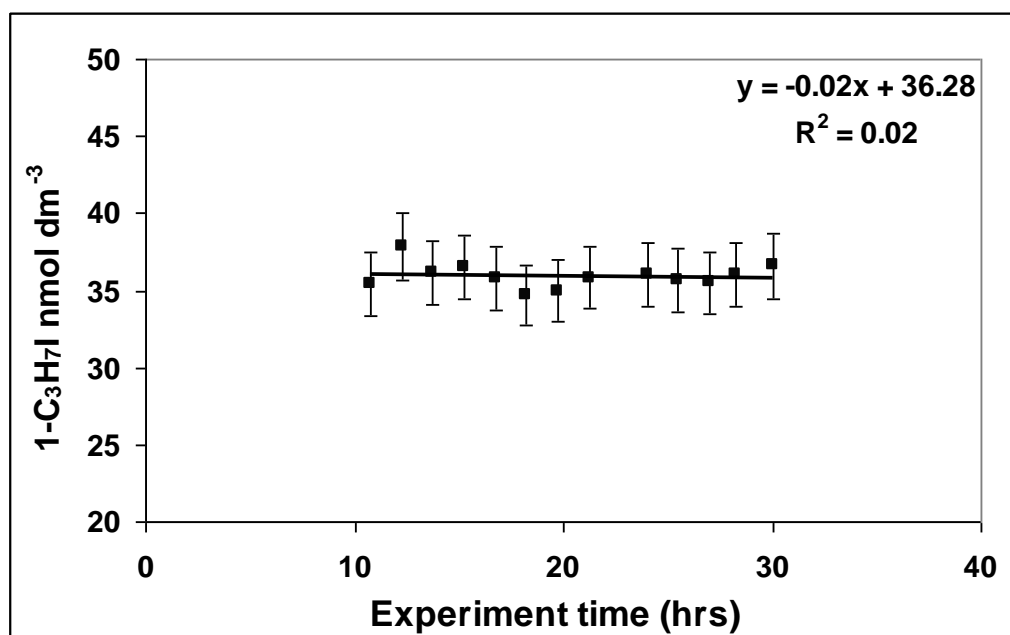
Appendix 5.16 1-C_3H_7I concentrations observed in freshwater during experiment 4.
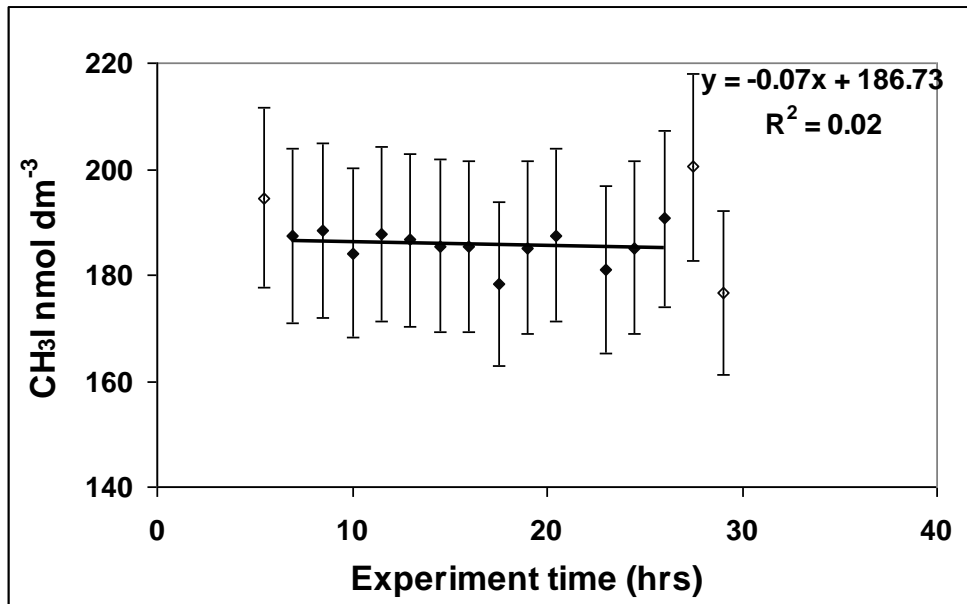
Appendix 5.17 CH_3I concentrations observed in freshwater during experiment 5. Empty diamonds, excluded data; filled diamonds, included data.
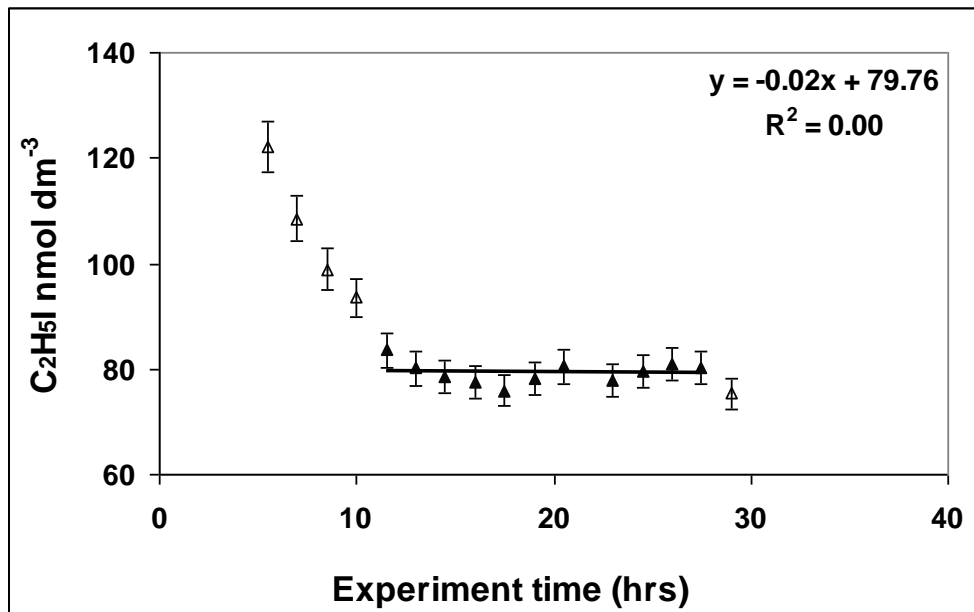
Appendix 5.18 C_2H_5I concentrations observed in freshwater during experiment 5. Empty triangles, excluded data; filled diamonds, included data.
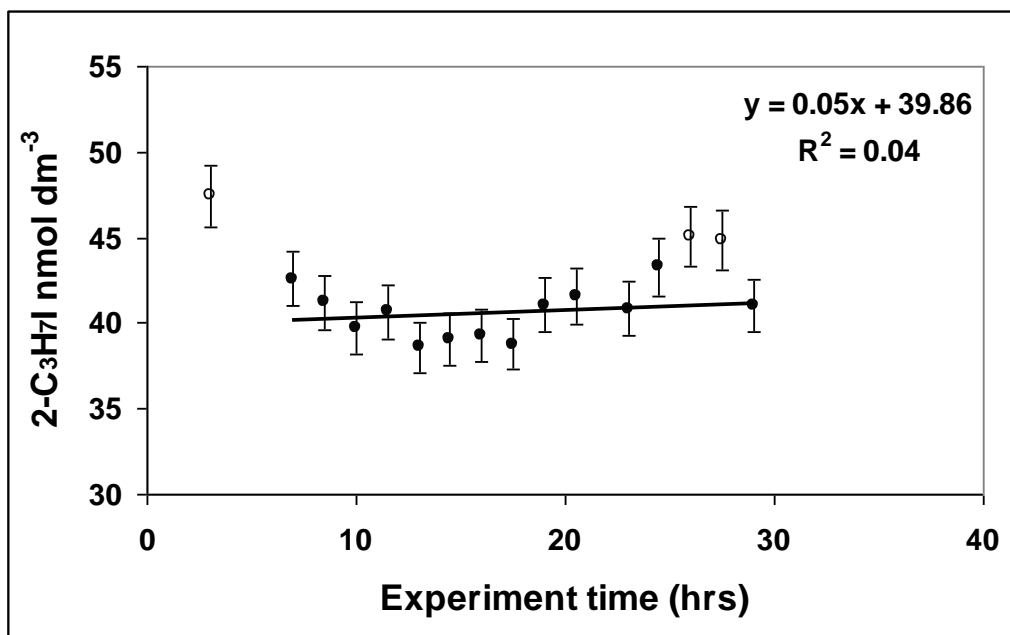
Appendix 5.19. 2-C_3H_7I concentrations observed in freshwater during experiment 5. Empty circles, excluded data; filled circles, included data.
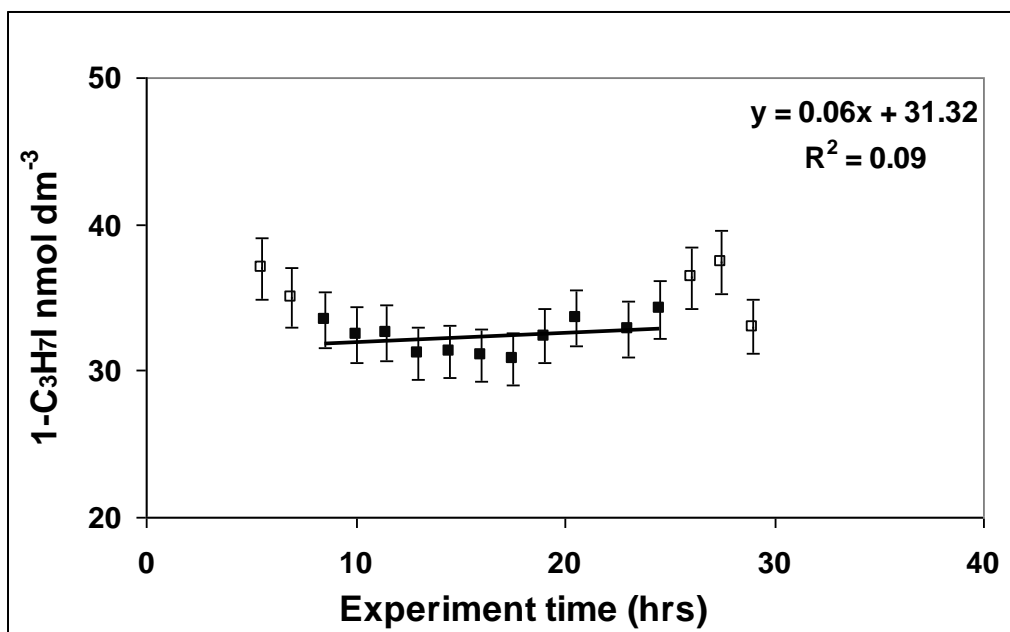
Appendix 5.20 1-C_3H_7I concentrations observed in freshwater during experiment 5. Empty squares, excluded data; filled squares, included data.

Glossary

AMDE	Atmospheric Mercury Depletion Event
BBCEAS	Broad Band Cavity Enhanced Absorption Spectroscopy.
BOC	British Oxygen Company
CCN	Cloud Condensation Nuclei
COBRA	COmbined impact of BRomine and iodine release on the Arctic atmosphere
CVAO	Cape Verde Atmospheric Observatory
DMS	Dimethylsulphide
DOC	Dissolved Organic Carbon
DOI	Dissolved Organic Iodine
DOM	Dissolved Organic Material
EI	Electron Ionisation
EPS	Exopolymeric Substances
FA	Fulvic acids
GEM	Gaseous Elemental Mercury
GC	Gas Chromatography
GC/MS	Gas Chromatography Mass Spectrometry
HCV	Leuco Crystal Violet indicator
HETP	Height Equivalent of a Theoretical Plate
HPLC	High Performance Liquid Chromatography
HS	Humic Substances

HO$_X$	OH + HO$_2$
I$^-$	Iodide
I$_2$	Molecular iodine
I$_3^-$	Tri-iodide
IO$_3^-$	Iodate
IO	Iodine Monoxide
IOP	Iodine Oxide Particles
ICP-MS	Inductively coupled plasma mass spectrometry
IPCC	The Intergovernmental Panel on Climate Change
LoD	Limit of detection
LoQ	Limit of Quantitiation
LP-DOAS	Long Path Differential Optical Absorption Spectroscopy
MAX-DOAS	Multi Axial Differential Optical Absorption Spectroscopy
MBL	Marine Boundary Layer
MFC	Mass Flow Controller
MS	Mass Spectrometer
NPL	UK National Physics Laboratory
NO$_X$	NO + NO$_2$
O$_3$	Ozone
O(^{1}D)	Excited State Atomic Oxygen
O(^{3}P)	Ground State Atomic Oxygen

ODE	Ozone Depletion Event	**TD-GC/MS**	Thermal Desorption-Gas Chromatography Mass Spectrometry
OH	Hydroxyl radical		
PBS	Phosphate Buffer Solution	**T E**	Trapping Efficiency
P_c	Critical Brine Volume Fraction	**THAMO**	Tropospheric Halogen Atmospheric Chemistry Model
P	Brine Volume Fraction		
P&T	Purge and Trap	**VOC**	Volatile Organic Compounds
PMT	Photomultiplier Tube	**VOBC**	Volatile Organic Brominated Compounds
QMS	Quadrupole Mass Spectrometer	**VOIC**	Volatile Organic Iodinated Compounds
REM	Reactive Elemental Mercury		
RSD	Relative Standard Deviation	**VSLH**	Very Short Lived Halogenated Substances
SIR	Selective Ion Recording		
TDU	Thermal Desorption Unit	**WCOT**	Wall Coated Open Tubular

References

Ackley, S. F. Ice scavenging and nucleation: two mechanisms for the incorporation of algae into newly formed sea ice. *EOS, 63, 64,* (1982).

Adamson, A. *Physical Chemistry of Surfaces (fifth ed), Wiley-Interscope, New York* (1990).

Akkanen, J. Does dissolved organic matter matter? Implications for bioavailability of organic chemicals.*University of Joensuu, PhD Dissertations in Biology, 16, 7,* (2008).

Aldaz, L. Flux measurements of atmospheric ozone over land and water. *Journal of Geophysical Research, 74, 28, 6943-6946* (1969).

Allen, N. D. C. Bernath, P. F. Boone, C. D. Global carbon tetrachloride distributions obtained from the atmospheric chemistry experiment (ACE). *Atmospheric Chemistry and Physics, 9, 13299 - 13325,* (2009).

Ambrose, D. Gas Chromatography, second edition. *The Butterworth group,* (1971).

Andrae, M. O. and Raemdonck, H. Dimethyl sulfide in the surface ocean and the marine atmosphere: a global review. *Science, 221, 774-777,* (1983).

Ariya, P. A. Dastoor, A. P. Amyot, M. S. Schroeder, W. H. Barrie, L. A. Anlauf, K. Raofie, F. Ryzhov, A. Davignon, D. Lalonde, J. and Steffen, A. The Arctic: a sink for mercury. *Tellus, 56B, 56, 5, 397- 403,* (2004).

Ashworth, S. H. Allan, B. J. and Plane, J. M. C. High resolution spectroscopy of the OIO radical; implications for the ozone depletion potential of iodine in the marine boundary layer. *Geophysical Research Letters, 29, 10, doi:10.1029/2001GL013851* (2002).

Augdahl, E. and Klaebo, P. Spectroscopic studies of charge transfer complexes XIII. Dimethylcyanamide and iodine, iodine monochloride and iodine monobromide. *Acta Chemica Scandinavica, 19, 807-816,* (1965).

Avallone, L. M. Toohey, D. W. Fortin, T. J. McKinney, K. A. and Fuentes, J. D. In situ measurements of bromine oxide at two high latitude boundary layer sites: Implications of variability. *Journal of Geophysical Research, 108, D3, 4089, doi:10.1029/2002JD002843,* (2003).

Badgely, F. Heat budget at the surface of the Arctic Ocean. Proceeding of the symposium on the Arctic heat budget. *The Rand corporation report RM-52233-NSF, 267-277,* (1966).

Bainbridge, R. The size, shape and density of marine phytoplankton concentrations. *Biological Reviews , 32, 91 – 115,* (1957).

Banic, C. Beauchamp, S. Tordon, R. Schroeder, W. Steffen, A. and Anlauf, K. Vertical distribution of gaseous elemental mercury in Canada. *Journal of Geophysical Research, 10, 4264 - 4278,* (2002).

Barrie, L. A. Bottenheim, J. W. Scnell, R. C. Crutzen, P. J. and Rasmussen, R. A. Ozone destruction and photochemical reactions at polar sunrise in the lower Arctic atmosphere. *Nature, 334, 138 – 141,* (1988).

Bell, N. Hsu, L. Jacob, D. J. Schultz, M. G. Blake, D. R. Butler, J. H. King, D. B. Lobert, J. M. Methyl iodide: Atmospheric budget and use as a tracer of marine convection in global models. *Journal of Geophysical Research, 107, D17, 4340 - 4352,* (2002).

Bichsel, Y. and von Gunten, H. Oxidation of iodide and hypoiodous acid in the disinfection of natural waters. *Environental Science and Technology, 33, 22, 4040-4045,* (1999).

Bloss, W. J. Lee, J. D. Johnson, G. P. Sommariva, R. Heard, D. E. Saiz-Lopez, A. Plane, J. M. C. McFiggans, G. Coe, H. Flynn, M. Williams, P. Rickard, A. and Fleming, Z. L. Impact of halogen monoxide chemistry upon boundary layer OH and HO_2 concentrations at a coastal site. *Geophysical Research Letters, 32, L06814, doi:10.1029/2004GL022084,* (2005).

Bobrowski, N. Hönninger, G. Galle, B. and Platt, U. Detection of bromine monoxide in a volcanic plume. *Nature, 423, 273 – 276,* (2003).

Bobrowski, N. Hönninger, G. Galle, B. and Platt, U. Reactive halogen chemistry in volcanic plumes. *Journal of Geophysical Research., 112, 17, D06311, doi:10.1029/2006JD007206,* (2004).

Bottenheim, J. W. Dibb, J. E. Honrath, R. E. and Shepson, P. B. An introduction to the ALERT 2000 and SUMMIT 2000 Arctic research studies. *Atmospheric Environment, 36, 34, 2467 – 2469,* (2002).

Bottenheim, J. W. Matrai, P. Netcheva, S. Perovich, D. Shepson, P. B. Simpson, W. Longterm measurements of ozone, bromine monoxide and carbon dioxide over the Frozen Arctic Ocean Surface. *American Geophysical Union, fall meeting abstract,* (2010).

Boundries, H. and Bottenheim, J. W. Cl and Br atom concentrations during a surface boundary layer ozone depletion event in the Canadian high Arctic. *Geophysical Research Letters, 27, 517 – 520,* (2000).

Broadgate, W. J. Liss, P. S. Penkett, S. A. Seasonal emissions of isoprene and other reactive hydrocarbon gases from the ocean. *Geophysical Research Letters, 24, 21, 2675-2678,* (1997).

Cainey, J. Keywood, M. Grose, M. Krummel, P. Galbally, I. Johnston, P. Gillett, R. Meyer, M. Fraser, P. Steel, P. Precursors to particles at Cape Grim: a campaign overview. *Environental Chemistry, 4, 3, 143-150,* (2007).

Calace, N. Catrambone, T. Petronio, B. M. Pietroletti, M. and Rugo, C. Fulvic acid enrichment in the microlayer of the gerlache inlet sea (Antarctica): Preliminary results. *Water Reasearch, 41, 6 - 7, 1, 152 - 158,* (2004).

Calvert, J. G. and Lindberg, S. E. A modelling study of the mechanism of the halogen-ozone-mercury homogenous reactions in the troposphere during the polar spring. *Atmospheric Environment, 37, 32, 4467 - 4481,* (2003).

Campos, M. L. Sanders, R. Jickells, T. The dissolved iodate and iodide distribution in the South Atlantic from the Weddell Sea to Brazil. *Marine Chemistry, 65, 3-4, 167 – 175,* (1999).

Carlson, D. J. Dissolved organic materials in surface microlayers: temporal and spatial variability and relation to sea state. *Limnology and Oceanography, 28, 3, 415 - 431,* (1983).

Carpenter, L. J. Iodine in the marine boundary layer. *Chemical Reviews, 103, 12, 4953 – 4962,* (2003).

Carpenter, L. J. Jones, C. E. Dunk, R. M. Hornsby, K. E and Woeltjen, J. Air sea fluxes of biogenic bromine from the tropical and North Atlantic Ocean. *Atmospheric Chemistry and Physics, 5, 2927 – 2934,* (2009).

Carpenter, L. J. Hopkins, J. R. Jones, C. E. Lewis, A. C. Parthipan, R. Wevill, D. J. Abiotic source of reactive organic halogens in the sub-Arctic atmosphere. *Environmental Science and Technology, 39, 22, 8812 – 8816,* (2005).

Cavalieri, D. J. Parkinson, C. L. Antarctic sea-ice variability and trends, 1979 – 2006. *Journal of Geophysical Research, 113, 19, C07004, doi:10.1029/2007JC004564* (2008).

Chance. R. J. Shaw, M. D. Telgramm, L. Baxter, M and Carpenter, L. J. A comparison of spectrophotometric and denuder based approaches for the determination of gaseous molecular iodine. *Atmospheric Measurement Techniques, 3, 177 - 185* (2010).

Chang, W. Heikes, B. G. and Lee, M. Ozone deposition to the sea surface: chemical enhancement and wind speed dependence. *Atmospheric Environment, 38, 7, 1053-1059* (2004).

Cheng, J. Hoffmann, M. R. and Colussi, A. J. Anion fractionation and reactivity at air/water : methanol interfaces. Implications for the origin of Hofmeister effects. *Journal of Physical Chemistry B, 112, 24, 7157 - 7167,* (2008).

Christian, G. D. Analytical chemistry, fifth edition, (1994).

Christie, W. W. Gas Chromatography and Lipids. *P. J Barnes and Associates (The Oily Press),* (1989).

Chuck, A. L. Turner, S. M. and Liss, P. S. Oceanic distributions and air-sea fluxes of biogenic halocarbons in the open ocean. *Journal of Geophysical Research, 110, 10, doi:10.1029/2004JC002741,* (2005).

Clifford, D. Donaldson, D. J. Brigante, M. Anna, B. and George, C. Reactive uptake of ozone by chlorophyll at aqueous surfaces. *Environmental Science and Technology, 42, 4, 1138 - 1143,* (2008).

Conklin, M. H. and Bales, R. C. SO_2 uptake on ice spheres: Liquid Nature of the Ice-Air interface. *Journal of Geophysical Research, 98, D9,* (1993).

Cooper, W. J. Lean, D. R. S. Carey, J. H. Spatial and temporal patterns of hydrogen peroxide in lake waters. *Canadian Journal of Fisheries and Aquatic Science, 46, 7, 1227 – 1231,* (1981).

Cotter, E. S. N. Booth, N. J. Canosa-Mas, C. E. Gray, D. J. Shallcross, D. E. Wayne, R. P. Reactions of Cl atoms with CH_3I, C_2H_5I, 1-C_3H_7I, 2-C_3H_7I and CF_3I: kinetics and atmospheric relevance. *Physical Chemistry Chemical Physics*, *3*, *402 – 408,* (2001).

Cox, G. F. and Weeks, W. F. Brine drainage and initial salt entrapment in sodium chloride ice. *CRREL Research Report 354, Cold Regions Research and Engineering laboratory, Hanover,* (1975)

Cox, G. F and Weeks, W. F. Numerical simulations of the profile properties of underformed first year sea ice during the growth season. *Journal of Geophysical Research, 93, 10, 12449 – 12460,* (1980).

Crawford, J. Davis, D. Chen, G. Bradshaw, J. Sandholm, S. Gregory, G. Sachse, G. Anderson, B. Collins, J. Blake, D. Singh, H. Heikes, B. Talbot, R. Rodriguez, J. Photostationary state analysis of the NO_2 – NO system based on airborne observations from the western and central North Pacific. *Journal of Geophysical Research, 101, 2053 – 2072,* (1996).

Davidovits, P. Kolb, C. E. Williams, L. R. Jayne, J. T. Mass accommodation and chemical reactions at gas-liquid interfaces. *Chemical Reviews, 106, 4, 1323 – 1354,* (2006).

Decho, A.W. Microbial exopolymer substances in ocean environments-their roles in food webs and marine processes. *Oceanography and Marine Biology, an annual review, 28, 73 - 153,* (1990).

Decho, A. W. Microbial biofilms in intertidal systems: an overview. *Continental Shelf Research, 20, 1257 – 1273,* (2000).

Delille, B. Jourdain, B. Borges, A. V. Tison, J. L. and Delille, D. Biogas dynamics in spring Antarctic fast ice. *Limnology Oceanography, 52, 4, 1367 – 1379,* (2007).

Desjardins, S. Landry, J. A. and Farrant, J. P. Effects of water and pH on the oxidative oligomerization of chloro and methoxyphenol by montmorillonite clay. *Journal of Soil Contamination, 8, 175 – 195,* (1999).

Dieckmann, G. S. Lange, M. A. Ackley, S. F. and Jennings. J. C. The nutrient status in sea ice of the Weddell Sea during winter: effects of sea ice texture and algae. *Polar Biology, 11, 7, 449 – 456,* (1991).

Dimmer, C. H. Simmonds, P. G. Nickless, G. and Bassford, M. R. Biogenic fluxes of halomethanes from Irish peatland ecosystems. *Atmospheric Environment, 31, 2, 321 – 330,* (2000).

Dixneuf, S. Ruth, A. A. Vaughan, S. Varma, R. M. and Orpha, J. The time dependence of molecular iodine emission from *Laminaria digitata. Atmospheric Chemistry and Physics, 9, 823-829* (2009).

Domine, F. Taillandier, A. S. Simpson, W. R. and Severin, K. Specific surface area, density and microstructure of frost flowers. *Geophysical Research Letters, 32, 4, L13502, doi: 10.1029/2005GL023245,* (2005).

Dowideit, P. von Sonntag, C. Reaction of ozone with ethane and its methyl- and chlorine substituted derivatives in aqueous solution. *Environental Science and Technology, 32, 1112 - 1119,* (1998).

Duce, R. A. and Woodcock, A. H. Difference in chemical composition of atmospheric sea salt particles produced in the surf zone and on the open sea in Hawaii. *Tellus, 23, 427 – 435,* (1971).

Duce, R. A. Liss, P. S. Merrill, J. T. Atlas, E. L. Buat-Meriard, P. Hicks, B. B. Miller, J. M. Prospero, J. M. Arimoto, R. Church, T. M. Ellis, W. Galloway, J. N. Hansen, L. Kichells, T. D. Knap, A. H. Reinhardt, K. H. Schneider, B. Soudine, A. Tokos, J. J. Tsunogai, S. Zhou, M. The atmospheric input of trace species to the World Ocean. *Global Biogeochemical Cycles, 5, 193 – 259,* (1991).

Dunnivant, F. M and Ginsbach, J. W. Gas Chromatography, Liquid Chromatography, Capillary Electrophoresis – Mass Spectrometry. *Whitman College Chemistry Department, Walla Walla,* (2010).

Eicken, H. From the microscopic to the macroscopic, to the regional scale: Growth, microstructure and properties of sea ice. *Sea ice: An Introduction to it's physics, chemistry, biology and geology.* (2008).

Enami, S. Yamanaka, T. Nakayama, T. Hashimoto, S. Kawasaki, M. A gas phase kinetic study of the reaction between BrO and methyl peroxy radicals at atmospheric temperatures. *Journal of Physical Chemistry A, 111, 17, 3342 – 3348,* (2007).

Ewing, G. W. Analytical Instrumentation handbook, second edition. *Marcel Dekker INC,* (1997).

Fan, S. M. and Jacob, D. J. Surface ozone depletion in Arctic spring sustained by bromine reactions on aerosols. *Nature, 359, 522 – 524,* (1992).

Farman, J. C. Gardiner, B. G. Shanklin, J. D. Large losses of total ozone in Antarctica reveal seasonal ClOx/NOx interaction. *Nature, 315, 207 – 210,* (1985).

Fenical, W. Natural halogenated organics. *Marine Organic Chemistry, Elsevier Oceanography Series, 31, 375 – 393,* (1981).

Fickert, S. Adams, J. W. and Crowley, J. N. Activation of Br_2 and BrCl via uptake of HOBr onto aqueous salt solutions. *Journal of Geophysical Research, 104, 23719-23727,* (1999).

Finlay, B. D. and Saltzman, E. S. Observations of Cl_2, Br_2 and I_2 in coastal marine air. *Journal Geophysical Research, 113, D21301, doi:10.1029/2008JD010269,* (2008).

Foster, K. L. Plastridge, R. A. Bottenheim, J. W. Shepson, P. B. Finlayson-Pitts, B. J. and Spicer, C. W. The role of Br_2 and BrCl in surface ozone destruction at Polar Sunrise, *Science, 291, 471 - 474,* (2001).

Foster, T. D. and Weiss, R. F. Antarctic bottom water formation in the north western weddell sea. *Antarctic Journal of the United States, 23,* (1989).

Frankenstein, G. E. and Garner, R. Equations for determining the brine volume of sea ice from –0.5 to –22.9 ℃. *Journal of Glaciology, 6, 943 – 944,* (1967).

Frew, N. M. Goldman, J. C. Dennett, M. R. Johnson, A. S. Impact of phytoplankton generated surfactants on air-sea gas exchange. *Journal Geophysical Research, 95, 3, 3337 - 3352,* (1990).

Frew, N. M. Air-sea gas transfer: its dependence on wind stress, small scale roughness, and surface films. *Journal of Geophysical Research, 109, 3452 – 3460,* (2004).

Frieβ, U. Wagner, T. Pundt, L. Pfeilsticker, K and Platt, U. Spectroscopic measurements of tropospheric iodine oxide at Neumayer station, Antartica. *Journal Geophysical Research Letters, 28, 1941 - 1944,* (2001).

Frieβ, U. Hollwedel, J. König-Langlo, G. Wagner, T. and Platt, U. Dynamics and chemistry of tropospheric bromine explosion events in the Antarctic coastal region. *Journal of Geophysical Research, 109, D06305, doi: 10.1029/2003JD004133,* (2004).

274

Gabric, A. J. Shepard, J. M. Knight, J. M. Jones, G. Trevena, A. J. Correlations between the satellite derived seasonal cycles of phytoplankton biomass and aerosol optical depth in the Southern Ocean: Evidence for the influence of sea ice. *Global Biogeochemical Cycles, 19, GB4018, doi:10.1029/2005GB002546,* (2005).

Galbany, I. E. and Roy, C. R. Destruction of ozone at the Earth's surface. *Quarterly Journal of Royal Meteorological Society, 106, 449, 599-620,* (1980).

Gallagher, M. W. Beswick, K. M. Coe, H. Ozone deposition to coastal waters. *Quarterly Journal of Royal Meteorological Society, 127, 572, 539 - 558* (2006).

Ganzeveld, L. Helmig, D. Fairall, C. W. Hare, J. and Pozzer, A. Atmosphere-ocean ozone exchange: A global modeling study of biogeochemical, atmospheric, and waterside turbulence dependencies. *Global Biogeochemical Cycles, 23, GB4021, doi:10.1029/2008GB003301,* (2009).

Garland, J. A. and Curtis, H. Emission of iodine from the sea surface in the presence of ozone. *Journal of Geophysical Research, 86, 4, 3183 – 3186,* (1981).

Garland, J. A. Elzerman, A. W. and Penkett, S. A. The mechanism for dry deposition of ozone to seawater surfaces. *Journal of Geophysical Research, 85, 12, 748 - 7492* (1980).

Garratt, J. The Atmospheric Boundary Layer. *Cambridge atmospheric and space science series. Cambridge University Press,* (1992).

Garrison, D. L Ackley, S. F, and Buck, K. R. A physical mechanism for establishing algal populations in frazil ice. *Nature, 306, 363-365, doi:10.1038/306363a0,* (1983).

Garrison, D. L. and Buck, K. R. The biota of Antarctic pack ice in the Weddell Sea and Antartic Peninsula regions, *Polar Biology, 10, 3, 211 – 219,* (1989).

Gershenzon, M. Davidovits, P. Jayne, J. T. Kolb, C. E. Worsnop, D. R. Simultaneous uptake of DMS and ozone on water. *Journal of Physical Chemistry, 105, 29, 7031 - 7036,* (2001).

Ghosal, S. Hemminger, J. C. Bluhm, H. Mun, B. S. Electron Spectroscopy of aqueous solution interfaces reveals surface enhancements of halides. *Science, 307, 5709, 563 – 566,* (2005).

Gloersen, P and Campbell, W. J. Recent variations in Arctic and Antarctic sea-ice covers. *Nature, 352, 33-36, doi:10.1038/352033a0* (1991).

Goldman, J. C. Dennett, M. R. and Frew, N. M. Surfactant effects on air sea gas-exchange under turbulent conditions. *Deep Sea Research Part A, 35, 12, 1953 - 1970,* (1988).

Golden, K. M. Eicken, A. L. Heaton, J. Milner, D. J. Pringle and Zhu, J. Thermal evolution of permeability and microstructure in sea ice. *Geophysical Research Letters, 34, L16501, doi: 10.1029/1007GL030,* (2007).

Goodwin, K. D. North, W. J. and Lidstrom, M. E. Production of bromoform and dibromomethane by giant kelp: Factors affecting release and comparison to anthropogenic bromine sources. *Limnology and Oceanography , 42, 1752 – 734,* (1997).

Gribble, G. The diversity of naturally produced organohalogens. *Chemosphere, 52, 289 – 297,* (2003).

Haas, C. Ice tank investigations of the microstructure of artificial sea ice grown under different boundary conditions during INTERICE II., *Epic publications*, *Alfred Wegner Institute, Germany* (2000).

Hakkinen, P. J. Anesio, A. M. Graneli, W. Hydrogen peroxide distribution, production and decay in boreal lakes. *Canadian Journal of Fisheries and Aquatic Sciences, 61, 8, 1520 – 1527,* (2004).

Happell, J. D. Walace, W. R. Methyl iodide in the Greenland/Norwegian Seas and the tropical Atlantic Ocean: Evidence for photochemical production. *Geophysical Research Letters, 23, 16, 2105 - 2108,* (1996).

Hansson, R. C. Henderson, M. J. Jack, P. Taylor, R. D. Iodoform taste complaints in chloramination. *Water Research, 21, 10, 1265 – 1271,* (1987).

Harper, D. B. Halomethane from halide ions − a highly efficient fungal conversion of environmental significance. *Nature., 315, 55 – 57, doi:10.1038/315055a0*, (1985).

Harris, D. Quantitative chemical analysis, 6[th]edn. *Freeman, W. H. New York, USA* (2002).

Hatch, G. L. Hypoiodous acid, iodine, and iodide determination with leuco crystal violet and N-chlorosuccinimide-succinimide reagents. *Analytical Chemistry, 56, 12, 2238 - 2241,* (1984).

Hayase, S. Yabushita, A. and Kawasaki, M. Heterogeneous reaction of gaseous ozone with aqueous iodide in the presence of aqueous organic species. *Journal of Physical Chemistry A, 114, 19, 6016 - 6021,* (2010).

Hinshaw, V. Ettre, L. Introduction to Open Tubular Gas Chromatography. *Cleveland, OH: Advanstar Communications,* (1994).

Hönninger, G. Leser, H. Sebastian, O. and Platt, U. Ground-based measurements of halogen oxides at Hudson Bay by active LP-DOAS and passive MAX-DOAS. *Geophysical Research Letters, 31, 4, 1 – 5, doi:10.1029/2003GL018982*, (2004).

Hopper, J. F. Peters, B. Yokuchi, Y. Niki, H. Jobson, B. T. Shepson, P. B. Muthuramu, K. Chemical and meterology observations at ice camp SWAN during the 1992 Polar Sunrise Experiment. *Journal of Geophysical Research, 99, 12, 25489 – 25498,* (1994).

Hopper, J. F. Barrie, L. A. Silis, A. Hart, W. Gallant, A. J. and Dryfhout, H. Ozone and metereology during the 1994 Polar Sunrise Experiment. *Journal of Geophysical Research, 103, 1, 1481 – 1492,* (1998).

Holland, M. M. Bitz, C. M. and Tremblay, B. Future abrupt reductions in summer Arctic sea ice. *Geophysical Research Letters, 33, L23503, doi:10.1029/2006GL028024,* (2006).

Houghton, J. T. Ding, Y. Griggs, D. J. Noguer, N. van der Linden, P. J. Dai, X. Maskell, K. Johnson, C. A. Climate Change 2001: The Scientific Basis. *Cambridge University Press, Cambridge, 10,* (2001).

Hughes, C. Malin, G. Turley, C. M. Keely, B. J. Nightingale, P. D. Liss, P. S. The production of iodocarbons by biogenic marine aggregates. *Limnology and oceanography,* 53, 2, 867 – 872, (2008).

Hughes, C. Chuck, A. L. Rossetti, H. Mann, P. J. Turner, S. M. Clarke, A. Chance, R. Liss, P. S. Seasonal cycle of seawater bromoform and dibromomethane concentrations in a coastal bay on the western Antarctic Peninsula. *Global Geochemical Cycles, 23, 13, GB2024, doi:10.1029/2008GB003268,* (2009).

Huang, R. J. and Hoffman, T. Development of a coupled diffusion denuder system combined with gas chromatography/Mass Spectrometry for the separation and quantification of molecular iodine and activated iodine compounds iodine monchloride and hypoiodous acid in the marine atmosphere. *Analytical Chemistry, 81, 5, 1777 – 1783,* (2009).

Hylander, L. D. And Goodsite, M. E. Environmental costs of Mercury pollution. *Science of the Total Environment, 368, 1, 352 – 370,* (2006).

Impey, G. A. Mihele, C. M. Anlauf, K. G. Barrie, L. A. Hastie, D. R. and Shepson, P. B. Measurements of photolyzable chlorine and bromine radicals the Polar Sunrise Experiment 1997. *Journal of Geophysical Research, 102, 1, 16005 – 16010,* (1997).

Ingram, R. Characteristics of the Great Whale River plume. *Journal Geophysical Research, 86, 3, 2017 – 2023,* (1981).

Ingram, T. Cameron, M. and Crowley, J. N. Photodissociation of IO (355 nm) and OIO (532 nm): Quantum yields for $O(^3P)/I$ production. *Journal of Physical Chemistry A, 104, 34, 8010,* (2000).

Ingham, M. Pringle, D. J. and Eicken, H. Cross borehole resistivity tomography of sea ice. *Cold Regoins Science and Technology, 52, 263 - 277,* (2008).

Itoh, N. Tsujita, M. Ando, T. Hisatomi, G. Higashi, T. Formation and emission of monohalomethanes from marine algae. *Phytochemistry, 45, 1, 67 - 73,* (1997).

Jacobi, H. W. Kaleschke, L. Richter, A. Rozanov, A. and Burrows, J. P. Observation of a fast ozone loss in the marginal ice zone of the Arctic Ocean. *Journal of Geophysical Research, 111, 15, D15309,* (2006).

Jerrett, M. Burnett, R. T. Pope, C. M. Ito, K. Thurston, G. T. Krewski, D. K. Shi, Y. Calle, E. Thun, M. Long term ozone exposure and mortality. *New England Journal of Medicine. 360, 11, 1085 – 1095,* (2009).

Jobson, B. T. Yokouchi, Y. Bottenheim, J. W. Hopper, F. and Leaitch, R. Measurements of $C_2 – C_6$ hydrocarbons during the Polar Sunrise 1992 Experiment: Evidence for Cl atom and Br atom chemistry. *Journal of Geophysical Research, 99, 12, 25355 – 25368,* (1994).

Johnson, M. T. A numerical scheme to calculate temperature and salinity dependent air-water velocities for any gas. Ocean science, *6, 4, 913 - 932,* (2010).

Jones. C. E. Aqueous chemistry and photochemistry of volatile organic iodine in seawater. *PhD thesis, Department of chemistry, University of York,* (2006).

Jones, A. E. Anderson, P. S. Wolff, E. W. Turner, J. Rankin, A. M. and Colwell, S. R. A role for newly forming sea ice in springtime polar tropospheric ozone loss? Observational evidence from Halley Station, Antarctica. *Journal of Geophysical Research, 111, D08306, doi: 10.1029/2005JD006566,* (2006).

Jones. C. E. and Carpenter. L. J. Chemical destruction of CH_3I, C_2H_5I, 1-C_3H_7I and 2-C_3H_7I in seawater. *Geophysical Research Letters, 34, 13, 1 – 6, doi:10.1029/2007GL0297775,* (2007).

Jones, C. E. Hornsby, K. J. Sommariva, R. Dunk, R. M Glasow, R. McFiggans, G. Carpenter, L. J. Quantifying sources and atmospheric impact of marine organic iodine gases. *Geophysical Research Letters, 37, 18804, doi: 10.1029/2010GL043990,* (2010).

Kalnajs, L. E. and Avallone, L. M. Frost flower influence on springtime boundary layer ozone depletion events and atmospheric bromine levels. *Geophysical Research Letters , 33, L10810, doi: 10.1029/2006GL025809,* (2006).

Kaltsoyannis, N. and Plane, J. M. C. Quantum chemical calculations on a selection of iodine containing species. (IO, OIO, INO_3, I_2O_2, I_2O_3, I_2O_4 and I_2O_5) of importance in the atmosphere. *Physical Chemisrty Chemical Physics, 10, 1723 – 1733,* (2008).

Kettle, A. J. Andrae, M. O. Amouroux, D. A global database of sea surface DMS measurements and a procedure to predict sea surface DMS as a function of latitude, longitude and month. *Global Biogeochemical Cycles, 13, 2, 399 - 444,* (1999).

Keppler, F. Eiden, R. Niedan, V. Pracht, J. and Scholer, H. Halocarbons produced by natural oxidation processes during degradation of organic matter. *Nature, 403, 298-301* (2000).

Kennedy, H. Thomas, D. Kattner, G. Haas, C. and Dieckmann, G. S. Particulate organic carbon in Antarctic summer sea ice: concentration and stable carbon isotopic composition. *Marine Ecology Progress Series, 238, 1, 1 - 13,* (2002).

Kolb, C. Atmospheric chemistry : Iodine's air of importance. *Nature, 417, 597 – 598,* (2002).

Kramm, G. Dlugi, R. Dollard, G. J. Foken, T. Molders, N. Muller, H. Seiler, W. Sievering, H. On the dry deposition of ozone and reactive nitrogen species. *Atmospheric Environment, 29, 21, 3209 - 3231* (1995).

Krembs, C. Eicken, H. Junge, K and Deming, J.W. High concentrations of exopolymeric substances in Arctic winter sea ice; implications for the Polar ocean carbon cycle and cryoprotection of diatoms. *Deep Sea Research I, 49, 2163 – 2181,* (2002).

Kuhn, M. and Siogas, L. Spectroscopic studies at McMurdo Southpole and Siple stations during the austral summer 1977-78. *Antarctic Journal of U.S, 13, 178 - 179,* (1978).

Kupper, F. C. Carpenter, L. J. McFiggans, G. B. Palmer, C. J. Waite, T. J. Boneberg, E. Woitsch, S. Weiller, M. Abela, R. Iodide accumulation provides kelp with an inorganic antioxidant impacting atmospheric chemistry. *PNAS., 105, 6954 - 6958* (2008).

Laliberte, M. Model for calculating the viscosity of aqueous solutions. *Journal of Chemical Engineering Data, 52, 2, 321 - 335,* (2007).

Lambert, J. *Fina, L. R. U.S. Patent 3, 923, 665,* (1975).

Lancaster, P. A. Photomultiplier Handbook. *Burle Industries,* (1980).

Laturnus, F. Release of volatile halogenated organic compounds by unialgal cultures of polar macroalgae. *Chemosphere, 31, 3387 – 3395,* (1995).

Laturnus, F. Giese, B. Weincke, C. and Adams, F. Low molecular weight organoiodine and organobromine compounds released by polar macroalgae- the influence of abiotic factors. *Journal of Analytical Chemistry, 368, 2-3, 297 – 302,* (2000).

LeBras, G. and Platt, U. A possible mechanism for combined chlorine and bromine catalytic destruction of tropospheric ozone in the Arctic. *Geophysical Research Letters, 22, 599 – 602,* (1995).

Leenheer, J. A. Wershaw, R. L. Reddy, M. M. *Environmental Science and Technology, 29, 2, 399,* (1995).

Legendre, L Ingram, R.G and Poulin, M. Physical control of phytoplankton production under sea ice (Manitounuk Sound, Hudson Bay). *Canadian Journal of Fisheries and Aquatic Science, 38, 11, 1385 - 1392,* (1981).

Legendre, L. Robineau, B. Gosselin, N. Michel, C. Ingram, R.G. Fortier, L. Therriault, S. Impact of freshwater on subarctic coastal ecosystem under seasonal sea ice (south eastern Hudson Bay, Canada). Production and export of microalgae. *Journal of marine systems, 7, 2 - 4, 233 – 250,* (1996).

Lehrer, E. Honniger, G. and Platt, U. A one dimensional model study of the mechanism of halogen liberation and vertical transport in the polar troposphere. *Atmospheric Chemistry and Physics, 4, 11- 12, 2427 – 2440,* (2004).

Lenschow, D. H. Pearson, R. Stankov, B. B. Measurements of ozone vertical flux to ocean and forest. *Journal of Geophysical Research, 87, 11, 8833 – 8837,* (1982).

Levy H. Normal atmosphere – large radical and formaldehyde concentrations predicted. *Science, 173, 3992, 141 – 143,* (1971).

Light, B. Maykut, A. and Grenfell, T. Effects of temperature on the microstructure of first-year Arctic sea-ice. *Journal of Geophysical Research*, 108, 2, 3051, *doi:10.1029/2001JC000887,* (2003).

Lindberg, S. E. Brooks, S. Lin, C. J. Scott, K. J. Landis, M. S. Stevens, R. K. Goodsite, M. and Richter, A. Dynamic oxidation of gaseous mercury in the Arctic troposphere at Polar Sunrise. *Environmental Science and Technology, 36, 6, 1245 – 1256,* (2002).

Lindsay, R. W. and Zheng, J. The thinning of Arctic sea ice, 1988 – 2003. Have we reached a tipping point? *Journal of Climate, 18, 4879 – 4899,* (2005).

Liss, P. S. and Slater, P. G. Flux of gases across the Air-Sea interface. *Nature, 247, 181-184,* (1974).

Liss, P. S. Gas transfer experiment and geochemical implications. *Air-Sea exchange of gases and particles, Riedel, New York, 241 - 298,* (1983).

Loose, B. McGillis, W. R. Schlosser, P. Perovich, D and Takahashi. T. Effects of freezing, growth and ice cover on gas transport processes in laboratory seawater experiments. *Geophysical Research Letters, 36, L05603, doi: 10.1029/2008GL036318* (2009).

Loose, B. Schlosser, P. Perovich, D. Ringelberg, D. Takashi, T. Reynolds, C. M. McGillis, W. R. Tison, J. L. Gas diffusion through columnar laboratory sea ice: implications for mixed-layer ventillation of CO_2 in the seasonal ice zone. *Tellus, 63B, 1, 23 - 39,* (2011).

Lu, J. Y. Schroeder, W. H. Barrie, L. A. Steffen, A. Welch, H. Martin, K. Lockhart, L. Hunt, R. Boila, G. and Richter, A. Magnification of atmospheric mercury deposition to polar regions in springtime: the link to tropospheric ozone depletion chemistry. *Geophysical Research Letters, 28, 17, 3219 – 3222,* (2001).

Lui, Q. Schurter, L. Muller, C. Aloisio, S. Francisco, J. Kinetics and Mechanisms of Aqueous Ozone Reactions with Bromide, Sulfite, Hydrogen Sulfite, Iodide, and Nitrite Ions. *Inorganic Chemistry, 40, 17, 4436 – 4442,* (2001).

Lűpkes, C. Vihma, T. Birnbaum, G. Wacker, U. Influence of leads in sea ice on the temperature of the atmospheric boundary layer during polar night. *Geophysical Research Letters, 35, L03805, doi: 10.1029/2007GL032461,* (2008).

Ma, H. Allen, H. E. and Yin, Y. Characterization of isolated fractions of dissolved organic matter from natural waters and wastewater effluent. *Water Research, 35, 4, 985 - 996,* (2001).

Mahajan, A. S. Plane, J. M. C. Oetjen, H. Mendes, L. Saunders, R. W. Saiz-Lopez, A. Jones, C. E. Carpenter, L. J. and McFiggans. G. B. Measurement and modeling of tropospheric reactive halogen species over the tropical atlantic ocean. *Atmospheric Chemistry and Physics, 10, 4611 - 4624,* (2010).

Mahajan, A. S. Shaw, M. D. Oetjen, H. Evidence of reactive iodine chemistry in the Arctic boundary layer. *Journal of Geophysical Research, 115, 11,* D20303, *doi:10.1029/2009JD013665*, (2010).

Mäkelä, J. Hoffmann, T. Holzke, C. Väkevä, M. Suni, T. Mattila, T. Aalto, P. Tapper, U. Kauppinen, E. and O'Dowd, C. Biogenic iodine emissions and identification of end products in coastal ultra-fine particles during nucleation bursts. *Journal of Geophysical Research, 107, 8110,* (2002).

Mallik, B. Chakravarti, B. Chakravarti, D. Current Protocols and Essential Laboratory techniques. *doi: 10.1002/9780470089941.et0601s00,* (2008).

Manley, S. L. Barbero, P. E. Physiological constraints on bromoform production by Ulva lactuca (Chlorophyta). *Limnology and Oceanography, 46, 1392 – 1399,* (2001).

Martin, S. Frazil ice in rivers and oceans. *Annual review of fluid mechanics. 13, 379-397, doi: 10.1146/annurev.fl.13.010181.002115,* (1981).

Martino, M. Mills, G. P. Woeltjen, J. Liss, P. S. A new source of organoiodine compounds in surface seawater. *Geophysical Research Letters, 36, L01609, doi:10.1029/2008GL036334,* (2009).

Mason, R. P. Fitzgerald, W. F. and Morrel, F. M. M. The Biogeochemical cycling of elemental mercury- Anthropogenic influences. *Geochimica et Cosmochimica Acta, 58, 15, 3191 – 3198* (1994).

Matveev, V. Peleg, M. Rosen, D. Siman, D. Alper, T. Hebestriet, K. Stutz, J. Platt, U. Blake, U. Blake, D. Menachem, L. Bromine oxide – ozone interaction over the Dead Sea. *Journal of Geophysical Research, 106, D10, 10375 – 10387,* (2001).

McElroy, C. T. McLinden, C. A. and McConnell, J. C. Evidence for bromine monoxide in the free troposphere during the Arctic Polar sunrise. *Nature, 397, 338 – 341,* (1999).
McFiggans, G. B. Coe, H. Burgess, R. Allan, J. Cubison, M. Alfarra, M. R. Saunders, R. Saiz-Lopez, A. Plane, J.M.C. Carpenter, L. J. Wevill, D. J. Rickard, A. R. and Monks, P. S. Direct evidence for coastal iodine particles from *Laminaria* macroalgae – linkage to emissions of molecular iodine. *Atmospheric Chemistry and Physics, 4, 701 – 713,* (2004).

McConnell, J. C. Henderson, G. S. Barrie, L. Bottenheim, J. Niki, H. Langford, C. H. and Templeton, E. Photochemical bromine production implicated in Arctic boundary layer ozone depletion. *Nature, 355, 150 - 152,* (1992).

McMinn, A. Skerratt, J. Trull, T. Ashworth, C and Lizotte, M. Nutrient stress gradient in the bottom 5cm of fast ice, McMurdo Sound, Antarctica. *Polar Biology, 21, 4, 220-227,* (1999).

McPhee, M. G. Ackley, S. F. Guest, P. Huber, B. A. Martinson, D. G. Morison, J. H. Muench, R. D. Padman, L. Stanton, T. P. The Antarctic Zone Flux Experiment. *Bulletin of the American Meterological Society 77, 6, 1221 – 1232*, (1996).

Millero, F. Waters, J. Woolsley, R. Huang, F. and Chanson, M. The effect of composition on the density of Indian Ocean waters. *Deep Sea Research part I: Oceanography papers, 55, 4, 460 – 470,* (2008).

Miyake, Y. and Tsunogai, S. Evaporation of iodine from the ocean. *Journal of Geophysical Research, 68, 3989 - 3993,* (1963).

Mmereki, B. and Donaldson, D. J. Direct observation of the kinetics of an atmospherically important reaction at the air-water interface. *Journal of Physical Chemistry A, 107, 50, 11038 – 11042,* (2003).

Molina, M. and Rowland, F. S. Stratospheric sink for chlorofluoromethanes-chlorine atomic catalysed destruction of ozone. *Nature, 249, 810 – 812,* (1974).

Moller, A. Lovric, M. Scholz, F. Evidence for the occasional appearance of molecular iodine in seawater. *International Journal of Environmental Analytical Chemistry, 63, 2, 99 – 106,* (1995).

Monks, P. S. Gas phase radical chemistry in the troposphere. *Chemical Society Reviews, 34, 376 – 395,* (2005).

Moody, H. W. The Evaluation of the Parameters for the Van Deemter Equation. *Journal of Chemical Education, 59, 290,* (1982).

Moore, R. M. and Zafirou, O.C. Photochemical production of methyl iodide in seawater. *Journal of Geophysical Research, 99, 16415 – 16420*, (1994).

Moore, R. M. Webb, M. Tokarczyk, R. Wever, R. Bromoperoxidase and iodoperoxidase enzymes and production of halogenated methanes in marine diatom cultures. *Journal of Geophysical Research, 101, 9, 20899 – 20908,* (1996).

Moortgat, G. Meller, R. Schneider, W. Temperature dependence (256 – 296K) of the absorption cross section of bromoform in the wavelength range 285 – 360 nm, in: Tropospheric Chemistry of ozone in Polar regions, NATO ASI. *Global environmental change, 359 – 370,* (1993).

Morrison, J. Mcphee, M. Curtin, T. and Paulson, C. The oceanography of winter leads. *Journal of Geophysical Research, 97, 7, 11199 - 11218,* (1992).

Muller, J. F. Geographical distribution and seasonal variation of surface emissions and deposition velocities of atmospheric trace gases. *Journal Geophysical Research, 97, 4, 3787 - 3804* (1992).

Nakawo, M. and Sinha, N.K. Growth rate and salinity profile of first year sea-ice in the high Arctic. *Journal of Glaciology, 27, 96, 315 – 330,* (1981).

Nightingale, P. D Malin, G. Law, C. S. Watson, A. J. Liss, P. S. Liddicoat, M. I. Boutin, J. Upstill-Goddard, R. C. In situ evaluation of air-sea gas exchange parameterizations using novel conservative and volatile tracers. *Global Biogeochemical Cycles, 14, 1, 373 - 387,* (2000).

Obbard, R. W. Roscoe, H. W. Wolff, E. W. and Atkinson, H. M. Frost flower surface area and chemistry as a function of salinity and temperature. *Journal of Geophysical Research, 114, D20, 305 – 314,* (2009).

O'Doherty, S. Simmonds, P.G. Cummold, C. M. Wang, H. J. Sturrock, G. A. Fraser, P. J. Ryall, D. In situ chloroform measurements at Advanced Global Atmospheric Gases Experiment at research stations from 1994 to 1998. *Journal of Geophysical Research, 106, 429 – 444,* (2001).

O'Dowd, C. D. Jimenez, J. L. Bahreini, R. Flagan, R. C. Seinfeld, J. H. Hameri, K. Pirjola, L. Kulmala, M. Jennings, S. G. Hoffmann, T. Marine aerosol formation from biogenic iodine emissions. *Nature, 417, 632 – 636,* (2002).

O'Dowd, C. D. and Hoffmann, T. Coastal new particle formation: A review of the current state of the art. *Environmental Chemistry, 2, 245 – 255,* (2005).

Oh, I. B. Byun, D. W. Kim, H. C. Kim, S. and Cameron, B. Modelling the effect of iodide distribution on ozone deposition to seawater surface. *Atmospheric environment, 42, 19, 4453 - 4466* (2008).

Ono, N. and Kasai, T. Surface layer salinity of young sea ice. *Journal of Glaciology, 6, 298 - 299,* (1985).

Oostdam, J. V. Donalson, S. Feeley, M. Arnold, D. Ayotte, P. Bondy, G. Chan, E. Dewaily, C. Furgal, C. Kuhnlein, H. Loring, E. Muckle, G. Myles, E. Receveur, O. Tracy, B. Gill, U. and Kalhok, S. Human health implications of environmental contaminants in Arctic Canada: a review. *The science of the total environment, 230, 1-3, 1 - 82,* (2005). Ozone Secretariat United Nations Environment Programme (Ed.). *Handbook for the Montreal Protocol on substances that deplete the ozone layer, 7, 9,* (2006).

Palmer, C. J. Carpenter, L. J. Kupper, F. and McFiggans, G. B. Iodine and halocarbon response of *Laminaria Digitata* to oxidative stress and links to atmospheric new particle production. *Environmental Chemistry, 2, 282 – 290,* (2005).

Palmer, D. A. and Lietzke, M. H. The equillibria and kinetics of iodine hydrolysis. *Rad Chimica Acta*, *31, 37 – 44,* (1982).

Paquette, J. and Ford, B. L. Iodine chemistry in the +1 oxidation state. The electronic spectra of OI^-, HOI and H_2OI^+. *Canadian Journal of Chemistry, 63, 9, 2444 – 2448,* (1985).

Parthipan, R. Aqueous chemistry of iodine in seawater: potential chemical sources of iodine in the marine atmosphere. *Ph.D. Thesis, Department of Chemistry, University of York, York, 67 - 68, 78 - 80, 177 – 187,* (2008).

Pedder, R. E. Practical Quadrupole Theory: Graphical Theory. *Extrel Application Note RA_2010A,* (2010).

Perovich, D. K. Theoretical estimates of light reflection and transmission by spatially complex and temporally varying sea ice covers. *Journal of Geophysical Research, 95, 6, 9557 - 9567,* (1990).

Petrich, C. Langhorne, P. J and Sun, Z. F. Modelling the interrelationships between permeability, effective porosity and total porosity in sea-ice. *Cold Regions Science and Technology, 44, 2, 131 – 144,* (2006).

Piot, M. and von Glasow, R. The potential importance of frost flowers, recycling on snow, and open leads for ozone depletion events. *Atmospheric Chemistry and Physics Discussion, 7, 4521 – 4595,* (2007).

Platt, U. and Lehrer, U. Arctic Tropospheric Ozone Chemistry, ARTOC. *Report of the EU-Project NO. EV5V-CT93-0318,* (1996).

Platt, U. and Honninger, G. The role of halogen species in the troposphere. *Chemosphere., 52, 2, 325 – 338,* (2003).

Poling, B. Pruasnitz, J. O'Connell, J. The properties of gases and liquids. *McGraw Hill, New York, 5th edition,* (2001).

Pringle, D. J. Miner, J. E. Eicken, H. and Golden K. M. Pore space percolation in sea-ice crystals. *Journal of Geophysical Research, 114, C12017, doi:10.129/2008JC005145,* (2007).

Prinn, R. G. Weiss, R. Miller, B. Huang, J. Alyea, F. Cunnold, D. Fraser, P. Hartley, D. Simmonds, P. Atmospheric trends and lifetimes of $CHCCl_3$ and global OH concentrations. *Science, 269, 8, 9, 187 – 192,* (1995).

Prinn, R. G. The cleansing capacity of the atmosphere. *Annual Review of Environment and Resources*, *28, 29 – 57*, (2003).

Rajendran, P. Aqueous chemistry of iodine in seawater: potential chemical sources of iodine in the marine atmosphere, Ph.D. Thesis, Department of Chemistry, University of York, 67 - 68, 78 - 80, 177 - 187 (2008).

Rankin, A. M. Wolff, E. W. and Martin, S. Frost flowers: Implications for troposheric chemistry and ice core interpretation. *Journal of Geophysical Research, 107, D23, 4683, doi:10.1029/2002JD002492* (2002).

Raofie, F. and Ariya, P. A. Product study of the gas phase BrO-initiated oxidation of HgO: evidence for stable Hg^{2+} compounds. *Environmental Science Technology, 38, 16, 4319 - 4326,* (2004).

Raofie, F. and Ariya, P. A. Reaction of gaseous mercury with molecular iodine and iodine radicals: Kinetics, product states, and atmospheric implications, in: *AGU Fall meeting, San Francisco,* (2006).

Rattigan, O. V. Cox, R. A. and Jones, R. L. Br_2 sensitized decomposition of ozone: kinetics of the reaction $BrO + O_3 \rightarrow$ products. *Faraday Transactions, 91, 4189 – 4197,* (1995).

Razumovski, S. D. and Zaikov, G. E. The solubility of ozone in various solvents. *Russian Chemical Bulletin, 20, 4, 686 – 691,* (1971).

Read, K. A. Mahajan, A. S. Carpenter, L. J. Evans, M. J. Faria, B. Heard, D. E. Hopkins, J. R. Lee, J. D. Moller, S. J. Lewis, A. C. Mendes, L. McQuaid, J. B. Oetjen, H. Saiz-Lopez, A. Pilling, M. J. Plane, J. M. C. Extensive halogen mediated ozone destruction over the tropical Atlantic Ocean. *Nature., 453, 1232 – 1235, doi:10.1038/nature07035,* (2008).

Redeker, K. R. Wang, N. Y. Low, J. C. McMillan, A. Tyler, S. J. and Cicerone, R. C. Emissions of methyl halides and methane from rice paddies. *Science, 290, 966 – 969,* (2000).

Regener, V. H. Destruction of atmospheric ozone at the ocean surface. *Meterology and Atmospheric Physics, 23, 2, 131 - 135,* (1974).

Reifenhauser, W. and Heumann, K. G. Bromo- and Bromochloromethanes in the Antarctic atmosphere and the South Polar Sea. *Chemosphere, 24, 9, 1293 - 1300,* (1992).

Richardson, C. Phase relationships in sea ice as a function of temperature. *Journal of Glaciology, 17, 77, 507 – 519,* (1976).

Richter, U. and Wallace, D. W. R. Production of methyl iodide in tropical Atlantic Ocean. *Geophysical Research Letters, 31, L23303, doi:10.1029/2008JC005145,* (2004).

Riemer, D. D. Milne, P. J. Zika, R. G. Pos, W. Photoproduction of non methane hydrocarbons (NMHCs) in seawater. *Marine Chemistry, 71, 3 - 4, 177 - 198,* (2000).

Roscoe, H. K. Brooks, B. Jackson, A. V. Smith, M. H. Walker, S. J. Obbard, R. W. Wolff, E. W. Frost flowers in the laboratory: Growth, characteristics, aerosol, and the underlying sea ice. *Journal of Geophysical Research, 116, D12, 301 – 312,* (2011).

Rowland, G. and Grannas, A. A solid phase chemical actinometer film for measurement of solar UV penetration into snowpack. *Cold Regions Science and Technology, 66, 2–3, 75–83,* (2011).

Poulin, M. Cardinal, A Legendre, L. Reponse d'une communaute de diatomees de glace a un gradient de salinite (Baie d Hudson). *Marine Biology, 76, 2, 191 – 202,* (1983).

Saiz-Lopez, A. S. Plane, J. M. C. Novel iodine chemistry in the marine boundary layer. *Geophysical Research Letters, 31, 4, L04112*, *doi:10.1029/2003GL019215* (2004).

Saiz-Lopez, A. Plane, J. M. C. McFiggans, G. B. Williams, P. I. Ball, S. M. Bitter, M. Jones, R. L. Hongwei, C. and Hofmann, T. Modelling molecular iodine emissions in a coastal marine environment: the link to new particle formation. *Atmospheric Chemistry and Physics, 6, 4, 883 – 895,* (2006).

Saiz-Lopez, A. Mahajan, A. S. Salmon, R. A. Bauguitte, S. J. Jones, A. E. Roscoe, H. K. Plane, J. M. C. Schönhardt, A. Richter, A. Wittrock, F. Kirk, H. Oetjen, H. Roscoe, H. K. Burrows, J. P. Boundary layer halogens in coastal Antarctica. *Science, 317, 5836, 348 – 351,* (2007).

Saiz-Lopez, A. and Boxe, C. S. A mechanism for biologically induced iodine emissions from sea-ice. *Atmospheric Chemistry and Physics Discussions*, 8, 2953 - 2976, *doi:10.5194/acpd-8-2953-2008*, (2008).

Sakamoto, Y. Yabushita, A. and Kawasaki, M. Direct emission of I_2 molecule and IO radical from the heterogeneous reactions of gaseous ozone with aqueous potassium iodide solution. *Journal of Physical Chemistry A, 113, 27, 7707 – 7713,* (2009).

Sander, R. Rudich, Y. von Glasow, R. and Crutzen, P. J. The role of $BrNO_3$ in marine tropospheric chemistry : A model study. *Geophysical Research Letters, 26, 18, 2857 – 2860,* (1999).

Sander, R. Inorganic bromine in the marine boundary layer: a critical review. *Atmospheric Chemistry and Physics, 3, 1301 – 1336,* (2003).

Sander, R. Burrows, J. Kaleschke, L. Carbonate precipitation in brine- the trigger for tropospheric ozone depletion events. *Atmospheric Chemistry and Physics Discussions, 6, 4653 – 4658,* (2006).

Sartor, F. Snacken, R. Demuth, C. Walckiers, D. Temperature, ambient ozone levels and mortality during summer, 1994, in Belgium. *Environmental Research, 70, 2, 105 – 113,* (1995).

Saunders, R. Plane, J. M. C. Formation pathways and composition of iodine oxide ultrafine particles. *Environmental Chemistry, 2, 4, 299 – 303,* (2005).

Saunders, R. W. Kumar, R. Martin, J. C. Mahajan, A. S. Murray, B. J. and Plane, J. M. C. Studies of the formation and growth of aerosol from molecular iodine precursor. *Journal of Physical Chemistry, 224, 7- 8, 1099 - 1117,* (2010).

Schall, C. and Heumann, K. G. GC determination of volatile organoiodine and organobromine compounds in Arctic seawater and air samples. *Journal of Analytical Chemistry, 346, 6 - 9, 717 – 722,* (1993).

Schall, C. Laturnus, F. and Heumann, K. G. Biogenic volatile organoiodine and organobromine compounds released from polar macro algae. *Chemosphere, 28, 7, 1315 – 1324,* (1994).

Schroeder, W. H. and Munthe, J. Atmospheric mercury- An overview. *Atmospheric Environment, 32, 5, 809 – 822,* (1998).

Schroeder, W. H. Anlauf, K. G. Barrie, L. A. Lu, J. Y. Steffen, A. Schneeberger, D. R. and Berg, T. Arctic springtime depletion of mercury. *Nature, 394, 331- 332,* (1998).

Schonhardt, A. Richter, F. Wittrock, H. Kirk, H. Oetjen, H. Roscoe, H. K. and Burrows, J. P. Observations of iodine monoxide (IO) columns from satellite. *Atmospheric Chemistry and Physics, 8, 637 – 653,* (2008).

Schwartz, S. E. Factors governing dry deposition of gases to surface water. *Precipitation Scavenging and Atmosphere-Surface Exchange, 2, 789-801,* (1992).

Sellegri, K. Yoon, Y. J. Jennings, S. G. O'Dowd, C. D. Pirjola, L. Cautenet, S. Chen, H. and Hoffmann, T. Quantification of Coastal new ultra fine particles formation from in-situ and chamber measurements during the BIOFLUX campaign. *Environmental Chemistry, 2, 4, 260,* (2005).

Sherrill, J. Whitaker, B. R. Wong, G. T. F. Effects of ozonation on the speciation of dissolved iodine in artificial seawater. *Journal of Zoo and Wildlife Medicine, 35, 3, 347-355,* (2005).

Skoog, D. West, D. Holler, F. Fundamentals of Analytical Chemistry, sixth edition. *Saunders College publishing,* (1991).

Siedel. C. Personal correspondence. Hobby marine salt sales representative, (2010).

Simpson, W. R. King, M. Beine, H. Honrath, R. and Peterson, M. Atmospheric photolysis rate coefficients during the Polar Sunrise Experiment ALERT 2000. *Atmospheric Environment, 36, 2471 – 2480,* (2002).

Simpson, W. R. Alvarez-Aviles, L. Douglas, T. A. Sturm, M. and Domine, F. Halogens in the coastal snow pack near Barrow, Alaska: Evidence for active bromine air-snow chemistry during springtime. *Geophysical Research Letters, 32, L04811, doi: 10.1029/2004GL021748,* (2005).

Simpson, W. R. Carlson, D. Honninger, G. Douglas, T. A. Sturm, M. Perovich, D. and Platt, U. First year sea-ice contact predicts bromine monoxide levels better than potential frost flower contact. *Atmospheric Chemistry and Physics Discussions, 6, 11051 - 11066,* (2006).

Simpson, W. R. von Glasow, R. Riedel, K. Anderson, P. Ariya, P. Bottenheim, J. W. Burrows, J. Carpenter, L. J. Frieβ, U. Goodsite, M. E. Heard, D. Hutterli, M. Jacobi, H. Halogens and their role in polar boundary layer ozone depletion. *Atmospheric Chemistry Physics, 7, 2, 4375 - 4418* (2007).

Slemr, F. Brunke, E. G. Ebinghaus, R. Temme., C. Munthe, J. Wangberg, L. Scroeder, W. Steffen, A. and Berg, T. Worldwide trend of atmospheric chemistry mercury since 1977. *Geophysical Research Letters, 30, 10, 1516,* (2003).

Solberg, S. Schmidbauer, N. Semb, A. and Stordal, F. Boundary layer ozone depletion as seen in the Norwegian Arctic in spring. *Journal of Atmospheric Chemistry, 23, 3, 301 – 332,* (1996).

Spicer, C. W. Plastridge, R. A. Foster, K. L. Finlayson-Pitts, B. J. Bottenheim, J. W. Grannas, A. M. and Shepson, P. B. Molecular halogens before and during ozone depletion events in the Arctic at polar sunrise: concentrations and sources. *Atmospheric Environment, 36, 15 - 16, 2721 - 2731,* (2002).

Springer, T. G. and Pigford, R. L. Influence of surface turbulence and surfactants on gas transport through liquid interfaces. *Industrial Engineering and Chemistry Fundamentals, 9, 3, 458-465,* (1970).

Stavn, H. R. The horizontal-vertical distribution hypothesis:- Langmuir circulations and *Daphnia* distributions. *Limnology and Oceanography, 16, 2, 453 – 466*, (1971).

Sturges, W. T. Cota, G. F. and Buckley, P. T. Bromoform emission from Arctic ice algae. *Nature, 358, 660 – 662, doi:10.1038/358660a0,* (1992).

Sturges, W. T. and Shaw, G. E. Halogens in aerosols in central Alaska. *Atmospheric Environment, 27, 17 - 18, 2969 – 2977,* (1993).

Sturges, W. Cota, G. Buckley,P. Vertical profiles of bromoform in snow, sea ice and seawater in the Canadian Arctic. *Journal of Geophysical Research, 102, 11, 25073 - 25083,* (1997).

Swanson, A. J. Blake, N. J. Dibb, J. E. Albert, M. R. Blake, D. R. and Rowland, F. S. Photochemically induced production of CH_3Br, CH_3I, C_2H_5I, ethane and propene within surface snow at Summit, Greenland. *Atmospheric Environment, 36, 15 – 16, 2671 – 2682,* (2002).

Tanning, L. M. and Fanning, K. A. ^{222}Rn and ^{226}Ra: indicators of sea-ice effects on air-sea gas exchange. *Norsk Polarinstitutt, Polar Research 10, 1, 51 – 58,* (1991).

Taguchi, S. Smith, R. Shirasawa, K. Effect of silicate enrichment on ice algae at low salinity in Saroma-Ko lagoon, Hokkaido, Japan. *Journal of Marine Systems, 11, 1 – 2, 45 – 52,* (1997).

Tarasick, D. W. and Bottenheim, J. W. Surface ozone depletion episodes in the Arctic and Antarctic from historical ozonesonde records. *Atmospheric Chemistry and Physics, 2, 3, 197 – 205,* (2002).

Thomas, D. N, Lara, R. J. Eicken, H. Kattner, G. and Skoog, A. Dissolved organic matter in Arctic multi-year sea ice during winter: major components and relationship to ice characteristics. *Polar Biology, 15, 477 - 483*, (1995).

Thomas, D. N. Lara, R. J. Haas, C. Shnach, S. Dieckmann, G. S. Kattner, G. Nothig, E. Biological soup within decaying summer sea ice in the Amundsen Sea, Antarctica. *Antarctic Research Series, AGU, 161 – 171,* (1998).

Thomas, D. N. and Dieckmann, G. S. Sea ice: An introduction to its Physics, Chemistry, Biology and Geology. *Blackwell, Oxford, U.K,* (2003).
Thomas, D and Papadimitriou, S. Biogeochemistry of Sea ice *: An Introduction to it's physics, chemistry, biology and geology,* (2008).

Thurman, E. M. Organic geochemistry of natural waters. Part one, organic carbon in natural waters: Amount, origin and classification. *Kluwer Academic Publishers, 5, 1,* (1985).

Tokarczyk, R. and Moore, R. M. Production of volatile organohalogens by phytoplankton cultures. *Geophysical Research Letters, 21, 4, 285 – 288,* (1994).

Truesdale, V. W. On the feasibility of some photochemical reactions of iodide in seawater. *Marine Chem*istry, 104, 3 - 4, 266 - 281, (2007).

Turekian, K. *Oceans, Prentice-Hall* (1968).

Tyn, M. and Klaus, W. Diffusion coefficients in dilute binary liquid mixtures. *Journal of Chemical Engineering Data, 20, 1, 106 -109,* (1975).

Tyshko, K. P. Fedotov, I. V. and Cherepanov, I. V. Spatio-temporal variability of the Arctic sea's ice cover structure. *Sea ice Gidrometereoizdat, 191 – 213,* (1997).

Van Dingenen, R. Dentener, F. J. Raes, F. Krol, M. C. Emberson, L. Cofala, J. The global impact of ozone on agricultural crop yields under current and future air quality legislation. *Atmospheric Environment, 43, 3, 604 – 618,* (2009).

Vikis, A. C. MacFarlane, R. Reaction of iodine with ozone in the gas phase. *Journal of Physical Chemistry, 85, 5, 812 – 815,* (1985).

Vogt, R. Crutzen, P. J. and Sander, R. A mechanism for halogen release from sea salt aerosol in the remote marine boundary layer. *Nature, 383, 327 – 330,* (1996).

Vogt, R. Sander, R. von Glasow, R. and Crutzen, P. J. Iodine chemistry and its role in halogen activation and ozone loss in the marine boundary layer: A model study. *Journal of Atmospheric Chemistry, 32, 375 – 395,* (1999).

Vogt, R. Sander, R. von Glasow, R. and Crutzen, P. J. Iodine chemistry and its role in halogen activation and ozone loss in the marine boundary layer: a model study. *Journal of Atmospheric Chemistry, 32, 3, 375 – 395,* (1999).

von Glasow, R. and Crutzen, P. J. Model study of multiphase DMS oxidation with a focus on halogens. *Atmospheric Chemistry and Physics, 4, 589 – 608,* (2004).

von Glasow, R. and Crutzen, P. J. Tropospheric halogen chemistry in the atmosphere. *Treatise on Geochemistry, 4, 21 – 64,* (2003).

von Glasow, R. Atmospheric chemistry in volcanic plumes. *PNAS, 107, 15, 6594 – 6599,* (2010).

Wada, R. Beames, J. Orr-Ewing, A. J. Measurement of IO radical concentrations in the marine boundary layer using a cavity ring-down spectrometer. *Journal of Atmospheric Chemistry, 58, 1, 69 - 87,* (2007).

Wagner, T. Leue, C. Wenig, M. Pfeilsticker, K. and Platt, U. Spatial and temporal distribution of enhanced boundary layer BrO concentrations measured by the GOME instrument aboard ERS-2. *Journal of Geophysical Research, 106, 20, 24225 – 24235,* (2001).

Wall, M. Tarnovsky, A. N. Pascher, T. Sundstrom, V. and Akesson, E. Photodissociation dynamics of iodoform in solution. *Journal of Physical Chemistry A, 107, 2, 211 – 217,* (2003).

Wayne, R. Earth's troposphere. *Chemistry of Atmospheres, Oxford University Press, Oxford, 208 – 275,* (1991).

Wayne, R. P. Poulet, G. Biggs, P. Burrows, J. P. Cox, R. A. Crutzen, P. J. Hayman, G. D. Jenkin, M. E. Le Bras, G. K. Moortgat, G. Platt, U. and Schindler, R. N. Halogen oxides: radicals, sources and reservoirs in the laboratory and in the atmosphere. *Atmospheric Environment, 29, 20, 2677 – 2884,* (1995).

Wayne, R. Chemistry of Atmospheres (3rd Edition). Oxford University Press, *Oxford, 2, 5, 22, 23.* (2000).

Weeks, W. and Lofgren, G. The effective solute distribution coefficient during the freezing of NaCl solutions. *Physics of Snow and Ice, 1, 1, 579 – 597,* (1967).

Weeks, W. F. and Ackley S. F. The growth, structure and properties of sea-ice. *Geophysics of Sea ice, N Untersteiner Ed, New York, 99 - 164,* (1986).

Wesely, M. S. Cook, D. R. and Williams, R. M. Field measurements of small ozone fluxes to snow, wet bare soil and lake water. *Bound-Layer Meteorology, 20, 4, 459 - 471,* (1981).

Wevill, D. J., and Carpenter, L. J. Automated measurement and calibration of reactive volatile halogenated organic compounds in the atmosphere. *The Analyst, 129, 634-638,* (2004).

Wilke, C. R and Chang, P. Correlation of Diffusion Coefficients in dilute solutions. *A.I.Ch.E. Journal, 1, 2, 264 - 270,* (1955).

Witmann, C. Fluxome Analysis using GC/MS. *Microbial cell Factories, 6, 6, doi: 10.1186/1475-2859-6-6,* (2007).

Wong, L. Dissolved inorganic and particulate iodine in the oceans, *PhD. Dissertation, Woods Hole Oceanographic Institute,* (1976).

Wuosmaa, A. M. and Hager, L. P. Methyl-chloride transferase- a carbocation route for biosynthesis of halometabolites. *Science, 249, 4965, 160 – 162,* (1990).

Yang, J. Honrath, R. E. Peterson, M. C. Dibb, J. E. Sumner, A. L. Shepson, P. B. Frey, M. Jacobi, H. W. Swanson, A. and Blake, N. Impacts of snowpack emissions on deduced levels of OH and peroxy radicals at Summit, Greenland. *Atmospheric Environment, 36, 15 - 16, 2523 – 2534,* (2002).

Yang, X. Pyle, J. A. Cox, R. A. Theys, N. and Van Roozendael, M. *Atmospheric Chemistry and Physics, 10, 7763 – 7773,* (2010).

Yokouchi, Y. Barrie, L. A. Toom, D. Akimoto, H. The seasonal variation of selected natural and anthropogenic halocarbons in the arctic troposphere. *Atmospheric Environment, 30, 10 - 11, 1723 – 1727,* (1996).

Zhang, J. Spitz, Y. Steele, M. Ashjan, C. Campbell, R. Berline, L. Matrai, P. Modelling the impact of declining sea ice on the Arctic marine phytoplanktonic ecosystem. *Journal of Geophysical Research 115, C10015, doi:10.1029/2009JC005387,* (2010).

Zhou, X. Mopper, K. Photochemical production of low molecular weight carbonyl compounds in seawater and surface microlayer and their air-sea exchange. *Marine Chemistry, 56, 3 - 4, 201- 214,* (1997).

Zotikov, I. A. Zagorodnov, V. S. and Raikovsky, J. V. Core drilling through the Ross Ice Shelf (Antarctica) confirmed Basal freezing. *Science, 207, 4438, 1463 - 1465,* (1980).